UAB
Universitat Autònoma de Barcelona

Departament de Química, Facultat de Ciències

Programa de Ciència de Materials

Universitat Autònoma de Barcelona

Nerea Murillo Cremaes

Multifunctional silica-based nanoparticles for biomedical applications

DOCTORAL THESIS

Supervised by Dr. Anna Roig Serra and Dr. Concepción Domingo Pascual

Tutor Prof. Jose Antonio Ayllón Esteve

2014

ICMAB   **CSIC**
Consejo Superior de Investigaciones Científicas

Dra. Anna Roig Serra i Dra. Concepción Domingo Pascual, Investigadoras Científicas del CSIC, i el **Dr. Jose Antonio Ayllón Esteve**, Titular d'Universitat, UAB

CERTIFIQUEN:

Que na Nerea Murillo Cremaes, Llicenciada en Química per la "Universidade de Vigo", Espanya, ha dut a terme aquesta tesis doctoral sota la seva direcció i que porta per títol **"Multifunctional silica-based nanoparticles for biomedical applications",** la qual queda recollida en aquesta memòria per optar al grau de Doctor.

I perquè així consti, signen el present certificat

Dr. Anna Roig Serra   Dr. Concepción Domingo Pascual   Prof. Jose Antonio Ayllón Esteve

Nerea Murillo Cremaes

Bellaterra, 22 de setembre 2014

Mais, si tu m'apprivoises nous aurons besoin l'un de l'autre. Tu seras pour moi unique au monde. Je serai pour toi unique au monde...

But if you tame me, then we shall need each other. To me, you will be unique in the entire world, to you; I shall be unique in the entire world...

Le Petit Prince. Antoine de Saint-Exupéry, French writer.

Acknowledgements

En primer lugar quiero agradecer a mis directoras de tesis Dr. Anna Roig y Dr. Concepción Domingo que me brindasen la oportunidad de formar parte de sus respectivos grupos de investigación para comenzar un nuevo proyecto común. Durante el desarrollo de esta tesis siempre han estado disponibles para mis dudas, inquietudes, alegrías y problemas haciéndome ver que todo es relativo y muy probablemente mejor de lo esperado.

En especial quiero agradecerte, Anna, tu paciencia infinita y sobre todo tu gran capacidad pedagógica. Ante cualquier cruce de caminos has sabido mostrar con lógica razonada porqué ambos merecían ser considerados. Puedo asegurar que a tu lado se aprende mucho, tanto a nivel profesional como personal.

Concha, muchas gracias por tu apoyo constante y esa gran fuerza que has demostrado siempre para salir de las dificultades e incluso transformarlas en anécdotas divertidas y positivas.

I am grateful to you, Pascale. You were all the time available for me in Bordeaux even when we were running out of time. I appreciate a lot the large discussions about supercritical fluids and thermodynamics that helped me to understand a bit more what was happening around our supercritical (or not) fluids.

Xavi, muchas gracias por tu fructífera ayuda en la utilización y posterior discusión de resultados "raros raros" con el HPLC.

Muchas gracias a "las chicas de administración", por su eficiente e imprescindible trabajo y estar siempre dispuestas a ayudar en todo lo posible con ese buen humor. También gracias a Don Vicentini, con el que las tediosas sesiones de papeleo incomprensible se hacen divertidas. Verte aparecer es sinónimo de pasar un buen rato.

Durante todos estos años en el ICMAB he ido conociendo a muchísima gente que de verdad merece la pena. En concreto me gustaría mencionar a ciertas personas cuya presencia ha tenido un valor incalculable traspasando de largo lo meramente profesional. Una mención muy muy especial a todos los miembros de la familia *OnFire*: Nina, Stefania, Laura, Ángela, Jessica, Jully, Javi, AnaMi, Tomate, A. Lo, Jacke, James, Dieguito, David, Kumara, Ela … Cada uno aportando su salsa haciendo que la mezcla explosiva se mantuviese en su preciso puntito de cocción. Ángela, largas y útiles conversaciones que nunca olvidaré, ¡eres una *peazo de mujé*!. Stefa, fuiste el mayor apoyo cuando creí que me caía… Y espero lo podamos seguir siendo la una para la otra siempre. Anita, tu energía siempre me contagió ganas de descubrir y no parar, gracias por ese "chute" de energía y por tu inestimable ayuda en la parte científica. Lauri, nuestra niña chica a la que en teoría todos teníamos que cuidad y proteger y que al final acaba siendo ella quien vela por todos. ¡Nini! Muchas risas, charlas y aventuras… ¡Quiero más! Next stop…??. David, sabes que te mereces un hueco muy significativo en la consecución de esta tesis, siempre con esa sonrisa, con ganas de ayudar y, además, de regalo repartiendo buenas canciones. Gracias de verdad, has sido un gran apoyo en todos los sentidos. *Oh, brother, when I come to knock on your door*.

Rouco, ¡mil gracias por tu ayuda en todos los sentidos!. No hay día en que no me saques una sonrisa. Juan Carlos, gracias también por tu buen humor y simpatía.

Por supuesto quiero agradecer toda la ayuda brindada a mis compañeros de grupo: Elisa, Muling, Si Ming, Peng Fei, Laura, Martí, Anna, Maria y las chicas que ya no están por el ICMAB Elena y Oana. Ha sido un placer compartir laboratorio, despacho y muchas cenas con vosotros. Os deseo lo mejor a todos y cada uno, ¡os lo merecéis!.

Querido papi Guanaco, si yo te brindé hace años el honor de dejar que velaras por mí, tú me brindaste el de querer hacerlo. Ojalá la vida nos ponga cerquita en otra ocasión para poder disfrutar de tu gran presencia.

Ottito, muy contenta de haber intercambiado confidencias contigo y de poder contarte, a fin de cuentas, entre mis amigos, sabio Otto…

Y muchísimas gracias también al mejor de los informáticos: Marc. Gracias por la incalculable ayuda en la parte más técnica y por las buenas charlas. El ICMAB nunca fue lo mismo desde tu marcha.

Sara, ¡has sido en muchos momentos como una mami sanluqueño-catalana!. Gracias por tus cuidados, tus impresionantes recetas y un sinfín de momentos que me hacen sonreír de oreja a oreja al recordarlos.

Muling, special thanks to you!! You have been such an amazing august-partner at the office and zumba-mate at SAF. For sure I will go to England to be cold there next to you!.

¡Pedrito, que ya no nos queda ná!. Has sido un compañero de aventuras irremplazable. Gracias por estar siempre ahí.

A un *panete*, que de una forma u otra, tiene una presencia enorme en esta tesis y todo mi mundo. Siempre cerca.

Son muchísimos los motivos por los que debería agradecerte tanto a ti, Jorge. Pero lo "resumiré" en uno sólo: gracias por devolverme LA PAZ.

A mi padres y a mi familia en general (mis tíos Esther y Javier y mi "prima" Charo), muchísimas gracias por confiar tanto en mí, por pensar a cada instante que "yo podía". He sentido a cada paso vuestra confianza ciega depositada en mí. Gracias por enseñarme "el camino".

Foreword and aim of the thesis

Materials science and especially nanoscience have attracted my attention since I had a first contact with those disciplines when I was studying my BSc in Chemistry at Universidade de Vigo. The possibility to synthesize different types of materials with tunable sizes, shapes and functionalities that hugely differ from the macroscopic behavior showed by the same material opened a new and amazing vision of science for me.

In November 2008, I was hired at the Institut de Ciència de Materials de Barcelona (ICMAB-CSIC) to develop a one-year study related to the preparation of iron oxide-silica porous composites towards their utility as drug delivery systems. The work also exploited the use of supercritical fluids (SCFs) as green and non toxic solvents for materials processing and it was supervised by Dr. Anna Roig and Dr. Concepción Domingo. After one year, I secured a FPU scholarship and began my doctoral thesis under their supervision. My assigned project was focused on the preparation of multifunctional silica-based nanoparticles for biomedical applications. At that time, Elena Taboada was a doctoral candidate in the group. She had developed a novel synthetic approach to prepare iron oxide-silica composite nanoparticles for their use as negative contrast agents in magnetic resonance imaging (MRI). The method was inspired by the drying procedure of silica aerogels and joined the sol-gel chemistry with the SCFs technology to form porous composite nanoparticles without the need of using porogenic agents. Since the utility of those particles for imaging diagnosis was proved by Elena, my thesis project was intended to explore the material capabilities for drug delivery. Therefore, the functionality of the material was extended creating a theranostic system (device with both diagnostic and therapeutic functionalities). The knowledge acquired during my MSc degree on colloidal science in combination with Elena's work and further functionalization of the particles in compressed fluids formed the bases of my project. Taking advantage of the expertise in the group on porous materials and treatment in supercritical conditions, initial efforts were conducted to the fabrication of silica aerogels and porous sub-micron particles and their impregnation with already known organic molecules. I had to spend quite an amount of time learning about supercritical fluids characteristics and how to work safely with high pressure equipments. SCFs have a set of properties that facilitates the processing of materials; in particular they are highly valuable for treating solids with fragile porous structure as aerogels, due to their almost null surface tension. Moreover, they present adjustable densities similar to that of liquids and high diffusivity values. The FPU scholarship allowed me to extend my knowledge in supercritical techniques and polymer coating of nanoparticles working during three months at the Institut de Chimie & Biologie des Membranes & des Nano-objets (CBMN) under the supervision of Dr. Pascale Subra-Paternault in Bordeaux.

This thesis aims to fabricate hybrid (organic-inorganic) complex materials as drug carriers with adequate properties using supercritical fluids for their application in biomedicine. For that purpose, two main objectives have been addressed: first, evaluation of the potentiality of

porous silica-based materials synthesized without using porogenic agents as drug delivery systems; and second, exploiting the utility of SCFs in the synthesis and functionalization of materials. During the realization of this thesis, silica-based nanostructured materials have been synthesized, loaded with a model drug, physical and chemically modified on their surface, and preliminarily studied as potential biomedical tools analyzing their interactions with relevant biological entities and media.

This manuscript is organized into eight chapters.

- **Chapter 1** provides a general introduction to nanotechnology and colloidal science (with a special mention to nanomedicine), together with the main strategies to synthesize both silica and iron oxide nanoparticles and their biomedical applications. A brief explanation on magnetism is also given, as well as a description and use of SCFs in materials science. The aim of the chapter is to place the reader in the scientific context of the thesis.
- **Chapter 2** describes the synthesis and characterization of the porous silica-based materials employed in the thesis: silica monolithic aerogels, silica submicron-sized particles and composite core(iron oxide)-shell(silica) nanoparticles.
- **Chapter 3** reports on the fabrication of hybrid products for biomedical applications by impregnating silica-based materials with a therapeutic agent trough dissolution in supercritical carbon dioxide. The chapter includes the simultaneous in situ preparation and encapsulation of two organic photosensitizers as a proof-of-concept. Details on the processes and characterization, in terms of organic load, structural and textural properties of the resulting materials, are presented. Special attention is devoted to the chemical conformation and stability of the drug inside the silica matrices and to the in vitro release kinetics in aqueous media.
- **Chapter 4** explains the use of biopolymers to coat the silica-based particles conferring them with enhanced properties for biomedical uses, such as sustain drug release and improved features for the interactions with cells. Coating methods involved the use of compressed carbon dioxide as antisolvent or as reaction medium and catalyst for the polymer formation. The morphological properties and thermal stability of the resulting materials are presented. Results on in vitro drug delivery in aqueous media and drug stability are presented and compared with those found for uncoated particles.
- **Chapter 5** shows preliminary studies of our materials as potential drug carriers, in terms of degradability, colloidal stability in biological media, cytotoxicity and cellular uptake. Strategies of silica surface functionalization with the goal of overcoming problems encounter in bioapplications are also gathered.
- **Chapter 6** lists the general conclusions derived from the present thesis and includes some suggestions for further research on the topic.
- **Chapter 7** gives brief introductions to the theoretical fundaments of the used experimental techniques and to the technical characteristics of the employed equipments.

- **Chapter 8** contains information about the author and the publications obtained during the PhD work.

Table of contents   **Page**

CHAPTER 3 . MOLECULAR IMPREGNATION OF SILICA-BASED MATERIALS

CHAPTER 4. POLYMER COATING OF SILICA-BASED PARTICLES

CHAPTER 5 . SILICA-BASED MATERIALS FOR BIOMEDICAL APPLICATIONS

CHAPTER 6 . CONCLUSIONS AND FUTURE WORK

CHAPTER 7. ANNEXES

CHAPTER 8

Attributions

I would like to acknowledge the persons, both researchers and technical staff, that somehow have contributed to this thesis, either by doing some activities themselves or because they train me on some particular technique.

- **Dr. Ana M. López-Periago** (ICMAB-CSIC) who trained me to operate the high-pressure equipment for the impregnation experiments.

- **Dr. Pascale Subra-Paternault** (Institut de Chimie & Biologie des Membranes & des Nano-objets, Bordeaux) who hosted and supervised me at the CBMN in Bordeaux for three months. She performed some of the experiments of polymer coating using carbon dioxide as antisolvent. She also helped me during my training with the use of high-pressure equipment for the antisolvent processes.

- **Dr. Xavier Saurina** (Departament of Analytical Chemistry, Chemistry Faculty, UB) trained and helped me to operate the HPLC equipment for the drug release experiments and the analytical processes involved. He also helped me with the diffuse-reflectance measurements and contributed to discuss and interpret some results.

- The synthesis of the iron oxide-silica nanoparticles was developed and optimized during the PhD Thesis **Dr. Elena Taboada** at ICMAB-CSIC. Besides, Elena trained me in the synthesis of iron oxide nanoparticles by thermal decomposition.

- **Dr. Maria Milla** (ICMAB-CSIC) who did the experiments of cell internalization of particles and MTT assays. She also took confocal images of labeled-particles uptaken by the cells and she performed further processing of the images.

- **Elif Ertem** (École Polytechnique Fédérale de Lausanne) who functionalized the composite nanoparticles with several organic groups and a fluorescence dye.

- **Pedro López-Aranguren** (ICMAB-CSIC) who carried out the experiments of silica nanoparticles PEI-coating in compressed carbon dioxide and performed the SLS and TGA measurements of the obtained products.

- **Raul Solanas** is the engineer responsible of the Laboratory of Supercritical Fluids at MATGAS 2000 AIE where the experiments at high pressure and high temperature for the preparation of the silica-based materials were performed. He was in charge of operating the plant.

- **Julio Fraile** is the laboratory technician of the Supercritical Fluids Group at ICMAB-CSIC and he carried out some of the BET measurements of the silica-based materials. Besides, he participated in discussions about practical aspects of the optimal condition in BET analysis.

List of symbols, abbreviations and acronyms

$(CH_3O)_2Ph_3C^+$	Dimethoxytrityl
A	Area
a	Kinectics constant
B	Magnetic field
BODIPY	Bodipy® 630/650-X
C	C parameter from BET
C^+	Dimethoxytrityl cation
$c-C^+$	Dimethoxytrityl cation
$c-Py^+$	2,4,6-triphenylpyrylium cation
CdSe-ZnS	Cadmiun selenide-zinc sulfide
CO_2	Carbon dioxide
EtOH	Ethanol
Fe_3O_4	Magnetite
H	Strength of a magnetic field
H_2O	Water
H_2SO_4	Sulfuric acid
H_C	Coercive field
HCl	Chloric acid
HF	Fluoric acid
HNO_3	Nitric acid
M	Magnetization
MeOH	Methanol
M_R	Remanent magnetization
M_S	Saturation magnetization
MUS	11-mercapto-1-undecanesulphonate
n	Release exponent
NaCl	Sodium chloride
Na_2HPO_4	Dibasic sodium phosphate
$NaH_2PO_4{\cdot}2H_2O$	Monobasic sodium phosphate
NH_4OH	Ammonium hydroxyde
OsO_4	Osmium tetroxide
OT	1-octanethiol
P	Pressure
P_0	Saturation pressure
P_C	Critical pressure
$PEG-(COOH)_2$	polyethylene glycol bis(carboxymethyl) ether
Ph_3Py^+	2,4,6-triphenylpyrylium
Ph_3CBF_4	Trityl tetrafluoroborate

Ph$_3$PyBF$_4$	2,4,6-triphenylpyryl tetrafluoroborate
Py$^+$	2,4,6-triphenylpyrylium cation
R^2	Correlation coefficients
SC	Supercritical
Si(OH)$_4$	Ortosilicic acid
Si(OR)$_4$	Alkoxysilanes
SiO$_2$	Silica or silicon dioxide
T$_2$	Transverse relaxation time
T$_B$	Blocking temperatura
T$_C$	Critical temperature
Trf	Triflusal
V	Volume
V$_{pore}$	Pore volume
γ-Fe$_2$O$_3$	Maghemite
ζ-potential	Zeta potential
ρ	Density
Φ	Diameter
Θ	Diffraction angle
χ	Magnetic susceptibility
Eud	Eudragit RL® 100
Hyd.	Hydrodinamic
min.	Minutes
AM	Aerogel silica monolith
AP	Aerogel-like silica particle
AP$_{Fe}$	Aerogel-like iron oxide-silica nanoparticle
API	Active pharmaceutical ingredient
BET	Brunauer, Emmet and Teller method
BJH	Barret, Joyne and Halenda
CBMN	Institut de Chimie & Biologie des Membranes & des Nano-objects
CD	Cyclodextrin
cgs	Centimeter-gram-second system
CVC	Chemical vapor condensation
DLS	Dinamic light scattering
DMF	Dimethylformamide
DNA	Deoxyribonucleic acid
DSC	Differential scanning calorimetry
EDTA	Ethylenediaminetetraacetic acid
EPFL	École Polytechnique Fédérale de Lausanne
EPR	Enhanced permeation and retention

EXD	Energy Dispersive X-ray
FBS	Fetal bovine serum
FPU	Formación personal universitario fellowship
FTIR	Fourier transform infrared spectroscopy
GAS	Gas ansitolvent
GRAS	Generally recognized as safe
H^+	Proton
HPLC	High performance liquid chromatography
HRTEM	High resolution transmission microsc(opy
ICMAB-CSIC	Institut de Ciència de Materials de Barcelona
ICP-MS	Inductively coupled plasma-mass spectrometry
IR	Infrared
IUPAC	International Union of Pure and Applied Chemistry
JPs	Janus particles
MALDI-TOF	Matrix-assisted laser desorption/ionization-time of flying
MCM	Mobile Composition of Matter
MEM	Minimum essential medium
MRI	Magnetic resonance imaging
MSNP	Mesoporous silica nanoparticle
MTT	3-(4,5-dimethylthiazol-2-yl)-2,5-diphenyltetrazolium bromide
NHS	n-hydroxysuccinimide
NP	Nanoparticle
OA	Oleic acid
OAm	Oleylamine
OMS	Ordered mesoporous silicas
PBS	Phosphate buffered saline
PCA	Semicontinous precipitation antisolvent
PEG	Polyethylene glycol
PEI	Polyethyleneimine
PMMA	Polymethyl metacrylate
PXRD	Powder X-Ray diffraction
RNA	Ribonucleic acid
RT	Room temperature
SAED	Selected area diffraction pattern
S_{BET}	Surface area by BET
$SCCO_2$	Supercritical carbon dioxide
SCF	Supercritical fluid
SEM	Scanning electron microscopy
siRNA	Small interfering ribonucleic acid

SLS	Static light scattering
SQUID	Superconductive quantum interference device
STM	Scanning tunneling microscope
TEM	Transmission electron microscopy
TEOS	Tetraethylortosilicate
TGA	Thermogravimetric analysis
TMOS	Tetramethylortosilicate
UAB	Universitat Autònoma de Barcelona
XRD	X-Ray diffraction
ZFC-FC	Zero-field cooling field-cooling
ZY	Faujasite-type zeolite

1

INTRODUCTION
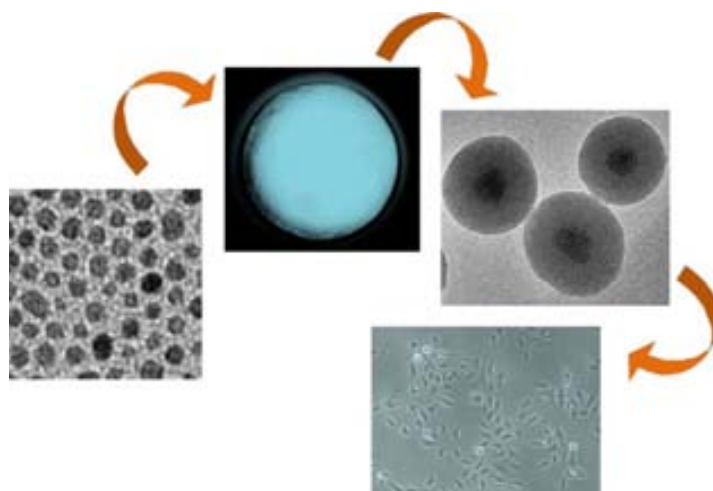
This chapter contains basic concepts on nanotechnology, nanomedicine and colloidal science. The most common strategies of colloidal stabilization of nanoparticles are also presented. General concepts on magnetism in bulk and at the nanoscale are briefly explained. The chapter contains descriptions of different synthetic approaches for silica and iron oxide nanoparticles and their main uses in biomedicine. Finally, an introduction to the supercritical fluids technology, including its utility in materials processing and the pharmaceutical industry is given.

1.1. NANOTECHNOLOGY AND NANOMEDICINE. GENERAL CONCEPTS

The definition of *nanotechnology* is currently a subject of confusion and disagreement among experts on the field. This controversy is mainly related to a size limitation. Whereas some authors consider that nanotechnology only involves systems from 1 nm up to 100 nm,[1,2] other experts have cautioned against such a restrictive size range and they include materials of several hundreds of nm within the definition of nanomaterials.[3,4] Bawa *et al.* proposed the following definition:[5]

> *Nanotechnology is the design, characterization, production, and application of structures, devices, and systems by controlled manipulation of size and shape at the nanometer scale (atomic, molecular, and macromolecular scale) that produces structures, devices, and systems with at least one novel/superior characteristic or property.*

The prefix *nano* comes from the Greek word for *dwarf* and one nanometer represents one billionth of a meter (1 nm = 10^{-9} m). Historically, the first nanotechnologists might have been medieval glass workers, who created stained glass windows with so many different colors. Those colors were due to the trapping of gold and silver nanoparticles (NPs) into the "glass matrix". One of the most renowned examples of ancient nanofabrication is materialized in the Lycurgus cup.[6] The modern origins of nanotechnology are attributed to the famous 1959 lecture by Nobel Prize-winning physicist Richard P. Feynman entitled "There's plenty of room at the bottom". He described a process in which scientists would be able to manipulate and control individual atoms and molecules. In 1974, Professor Norio Taniguchi from the Tokyo University of Science coined the term nanotechnology for the first time referring to his exploration on ultraprecision machining. The invention of the scanning tunneling microscope (STM) in 1981, which allows imaging solid surfaces with atomic scale resolution, brought the first experimental advance that supposed the beginning of the modern nanotechnology. But the term did not become popular until 1986, when engineer K. Eric Drexler published the book "Engines of Creation: The Coming Era of Nanotechnology".

Nanotechnology is a young, promising field that encompasses a wide range of disciplines including physics, chemistry, biology, electrical engineering, chemical engineering, and materials science.[7] It has supposed one the scientific revolutions of the 21st century having a great impact on the industry and society. Nanomaterials are nowadays present in many different areas such as memory and storage technologies, optics, photonics, energy, biotechnology, and health care.[8] On the other hand, the rapid technological advances and commercialization within the field has lead to new challenges, not only in the understanding of the nanoobjects behavior, but also in the potential hazards associated with the exposure to them.[9]

What makes materials in the nanoscale interesting is the fact that in many cases their physicochemical properties hugely differ from those of the same bulk counterparts. The size-dependent properties of the nanostructures are mainly due to the following phenomena:

- Extremely high surface area/volume ratio: nanosized materials have much larger surface areas than similar masses of larger-scale materials. To understand this, it is useful to imagine a solid cube with 1 cm on each side having an area (A) to volume (V) ratio of 2. If this cube is divided into one thousand identical cubes of 0.001 cm (1 μm) in side, the total volume of the solid is the same but the total area is 3000 times larger than before leading in a A/V = 6000. If each new cube is cut into other one thousand cubes having 0.001 μm (1 nm) of length side each, the A/V increases up to 600000. As surface area per volume of a material hugely rises, a greater amount of it might come into contact with surrounding materials, thus affecting reactivity.

- Quantum effects: at the nanoscale, electrons are confined in a reduced volume that the behavior and properties of the material might be ruled by the quantum mechanics. This enables the tunability of the materials properties just varying their size, without changing their chemical composition.[10]

Nanometric gold illustrates the unique properties that occur at the nanoscale. As a consequence of the restricted motion of the gold electrons, nanoparticles react differently with light compared to the larger-scale ones and they are not yellow-colored, but they appear red to purple.[11] Another example is the semiconductor nanocrsytals (or *quantum dots*), which, contrarily to what happens in bulk, do not present a fixed gap between the valence band and the conduction one. By changing the crystal size, the band gap of a nanometric semiconductor material can be modulated being able to emit at different wavelengths and with high intensity.[12,13]

Nanomedicine is defined as the application of nanotechnology to medicine, for diagnosis, prevention and treatment of disease and to gain and increased understanding of the complex underlying diseases mechanisms. It exploits the properties of materials at nanometric scale for medical purposes in an interdisciplinary scenario that combines aspects of medicine, biology, chemistry, physics and engineering. Nanomedicine is an emerging area that has gained much attention from the scientific community in the last two decades, especially since the first nanotherapeutic (Doxil®, a nanoliposomal formulation of anticancer drug Doxorubicin) product was approved in 1995.[14,15]

Among the nanomedicine areas in progress, such as fabrication of nanosensors for early point-of-care detection of diseases, preparation of stimuli-sensitive nanodevices or tissue engineering and regenerative medicine, theranostics has special relevance for the objectives aimed in this thesis. A *theranostic* is a multifunctional material that combines the modalities of therapy and diagnosis, commonly diagnostic imaging and drug delivery.[16,5] Releasing a bioactive agent at a specific rate and at a specific site is one of the main challenges of the pharmaceutical industry, and the drug delivery arena address this challenge.[17] Nanoparticles and other colloidal drug-

delivery systems can modify the kinetics, distribution at the body, chemical stability and release of an associated drug. Thus, a superior therapeutic efficacy with a reduced healthcare cost might be achieved.[18] In addition to classic medicine, nanomedicine is now dealing with the development of new therapeutic strategies such as target anticancer drug delivery,[19,20,21] peptide[22,23] and protein delivery[24,25] and gene therapy.[26,27] Since the size of nanometric materials is comparable to that of biological entities (**Figure 1.1**), a profound understanding of the interactions taking place between them is required for potential bioapplications.
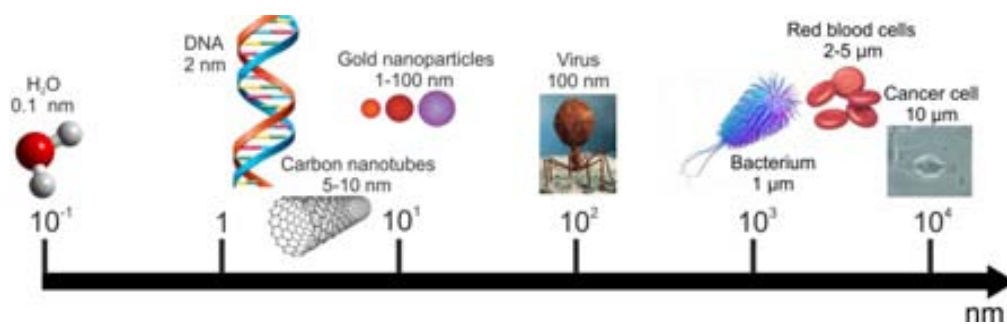
Figure 1.1. Size of common biological units compared with synthetic nanomaterials in the range of 0.1 nm to 10 µm.

1.2. STABILIZATION OF NANOPARTICLES AS COLLIDAL DISPERSIONS

Colloidal dispersions are defined as systems with particles of colloidal size (1-1000 nm) of any nature (solid, liquid of gas) dispersed in a continuous phase of a different composition or state.[28]

In the view of nanoparticles dispersions (colloids formed by solid particles dispersed in a liquid), it is said that a colloid is stable when the particles are individually dispersed without forming large agglomerates or precipitating. Because of the large surface area/volume ratio in nanoparticles, the most part of the atoms are localized in the surface of the material, thus, having a high surface energy. To minimize this excess of energy, NPs follow different strategies like agglomeration that induces the destabilization of the system and, importantly, the loss of the characteristic properties of such material at the nano level. Since many applications of nanotechnology imply the use of colloidal dispersions, mechanisms to keep them stable are needed.

Van der Waal forces are the main attraction interactions that make particles to aggregate in a colloidal dispersion and they increase with increasing the particle size and decreasing the distance between particles. Colloidal stabilization strategies try to overcome those forces and are based in either *electrostatic* or *steric stabilization*.

Although the whole system must be electrically neutral, the effective surface charge of the particles is significant and it is determined by the distribution of ions and counter ions present in the liquid that moves with the particles placed at their surface. This organization formed the called *electrical double layer* (**Figure 1.2**). Considering a negatively charged particle, positive ions

close to the particle surface are strongly bound forming the Stern layer where the electrical potential drops linearly. On the other hand, ions that are further away are loosely bound forming the diffuse layer that is characterized by an exponential decay of the potential. The potential at the slipping plane, which separates the bulk solution from the Stern layer, is called the zeta potential (ζ-potential) and it is considered to be the effective surface charge of the nanoparticle. ζ-potential is used as a reference value to measure the electrostatic stability of a colloid. The repulsive interaction between the double layers of two close particles forces them to separate, thus, contributing to the system stability (**Figure 1.3a**). The higher the absolute value of the zeta potential, the stronger the electric repulsion between particles, and therefore the higher the stability of the colloid. Subsequently, a colloidal dispersion is unstable at the isoelectric point (pH at zero net electrical charge).

Steric stabilization consists on covering the particles surface with surfactants or polymers that must be chemical or physically attached onto the solid surface. When two particles approximate, the energetic and osmotic effects avoid the particles to agglomerate providing stability to the colloidal system (**Figure 1.3b**).

Comparing both strategies, electrostatic stabilization does not offer a long-term protection, because it is mainly based on physisorption of ions on the NPs surface. On the other hand, the coated organic molecules in steric stabilization are commonly thermally labile. Encapsulation of particles inside inorganic thermally stable shells is also used (*i.e.*, silica, Au, Pt, …).
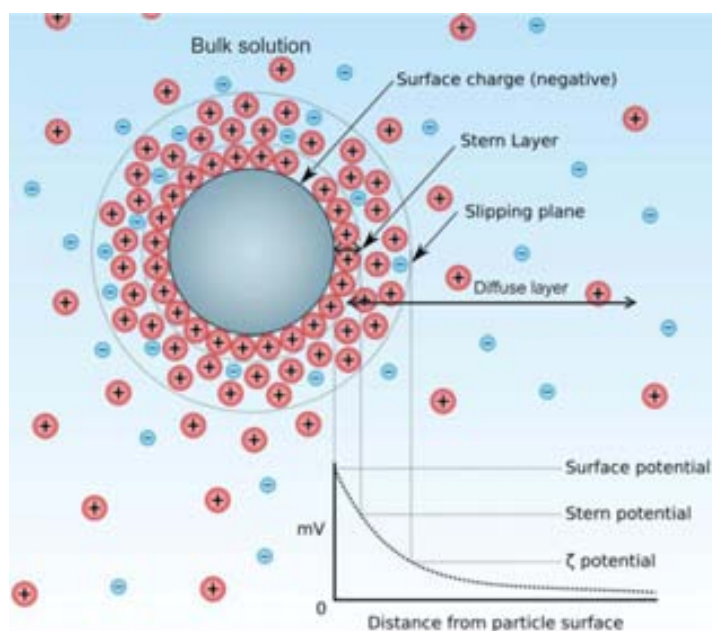
Figure 1.2. Schematic representation of the double electrical layer and the electric potential for a negatively charged particle. Figure adapted from en.wikipedia.org.
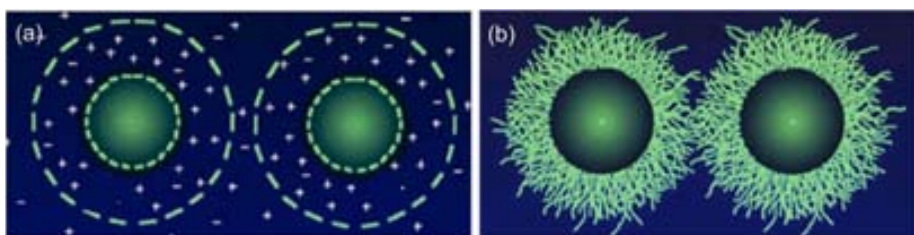
Figure 1.3. Schematic representation of two particles stabilized by: (a) electrostatic, and (b) steric repulsions. Pictures adapted from www.pall.com.

It is worth mentioning that attractive Van der Waals forces might not be the unique interaction responsible of particles aggregation. For example, in magnetic NPs there is a magnetic extra attractive force, which highlights the importance of strengthen the stabilization methods for these products.

1.3. SILICA NANOPARTICLES

Starting from the 1960s, silicon oxide (or silica) materials have become the subject of intense academic and industrial applications.[29] Whereas silica is mainly found in nature as crystalline products, the most part of the synthetic fabrication routes aims at obtaining amorphous materials. This is due to the fact that amorphous silica presents more suitable properties for a wide range of application fields than their crystalline analogues.

One of the most studied systems of silicon oxide is the one constituted by silica nanoparticles, which is synthesized in a broad range of sizes[30,31] and controlled structures.[32,33] Since those nanoparticles present excellent chemical stability, low toxicity and versatile functionalization chemistry, the range of applications includes very different fields, such as photonics and biomedicine.[34]

Hereafter, a brief introduction to the methods used for preparing amorphous silica nanoparticles with different structural properties is given.

1.3.1. Synthesis of silica nanoparticles

The size and size distribution of silica particles highly affects their properties.[35] Different approaches have been developed to synthesize silica particles, these can be categorized as either wet- or vapor-phase processes.[36] In the wet methods, the sol-gel, reverse microemulsion, chemical precipitation,[37] hydrothermal and pressurized carbonation processes[38] are included.

The **sol-gel process** is used to fabricate metal oxides and consists on the preparation of a solution that trough hydrolysis and condensation reactions forms a sol (stable colloidal dispersion of solid particles in a liquid) and its further polymerization from an interconnected network of the primary particles. Regarding the synthesis of silica nanoparticles, the sol-gel route offers a number of advantages: spherical, homogeneous and monodispersed products can be obtained with high control over the size by adjusting the molar ratio of water to metal precursor

or the type of catalyst. It is also an easy, cheap and robust method that leads to highly pure particles.[39,40] Stöber *et al*.[41] reported a pioneering approach to synthesize monodispersed silica particles by hydrolysis and polycondensation of silicon alkoxydes in mixed solutions of ammonia, used as a catalyst, alcohol and water. Silica spheres were prepared ranging from 50 nm to 2 μm with a narrow size distribution. The size of particles depends on the type of silicon alkoxyde and alcohol. In general, the shorter the chain length of the alcohol, the smaller the particle size and the narrower the size distribution. Since the Stöber study, many researchers have been analyzing the effects of various variables[42,43] on the structure and properties of silica nanoparticles trying to optimize such method (**Figure 1.4**).[44,45] For instance, it has been shown that the size of the particles increases with the concentration of ammonia[46]; and that by fixing the concentration of reactants and the temperature, the particle size and size distribution are highly dependent on mixing modes.[47]
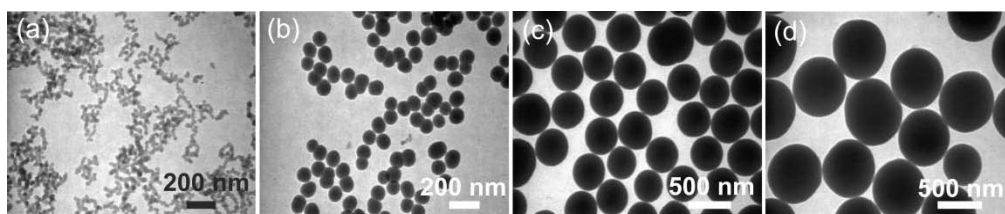
Figure 1.4. Different sizes of silica particles obtained by controlling different reaction parameters: (a) ~21 nm, (b) ~131 nm, (c) ~369 nm, (d) ~565 nm. Image modified from Rahman and Vejayakumaran.[48]

A special mention is here devoted to the preparation of porous silica NPs, in particular those having mesopores (pores with diameters between 2 and 50 nm). In 1992, researchers of the Mobile Oil Corporation developed a new family of ordered mesoporous silicas with tunable pore diameters in the range of 1.5-30 nm. Those structures that are commonly known as MCM (Mobil Composition of Matter) have high specific surface areas and pore volumes.[49] MCM-41 is one of the most extensively researched types of MCM. It is a highly ordered material that presents pores with amorphous silica walls spatially arranged in a periodic hexagonal pattern (**Figure 1.5**). A rapid progress has been attained during the last two decades in the synthesis and applications of mesoporous silica nanoparticles (MSNPs) in catalysis, adsorption, separation, sensing and drug delivery.[50,51,52] Although different methods have been used to synthesize MSNPs, such as self assembly[53] and emulsion thecniques,[50] a templating agent that directs the polymerization of silicates from a precursor is usually required. Typically, it is a surfactant that is either neutral of charged.[54] The control of particle size and morphology is accomplished by varying parameters such as pH and agitation speed or by using co-solvents and additives during the synthetic process. MSNP have also been prepared with disordered porous structures.
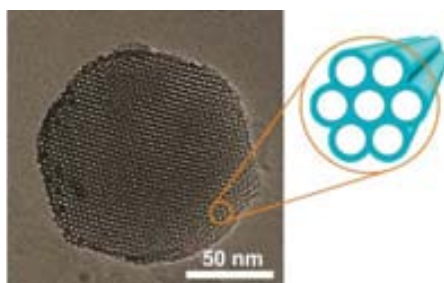
Figure 1.5. TEM image of a MCM-41-type silica nanoparticle. The inset shows the hexagonal pore arrangement in the microscope image and a schematic representation. Image adapted from Rimola *et al.*[49] and Zhao *et al.*[50]

Reverse microemulsions (water dispersed in oil) are formed by spherical micelles of surfactant molecules with the polar head groups organized to form microcavities containing water and the nonpolar chains in contact with the organic solvent. At these conditions, silica nanoparticles can be grown inside the microcavities by carefully controlling the addition of silicon alkoxydes and catalyst.[55,56] The major drawbacks of the reverse microemulsion approach are high cost and difficulties in removal of surfactants in the final products.

The **vapor-phase synthesis** is based on high temperature flame decomposition of metal-organic precursors. This process is also referred to as chemical vapor condensation (CVC). Typically, particles are produced by reacting silicon tetrachloride ($SiCl_4$) with hydrogen and oxygen.[57] Although it is a simple method, controlling the particle size, morphology, and phase composition is difficult.[58] Nevertheless, this is the prominent method that has been used to commercially produce silica nanoparticles in powder form.

1.3.2. Magnetic silica nanoparticles

The surface of iron oxide nanoparticles (IONPs), among other types of nanoparticles, can be modified to provide them with functionality, biocompatibility and also colloidal stability. Encapsulation of iron oxide nanoparticles in either organic, such as polymeric surfactants, or inorganic matrices, mainly silica, prevents their aggregation. Furthermore, the modified surface can impart non toxicity and bear functional groups to allow the covalent grafting of biomolecules, therapeutic agents or specific ligands for targeting.

Silica coating has some advantages over polymeric matrices, such as chemical, thermal and mechanical stability and lack of swelling or porosity changes with pH or electrolyte concentration. This coating also prevents oxidation and degradation of the IONPs during and after synthesis. Concerning biomedical applications, an important advantage of having a silica surface is the presence of silanol groups that can easily react with silane coupling agents and provide an ideal anchorage for covalent binding of specific ligands.[59]

Using conventional approaches for the synthesis of silica but having IONPs in the initial solution, multifunctional core-shell nanostructures can be produced. The final products combine the properties and functionalities of both the magnetic core and silica shell, being a unique platform

for the design of theranostic devices. Materials capable of carrying high drug payloads and enhance the contrast in MRI imaging for diagnosis at the same time, such as porous magnetic silica nanoparticles (**Figure 1.6**), deserve an especial consideration in this field.[60]
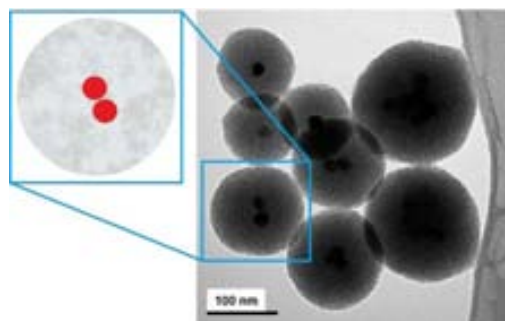
Figure 1.6. Schematic representation and TEM image of iron oxide nanoparticles inserted within mesoporous silica. Image adapted from Liong *et al.*[61]

1.3.3. Biomedical applications of silica nanoparticles

Silica particles are nowadays synthesized as monodispersed and highly size-controlled spheres in the range of 5 to 1000 nm. Moreover, they have high adsorption capacity, easy chemical functionalization and they have been reported as biocompatible.[62] These characteristics have promoted an intensive research on the design of silica nanoparticles for biomedical applications.[63] Unfortunately, the fast improvement on fabricating silica nonoparticles with specific biofunctionalities is not encompassed with a sufficient understanding of the biological response of these materials, mostly for porous structures. Much more experiments studying the influence of the physicochemical features of the particles are needed to make effective and safe devices to be used in biomedicine.[64] Nonetheless, both pristine and functionalized SiO_2 NPs have an ongoing role for designing advanced tools and systems for *in vitro* and *in vivo* applications, which can be summarized as follows:

- **Drug delivery**: An ideal device for drug delivery would consist of a drug nanocarrier capable of specifically targeting the damaged tissue facilitating the transfer of a high drug payload across target the cell membrane. This system could then undergo a controlled-release trough drug diffusion, matrix degradation or upon activation by external stimuli.[65] This would be an efficient therapeutic treatment, without causing side effects in healthy cells. Porous silica nanoparticles, primarily MSNPs, have been widely investigated as drug carriers because, in addition to the aforementioned properties of SiO_2 NPs, they have high surface area and pore volume available to host large amount of therapeutic agents.[66] Several studies have proved that porous silica particles can release drugs in a controlled manner through a combination of passive diffusion and matrix degradation.[67,68,69] Owing it to triggered release of the cargo, two different strategies have been developed: linking the drug on the silica trough covalent cleavage or functionalizing the silica surface with protective coatings or *gatekeepers*. The gatekeepers are nanogates capping the pore entrances with the ability to open or close them

by responding to external stimuli, typically, pH, redox level or temperature. Those systems can be organic molecules, biomolecules, polymers, nanoparticles, etc. For example, the group of Prof. Zink[70] has positioned cyclodextrin (CD) molecules around the orifices of the silica mesopores. Stalks of rhodamine/benzidine acted as nanopistons that move in and out the CD cylindrical cavities in response to changes in pH. Luo *et al.*[71] immobilized collagen on the outer surface of MSNPs as redox potential-responsive gatekeepers for targeted drug delivery of cancer cells. Targeting of silica particles to special cell types can be achieved by attaching different ligands or antibodies, such as folic acid[72] or growth factors,[73] to the particles surface. A targeted drug release is particularly relevant in cancer treatment, where the majority of the used therapeutics are highly toxic.

- **Gene delivery**: Gene therapy has emerged as a crucial therapeutic avenue, where deoxyribonucleic acid (DNA) and ribonucleic acid (RNA) are utilized as therapeutics to antagonize abnormal gene regulation.[74] Since DNAs/RNAs suffer from poor bioavailability and cellular uptake profile *in vivo*, they can only be delivered through systemic administration being encapsulated in suitable carriers. Porous silica nanoparticles are considered a promising alternative to the gene currently used delivery devices based on viral vectors. In order to be readily internalized by cells, the gene-loaded silica particles have been functionalized with positively charged groups. For instance, Bharali *et al.*[75] reported *in vivo* applications of amino-surface functionalized SiO_2 NPs in gene release.

- **Protein adsorption and separation**: The extensively studied interaction between silica surfaces and proteins has been applied for specific protein detection[76,77] and reverse interaction for separation of proteins from biologic media.[78] Functionalized silica NPs have successfully target proteins with high specificity, thanks to the many options for functionalization provided by silica surfaces.

- **Nucleic acid detection and purification**: Significant information can be obtained from DNA molecules used for diagnostic, genetic investigation and therapy. Hence, DNA detection, extraction and purification are important steps in those fields. Silica nanoparticles have an important role in building and developing a fast, cost-effective and robust isolation method for DNA extraction, purification and analysis.[79] SiO_2 NPs are also employed to design DNA biosensors by functionalizing them with oligonucleotides.[80] Using DNA adsorption onto silica, researchers have been also able to develop silica surfaces for more specific and efficient interaction.[81]

- **Pharmaceutical applications**: Silica NPs are widely used in the pharmaceutical industry for several other functionalities, for example, as adsorbents,[82] anticaking agents, emulsifiers and thermal stabilizers, or to increase the flowability of solid formulations,[83] with a percent ratio varying from 0.1 to 10 wt%.[84]

1.4. IRON OXIDE NANOPARTICLES

1.4.1. General concepts of magnetism

Magnetic properties in bulk

Macroscopic magnetism arises from two intrinsic characteristics of electrons: the orbital movement of the electron around the atomic nucleus and the movement of the electronic spin around its axis. This means that every electron has associated an orbital and a spin magnetic moment that makes it to behave like a tiny magnet. The vector sum of all the magnetic moments (m) of the atoms in a material per unit volume (V) is called magnetization (M) and it describes the degree to which a magnet is magnetized (**Equation 1.1**).

Equation 1.1 $$M = \frac{m}{V} \left(\frac{emu}{cm^3}\right)$$

For practical reasons, M is often referred to unit mass and expressed as emu/g in the centimeter-gram-second system of units (cgs). The magnetic properties of a material are characterized by the magnitude and sign of M, but also by the way in which it varies with the strength of a magnetic field (H, expressed as Oe in cgs). The magnetic susceptibility (χ) is expressed in **Equation 1.2**.

Equation 1.2 $$\chi = \frac{M}{H} \left(\frac{emu}{Oe\ cm^3}\right)$$

All the materials can be classified in regards of their magnetic behavior. A substance is **diamagnetic** when it has negative net magnetization in presence of a magnetic field (B). This means that the material is repelled by B. They are constituted by atoms with electrons forming a closed shell (*i.e.* noble gases, NaCl, most organic molecules,…), which usually have their spin and orbital magnetic moments oriented, so that atoms as wholes have no net magnetic moment. Diamagnetic materials have negative values of χ (around -10^{-6}). Only atoms with electrons in partially filled shells exhibit a net magnetic moment, and thus net magnetization. Materials with this characteristic might have four different types of magnetism (**Figure 1.7**):

- **Paramagnetism**: paramagnetic systems present a small net magnetization (with χ = 0-0.01) when applying B that is not retained after removal of the stimulus.
- **Ferromagnetism** and **ferrimagnetism**: in the presence of a magnetic field, materials have a strong net magnetization that partially remains when the magnet is not longer applied. Magnetic moments in ferromagnets, all with the same magnitude, are aligned in parallel. However, in ferrimagnets, they have different strength and align antiparallel to each other. These systems have positive and large magnetic susceptibilities ($0.01-10^6$).
- **Antiferromagnetism**: substances show zero net magnetization even being under the influence of a magnetic field due to the antiparallel alignment of magnetic moments of equal magnitude. Values of χ are positive but small (0-0.1).
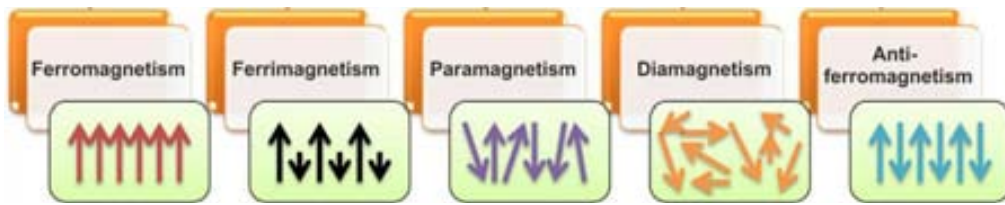
Figure 1.7. Different types of magnetism. Arrows represent the spin orientation.[85]

At the macroscopic scale, magnetic materials are composed by sub-regions where the magnetic moments are oriented in the same direction, while inside the sub-region the orientation is not the same. Those regions are called *magnetic domains* and they are separated by *magnetic walls*. By applying a magnetic field to a ferromagnet, the domains that have their orientation lying along the direction of B start to grow trough domain wall motion (**Figure 1.8a**). If the intensity of B is high enough, the domains grow while their magnetic moments align in parallel with the external stimulus until occupying all the space in the material. At this situation, the compound reaches its highest value of magnetization (saturation magnetization or M_S). After the removal of the external magnetic field, a ferromagnetic material tends to stay magnetized with a remanent magnetization (M_R) (**Figure 1.8b**). Besides, these materials present a coercive field (H_C) that is defined as the field of opposite sign needed to return the system to a state of null magnetization. The wall motion is enhanced by the *magnetic anisotropy* (MA), which describes the preferential magnetization orientation of a material in one particular direction of space. MA is also facilitated by the interaction occurring between the spin and the orbital magnetic moments (spin-orbit coupling). In crystals, this interaction strongly depends on the crystalline lattice.
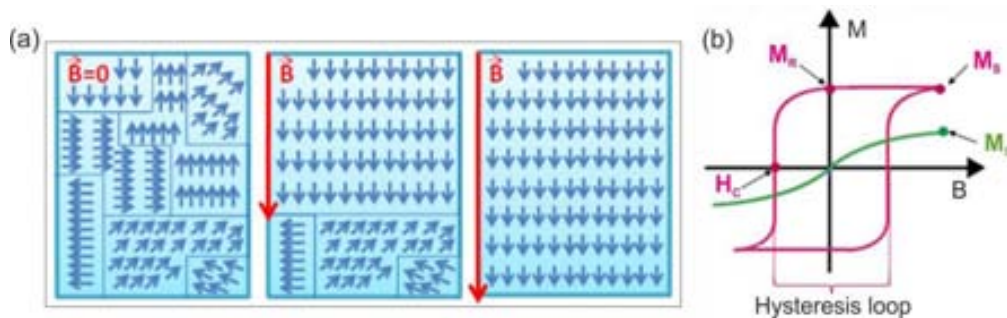
Figure 1.8. (a) Schematic representation of domain wall motion in presence of an applied magnetic field in a ferromagnet,[86] and (b) magnetization *vs.* applied magnetic field for a ferromagnetic (pink line) and a paramagnetic (green line) material.

Magnetic properties at the nanoscale

As previously mentioned, size effects have a tremendous importance over the properties of materials at the nanoscale. The multi-domain structure of a ferromagnetic material does not longer exist when its size is reduced below a critical value. Every magnetic material has a critical size below which the energy needed to create a domain overcomes the magnetostatic energy (energy required to orient the magnetic moments in parallel with an external magnetic field),

favoring the single-domain state. The critical diameter (D_C) of a monodomain in spherical and non-interacting particles is given by **Equation 1.3**:

Equation 1.3
$$D_C = 18\frac{\sqrt{AK_{eff}}}{\mu_0 M_S^2}$$

where A is the exchange constant , K_{eff} is the uniaxial anisotropy constant and μ_0 is the vacuum permeability. Although the critical diameter is an intrinsic property of each material, typically lies in the range of a few tens of nanometer.

In the presence of an applied magnetic field, a single-domain particle holds a permanent moment called "supermoment" resulting from the strong coupling of the individual magnetic moments within the particle (**Figure 1.9a,b**). The particle presents a large susceptibility with high M_S and neither M_R nor coercivity (**Figure 1.9c**). In the easiest case of a particle with uniaxial anisotropy, two possible opposite orientations of this "supermoment" along the easy axis are preferred (parallel/antiparallel). Those configurations are separated by an energy barrier (E_a) that is directly proportional to the particle volume (V). It is expressed in **Equation 1.4**:

Equation 1.4
$$E_a = K_{eff}V\sin^2\theta$$

being θ the angle between the magnetization direction and the easy axis of the particle (**Figure 1.10a**).

This expression describes two energy minima at θ = 0 and θ = π, corresponding with spin up and spin down configurations, by means parallel or antiparallel to an external magnetic field. In small enough particles (< 20 nm), E_a separating those minima is very small, comparable with the thermal energy needed for the supermoment to flip between the two possible orientations (**Figure 1.10b**). According to this, and in the absence of an applied magnetic field, thermal energy fluctuations can overcome E_a and reverse the magnetization of the particle leading to a zero net magnetization. Under these conditions the particle is in the superparamagnetic state.
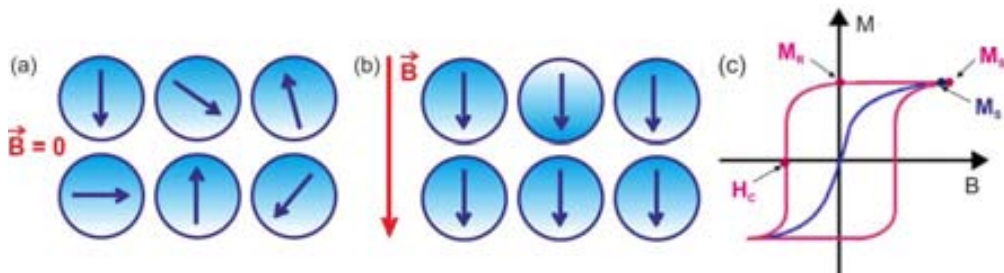
Figure 1.9. Schematic representation of single-domain particles having their magnetic moments: (a) randomly oriented in absence of an applied magnetic, and (b) aligned with the orientation of an applied magnetic field creating a supermoment, and (c) magnetization *vs.* applied magnetic field for a ferromagnetic material (pink line) and a single-domain particle (blue line).
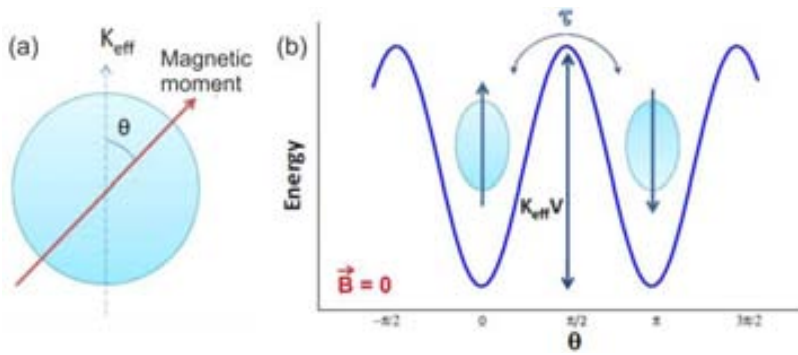
Figure 1.10. (a) schematic representation of a single-domain particle with uniaxial anisotropy, and (b) two possible spin configurations for a single-domain particle with uniaxial anisotropy and in the absence of a magnetic field.

The mean time of flipping is called *Néel relaxation time* (τ). The system is named blocked when τ is longer than the experimental measuring time. In this case the supermoment of the nanoparticle is "frozen" following the easy axis of magnetization. The transition temperature between blocked and superparamagnetic states is the *blocking temperature* (T_B) that depends, among other factors, on the size of the particle and the applied magnetic field.

It is important to remark that the blocking temperature of a given system obtained experimentally depends on the technique used to study its magnetic properties. Superconductive quantum interference device (SQUID) is a commonly used technique for this purpose. Zero-field cooling (ZFC)-field cooling (FC) measurements of magnetization versus temperature are usually performed with SQUID by heating the sample under a constant magnetic field. As it is depicted in **Figure 1.11**, in a FC measurement (with the sample previously cooled in presence of a magnetic field) the magnetization decreases as temperature increases; while in a ZFC measurement (with the sample previously cooled in the absence of a magnetic field) the magnetization increases with the temperature until reaching the energy barrier of the Néel relaxation at which starts decreasing. T_B is the temperature at the peak point of ZFC curve.
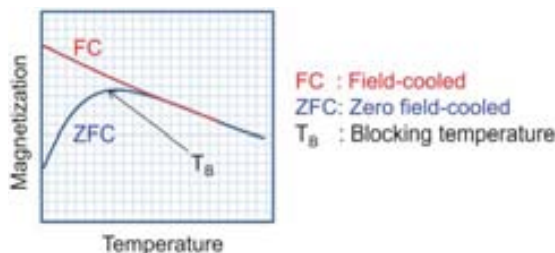
Figure 1.11. Schematic representation of a ZFC-FC curve for superparamagnetic nanoparticles.[87]

1.4.2. Synthesis of iron oxide nanoparticles

Many of the applications of iron oxide demand nanoparticles of specific size, shape, surface characteristics and magnetic properties. These features, and therefore the potential application of the nanoparticles, are determined by the method of synthesis,[88] which also rules the degree of structural defects or impurities in particles and the distribution of such defects.[89] In the last

decades, many reports have described efficient approaches to produce size and shape-controlled, monodispersed and highly crystalline iron oxide nanoparticles mainly trough chemical routes, either in liquid or vapor phase.[90,91] The most representative ones are coprecipitation, thermal decomposition, microemulsion, hydrothermal, sonochemical[92] and aerosol/vapor methods.[93]

In the **coprecipitation** synthesis, magnetite (Fe_3O_4) or maghemite (γ-Fe_2O_3) are obtained from aqueous Fe(II)/Fe(III) salt solutions by the addition of a base under inert atmosphere at room temperature or at elevated temperature. The size, shape, and crystalline phase of the magnetic nanoparticles strongly depends on the type of salts used (*i.e.* chlorides, sulfates, nitrates), the cations ratio, the reaction temperature, the pH value and the ionic strength of the media.[94] Massart reported in 1981 the most employed coprecipitation method. He used ferrous and ferric chlorides and hydroxides in an alkaline solution.[95] The influence of different parameters on the yield of the reaction and particle size was evaluated. It was concluded that the particle size decreased as the pH, ionic strength in the medium and/or Fe(III)/Fe(II) ratio increased.[96] Although this route produces a large amount of nanoparticles, the system is rather polydisperse in size due to the impossibility of controlling the crystal growth process. Some improvements have been made in this sense by the use of organic additives as stabilization and/or reducing agents, such as polyvinylalcohol (PVA).[97] Advances on the quality of nanoparticles synthesized by coprecipitation have been recently reported.[98]

High quality monodisperse and monocrystalline IONPs with small size can be obtained by the **thermal decomposition** of organometallic precursors in high-boiling organic solvents containing stabilizing surfactants, such as oleylamine,[99,100] oleic acid,[101] and steric acid.[102] Precursors that have been investigated include iron acetylacetonate,[103] iron carboxylate,[104] iron cupferronates[105] and iron carbonyls.[106] The control over the size and morphology of the particles is achieved by adjusting the ratio of the starting reagents, surfactant and solvent. The reaction temperature, reaction time and aging period might also be key factors for this porpose.[94] Peng *et al.* reported a general decomposition approach for the synthesis of size- and shape-controlled magnetic oxide nanocrystals based on the pyrolysis of metal fatty acid salts in non-aqueous solutions. Particles between 3 and 50 nm in size (**Figure 1.12**) with different shapes, including spheres and cubes, (**Figure 1.13**) were thus successfully prepared.[107] Maghemite nanoparticles with sizes ranging from 4 to 16 nm were produced by decomposition of iron pentacarbonyl in octyl ether and oleic or lauric acid by Hyeon *et al.*[108]
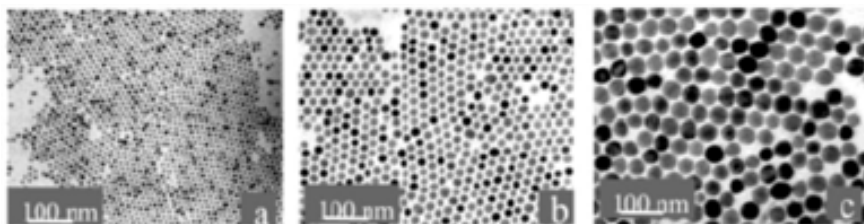
Figure 1.12. TEM images of the as-synthesized sphere-shaped Fe_3O_4 nanocrystals.[107]
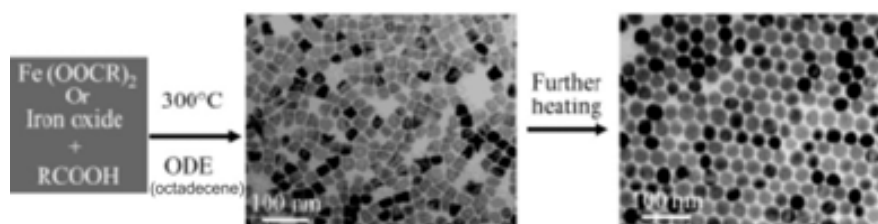
Figure 1.13. Schematic illustration of the formation of Fe$_3$O$_4$ nanocrystals. The middle and right panels are TEM images of the as-synthesized nanocrystals taken at different reaction times.[107]

Water-in-oil (w/o) or oil-in-water (o/w) **microemulsions** under the presence of a surfactant have been widely used to obtain IONPs.[109,110] The surfactant-covered pools, whose size is determined by the water to surfactant ratio in the size range of 1 to 100 nm, are used as nanoreactors for the formation of nanoparticles with limited growth. The eventual size of the particles might also be influenced by factors such as concentration of reactants and flexibility of the surfactant film.[111] Different self-assembled shapes and structures can be fabricated, such as spherical (reversed), lamellar phases, cylindrical micelles and bicontinuous microemulsions, which might accompany mainly aqueous or oil phases.[112] Although the fabrication of crystalline maghemite nanoparticles by the microemulsion route at high temperature has been reported,[113] one of the main disadvantages of this method is the difficulty in producing highly crystalline systems because of the low reaction temperature. Moreover, the obtained particle size and shape are not precisely controlled, the particles yield is low compared with other approaches and it is a hardly scale-up synthesis method.

Hydrothermal processes are based on the solubility of inorganic iron precursors in water at elevated temperatures (around 200 ºC) and pressures. A generalized method based on a liquid-solid solution reaction was proposed by Li *et al.* [114] It consisted of a metal linoleate (solid), an ethanol-linoleic, acid liquid phase and a water-ethanol solution at different reaction temperatures under hydrothermal conditions. During the synthesis, parameters such as water pressure,[115] water/polar solvent ratio and reaction time can be tuned to maintain a high and simultaneous nucleation rate and, thus, to ensure a good size distribution.[116]

A comparison between the four explained synthetic methods of IONPs is gathered in **Table 1.1**. The thermal decomposition approach seems to be the best one in terms of size, morphology, yield and magnetic properties of the produced nanoparticles.

Recently, microwave-assisted reactions have been developed to produce IONPs of different shapes and narrow size distributions at high temperatures (200 ºC) by dissolving iron precursors in polar solvents. In contrast with conventional methods, this process takes place in a short period of time (only a few minutes).[117] Iron oxide nanoparticles can be also fabricated by physical[118] or biological methods.[119]

Table 1.1. Summary comparison of four synthetic methods of iron oxide nanoparticles.[94]

Synthetic method	Co-precipitaton	Thermal decomposition	Microemulsion	Hydrothermal synthesis
Synthesis	very simple, ambient conditions	complicated, inert atmosphere	complicated, ambient conditions	simple, high pressure
Reaction temp. (°C)	20-90	100-320	20-50	200
Reaction period	minutes	Hours-days	hours	Hours, *ca.* days
Solvent	water	organic	organic	water-ethanol
Surface-capping agents	needed, added during or after reaction	needed, added during or after reaction	needed, added during or after reaction	needed, added during or after reaction
Size distribution	relatively narrow	very narrow	relatively narrow	very narrow
Shape control	not good	very good	good	very good
Yield	high/scalable	high/scalable	low	medium

1.4.3. Biomedical applications of iron oxide nanoparticles

Magnetite and maghemite nanoparticles have received considerable attention in biomedical applications because of their biocompatibility and low toxicity in the human body.[102,120] These applications require superparamagnetic particles at room temperature. Remanent magnetization could lead to agglomeration of particles favoring the blockage of blood vessels within the body. Due to its enhanced saturation magnetization, magnetite is preferred to maghemite. The particles need also to be colloidally stable in water at neutral pH and physiological conditions,[89,102] which commonly requires further functionalization of the magnetic nanoparticles. The main uses of IONPs in biomedicine are next explained:

- **Magnetic resonance imaging (MRI)**: Iron oxide nanoparticles have been developed for *in vivo* preclinical validation as targeted MRI contrast agents to differentiate between healthy and diseased tissue in molecular and cell imaging. They have a high T_2 (transverse relaxation time) sensitivity and high micromolar detection thresholds. IONPs can passively accumulate at certain types of cancer sites due to the *enhanced permeation and retention* (EPR) effect, which consist in the formation of leaky and permeable vasculature by malign cells.[121] In order to design a more versatile imaging device capable of selectively target the damaged area, the particles are conjugated with a wide variety of ligands and biomolecules,[122] such as small organic molecules,[123] peptides,[124] proteins,[125] antibodies,[126] and aptamers.[127] In addition to the type of ligand used, active targeting is affected by the targeting molecule density and by the size and shape of the nanoparticles. Since this application requires systemic administration, IONPs to be used as contrast agents for MRI should have prolonged blood circulation time (generally achieved by hydrophilic coating) and sizes between 10 and 100 nm to evade the rethiculoendothelial system (particles uptake by monocytces and macrophages).[121,128]

- **Drug delivery**: The called "magnetic drug delivery" is a promising application of the IONPs. It is based on magnetic targeting trough the injection of magnetic nanoparticles to which drug molecules are attached, guidance of these particles to a chosen site under the localized magnetic field gradients, holding them there until the therapy is complete, and finally removal of them. Different authors have reported the grafting of drugs onto the surface of iron oxide nanoparticles, especially for cancer therapy. For instance, Hwu *et al.*[129] reported the grafting of paclitaxel (PTX) on IONP surfaces through a phosphodiester moiety and Kohler *et al.*[130] developed a biostable methotrexate (MTX)-immobilized IONP drug carrier via a polyethylene glycol self assembled monolayer (PEG-SAM). Similarly, DNAs/RNAs[131] have been grafted on IONPs for gene delivery.

- **Hyperthermia**: Hyperthermia is considered as a supplementary treatment to chemotherapy, radiotherapy, and surgery in cancer therapy.[132] The idea of using magnetic induction hyperthermia is based on the fact that when magnetic nanoparticles are exposed to a varying magnetic field, heat is generated by the induced currents. Thus, when a magnetic fluid is exposed to an alternating magnetic field the particles become powerful heat sources destroying tumor cells, since these cells are more sensitive to temperatures in excess of 41 °C than their normal counterparts.[133] The amount of heat generated by magnetic nanoparticles depends strongly on the structural properties of the particles (*i.e.*, size, shape) and should be as high as possible to reduce the dose to a minimum level.

- **Magnetic bioseparation**: IONPs can be functionalized for *in vitro* protein or cell separation. Magnetic separation techniques present several advantages in comparison to traditional separation procedures. They are simple and all steps of the purification can take place in one container, thus reducing costs.[134] Fan *et al.*[135] have developed magnetic nanoparticles coated with charged bipyridinium carboxylic acids and biotin for affinity isolation of fluorescein-labeled protein avidin. The same strategy using dopamine has been reported by Xu.[136]

1.5. SUPERCRITICAL FLUIDS: GENERAL CONCEPTS AND PROPERTIES

A *supercritical fluid* (SCF) is formed by a single fluid phase, which occurs when both the temperature and pressure of a compound are above its critical temperature (T_C) and pressure (P_C), the critical point. The phenomenon can be easily explained using the phase diagram of a pure substance shown in **Figure 1.14**. It shows the areas where the compound exists as solid, liquid, gas or supercritical (SC). The curves represent the temperatures and pressures where two phases coexist in equilibrium (at the triple point, the three phases coexist). Moving upwards along the gas-liquid curve, increasing both temperature and pressure, the liquid becomes less dense and the gas becomes denser in such a way that the previously well defined meniscus separating the two phases **(a)** begins to appear unclear **(b)**. Once the T_C and P_C have been reached, the densities of the two phases become identical and the distinction between gas and liquid disappears. The curve comes to an end at the critical point, above which the system is a single homogeneous SCF **(c)**. Below T_C, the gas can be condensed into liquid by increasing the

pressure, but in supercritical conditions, the thermal energy of the molecules is high enough to overcome the potential energy provided by the neighboring molecules and the fluid cannot be condensed.
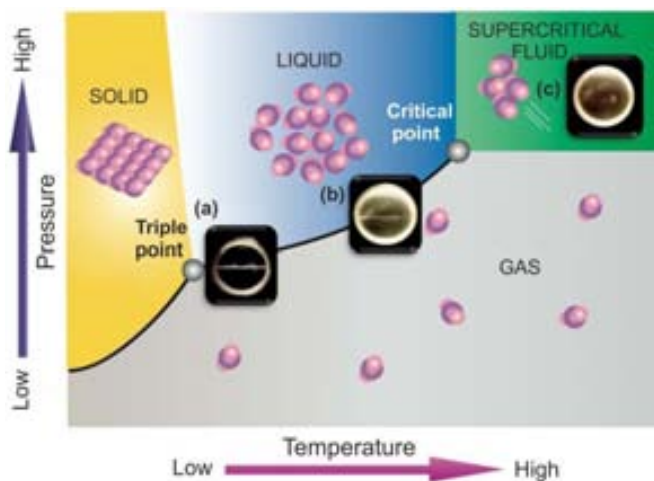
Figure 1.14. Schematic representation of the phase diagram for a pure substance showing the different states of matter. Insets show photographs demonstrating the disappearance of the meniscus at the critical point.

SCFs have physical properties between those of gases and liquids (**Table 1.2**). They present densities similar to that of liquids, low viscosities as gases and intermediate values of diffusivity. An important characteristic of SCFs is that they have almost null surface tension, diffusing rapidly to occupy the entire volume of the container. Notwithstanding, the properties of a substance might vary dramatically within the supercritical conditions, as its temperature and pressure are changed.[137]

Table 1.2. Comparison of typical physical properties of gases, liquids, and SCFs.[138]

Fluid properties	Gas	SCF	Liquid
Density (g/cm^3)	$0.6\text{-}2 \times 10^{-3}$	0.2-0.9	0.6-1.6
Diffusivity (m^2/s)	$1\text{-}4 \times 10^{-5}$	$2\text{-}7 \times 10^{-8}$	10^{-9}
Viscosity (Pa/s)	$1\text{-}3 \times 10^{-5}$	$1\text{-}9 \times 10^{-5}$	10^{-3}

The critical point is an inherent characteristic of each compound. Carbon dioxide (CO_2) is the preferred substance due to its easily accessible critical point (T_C = 31.2 ºC, $P_{C,}$ = 78.3 bar). These relatively mild conditions contrast with those of other fluids, such as acetone with a critical temperature more than seven times larger than that of CO_2 (**Table 1.3**). In addition, CO_2 is non toxic, non flammable, chemically inert and has a low cost.

Mixtures of several components can also reach the supercritical conditions. However, it has to be taken into account that the critical pressure of, *i.e.*, a CO_2/acetone binary mixture cannot be interpolated from the values of the pure substances. On the contrary, the T_C of a binary mixture lies always in between those values. Working with a supercritical mixture of two or more compounds is not that simple because only certain systems have been studied and the critical

point of many combinations still remains unknown. Some of the reported mixtures are CO_2/acetone,[139] CO_2/ethanol[140] and CO_2/dymethyl sulfoxide.[141]

Table 1.3. Critical properties of some SCFs.[138]

Fluid	T_C (ºC)	P_C (bar)	Remarks
Carbon dioxide	31.2	73.8	-
Ammonia	132.4	112.9	Toxic
Water	374.1	221	High T_C, corrosive
Ethane	32.5	49.1	Flammable
Propane	96.8	42.6	Flammable
Cyclohexane	279.9	40.3	High T_C
Methanol	240.0	79.5	High T_C
Ethanol	243.1	63.9	High T_C
Isopropanol	235.6	57.3	High T_C
Acetone	235.0	47.6	High T_C

1.5.1. Supercritical fluids for materials processing

The unique physical properties of the SCFs have been investigated in academia and/or industry since 1950. Interest in the use of SCFs has intensified during the past 30 years with the creation of large-scale plants using CO_2.[142] Useful characteristics of the SCFs are conveniently exploited for materials processing:[143]

- The possibility of tuning the fluids density with pressure and/or temperature changes provides new solvent power properties to them. Therefore, composition and structure of materials might be simultaneously controlled because of the additional degree of freedom related to density in supercritical conditions.
- The high diffusivity facilitates the mass transfer leading on highly homogenous products and reduced processing times.
- The low surface tension allows complete wetting of materials with intricate geometries, including microporous systems and the internal surface of aggregated nanoparticles.[144]

Concerning the physicochemical properties of supercritical carbon dioxide (scCO_2), a widespread set of alternative novel processing protocols and strategies have been proposed. Those strategies can be classified as function of the CO_2 role into four main groups:

- **ScCO_2 as solvent**: Only small organic compounds of low polarity are able to solubilize in scCO_2[145] as a consequence of its low dielectric constant and null dipole moment. Still, a large solubility enhancement has been observed for fluorinated substances[146] and molecules containing silicon atoms.[147] Moreover, small amounts (5-10 wt%) of different co-solvents, such as acetone or ethanol, can be added to increase the solubility of polar non volatile molecules in the resulting mixture.[148]

- **ScCO$_2$ as antisolvent**: Taking advantage of the lack of solubility in scCO$_2$ that certain substances present, this fluid is often used as an antisolvent to precipitate such solutes from a liquid solution. The scCO$_2$ must be at least partially miscible with the liquid solvent. When it occurs, a simultaneous mass transfer in two directions is produced: CO$_2$ rapidly diffuses into the liquid solution and the solvent into the CO$_2$ phase. Hence, the solvent power of the liquid is reduced causing the precipitation of the solute.

- **ScCO$_2$ as solute**: when scCO$_2$ is utilized as a solute, commonly it is dissolved in the bulk or melted solid at high concentrations. Next, the mixture is quickly expanded trough a nozzle into a chamber with the subsequent loss of the supercritical conditions. At these conditions, the gaseous CO$_2$ evaporates while its liquid counterpart solidifies. Techniques using scCO$_2$ as a solute are mainly devoted to the solvent-free precipitation of particles[149] (*i.e.* polymer of lipid particles), to induce pore-formation[150] and in extrusion processes.

- **ScCO$_2$ as reagent**: Much research is nowadays focused on the development of approaches having CO$_2$ as a green reactive in sustainable chemical processes. Although the economical aspect is still an obstacle for those methods to be extended, inorganic carbonates have been synthesized with CO$_2$ as a carbonation agent[151] and to produce organic chemicals such ureas, carbamates and isocyanate carboiimides.[152]

Although this section is mainly refer to the use of carbon dioxide, these processes can also be performed with other supercritical fluids or with mixtures of them obtaining similar results.

In addition, some post-processing steps (*e.g.* solvent removal or extraction) needed in some specific fields such as coating of drug delivery is usually avoided by using SCFs.

1.5.2. Supercritical carbon dioxide in the pharmaceutical industry

ScCO$_2$ is currently the basis of an important technology with presence in a variety of fields, including synthetic chemistry, environmental chemistry, analytical chemistry, material science, food industry and powder technology.[57,153] Particularly, its characteristics have been exploited in extraction, separation and crystallization processes.[154]

Regarding the pharmaceutical industry, scCO$_2$ is nowadays a promising alternative to conventional methods for pharmaceuticals processing. Those methodologies typically imply the use of organic solvents (*e.g.*, methanol, toluene or dichloromethane) that have well-known disadvantages like toxicity, flammability and environmental concerns. Furthermore, the manipulation of nano-objects in such solvents is difficult due to undesired processes such as agglomeration, degradation or contamination that might damage the labile surface of nanomaterials. In this context, replacing of classical methods for *green manufacturing* aims to overcome upscaling problems associated with both organic solvents and nanostructuring. In addition to the aforementioned advantages that scCO$_2$ offers for materials processing, this fluid allows straightforward and scalable up preparation of dry products and it is fully compatible with most of thermally labile materials.[155]

Some of the most relevant applications of $scCO_2$ in the pharmaceutical industry are:

- **Drug delivery**: Processes such drug impregnation, preparation of solid dispersions, micronization of pharmaceuticals or particle formation have been addressed by using $scCO_2$. Most of the solid dispersions prepared in this way are designed to enhance the dissolution and bioability of poorly-water-soluble drugs, thus involving studies with hydrophilic polymers leading to size-controlled particles that rapidly release the active compound in aqueous media.[156] Concerning micronization approaches, SCFs in general have been used to reduce the particle size of active pharmaceutical ingredients (APIs) to sizes of 2000-5 nm.[157] In the pharmaceutical industry, fine particles (micro or nano-sized) with uniform and narrow size distributions are of particular interest[158]

- **Coating**: An improved process for coating medical devices, particularly surgical devices, with polymer or polymer and a therapeutic agent using $scCO_2$ has been patented.[159]

- **Tissue engineering**: $scCO_2$ processing might be used to form porous three-dimensional scaffolds in which the escapes of CO_2 from a plasticized polymer melt generate gas bubbles that shape the pores.[160]

1.6. REFERENCES

[1] Ratner, M., Ratner, D. Nanotechnology: A gentle introduction to the next big idea. *Prentice Hall*: New Jersey, **2003**.

[2] European Comission. The appropriateness of existing methodologies to assess the potential risks associated with engineered and adventitious products of nanotechnologies. March **2006**.

[3] Bawa, R. A comprehensive nanotechnology library in miniature: a review of the Springer Handbook of Nanotechnology. *Nanotechnology Law Bus*, **2004**, 1, 341-343.

[4] Peterson, D.R. The CRC biomedical engineering handbook. 3rd Edition. *CRC Press*, **2006**.

[5] Bawa, R., Bawa, T.S.R., Maebius, S.B., Flynn, T., Wei, C. Protecting new ideas and inventions in nanomedicine with patents. *Nanomed-Nanotechnol.*, **2005**, *1*, 150-158.

[6] Freestone, I., Meeks, N., Sax, M., Higgitt, C. The Lycurgus cup-A roman nanotechnology. *Gold Bull.*, **2007**, *40/4*, 270-277.

[7] Van der Spiegel, J. Introduction to Nanoscale science and Technology. *Springer*, **2004**.

[8] Environmental health perspectives, *Brogan & Partners*, **2012**.

[9] Kuhlbusch, T.A.J., Asbach, C., Fissan, H., Göhler, D., Stintz, M. Nanoparticle exposure at nanotechnology workplaces: A review. *Part. Fibre Toxicol.*, **2011**, *8*, 1-18.

[10] Mansoori, G.A., Principles of nanotechnology. Molecular-based study of condensed matter in small systems. *World Scientific*: Singapore, **2005**.

[11] Njoki, P.N., Lim, S.I.-I., Mott, D., Park, H.-Y., Khan, B., Mishra, S., Sujakumar, R., Luo, J., Zhong, C.J. Size correlation of optical and spectroscopic properties for gold nanoparticles. *J. Phys. Chem., C*, **2007**, *111*, 14664-14669.

[12] Ruedas-Rama, M.J., Orte., A., Hall, E.A.H., Alvarez-Pez, J.M., Talavera, E.M. Effect of surface modification on semiconductor nanocrystal fluorescence lifetime. *Chem.Phys.Chem.*, **2011**, *12*, 919-929.

[13] Di Corato, R., Bigall, N.C., Ragusa, A., Dorfs, D., Genovese, A., Marotta, R., Manna, L., Pellegrino, T. Multifunctional nanobeads based on quantum dots and magnetic nanoparticles: synthesis and cancer cell targeting and sorting. *ACS Nano*, **2011**, *5*, 1109-1121.

[14] Venkatraman, S. Has nanomedicine live up to its promise?. *Nanotechnology.*, **2014**, *25*, 372501, 4pp.

[15] Barenholz, Y. Doxil®--the first FDA-approved nano-drug: lessons learned. *J. Control. Release*, **2012**, *160*, 117-134.

[16] Kelkar, S.S., Reineke, T.M. Theranostics: combining imaging and therapy. *Bioconjugate Chem.*, **2011**, *22*, 1879-1903.

[17] Orive, G., Hernandez, R.M., Rodriguez, Gascon, A., Dominguez-Gil, A., Pedraz, J.L. Drug delivery in biotechnology: present and future. *Curr. Opin. Biotechnol.*, **2003**, *14*, 659-664.

[18] Parveen, S., Misra, R., Sahoo, S.K. Nanoparticles: a boon to drug delivery, therapeutics, diagnostics and imaging. *Nanomed-Nanotechnol.*, **2012**, *8*, 147-166.

[19] Mo, R., Jiang, T., DiSanto, R., Tai, W., Gu, Z. ATP-triggered anticancer drug delivery. *Nat. Comm.*, **2014**, *5*:3364, 1-10.

[20] Chen, J.-X., Liu, W., Zhang, M., Chen, J.-H. Heparosan based negatively charged nanocarrier for rapid intracellular drug delivery. *Int. J. Pharm.*, **2014**, *473*, 493-500.

[21] Sahoo, B., Devi, J.S.P., Dutta, S., Maiti, T.K., Pramanik, P., Dhara, D. Biocompatible mesoporous silica-coated superparamagnetic manganese ferrite nanoparticles for targeted drug delivery and MR imaging applications. *J. Colloid Interface Sci.*, **2014**, *431*, 31-41.

[22] Li, X., Yu, M., Fan, W., Gan, Y., Hovgaard, L., Yang, M. Orally active-targeted drug delivery systems for proteins and peptides. *Exp. Opin. Drug Deliv.*, **2014**, *11*, 1435-1447.

[23] Iqbal, J., Vigl, C., Moser, G., Gasteiger, M., Perera, G., Bernkop-Schnürch, A. Development and in vivo evaluation of a new oral nanoparticulate dosage form for leuprolide based on polyacrylic acid. *Drug Deliv.*, **2011**, *18*, 432-440.

[24] Yun, Y., Cho, Y.W., Park, K. Nanoparticles for oral delivery: targeted nanoparticles with peptidic ligands for oral protein delivery. *Adv. Drug Deliv. Rev.*, **2013**, *65*, 822-832.

[25] Bysell, H., Månsson, R., Hansson, P., Malmsten, M. Microgels and microcapsules in peptide and protein drug delivery. *Adv. Drug Deliv. Rev.*, **2011**, *63*, 1172-1185.

[26] Ediriwickrema, A., Zhou, J., Deng, Y., Saltzman, W.M. Multi-layered nanoparticles for combination gene and drug delivery to tumors. *Biomaterials*, **2014**, *35*, 9343-9354.

[27] Miao, L., Liu, C., Ge, J., Yang, W., Liu, J., Sun, W., Yang, B., Zheng, C., Sun, H., Hu, Q. Antitumor effect of TRAIL on oral squamous cell carcinoma using magnetic nanoparticle-mediated gene expression. *Cell Biochem. Biophys.*, **2014**, *69*, 663-672.

[28] Everett, D.H. Manual of symbols and terminology for physicochemical quantities and units, appendix II: definitions, terminology and symbols in colloid and surface chemistry. Pure & Apl. Chem., 46, 71-90. *Pergamon Pres.*: Great Britain, **1976**.

[29] Blum, J., Avnir, D. Handbook of Sol-Gel Science and Technology, Vol. III. *Springer*: New York, **2003**.

[30] Mine, E., Nagao, D., Kobayashi, Y., Konno, M. Solvent Effects on Particle Formation in Hydrolysis of Tetraethyl Orthosilicate. *J. Sol-Gel Sci. Technol.*, **2005**, *35*, 197-201.

[31] Ab Wab, H.A., Razak, K.A., Zakaria, N.D. Properties of amorphous silica nanoparticles colloid drug delivery system synthesized using the micelle formation method. *J. Nanopart. Res.*, **2014**, *16*:2256, 1-14.

[32] Yano, K., Katz, M.B., Pan, X., Tatsuda, N. Monodispersed mesoporous silica spheres with various mesopore symmetries. *J. Colloid Interface Sci.*, **2014**, *418*, 61-65.

[33] Chen, D., Li, L., Tang, F., Qi, S. Facile and scalable synthesis of tailored silica ''nanorattle'' structures. *Adv. Mater.*, **2009**, *21*, 3804-3807.

[34] Suteewong, T., Sai, H., Lee, J., Bradbury, M., Hyeon, T., Gruner, S.M., Wiesner, U. Ordered mesoporous silica nanoparticles with and without embedded iron oxide nanoparticles: structure evolution during synthesis. *J. Mater. Chem.*, **2010**, *20*, 7807-7814.

[35] Giesche, H. Synthesis of Monodispersed silica powders II. Controlled growth reaction and continuous production process. *J. Eur. Ceram. Soc.*, **1994**, *14*, 205-214.

[36] Yan, F., Jiang, J., Chen, X., Tian, S., Li, K. Synthesis and characterization of silica nanoparticles preparing by low-temperature vapor-phase hydrolysis of $SiCl_4$. *Ind. Eng. Chem. Res.*, **2014**, *53*, 11884–11890.

[37] Jal, P.K., Sudarshan, M., Saha, A., Patel, S., Mishra, B. K. Synthesis and characterization of nanosilica prepared by precipitation method. *Colloids Surf. A*, **2004**, *240*, 173–178.

[38] Cai, X., Hong, R.Y., Wang, L.S., Li, H.Z., Zheng, Y., Wei, D.G. Synthesis of silica powders by pressured carbonation. *Chem. Eng. J.*, **2009**, *151*, 380-386.

[39] Brinker, C.J., Scherer, G.W. Sol-Gel Science: The Physics and Chemistry of Sol-Gel Processing, *Harcourt Brace*: San Diego, **1990**.

[40] Fardad, M.A. Catalysts and the structure of SiO_2 sol-gel films. *J. Mater. Sci.*, **2000**, *35*, 1835-1841.

[41] Stöber, W., Fink, A., Bohn. E. Controlled growth of monodisperse silica spheres in the micron size range. *J. Colloid Interface Sci.*, **1968**, *26*, 62-69.

[42] Rao, K.S., El-Hami, K., Kodaki, T., Matsushige, K., Makino, K. A novel method for synthesis of silica nanoparticles. *J. Colloid Interface Sci.*, **2005**, *289*, 125-131.

[43] Edrissi, M., Soleymani, M., Adinehnia, M. Synthesis of silica nanoparticles by ultrasound-assisted sol-gel method: optimized by taguchi robust design. *Chem. Eng. Technol.*, **2011**, *34*, 1813-1819.

[44] Vasconcelos, D.C.L., Campos, W.R., Vasconcelos, V., Vasconcelos, W.L. Influence of process parameters on the morphological evolution and fractal dimension of sol-gel colloidal silica particles. *Mater. Sci. Eng.*, **2002**, *334*, 53-58.

[45] Bogush, G.H., Tracy, M.A., Zukoski IV, C.F. Preparation of monodisperse silica particles: control of size and mass fraction. *J. Non-Cryst. Solids*, **1988**, *104*, 95-106.

[46] Rahman, I.A., Vejayakumaran, P., Sipaut, C.S., Ismail, J., Bakar, M.A., Adnan, R., Chee, C.K. An optimized sol-gel synthesis of stable primary equivalent silica particles. *Coll. Surf. A*, **2007**, *294*, 102-110.

[47] Jafarzadeh, M., Rahman, I.A., Sipaut, C.S. Synthesis of silica nanoparticles by modified sol-gel process: the effect of mixing modes of the reactants and drying techniques. *J. Sol-Gel Sci. Technol.*, **2009**, *50*, 328-336.

[48] Rahman, I.A., Vejayakumaran, P. *J. Nanomater.*, **2012**, Article ID 132424, 15 pp.

[49] Rimola, A., Costa, D., Sodupe, M., Lambert, J.F., Ugliengo, P. Silica surface features and their role in the adsorption on biomolecules: computational modeling and experiments. *Chem. Rev.*, **2013**, *113*, 4216-4313.

[50] Zhao, Y., Sun, X., Zhang, G., Trewyn, B.G., Slowing, I.I., Lin, V.S.-Y. Interaction of mesoporous silica nanoparticles with human red blood cell membranes: size and surface effects. *ACS Nano*, **2011**, *5*, 1366-1375.

[51] Tang, F., Li, L., Chen, D. Mesoporous silica nanoparticles: synthesis, biocompatibility and drug delivery. Adv. *Mater.*, **2012**, *24*, 1504-1534.

[52] Miletto, I., Bottinelli, E., Caputo, G., Colucciaa, S., Gianotti, E. Bright photoluminescent hybrid mesostructured silica nanoparticles. *Phys. Chem. Chem. Phys.*, **2012**, *14*, 10015-10021.

[53] Yokoi, T., Karouji, T., Ohta, S., Kondo, J.N., Tatsumi, T. Synthesis of mesoporous silica nanospheres promoted by basic amino acids and their catalytic application. *Chem. Mater.*, **2010**, *22*, 3900-3908.

[54] Slowing, I.I., Vivero-Escoto, J.L., Trewyn, B.G., Lin, V.S.-Y. Mesoporous silica nanoparticles: structural design and applications. *J. Mater. Chem.*, **2010**, *20*, 7924-7937.

[55] Finnie, K.S., Bartlett, J.R., Barbé, C.J.A., Kong, L. Formation of Silica Nanoparticles in Microemulsions. *Langmuir*, **2007**, *23*, 3017-3024.

[56] Tan, T.T.Y., Liu, S., Zhang, Y., Han, M-Y., Selvan, S.T. Microemulsion preparative method (Overview). Comprehensive Nanoscience and Technology. *Academic press*, **2011**, 5, 399-441.

[57] Reverchon, E., Adami, R. Nanomaterials and supercritical fluids. *J. Supercrit. Fluids*, **2006**, *37*, 1-22.

[58] Klabunde, K.J. Nanoscale Materials in Chemistry. *Wiley-Interscience*: New York, **2001**.

[59] Colilla, M., González, B., Vallet-Regí, M. Mesoporous silica nanoparticles for the design of smart delivery nanodevices. *Biomater. Sci.*, **2013**, *1*, 114-134.

[60] Liong, M., Lu, J., Kovochich, M., Xia, T., Ruehm, S.G., Nel, A.E., Tamanoi, F., Zink, J.I. Multifunctional inorganic nanoparticles for imaging, targeting, and drug delivery. *ACS Nano*, **2008**, *2*, 889-896.

[61] Liong, M., Angelos, S., Choi, E., Patel, K., Stoddart, J.F., Zink, J.I. Mesostructured multifunctional nanoparticles for imaging and drug delivery. *J. Mater. Chem.*, **2009**, *19,* 6251-6257.

[62] Halas, N.J. Nanoscience under glass: the versatile chemistry of silica nanostructures. *ACS Nano*, **2008**, *2*, 179-183.

[63] Bitar, A., Ahmad, N.M., Fessi, H., Elaissari, A. Silica-based nanoparticles for biomedical applications. *Drug Discov. Today*, **2012**, *17*, 1147-1154.

[64] Lin, Y.-S., Hurley, K.R., Haynes, C.L. Critical considerations in the biomedical use of mesoporous silica nanoparticles. *J. Phys. Chem. Lett.*, **2012**, *3*, 364−374.

[65] Li, Z., Barnes, J.C., Bosoy, A., Stoddart, J.F., Zink, J.I Mesoporous silica nanoparticles in biomedical applications. *Chem. Soc. Rev.*, **2012**, *41*, 2590-2605.

[66] Mamaeva, V., Sahlgren, C., Lindén, M. Mesoporous silica nanoparticles in medicine-Recent advances. *Adv. Drug Deliv. Rev.*, **2013**, *65*, 689-702.

[67] Anglin, E.J., Cheng, L., Freeman, W.R., Sailor, M.J. Porous silicon in drug delivery devices and materials. *Adv. Drug Deliv. Rev.*, **2008**, *60*, 1266-1277.

[68] Charnay, C., Begu, S., Tourne-Peteilh, C., Nicole, L., Lerner, D.A., Devoisselle, J.M. Inclusion of ibuprofen in mesoporous templated silica: drug loading and release property. *Eur. J. Pharm. Biopharm.*, **2004**, *57*, 533-540.

[69] Vaccari, L., Canton, D., Zaffaroni, N., Villa, R., Tormen, M., Di Fabrizio, E. Porous silicon as drug carrier for controlled delivery of doxorubicin anticancer agent. *Microelectron. Eng.*, **2006**, *83*, 1598-1601.

[70] Zhao, Y.-L., Li, Z., Kabehie, S., Botros, Y.Y., Stoddart, J.F., Zink, J.I. pH-Operated nanopistons on the surfaces of mesoporous silica nanoparticles. *J. Am. Chem. Soc.*, **2010**, *132*, 13016-13025.

[71] Luo, Z., Cai, K., Hu, Y., Zhao, L., Liu, P., Duan, L., Yang, W. Mesoporous silica nanoparticles end-capped with collagen: redox-responsive nanoreservoirs for targeted drug delivery. *Angew. Chem. Int. Ed.*, **2011**, *50*, 640-643.

[72] Lu, J., Liong, M., Li, Z., Zink, J.I., Tamanoi, F. Biocompatibility, biodistribution, and drug delivery efficiency of mesoporous silica nanoparticles for cancer therapy in animals. *Small*, **2010**, *6*, 1794-1805.

[73] Sundarraj, S., Thangam, R., Sujitha, M.V., Vimala, K., Kannan, S. Ligand-conjugated mesoporous silica nanorattles based on enzyme targeted prodrug delivery system for effective lung cancer therapy. *Toxicol. Appl. Pharmacol.*, **2014**, *275*, 232-243.

[74] Xie, J., Lee, S., Chen, X. Nanoparticle-based theranostic agents. *Adv. Drug Deliv. Rev.*, **2010**, *62*, 1064-1079.

[75] Bharali, D.J., Klejbor, I., Stachowiak, E.K., Dutta, P.D., Roy, I.R., Kaur, N., Bergey, E.J., Prasad, P.N., Stachowiak, M.K. Organically modified silica nanoparticles: a nonviral vector for in vivo gene delivery and expression in the brain. *Proc. Natl. Acad. Sci. U.S.A.*, **2005**, *102*, 11539-11544.

[76] Azioune, A., Slimane, A.B., Hamou, L.A., Pleuvy, A., Chehimi, M.M., Perruchot, C., Armes, S.P. Synthesis and characterization of active ester-functionalized polypyrrole-silica nanoparticles: application to the covalent attachment of proteins. *Langmuir*, **2004**, *20*, 3350-3356.

[77] Kim, S.H., Jeyakumar, M., Katzenellenbogen, J.A. Dual-mode fluorophore-doped nickel nitrilotriacetic acid-modified silica nanoparticles combine histidine-tagged protein purification with site-specific fluorophore labeling. *J. Am. Chem. Soc.*, **2007**, *129*, 13254-13264.

[78] Shiomia, T., Matsuia, M., Mizukamib, F., Sakaguchi, K. A method for the molecular imprinting of hemoglobin on silica surfaces using silanes. *Biomaterials*, **2005**, *26*, 5564-5571.

[79] Nguyen, T.H., Elimelech, M. Plasmid DNA adsorption on silica: kinetics and conformational changes in monovalent and divalent salts. *Biomacromolecules*, **2007**, *8*, 24-32.

[80] Hilliard, L.R., Zhao, X., Tan, W. Immobilization of oligonucleotides onto silica nanoparticles for DNA hybridization studies. *Anal. Chim. Acta*, **2002**, *470*, 51-56.

[81] Kneuer, C., Sameti, M., Haltner, E.G., Schiestel, T., Schirra, H., Schmidt, H., Lehr, C.M. Silica nanoparticles modified with aminosilanes as carriers for plasmid DNA. *Int. J. Pharm.*, **2000**, *196*, 257-261.

[82] Gore, A.Y., Banker, G.S. Surface chemistry of colloidal silica and a possible application to stabilize aspirin in solid matrixes. *J. Pharm. Sci.*, **1979**, *68*, 197-202.

[83] Jonat, S. Investigation of compacted hydrophilic and hydrophobic colloidal silicon dioxides as glidants for pharmaceutical excipients. *Powder Technol.*, **2004**, *141*, 31-43.

[84] Owen, S.C. Colloid silicone dioxide. In Handbook of Pharmaceutical Excipients. *Pharmaceutical Press*. North Yorkshire, **2006**.

[85] Ramimoghadam, D., Bagheri, S., Hamid, S.B.A. Progress in electrochemical synthesis of magnetic iron oxide nanoparticles. *J. Magn. Magn. Mater.*, **2014**, *368*, 207-229.

[86] Comesaña-Hermo, M. Synthesis of cobalt-based nanohybrids and study of their magnetic and optical properties. Carbon coating and functionalization with luminescent dyes. PhD Thesis, **2011**.

[87] Kolhatkar, A.G., Jamison, A.C., Litvinov, D., Willson, R.C., Lee, T.R. Tuning the magnetic properties of nanoparticles. *Int. J. Mol. Sci.*, **2013**, *14*, 15977-16009.

[88] Jeong, U., Teng, X., Wang, Y., Yang, H., Xia, Y. Superparamagnetic colloids: controlled synthesis and niche applications. *Adv. Mater.*, **2007**, *19*, 33-60.

[89] Tartaj, P., Morales, M.P., Veintemillas-Verdaguer, S., González-Carreño, T., Serna, C.J. The preparation of magnetic nanoparticles for applications in biomedicine. *J. Phys. D: Appl. Phys.*, **2003**, *36*, R182-R197.

[90] Teja, A.S., Koh, P.-Y. Synthesis, properties, and applications of magnetic iron oxide nanoparticles. *Prog. Cryst. Growth Ch.*, 2009, *55*, **2009**, 22-45.

[91] Xu, C., Sun, S. New forms of superparamagnetic nanoparticles for biomedical applications. *Adv. Drug Deliv. Rev.*, **2013**, *65*, 732-743.

[92] Pinkas, J., Reichlova, V., Zboril, R., Moravec, Z., Bezdicka, P., Matejkova, J. *Ultrason. Sonochem.*, 2008, *15*, **2008**, 257-264.

[93] Gonzalez-Carreiio, T., Morales, M.P., Gracia, M., Serna, C.J. Preparation of uniform γ-Fe₂O₃ particles with nanometer size by spray pyrolysis. *Mater. Lett.*, **1993**, *18*, 151-155.

[94] Lu, A.-H., Salabas, E.L., Schüth, F. Magnetic nanoparticles: synthesis, protection, functionalization, and application. *Angew. Chem. Int. Ed.*, **2007**, *46*, 1222-1244.

[95] Massart, R. Preparation of aqueous magntic liquids in alkaline and acid media. *IEEE Trans. Magn.*, **1981**, *17*, 1247-1248.

[96] Lodhia, J., Mandarano, G., Ferris, N.J., Eu, P., Cowell, S.F. Development and use of iron oxide nanoparticles (Part 1): Synthesis of iron oxide nanoparticles for MRI. *Biomed. Imag. Interv. J.*, **2010**, *6*:e12.

[97] Lee, J., Isobe, T., Senna, M. Magnetic properties of ultrafine magnetite particles and their slurries prepared via in-situ precipitation. *Colloids Surf. A.*, **1996**, *109*, 121-127.

[98] Marciello,, M., Connord, V., Veintemillas-Verdaguer, S., Vergés, M.A., Carrey, J., Respaud, M., Serna, C.J., Puerto Morales, M. Large scale production of biocompatible magnetite nanocrystals with high saturation magnetization values through green aqueous synthesis. *J. Mater. Chem. B*, **2013**, *1*, 5995-6004.

[99] Kwon, S.G., Piao, Y., Park, J., Angappane, S., Jo, Y., Hwang, N.M., Park, G.J., Hyeon, T. Kinetics of monodisperse iron oxide nanocrystal formation by "heating-up" process. *J. Am. Chem. Soc.*, **2007**, *129*, 12571-12584.

[100] Sun, S., Zeng, H., Robinson, D.B., Raoux, S., Rice, P.M., Wang, S.X., Li, G. Monodisperse MFe₂O₄ (M = Fe, Co, Mn) Nanoparticles. *J. Am. Chem. Soc.*, **2004**, *126*, 273-279.

[101] Bronstein, L.M., Huang, X.L., Retrum, J., Schmucker, A., Pink, M., Stein, B.D., Dragnea, B. Influence of iron oleate complex structure on iron oxide nanoparticle formation. *Chem. Mater.*, **2007**, *19*, 3624-3632.

[102] Majewski, P., Thierry, B. Functionalized magnetite nanoparticles-synthesis, properties, and bio-applications. *Crit. Rev. Solid State Mater. Sci.*, **2007**, *32*, 203-215.

[103] Roca, A.G., Morales, M.P., O'Grady, K., Serna, C.J. Structural and magnetic properties of uniform magnetite nanoparticles prepared by high temperature decomposition of organic precursors. *Nanotechnology*, **2006**, *17*, 2783-2788.

[104] Music, S., Gotic, M., Popovic, S., Czako-Nagy, I. Formation of γ-Fe₂O₃ by thermal decomposition of a mixture of Fe(Ⅱ)- and Fe(Ⅲ)-oxalate salts. *Mater. Lett.*, **1994**, *20*, 143-148.

[105] Rockenberger, J., Scher, E.C., Alivisatos, A.P. A New nonhydrolytic single-precursor approach to surfactant-capped nanocrystals of transition metal oxides. *J. Am. Chem. Soc.*, **1999**, *121*, 11595-11596.

[106] Amiens, C., Chaudret, B. Organometallic synthesis of nanoparticles Mod. Phys. Lett. B, 2007, 21, 1133-1141.

[107] Jana, N.R., Chen, Y., Peng, X. Size- and Shape-Controlled Magnetic (Cr, Mn, Fe, Co, Ni) Oxide nanocrystals via a simple and general approach. *Chem. Mater.*, **2004**, *16*, 3931-3935.

[108] Hyeon, T., Lee, S.S., Park, J., Chung, Y., Na, H.B. Synthesis of highly crystalline and monodisperse maghemite nanocrystallites without a size-selection process. *J. Am. Chem. Soc.*, **2001**, *123*, 12798-12801.

[109] Zhang, Y., Zhang, J. Surface modification of monodisperse magnetite nano-particles for improved intracellular uptake to breast cancer cells. *J. Colloid Interface Sci.*, **2005**, *283*, 352-357.

[110] Vidal-Vidal, J., Rivas,J., Lopez-Quintela, M. Synthesis of monodisperse maghemite nanoparticles by the microemulsion method. *Colloids Surf. A,* **2006**, *288,* 44-51.

[111] Capek, I. Preparation of metal nanoparticles in water-in-oil (w/o) microemulsions. *Adv. Colloid Interface Sci.*, **2004**, *110*, 49-74.

[112] Maliar, T., Bozenko, J., Cesiulis, H., Prosycevas, I. Electrochemical aspects of the synthesis of iron particles. *Mater. Sci.*, **2012**, *18*, 223-227.

[113] Lee, C.W., Huang, K.T., Wei, P.K., Yao, Y.D. Conjugation of γ-Fe₂O₃ nanoparticles with single strand oligonucleotides. *J. Magn. Magn. Mater.*, **2006**, *304*, e412-e414.

[114] Wang, X., Zhuang, J., Peng, Q., Li, Y. A general strategy for nanocrystal synthesis. *Nature*, **2005**, *437*, 121-124.

[115] Lam, U.T., Mammucari, R., Suzuki, K., Foster, N.R. Processing of iron oxide nanoparticles by supercritical fluids. *Ind. Eng. Chem. Res.*, **2008**, *47*, 599-614.

[116] Xuan, S., Wang, Y.-X.J., Yu, J.C., Leung, K. C.-F. Tuning the grain size and particle size of superparamagnetic Fe_3O_4 microparticles. *Chem. Mater.*, **2009**, *21*, 5079–5087

[117] Bilecka, I., Niederberger, M. Microwave chemistry for inorganic nanomaterials synthesis. *Nanoscale*, **2010**, *2*, 1358-1374.

[118] Basak, S., Chen, D.-R., Biswas, P. Electrospray of ionic precursor solutions to synthesize iron oxide nanoparticles: modified scaling law. *Chem. Eng. Sci.*, **2007**, *62*, 1263-1268.

[119] Bhargava, A., Jain, N., Barathi L., M., Akhtar, M.S., Yun, Y.-S., Panwar, J. Synthesis, characterization and mechanistic insights of mycogenic iron oxide nanoparticles. *J. Nanopart. Res.*, **2013**, *15*:11, 12pp.

[120] Kim, J.S., Yoon, T.J., Kim, B.G., Park, S.J., Kim, H.W., Lee, K.H., Park, S.B., Lee, J.K., Cho, M.H. Toxicity and tissue distribution of magnetic nanoparticles in mice. *Toxicol. Sci.*, **2006**, *89*, 338-347.

[121] Arruebo, M., Fernández-Pacheco, R., Ibarra, M.R., Santamaría, J. Magnetic nanoparticles for drug delivery. *Nano Today*, **2007**, *2*, 22-32.

[122] Bulte, J.W., Kraitchman, D.L. Iron oxide MR contrast agents for molecular and cellular imaging. *NMR Biomed.*, **2004**, *17*, 484-499.

[123] Sun, C., Sze, R., Zhang, M.Q. Folic acid-PEG conjugated superparamagnetic nanoparticles for targeted cellular uptake and detection by MRI. *J. Biomed. Mater. Res. A*, **2006**, *78A*, 550-557.

[124] Park, J.H., Von Maltzahn, G., Zhang, L.L., Schwartz, M.P., Ruoslahti, E., Bhatia, S.N., Sailor, M.J. Magnetic iron oxide nanoworms for tumor targeting and imaging. *Adv. Mater.*, **2008**, *20*, 1630-1635.

[125] Gunn, J., Wallen, H., Veiseh, O., Sun, C., Fang, C., Cao, J.H., Yee, C., Zhang, M.Q. A multimodal targeting nanoparticle for selectively labeling T cells. *Small*, **2008**, *4*, 712-715.

[126] Artemov, D., Mori, N., Okollie, B., Bhujwalla, Z.M. MR molecular imaging of the Her-2/neu receptor in breast cancer cells using targeted iron oxide nanoparticles. *Magn. Reson. Med.*, **2003**, *49*, 403-408.

[127] Yigit, M.V., Mazumdar, D., Lu, Y. MRI detection of thrombin with aptamer functionalized superparamagnetic iron oxide nanoparticles. *Bioconjugate Chem.*, **2008**, *19*, 412-417.

[128] Laurent, S., Forge, D., Port, M., Roch, A., Robic, C., Elst,, L.V., Muller, R.N. Magnetic iron oxide nanoparticles: synthesis, stabilization, vectorization, physicochemical characterizations, and biological applications. *Chem. Rev.*, **2008**, *108*, 2064-2110.

[129] Hwu, J.R., Lin, Y.S., Josephrajan, T., Hsu, M.H., Cheng, F.Y., Yeh, C.S., Su, W.C., Shieh, D.B. Targeted paclitaxel by conjugation to iron oxide and gold nanoparticles. *J. Am. Chem. Soc.*, **2009**, *131*, 66-68.

[130] Kohler, N., Sun, C., Fichtenholtz, A., Gunn, J., Fang, C., Zhang, M. Methotrexate-immobilized poly(ethylene glycol) magnetic nanoparticles for MR imaging and drug delivery. *Small*, **2006**, *2*, 785-792.

[131] Neveu, S., Bee, A., Robineau, M., Talbot, D. Size-Selective Chemical Synthesis of Tartrate Stabilized Cobalt Ferrite Ionic Magnetic Fluid. *J. Colloid Interface Sci.*, **2002**, *255*, 293-298.

[132] Gupta, A.K., Gupta, M. Synthesis and surface engineering of iron oxide nanoparticles for biomedical applications. *Biomaterials*, **2005**, *26*, 3995-4021.

[133] Neuberger, T., Schopf, B., Hofmann, H., Hofmann, M., Von Rechenberg, B. Superparamagnetic nanoparticles for biomedical applications: possibilities and limitations of a new drug delivery system. *J. Magn. Magn. Mater.*, **2005**, *293*, 483-496.

[134] Safarik, I., Safarikova, M. Magnetic techniques for the isolation and purification of proteins and peptides. *Biomagn. Res. Technol.*, **2004**, *2*:7, 17pp.

[135] Fan, J., Lu, J., Xu, R., Jiang, R., Gao, Y. Use of water-dispersible Fe_2O_3 nanoparticles with narrow size distributions in isolating avidin. *J. Colloid Interface Sci.*, **2003**, *266*, 215-218.

[136] Xu, C., Xu, K., Gu, H., Zheng, R., Liu, H., Zhang, X., Guo, Z., Xu, B. Dopamine as a robust anchor to immobilize functional molecules on the iron oxide shell of magnetic nanoparticles. *J. Am. Chem. Soc.*, **2004**, *126*, 9938-9939.

[137] Clifford, A.A. Fundamentals of Supercritical Fluids. *Oxford University Press*: Oxford, **1998**.

[138] Sanli, D., Bozbag, S.E., Erkey, C. Synthesis of nanostructured materials using supercritical CO_2: Part I. Physical transformations. *J. Mater. Sci.*, **2012**, *47*, 2995-3025.

[139] Pöhler, H., Kiran, E., Volumetric properties of cabon dioxide + acetone at high pressures. *J. Chem. Eng. Data*, **1997**, *42*, 379-383.

[140] Day, C.-Y., Chang, C.J., Chen, C.-Y. Phase Equilibrium of ethanol + CO_2 and acetone + CO_2 at elevated pressures. *J. Chem. Eng. Data*, **1996**, *41*, 839-843.

[141] Gonzalez, A.V., Tufeu, R., Subra, P. High-pressure vapor-liquid equilibrium for the binary systems carbon dioxide + dimethyl sulfoxide and carbon dioxide + dichloromethane. *J. Chem. Eng. Data*, **2002**, *47*, 492-495.

[142] Beckman, E.J. Supercritical and near-critical CO_2 in green chemical synthesis and processing. *J. Supercrit. Fluids*, **2004**, *28*, 121-191.

[143] Zhang, A., Zhang, Q., Bai, H., Li, L., Li, J. Polymeric nanoporous materials fabricated with supercritical CO_2 and CO_2-expanded liquids. *Chem. Soc. Rev.*, **2014**, *43*, 6938-6953.

[144] García-Carmona, J., Fanovich, M.A., Llibre, J., Rodríguez-Clemente, R., Domingo, C. Processing of microporous VPI-5 molecular sieve by using supercritical CO_2: stability and adsorption properties. Microp. *Mesop. Mater.*, **2002**, *54*, 127-137.

[145] Sun, Y. Supercritical fluid technology in materials science and engineering. *Malcel Dekker*. New York, **2002**.

[146] McHugh, M.A., Krukonis, V.J., Supercritical fluid extraction: principles and practice. *Butterworth-Heinemann*. Boston, **1994**.

[147] García-González, C.A., Fraile, J., López-Periago, A., Saurina, J., Domingo, C. Measurements and correlation of octyltriethoxysilane solubility in supercritical CO_2 and assembly of functional silane monolayers on the surface of nanometric particles. *Ind. Eng. Chem. Res.*, **2009**, *48*, 9952-9960.

[148] Ting, S.S.T., Tomasko, D.L., Macnaughton, S.J., Foster, N.R. Chemical-physical interpretation of cosolvent effects in supercritical fluids. *Ind. Eng. Chem. Res.*, **1993**, *32*, 1482-1487.

[149] Weidner, E., Petermann, M., Knez, Z. Multifuncional composites by high-pressure spray processes. *Curr. Opin. Solid State Mater. Sci.*, **2003**, *7*, 385-390.

[150] López-Periago, A., Argemí, A., Adanson, J.M., Fernández, V., García-González, C.A., Kazarian, S.G., Surina, J., Domingo, C. Impregnation of a biocompatible polymer aided by supercritical CO_2: evaluation of drug stability, drug-matrix interactions. *J. Supercrit. Fluids*, **2009**, *48*, 56-63.

[151] López-Periago, A.M., Pacciani, R., Vega, L.F., Domingo, C. Monitoring the effect of mineral precursor, fluid phase CO_2-H_2O composition, and stirring on $CaCO_3$ crystallization in a supercritical-ultrasound carbonation process. *Cryst. Growth Des.*, **2011**, *11*, 5324-5332.

[152] Scondo, A., Dumarcay-Charbonnier, F., Marsura, A., Barth, D. Supercritical CO_2 phosphine imide reaction on peracetylated β-cyclodextrins. *J. Supercrit. Fluids*, **2009**, *48*, 41-47.

[153] Cheah, E.L.C., Chan, L.W., Heng, P.W.S. Supercritical carbon dioxide and its application in the extraction of active principles from plant materials. *Asian J. Pharm. Sci.*, **2006**, *1*, 59-71.

[154] Jarmer, D.J., Lengsfeld, C.S., Anseth, K.S., Randolph, T.W. Supercritical fluid crystallization of griseofulvin: crystal habit modification with a selective growth inhibitor. *J. Pharm. Sci.*, **2005**, *94*, 2688-2702.

[155] Domingo, C., Saurina, J. An overview of the analytical characterization of nanostructured drug delivery systems: Towards green and sustainable pharmaceuticals: A review. *Anal. Chim. Acta*, **2012**, *744*, 8-22.

[156] Perrut, M., Jung, J., Leboeuf, F. Is it possible to enhance the dissolution rate of poorly-soluble active ingredients by supercritical fluid processes? *Proc. 9th Meeting Supercrit. Fluids*. Trieste, **2004**.

[157] Ventosa, N., Veciana, J., Sala, S., Muntó, M., Cano, M., Gimeno, M. New technologies for the preparation of micro- and nanostructured materials with potential applications in drug delivery and clinical diagnostics. *Contrib. Sci.*, **2005**, *3*, 11-18.

[158] De Matosa, M.B.C., Piedadeb, A.P., Alvarez-Lorenzoc, C., Concheiroc, A., Bragaa, M.E.M., De Sousa, H.C. Dexamethasone-loaded poly(-caprolactone)/silica nanoparticles composites prepared by supercritical CO_2 foaming/mixing and deposition. *Int. J. Pharm.*, **2013**, *456*, 269-281.

[159] Mehta, D.B., Corbo, M. Process for coating stents and other medical devices using supercritical carbon dioxide, US Patent 6627246, September 30, **2003**.

[160] Tai, H., Popov, V.K., Shakesheff, K.M., Howdle, S.M. Putting the fizz into chemistry: applications of supercritical carbon dioxide in tissue engineering, drug delivery and synthesis of novel block copolymers. *Biochem. Soc. Trans.*, **2007**, *35*, 516-521.

2

SYNTHESIS OF SILICA-BASED MATERIALS
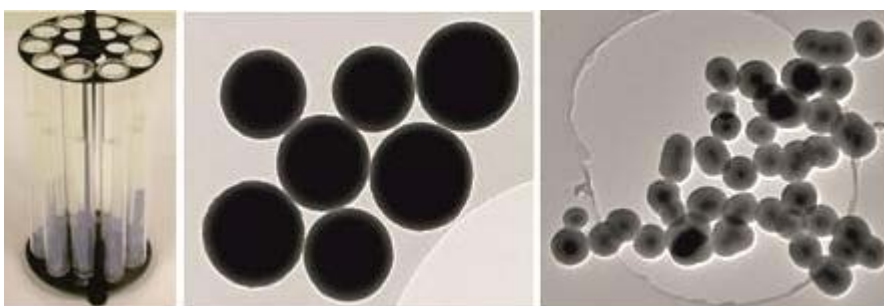
The materials made of silicon dioxide (SiO_2) with potential bioapplications are the basis of this thesis's project. In particular, three different types of silica-based systems were prepared as matrices to host active pharmaceutical ingredients: SiO_2 monolithic aerogels, submicron-sized SiO_2 particles and composite core(iron oxide)-shell(SiO_2) nanoparticles.

In this chapter, the methodologies used to synthesize the materials, as well as the iron oxide particles prior to silica coating, are explained in detail. The obtained materials and their characterization are also shown and carefully analyzed. The morphology and the size of the particles are studied. Specifically, the obtained particle diameter by electron microscopy observations and the hydrodynamic diameter in polar solvents are presented.

2.1. SOL-GEL CHEMISTRY OF SILICA

Products under the name of *silica* involve a large amount of materials with the general formula of SiO_2 or $SiO_2 \cdot xH_2O$. Although silica compounds appear naturally in mineral form, such as quartz and flint, and in some plants (*f.i.* rice, barley or bamboo), the most commonly used silica products in the industry come from synthetic routes. When silica occurs in nature the preferred conformation is the crystalline phase, while synthesized silicon oxide materials are often amorphous and with an intrinsic porosity susceptible of control. Silica materials can be obtained in the form of gels, particles, fibers, etc... products that have a large surface/mass ratio. The crystalline counterparts only possess a specific surface area related to their geometric surface.[1]

Among many routes developed for the fabrication of amorphous silica, the most studied one is the *sol-gel* process. In this method, *alkoxysilanes* are commonly used as silicon precursors due to their facility to react with water. They have the general formula of $Si(OR)_4$ and belong to the family of the *metalorganic* compounds. Specifically, TEOS (tetraethylortosilicate) and TMOS (tetramethylortosilicate) are the most used precursors in silica sol-gel research. Since TEOS and TMOS are both immiscible with water, a mutual solvent must be used in the sol gel process. Ethanol and methanol are the most employed ones. When possible, it is advisable to select a solvent with the same alkyl group than the silicon precursor (ethyl or methyl group) in order to avoid transesterification reactions. In a sol-gel reaction, the precursor is hydrolyzed in presence of water (**Reaction 2.1)** and the products condense according to **Reaction 2.2** and **Reaction 2.3**.

Reaction 2.1 $Si(OR)_4 + H_2O \rightarrow (RO)_{4-n}\text{-}Si\text{-}(OH)_n + nROH$

Reaction 2.2 $(RO)_{4-n}\text{-}Si\text{-}(OH)_n + Si(OR)_4 \rightarrow (RO)_{4-n}\text{-}Si\text{-}O\text{-}Si\text{-}(OR)_{4-n} + nROH$

Reaction 2.3 $(RO)_{4-n}\text{-}Si\text{-}(OH)_n + (RO)_{4-n}\text{-}Si\text{-}(OH)_n \rightarrow (RO)_{4-n}\text{-}Si\text{-}O\text{-}Si\text{-}(OR)_{4-n} + nH_2O$
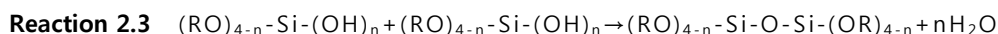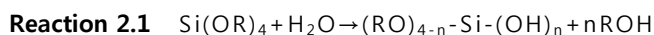
The **Reaction 2.1** proceeds completely, i.e., all the OR groups are hydrolyzed to OH, when enough water is present in the medium. By following the **Reaction 2.2** and **Reaction 2.3**, siloxane bonds Si-O-Si are formed releasing a molecule of alcohol or water. These chemical processes may extend to polymerization, building different silicon oxide-based structures. If the silicon alkoxyde is fully hydrolyzed to ortosilicic acid ($Si(OH)_4$), it is capable to build three-dimensional structures by *cross-linking*. The mechanism of polymerization of silicic acid has been explained as occurring in three stages:[2]

- **Step 1**: Polymerization of monomers into primary particles.
- **Step 2**: Growth of those particles by *Ostwald ripening*.
- **Step 3**: Association of particles to from chains and then networks in the liquid medium.

The final conformation of the silica product depends on **Reaction 2.1-Reaction 2.3**, which are governed by factors such as the amount of water, temperature or the presence of a catalyst.

The sol-gel process has the possibility of adding a catalyst of acid or basic nature, not only to accelerate the process, but also to modulate the structure and properties of the resulting materials by varying the relative importance of the steps 2 and 3 in the polymerization reaction. The condensation rate is proportional to the concentration of OH$^-$ and it is controls **Reaction 2.4** and **Reaction 2.5**. In acidic conditions, the particles that have reached a diameter between 2 and 4 nm do not grow anymore due to the limited solubility of silica in this pH range. In basic medium, the condensed species are more ionized than in acid pH, promoting the growth by interaction between monomers instead of by aggregation (**Figure 2.1**). Since silica dissolves easily in basic pH, further growth continues by Ostwald ripening. The final size of the particles also depends on temperature: the higher the temperature, the larger the particle diameter. Moreover, the incorporation of salts in either acid or basic media reduces the *double electrical layer*, facilitating the interaction between particles and the formation of a gel network. Other factors that also influence the sol-gel process are the type of precursor used, the precursor to water ratio and the solvent.

Reaction 2.4 $(RO)_{4-n}-Si-(OH)_n+OH^-\rightarrow(RO)_{4-n}-Si-(O^-)_n+nH_2O$

Reaction 2.5 $(RO)_{4-n}-Si-(O^-)_n+(RO)_{4-n}-Si-(OH)_n\rightarrow(RO)_{4-n}-Si-O-Si-(OR)_{4-n}+nOH^-$
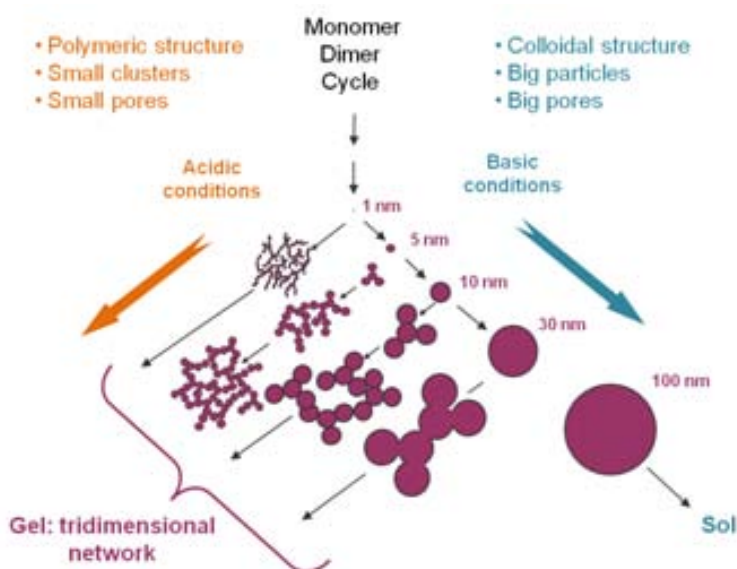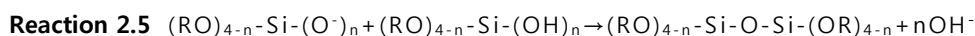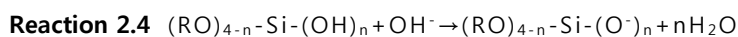
Figure 2.1. Scheme of the polymerization behavior of aqueous silica depending on the pH.[3]

In this thesis, silica sol-gel chemistry is combined with the use of supercritical fluids to prepare three different types of porous materials for biomedical applications: silica aerogels, silica sub-micron particles and composite core(iron oxide)-shell(SiO_2) nanoparticles.

To demonstrate the versatility of the synthetic approach, other materials with potential bioapplications have been synthesized during the experimental work of this thesis following the same procedure. In particular, core(quantum dots)-shell(SiO_2) nanoparticles with both CdSe-ZnS

and iron oxdie + CdSe-ZnS cores and tuned silica shell thickness. Results on these experiments were similar to those found for iron oxide-silica nanoparticles.

The silicon precursor hydrolyzes and condenses when dissolved in a solvent, forming a sol of primary silica particles dispersed in the liquid phase. The sol can either suffer aggregation creating larger entities or the formation of a polymeric matrix by gelling. Whatever the material formed either spherical particles or bulk gels, the supercritical solvent extraction leads to the preservation of the original porous structure producing aerogel particles (porous spheres) or aerogels monoliths. On the contrary, room temperature solvent evaporation results in the collapse of the structure giving low porosity particles or xerogels. These processes are schematized in **Figure 2.2**.

The guarantee to perform a correct supercritical drying lies in assuring a solvent extraction that goes straight to the gas state from the supercritical conditions avoiding the liquid phase. **Figure 2.3** illustrates this process (red pathway, a). When the solvent is in the liquid state and evaporates, strong capillary tensions inside the pores are created. Those forces are inversely proportional to the pore diameters, as defined in **Equation 2.1**. Since the gels or particles in the sol have nanometric pores, the capillary pressure generated in the pore walls (ρ_C) is too high to be stand by the walls, leading to the breakage of the silica network and the solid structure collapse, as shown in the "b" pathway (green arrow) of **Figure 2.3**.
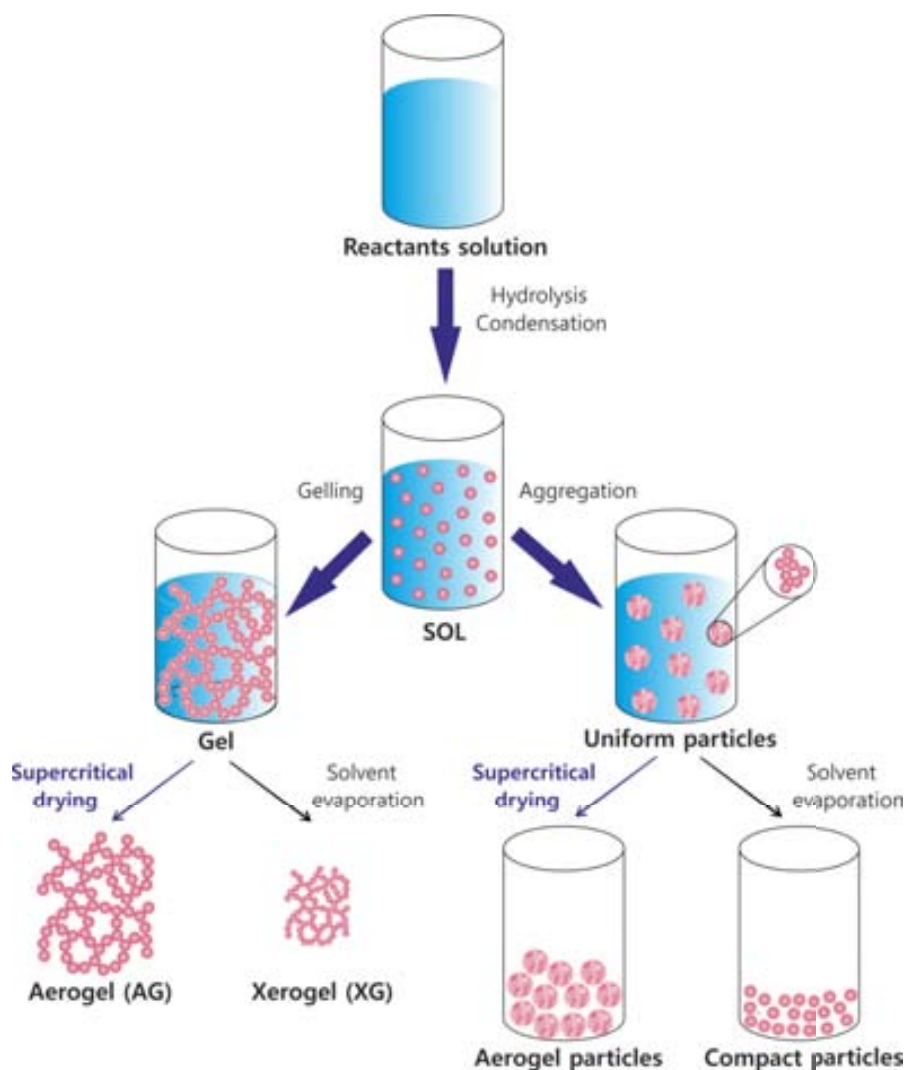
Figure 2.2. Scheme of the different silica-based materials produced in this work by combining sol-gel chemistry and different solvent extraction procedures. *Aerogel particles* is referred both to silica sub-micron spheres and composite nanoparticles.
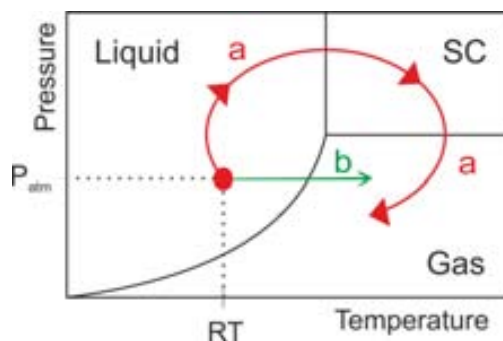
Figure 2.3. For a drying process, scheme of the solvent phase changes depending on the type of process: (a) supercritical drying and (b) evaporation.

35

Equation 2.1 $$\rho_C = \frac{2\gamma\cos\theta}{r}$$

where γ is the surface tension (strength per unit of length), θ is the wetting angle and r is the pore radius.

2.2. POROUS STRUCTURE OF SILICA-BASED MATERIALS

From a textural point of view, considering drug delivery applications, one of the most remarkable features of the silica-based materials is their intrinsic porosity. Aerogels and aerogel inspired materials present an open porous framework. In contrast to a compact material or materials involving a closed-pore arrangement, in the aerogels, the gases or liquids can flow through the interconnected open pores. According to the IUPAC,[4] the pores in any kind of porous solid are classified as a function of the mean pore diameter (**Table 2.1**). In agreement with this classification, silica aerogel monoliths are mainly mesoporous and the particulate systems, both the silica sub-micron particles and the composite nanospheres are microporous.

Table 2.1. The IUPAC pore size classification.

Type of pore	Micropore	Mesopore	Macropore
Pore size (nm)	< 2	2-50	> 50

The most important methods of porous matter characterization are based in adsorption phenomena. Two different kinds of adsorption processes can be distinguished depending upon the strength of the interaction between an adsorbate and the solid adsorbent: chemical or physical adsorption. The first one is defined by the formation of chemical bonds and gives place to *chemisorption* processes. In this case, a direct contact between adsorbate and adsorbent is needed to enable the chemical linkage. Thus, chemisorption can only occurs in a monolayer even at saturation pressure. In the physical adsorption (or *physisorption*) processes, the pores at saturation are completely filled by the adsorbate because a multilayer is formed.

Brunauer, Deming, Deming and Teller classified the physisorption isotherms into five types.[5] Later on, Sing introduced an additional one. These six types of isotherms compose the current IUPAC classification[6] and they are illustrated in **Figure 2.4**. Type I corresponds to microporous materials with pore sizes not much larger than the molecular diameter of common adsorbates (< 2 nm). Type II describes the adsorption behavior of nonporous solids or solids with macroporosity. Type III is convex and represents systems in which the adsorbate molecules have more affinity between them than they do for the adsorbent surface. Characteristic features of type IV isotherm are its hysteresis loop, which is associated with capillary condensation taking place in mesopores. Type V is a variation of type III at weak adsorbate-adsorbent interactions. Finally, type VI is quite rare and represents stepwise multilayer adsorption on a uniform non-porous surface.
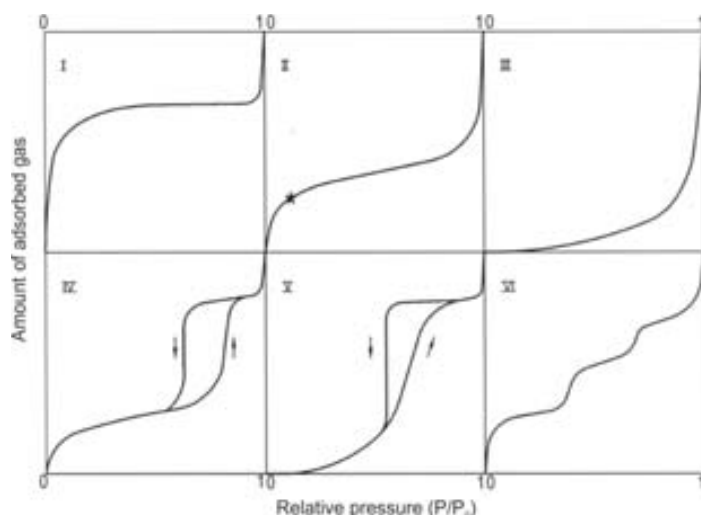
Figure 2.4. The IUAPC physisorption isotherms.

Brunauer, Emmet and Teller[7] developed in 1938 an important method to measure the specific surface area, known as the BET method. BET equation is proposed to describe adsorption of a gas on a solid surface. The BET equation is an extension of the Langmuir's monolayer adsorption equation, but considering multilayers formation (**Equation 2.2**).

Equation 2.2
$$\frac{P}{V_a(P_0\text{-}P)} = \frac{1}{V_mC} + \frac{C\text{-}1}{V_mC}\left(\frac{P}{P_0}\right)$$

where V_a is the amount of gas adsorbed at a pressure P, V_m is the quantity of gas adsorbed once the whole solid surface is covered with a macromolecular layer, P_o is the saturation pressure of the gas and C is a constant.

The plot of $P/[V_a(P_0\text{-}P)]$ vs. P/P_0 results in a straight line. V_m and C can be thus extracted from the slope and the intercept, respectively.

The BET gas adsorption method has become the most widely used standard procedure for the determination of the surface area of finely-divided and porous materials. The classical pore size model developed by Barret, Joyne and Halenda (BJH) in 1951, which is based on the Kelvin equation and corrected for multilayer adsorption, is mostly used for calculations of the pore size distribution over the mesopore and part of the macropore range. For the micropore zone, the t-plot method is the most common way of determining the surface area and pore volume.

In this thesis, surface area, pore volume and pore size are calculated by applying the BET method to the nitrogen adsorption/desorption isotherms of each material while the micropore area is extracted from the t-plot method. The pore volume is taken at each saturation pressure. For particulate systems two different approaches to calculate the pore size have been used. In the first one, the pore diameter is calculated using pore volume and surface area values measured at the saturation pressure. This *mean pore size* value includes intraparticle micropores and interparticle mesopores in the calculation. In the second approach, the textural values are

taken at a relative pressure of 0.2. The resulting mean pore diameter corresponds to the filling of the micropores, and, thus, to intraparticle pore size. It is named as *intraparticle pore size* (pore size$_{intraparticle}$).

2.3. SILICA AEROGELS

2.3.1. Synthesis of silica aerogels

Aerogels are extremely light solids with a highly porous structure. The gel that is formed from the sol-gel process is filled with alcohol and called *alcogel*. Depending on the drying process applied to the alcogel, the structure of the resulting system is different. By exchanging the liquid in the gel with air at supercritical conditions, in which no or minimal pore collapse occurs, the resulting material is called aerogel.[8,9] Contrary, if the gel is dried by solvent evaporation, a xerogel is formed. Aerogel materials display interesting properties, such as low densities, porosities between 90 and 99% and high surface areas. Silica aerogels have been used in a wide variety of applications, including thermal and acoustics insulation,[10] drug delivery[11,12] and catalysis.[13] As a contrast, *xerogels* are much denser systems with lower porosity than aerogels.

Silica aerogels present an open porous framework formed by spherical primary particles of 5 nm in diameter. Those spheres cluster into secondary particles (around 20-50 nm) that are linked in chains creating the porous aerogel skeleton. This structure is schematized in **Figure 2.5**.
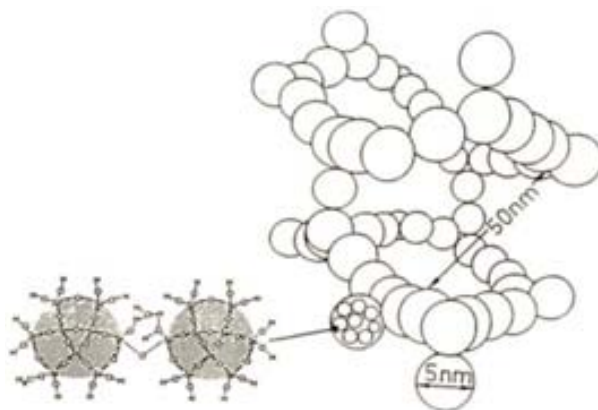
Figure 2.5. Basic scheme of silica aerogels structure

Silica aerogels were here synthesized by the sol-gel method and labeled as *AM(aerogel monolith)_number of experiment*. The optimal synthesis conditions for the aerogel monoliths were selected from Magda Moner's thesis:[14] tetramethylortosilicate (TMOS, 98 wt%, Sigma-Aldrich) was used as the silicon precursor and methanol (MeOH, anhydrous, 99.8 wt%, Sigma-Aldrich) as the solvent, in a TMOS/H_2O/MeOH molar ratio of 1/4/12.25, and ammonium hydroxyde (NH_4OH, 32 wt%, Merck) at a concentration of 0.06 M as the base catalyst. Note that the amount of water was stoichiometric with respect to the TMOS ([TMOS]/[H_2O] = 4) in order

to favor a complete hydrolysis of the TMOS. Two similar batches were performed to obtain the base materials for further processing. In **Table 2.2** details on reactants concentration ([ ]) and volume (V) are given.

Table 2.2. Concentration in methanol and volume of the reactants employed to prepare silica aerogel monoliths (AM).

Synthesis	[TMOS] (M)	V_{TMOS} (mL)	[H_2O] (M)	V_{H2O} (mL)	V_{MeOH} (mL)	[NH_3] (M)	V_{NH4OH} 32 wt% (mL)
AM_1	1.4	25.3	5.5	12.2	84.5	0.06	0.421
AM_2							

The procedure was based on the following steps:

Step 1: <u>Preparation of the gels</u>.

- A mixture of the catalyst and water was added, drop by drop, to a solution of TMOS in MeOH. Next, this solution was quickly poured into several Pyrex assay tubes. The gel network started to form immediately; therefore, it was important not to move the recipients during the gelling process to avoid gel cracking. Within 2-4 min., the gels were formed.
- Ageing process took place during 2 days and needed the gels to be wet with an extra volume of the fresh solvent (around 3 mL).

Step 2: The tubes were placed in a 2 L high pressure reactor for supercritical drying (**Figure 2.6a**) using a stainless steel holder with three platforms and several holes drained to fit the tubes (**Figure 2.6b**).
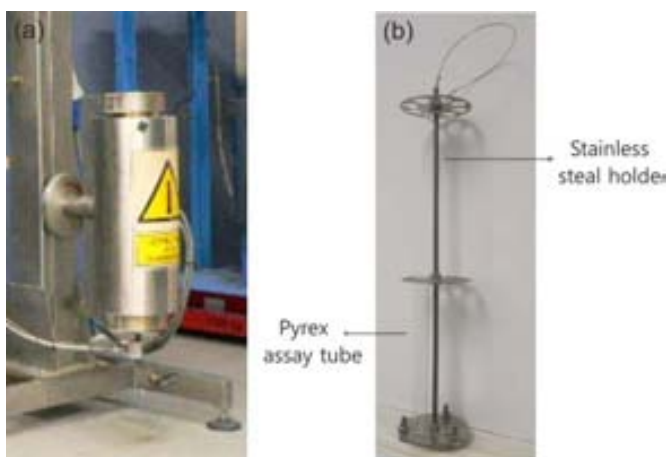
Figure 2.6. For the gels drying: (a) supercritical 2 L reactor, and (b) a Pyrex assay tube placed in the designed stainless steel holder.

Step 3: <u>Supercritical drying</u>. The temperature and pressure pathways of a representative experiment of supercritical gels drying are plotted in **Figure 2.7a** and **Figure 2.7b**, and described as follows: the reactor was sealed (**stage 1**) and the system was then pressurized by injecting compressed carbon dioxide (CO_2) up to a pressure of *c.a.* 50 bar (**stage 2**). The

temperature was increased in 30 °C every 10 min. until reaching 270 °C. This rising in the temperature brought a gradual increase in the pressure up to 240 bar (**stage 3**). The final conditions were in all cases above the critical point of the used CO_2/MeOH mixture.[15] These conditions were maintained for 2h. The system was first depressurized by venting out the solvent and the unreacted precursors into another chamber, but keeping the high temperature. This maintenance of the temperature was crucial to avoid the liquation of the solvents and the collapse of the pore structure due to capillary forces. In this way, the solvents reached directly the gaseous state from the supercritical conditions (see **Figure 2.3**). Once the reactor was at the atmospheric pressure, fresh CO_2 at 3 bar with a flow of 3 Kg/h was circulated during 30 min. to remove any unreacted species left (**stage 4**). The reactor was then completely depressurized and cool down to room temperature overnight (**stage 5**).
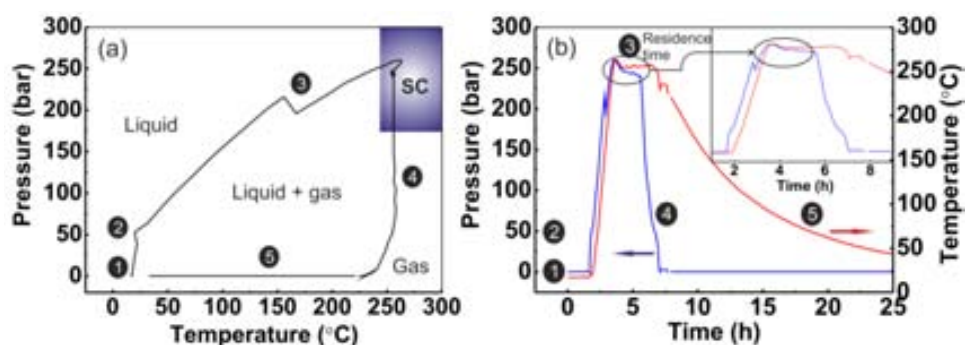
Figure 2.7. For the synthesis of AM, graphs of: (a) pressure vs. temperature cycle, and (b) evolution of pressure and temperature with time. The blue shadow area in (a) corresponds to the supercritical state for any CO_2/MeOH mixture

2.3.2. Results and discussion

2.3.2.1. Size and morphology of silica aerogels

Two batches for aerogel monolith synthesis were carried out (labeled as AM_1 and AM_2), obtaining in both similar results. Resulting materials were constituted by extremely light, transparent and fragile cylindrical bars of around 7 cm in length and 1.3 cm in diameter. By measuring the volume of the cylinder and weighing the bar, the bulk density can be calculated. This value is in the order of 0.11 ± 0.03 g/cm³. In **Figure 2.8**, a picture an aerogel monolith is depicted, showing its representative transparency. Using the calculated bulk densities, the aerogel porosity can be determined with **Equation 2.3,** where ρ_{SiO2} is taken as 2.19 g/cm³ (the density of the pure silica) and $\rho_{material}$ is the bulk material density. The porosity in both prepared monoliths was similar and fitted into the common data range of described silica aerogels, being 95.0% for AM_1 and 93.6% for AM_2.
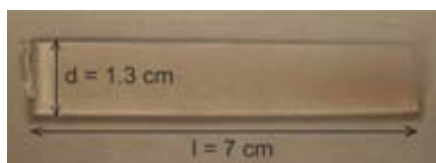
Figure 2.8. Photograph of a silica aerogel bar. l stands for length and d for diameter.

Equation 2.3 $$P(\%) = \left(\frac{\rho_{SiO_2} - \rho_{material}}{\rho_{SiO_2}}\right) * 100$$

Scanning and transmission electron microscopy (SEM, TEM)

The microstructure of the aerogel monoliths was studied by scanning and transmission electron microscopy (SEM and TEM, respectively). For SEM characterization, the monolith was first milled in an agate mortar and small pieces were stuck directly onto the SEM holder. Next, it was sputtered with gold for 2 min. with an intensity of 20 mA. For TEM observations, the milled monolith was dispersed in ethanol or acetone and then one drop of this dispersion was poured onto a holey carbon TEM grid coated with copper (Monocomp). Finally, the solvent was left to evaporate. The use of water for dispersing the monolith must be avoided, because in the aqueous environment the reactive groups that still have the silica surface can suffer further condensation when exposed to the electronic beam of the microscope. The utilization of ethanol or acetone is more appropriate for this purpose.

The synthesized aerogels presented a three-dimensional framework of interconnected silica nanoparticles with sizes around 50 nm as it is observed in the SEM image of **Figure 2.9a**. In the image, the porous arrangement is also exhibited; being distinguished from the granular structure of the silica network due to the different contrast: the less electrodense regions, the darkest the image. TEM observations evidenced the same structure: small silica particles linked to build a solid framework with pores arranged in a tortuous way (**Figure 2.9b**).
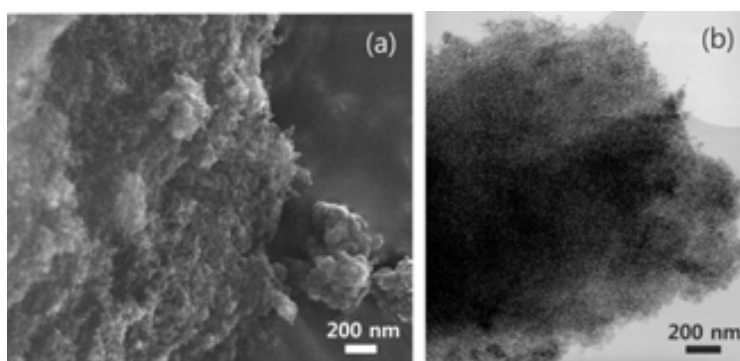
Figure 2.9. Images of (a) SEM, and (b) TEM of a representative sample of aerogel monolith.

2.3.2.2. Textural properties of silica aerogels

Nitrogen adsorption/desorption isotherms (BET method)

Silica aerogel monoliths were characterized in regards of their textural properties by analyzing the nitrogen adsorption/desorption isotherm with the BET method. Prior to measurements, both systems were degassed at 100 ºC for 24 h under reduced pressure (< 10^{-8} bar).

Figure 2.10 shows the low temperature adsorption/desorption curve of a characteristic aerogel monolith (AM_1). The monolith had an isotherm of type IV (see **Figure 2.4**), as it was expected for mesoporous aerogels according to the literature.[16] The adsorption in the first part of the curve (P/P_0 < 0.1), which corresponds to the microporous fraction of the system, was not significant. In the intermediate zones (at relative pressures from 0.1 to 0.9) the adsorption was important due to the existence of pores in the meso range. The abrupt rise above relative pressures of 0.9 relied on the condensation of the adsorbate gas molecules that takes place inside the pores.
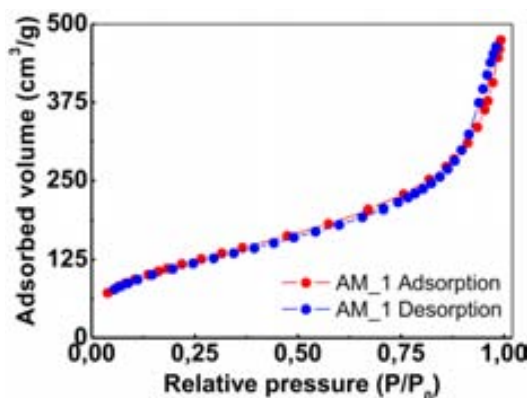
Figure 2.10. Low temperature nitrogen adsorption/desorption isotherms of samples AM_1.

In **Table 2.3** the parameters defining the textural properties of aerogel materials are shown. High porosities were obtained for both AM_1 and AM_2 samples (more than 90%). Surface areas (S_{BET}), pore volumes (V_{pore}) and mean pore sizes were similar for both materials. The intensity of the adsorption interactions of nitrogen with the surface of the adsorbent was assessed from the C constant of the BET equation. C parameter represents the surface adsorbate/adsorbent interaction energy, so it must take a positive value. Although rigorous interpretation of the C constant combined with its use for the determination of surface energies has fundamental limitations, this simplistic qualitative approach gives an idea of the hydrophobic character of the surface: the lower the C constant value, the lower the hydrophilicity. As it can be observed in **Table 2.3**, aerogels presented values of C around 50 that is a relatively low value for a hydrophilic material. This is related with the drying process used to obtain the aerogels: when the gels are exposed to the high temperatures needed to reach supercritical MeOH, the condensation of the hydroxyl groups is promoted and the silica surface is partially depleted of those hydrophilic moieties.

Table 2.3. For AG samples, data of porosity calculated by BET and the C parameter.

Sample	Porosity (%)	S_{BET} (m^2/g)	Mean V_{pore} (cm^3/g)	Mean pore size (nm)	C
AM_1	95	429	0.73	6.8	49
AM_2	94	331	1.00	12	51

2.4. SILICA PARTICLES

Two types of silica particles were fabricated: supercritically dried aerogel-like silica particles (AP) and silica particles prepared by a slight modification of the classical Stöber method. An intrinsic porosity was achieved in the first case, contrary to the more compact spheres obtained by the conventional procedure.

2.4.1. Synthesis of aerogel-like silica particles

Aerogel-like sub-micron silica particles were prepared by precipitation from a mixture of TMOS/H_2O/acetone, in a molar ratio of 1/2/88.34, following a similar procedure than that employed to synthesize aerogels (see **Section 2.3.1.**). In this approach, the sol is made just before starting the treatment in supercritical media. Hence, the sol-gel reaction takes place in a supercritical mixture CO_2/acetone without the addition of any catalyst. From Elena Taboada's thesis,[17] the parameters that result in monodisperse sub-micron sized spheres were selected. The particles obtained in these experiments are identified as *AP(aerogel particles)_number of experiment*. Two experiments were carried out at the same conditions to obtain particles around 300 nm in diameter (samples AP_1 and AP_2). Details on the reactants concentration in acetone (QP, Panreac) and volume are given in **Table 2.4**. It is worth to mention that a substoichiometric amount of water was used to prepare the particles.

Table 2.4. Concentration in acetone and volume of reagents used to prepare silica aerogel-like particles (AP).

Synthesis	[TMOS] (M)	V_{TMOS} (mL)	[H_2O] (M)	V_{H2O} (mL)	$V_{acetone}$ (mL)
AP_1	0.15	11.2	0.3	2.7	500
AP_2					

The synthetic procedure follows 4 important steps:

Step`1: Preparation of a sol. TMOS was poured into acetone and water was added drop by drop. The mixture was subjected to magnetic stirring for 10 min. Note that no catalyst was added.

Step 2: The sol was introduced in a 1 L Pyrex vessel designed to fit inside the 2 L high pressure reactor showed in **Figure 2.6a**. This Pyrex container is shown in **Figure 2.11¡Error! No se encuentra el origen de la referencia.**:

Figure 2.11. Pyrex vessel for the synthesis of aerogel-like silica particles, in which the sol is introduced inside the supercritical reactor.

Step 3: Supercritical drying. The temperature and pressure pathways of a characteristic experiment are plotted in **Figure 2.12a** and **Figure 2.12b**. The main stages of the protocol are labeled similar to **Section 2.3.1.** The Pyrex beaker containing the solution of reactants was placed inside the reactor (**1**), which was then pressurized with CO_2 up to 50 bar (**2**) and heated up stepwise to 250 ºC, causing a pressure rise to 280 bar (**3**). These conditions, which correspond to supercrtitical conditions of the mixture CO_2/acetone were kept for 2h. An additional part in this step, with respect to the synthesis of aerogel monoliths, was included. It consisted in the circulation of fresh CO_2 at 250 ºC and with flow rates of 0.5 Kg/h during 1 h and then of 1.5 Kg/h during 1 h more (**3**). The objective was the extraction of any alkoxyde precursor residue. The system was next depressurized to a pressure of 3 bar and the solid material was washed up for 30 min with a flow of fresh CO_2 at 3 $Kg·h^{-1}$ and 3 bar (**4**). Finally, it was left to cool down overnight (**5**).

A maximum of three uses of the Pyrex beaker was recommended to avoid the existence of silica nucleation sites in the Pyrex internal walls and the loosing of control over the particle size.
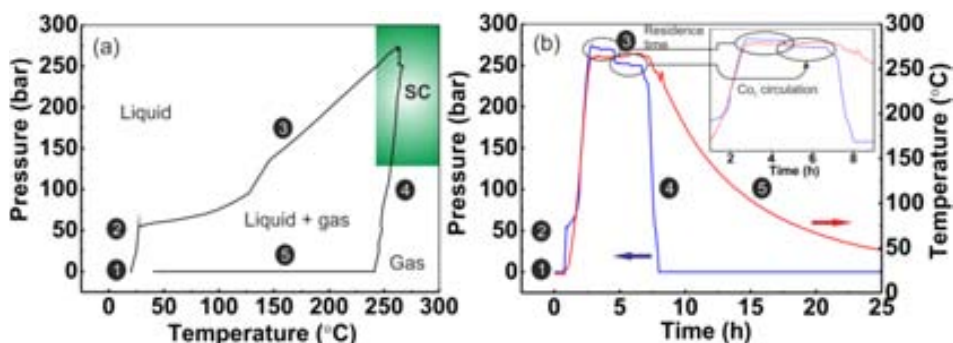
Figure 2.12. For the synthesis of AP, graphs of: (a) pressure vs. temperature cycle., and (b) evolution of pressure and temperature with time. The green shadow area in (a) corresponds to the supercritical state for any CO_2/acetone mixture.

2.4.2. Synthesis of Stöber silica particles

Silica nanoparticles were prepared by using a modification of the Stöber method.[18] The silicon precursor was tetraethylortosilicate (TEOS, 98 wt%, Sigma-Aldrich) and the solvent was ethanol (EtOH, 96% v/v, Panreac). NH_4OH 32 wt% was used as the catalyst. First at all, the lab beakers in contact with the reagents were carefully cleaned with a 5% v/v water solution of hydrofluoric

acid (48 wt%, Sigma-Aldrich). Briefly, 250 mL of a solution of H_2O 3 M and NH_4OH 0.5 M in EtOH was prepared. TEOS was then added up to a concentration of 0.3 M. The solution was magnetically stirred at a high speed. The container was covered to avoid the evaporation of the catalyst. After few minutes, the agitation speed was lowered and the reagents were allowed to react for 18 h. It was observed that after 2 h, the opacity of the solution increased considerably evidencing the presence of colloidal particles. Then, the solution was washed three times by re-suspending the particles in fresh EtOH and centrifuging 1 h at 5000 rpm. The final precipitate was re-dispersed in ethanol. This dispersion is labeled as *StöberP* (Stöber particles). The characteristics of those particles were compared with those of the aerogel silica particles.

2.4.3. Results and discussion

2.4.3.1. Size and morphology of silica particles

Table 2.5 summarizes some results obtained for the experiments performed in the synthesis of silica particles. The mass yield was calculated for each experiment using the ratio depicted in **Equation 2.4**.

Equation 2.4 $\quad$ $\text{Yield (\%)} = \frac{\text{mass}_{\text{AP sample}}}{\text{nominal 100\% mass}} * 100 = \frac{\text{mass}_{\text{AP sample}}}{\text{mol}_{\text{TMOS}} * \text{MW}_{\text{SiO}_2}} * 100$

where MW_{SiO2} is the molecular weight of silica.

Table 2.5. Results on the synthesis experiments of silica particles.

Sample	Mass (g)	Mass yield (%)	Φ_{TEM} (nm)	Polydispersity in size (%)	$\Phi_{\text{Hyd.}}$ (nm), by intensity	Necking
AP_1	3.4	76	303	9	528	
AP_2	1.8	40	385	12	638	No
StöberP	2.9	19	82	10	145	

Transmission electron microscopy (TEM) and dynamic light scattering (DLS)

Mean particle diameters (Φ_{TEM}) were statistically calculated for each sample from TEM images by counting 200 particles and fitting the obtained results to a Gaussian curve. A dynamic light scattering (DLS) technique was used to get information on the hydrodynamic diameter and, thus, on the colloidal behavior of the particles. The preparation of the grids for TEM analysis was made by dispersing the particles in ethanol or acetone, placing one or two drops onto a TEM grid and letting the solvent to evaporate. DLS measurements were done by analyzing stable colloidal dispersions of the particles in a concentration of around 0.5 mg/mL in EtOH or acetone. Hydrodynamic diameters were determined based on the average of the intensity-weighted particle size distribution of three measurements.

Aerogel silica particles

Aerogel particles were collected as white and very light dry powders (**Figure 2.13a**). The powder was placed mainly at the bottom of the Pyrex vessel, but also in its inner and outer walls and in the inner walls of the reactor, as it can be observed in **Figure 2.13b**.

Figure 2.13. Photographs of aerogel particles: (a) sample inside the Pyrex vessel, and (b) the reactor just opened.

Particles of *ca.* 300 and 400 nm diameter were recovered in batches AP_1 and AP_2, respectively.

TEM image in **Figure 2.14a** evidences the spherical shape and the low polydispersity in size of a characteristic AP sample (AP_1). For these particles, necking was insignificant (**Figure 2.14b**), understanding this parameter as the contact between adjacent particles in such a way that they interact and the boundary becomes unclear, thus, lowering the monodispersity of the system. The particles had a high degree of monodispersity (**Figure 2.14c**).
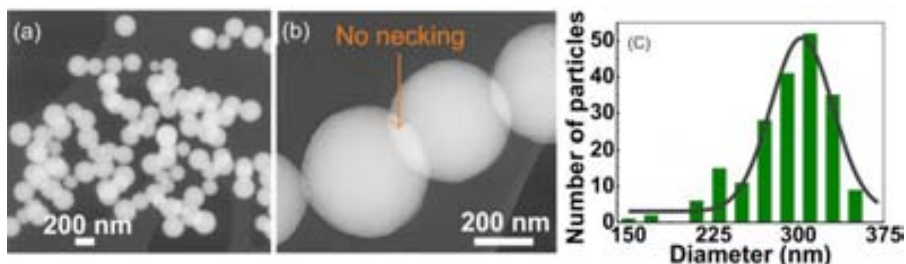
Figure 2.14. TEM images of AP_1 at: (a) low and (b) high magnification, and (c) size distribution fitted to a Gaussian function.

Stöber silica particles

The results obtained for the Stöber SiO_2 particles are also listed in **Table 2.5** for comparison. The particles made by the Stöber have a mean diameter of 82 nm, significantly smaller than the aerogel particles. **Figure 2.15a** and **Figure 2.15b** show the aspect of a colloidal dispersion of StöberP in EtOH. This suspension was very stable and remained several months at room temperature without sedimenting. The TEM observation showed spherical nanoparticles (**Figure 2.16a**). Nevertheless they were not as spherical as the particles synthesized in supercritical media, as it is shown in **Figure 2.16b**. This image also suggests the existence of two populations in size. To corroborate this finding, the size distribution was calculated by both number and volume of particles. TEM analysis reports measured particles size by number. To

recalculate data in volume, the geometric shape formula of a sphere was used: volume = $(4/3) \cdot \pi \cdot (diameter/2)^3$. The curve referred to number exhibits only one main peak centered at 85 nm (**Figure 2.16c**) with a relatively high monodispersity (**Table 2.5**). However, a bidomal distribution is clearly observed when the data is given by volume, with a major and a minor peak at 85 and 125 nm, respectively (**Figure 2.16d)**.
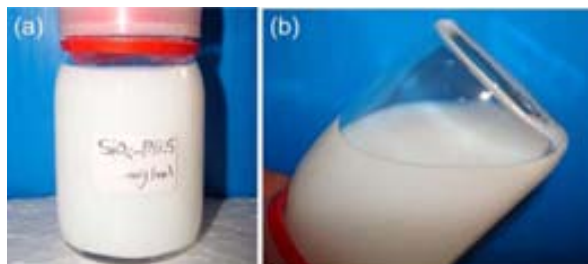
Figure 2.15. Photographs of StöberP dispersed in EtOH.
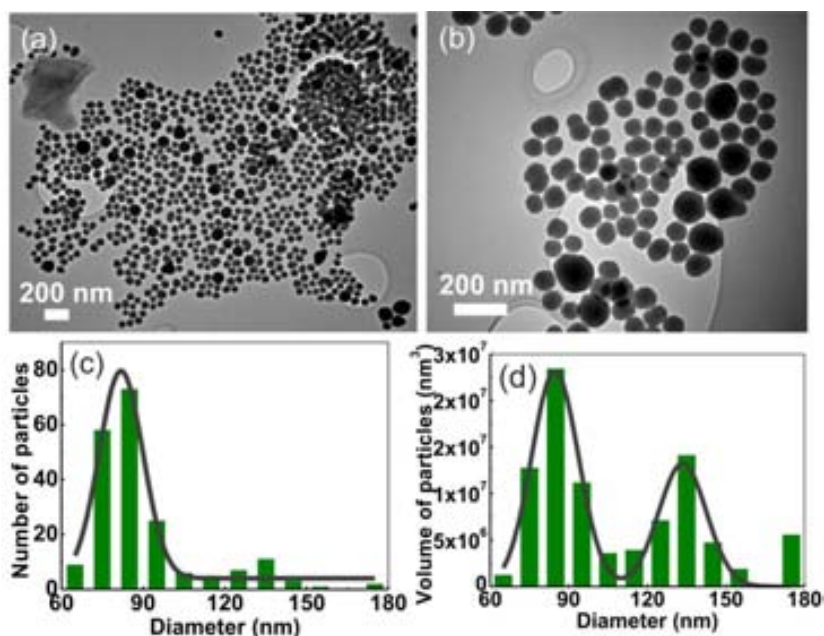
Figure 2.16. TEM images of the StöberP at: (a) low and (b) high magnification, and size distributions fitted to a Gaussian function by (c) number of particles and (d) volume of particles.

2.4.3.2. Textural properties of silica particles

Nitrogen adsorption/desorption isotherms (BET method)

Textural properties of the silica particles were assessed by measuring the N_2 adsorption/desorption isotherms. Before performing the measurements, samples were degassed at 300 ºC for 24 h under reduced pressure (< 10^{-8} bar).

Figure 2.17a and **Figure 2.17b** show the low temperature adsorption isotherms of sample AP_1 and the Stöber particles, respectively. Aerogel spheres presented isotherms of type I,

corresponding to microporous materials. For silica particles, textural data regarding the pore size was calculated at a relative pressure of 0.2 to take predominantly into account the micropore void. The surface area was in the order of 150-200 m^2/g with a micropore volume around 0.1 m^3/g and a micropore size of 1.6-1.7 nm. When also taking into account the interparticle void space, the mean pore size increased to 2.3 nm. The isotherm of the Stöber particles coincided with type II that belongs to nonporous solids. The smaller diameter of those particles conferred them a large surface area in the order of 130 m^2/g (**Table 2.6**). The particles agglomerates had a pore volume near 0.3 m^3/g and a mean interparticle pore size of 7.8 nm. The micropore area in StöberP was very low, suggesting that this sample did not have intrinsic microporosity, in contrast with the aerogel-like particles AP_1 and AP_2.
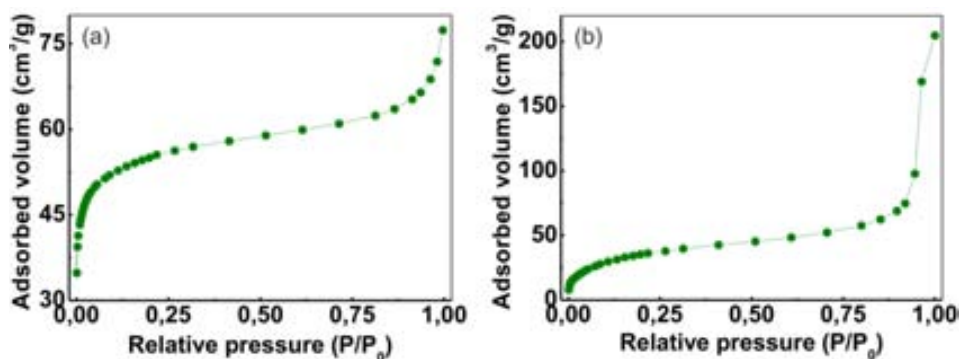
Figure 2.17. Low temperature nitrogen adsorption isotherms of samples: (a) AP_1, and (b) StöberP.

Table 2.6. Data of porosity calculated by BET of AP and Stöber samples.

Sample	S_{BET} (m^2/g)	Micropore area (%)	Mean V_{pore} (cm^3/g)	Pore size$_{intraparticle}$ (nm)	Mean pore size (nm)
AP_1	205	86	0.12	1.7	2.3
AP_2	146	68	0.08	1.6	2.3
StöberP	133	9.4	0.26	1.7	7.8

2.5. COMPOSITE IRON OXIDE-SILICA NANOPARTICLES

One important goal of this work was to fabricate aerogel-like nanoparticles with theranostic properties. In order to satisfy this purpose, iron oxide-silica core-shell particles were fabricated. These particles were designed for being magnetic drug carriers and contrast agents for magnetic resonance imaging (MRI). Porous silica offers a biocompatible host matrix for therapeutic agents while the magnetic properties of the nanoparticles in the core are responsible of an enhancement of the negative contrast in MRI and could also serve for the magnetic guidance of drugs to the target tissue.[19] They were synthesized following a similar method to the one employed in the preparation of AP spheres.

This work uses maghemite/magnetite nanoparticles to obtain the composite nanospheres. Magnetite formulation contains both oxidations states of iron $Fe(II)Fe(III)_2O_4$, while maghemite only has one: $Fe(III)_2O_3$. Both have the same crystalline structure, an inverse spinel with oxygen ions forming a close-packed face-centered cubic structure with the iron ions occupying both tetrahedral (Fe(III)) and octahedral (Fe(II) and Fe(III)) interstitial sites. The magnetic behavior is also similar for both crystalline phases, showing ferrimagnetism at low temperatures and paramagnetism over the Curie temperature (~ 570 °C). For small particle sizes (< 20 nm), maghemite and magnetite particles display superparamagnetic behavior at room temperature. However, magnetite presents higher magnetization than maghemite, which is desirable to exploit the magnetic properties of magnetic particles.

2.5.1. Iron oxide nanoparticles. Synthesis and characterization

High magnetic susceptibility and saturation magnetization and superparamagnetic behavior at room temperature are all desired properties for the selected bioapplications of the core-shell nanoparticles. These properties strongly depend on the size, shape, and crystallinity of the magnetic particles. The synthetic route of choice to prepare the iron oxide nanoparticles was an adaptation of the method developed by Sun *et al*.[20] It is based on the high temperature decomposition of organometallic compounds in the presence of capping ligands dissolved in organic solvents. This method produces spherical particles with controlled particle size, narrow size distribution and excellent crystallinity when compared with more traditional procedures, as for instance the co-precipitation route. The collected material remains stable in apolar solvents by steric repulsions of the capping ligands (typically long chain alkyl surfactants) deposited on the particles surface.

For a typical synthesis the following reactives were used as received: iron (III) acetylacetonate (Fe(acac)$_3$, 97 wt%), 1,2-hexadecanediol (90 wt%), oleylamine (70 wt%), benzyl acohol (99 wt%), all of them purchased from Sigma-Aldrich, oleic acid (Scharlab), hexane (≥ 98.5 wt%) and ethanol (96 % v/v) from Panreac.

The experimental set-up is described in **Figure 2.18**. Commonly, the process reads as follows:

1. A mixture of 2 mmol (0.71 g) of Fe(acac)$_3$, 10 mmol (2.58 g) of 1,2-hexadecanediol, 6 mmol (1.90 mL) of oleic acid, 6 mmol (1.97 mL) of oleylamine and 20 mL of benzylether is prepared in a three-neck round-bottom flask provided with a magnetic bar and 6 or 7 pumice stones.

2. Three cycles of vacuum/argon pumping and flushing were applied to the vessel to assure an inert atmosphere during the reaction. Finally, the system was filled with argon and closed.

3. The flask was heated up to 200 °C and maintained under magnetic stirring for 2 h. A first change of color was observed during the heating from yellowish orange-red, identified as dissolved iron precursor, to dark brown indicating the presence of a Fe(II)/Fe(III) intermediate obtained from the decomposition of the precursor.

4. The temperature in the system was increased to 300 °C and maintained under reflux for 1 h. The magnet was previously removed by quickly opening one of the taps under argon flow.

5. The solution was cooled down to room temperature. The first wash of the precipitated particles was performed with extra ethanol, centrifugation at 4500 rpm during 20 min and discarding the supernatant.

6. The process was followed by the addition of an extra amount of oleic acid and oleylamine (0.05 mL each) to the solid sediment and by re-dispersing the mixture in hexane with the aid of an ultrasound bath. The suspension was then centrifuged at 4000 rpm for 10 min to keep the supernatant.

7. A second wash was performed as in step 5.

8. Purification of the particles by further centrifugation (4500 rpm, 20 min) was required to eliminate any solid impurity, once the precipitate was re-dispersed again in hexane. The supernatant was kept as the final product.

The batches obtained in these experiments are called *Fe_number of experiment*.

1. Heating source: a) oil bath for first step heating (T = 200 °C).
   and b) heating mantle for second step heating (T = 300 °C).
2. Argon resorvoir.
3. Argon line.
4. Vacuum line.
5. Vacuum/argon valve.
6. Condenser with water refrigeration.
7. Reaction round-bottom flask.
8. Hg safety bubbler.

Figure 2.18. Experimental set-up for the synthesis of iron oxide nanoparticles by thermal decomposition of organometallic substances.

After the fabrication process, the obtained colloidal dispersion in hexane had a deep black color (**Figure 2.19a**). The magnetic properties of the material were clearly visible by attracting the colloid with a magnet (**Figure 2.19b**).

The mechanism of the iron oxide nanoparticles formation by this method is still non-fully unraveled, but some statements can be asserted based on bibliography.[20,21,22] A Fe(II)/Fe(III) intermediate (dark brown) seems to be formed from partial reduction of the Fe(III) precursor in presence of a dialcohol. This corresponds to the **stage 3** at 200ºC in the described procedure. Next, the particles nucleate and grow.[23] Nucleation occurs when the concentration of Fe(II) and Fe(III) ions exceeds the supersaturation limit. In the described procedure this situation is reached in the **stage 4** at 300 ºC. If this step occurs quickly and homogenously, the resulting particles are uniform in size.[24] Particles growth occurs by Ostwald ripening through the formation of surfactant-metal complexes that dissolve the smallest iron oxide particles. Besides, as it has been studied kinetically, the nucleation and growth processes are separated along time, which is crucial to obtain uniform particles.[25]

The oleic acid molecules are chemisorbed on the iron oxide nanoparticles surface through a bi-dentate bond.[26,27] The carboxylic groups at the *head* of these molecules can delocalize their electronic pair to establish and ionic bond with the positively charged surface of the particles. **Figure 2.19c** shows a sketch of this arrangement in which the apolar *tails* of the surfactant are in contact with the surrounding medium, thus making the nanoparticles dispersion stable in organic nonpolar solvents. It is worth mentioning that the oleic acid, as a carboxylic acid-type surfactant, is involved both in the growth of the iron oxide nanocrystals and in the particles stabilization in organic media.
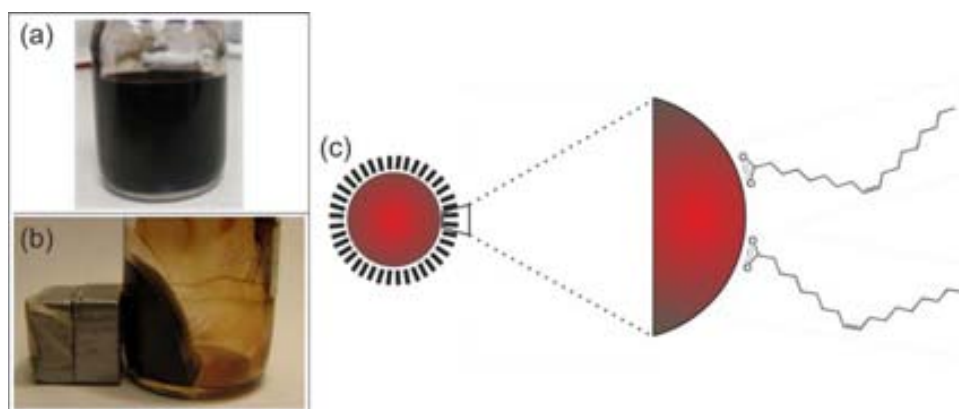
Figure 2.19. Photographs of a representative colloidal dispersion of iron oxide nanoparticles in hexane in: (a) natural state, and (b) when attracted by a magnet (0.5 T), and (c) schematic representation of oleic acid molecules chemisorbed on the surface of iron oxide nanoparticles

Titration of iron with potassium dichromate

The iron oxide nanoparticles concentration of the dispersion must be known to prepare core-shell composites. The characterization of the composition in terms of the crystalline phase is also important to understand the magnetic behavior. Titration of iron oxide with potassium dichromate was used to determine both the overall iron content and the Fe(III) and Fe(II) relative percentage. Titration is a process based on the oxidation of Fe(II) to Fe(III) by the action

of potassium dichromate. The experimental protocol consisted in two stages and reads as follows:

Stage 1: Determination of the Fe(II) amount. An aliquot of 0.1 mL of the nanoparticles dispersion in hexane was left to evaporate at ambient conditions and the sediment was dissolved in 0.2 mL of hydrochloric acid (HCl, 37 wt%), thus obtaining a bright yellow solution involving Fe(III) and Fe(II) cations. Next, 0.1 mL of a H_2SO_4 (95-98 wt%, Panreac) + HNO_3 (65 wt%, Panreac) mixture in a volume ratio of 1/3 and a few drops of the indicator (sodium diphenylaminosulphonate, 2 wt%) were added to the solution. By adding potassium dichromate ($K_2Cr_2O_7$, Aldrich), at a concentration of 0.5 mM, Fe(II) was oxidized to Fe(III) and the solution color changed from green to violet. The redox reaction is schematized in **Reaction 2.6**:

Reaction 2.6 $6Fe^{2+} + Cr_2O_7^{2-} + 14H^+ \rightarrow 2Cr^{3+} + 6Fe^{3+} + 7H_2O$
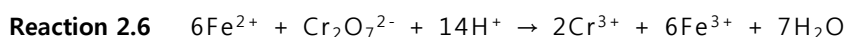
The concentration of Fe(II) ([Fe(II)]) was calculated with **Equation 2.5**:

Equation 2.5 $$[Fe(II)] = \frac{6.[K_2Cr_2O_7].V_{K_2Cr_2O_7}}{V_{sample}}$$

Stage 2: Determination of the total Fe amount. Tin chloride ($SnCl_2$, 98 wt%, Sigma-Aldrich) at a concentration of 0.25 M and ~ 30ºC was added dropwise until the solution turned colorless, which indicated the total reduction of the Fe(III) to Fe(II). At this point, the overall iron content was in the form of Fe(II). The process occurs by the redox reaction in **Reaction 2.7**:

Reaction 2.7 $2Fe^{3+} + Sn^{2+} \rightarrow 2Fe^{2+} Sn^{4+}$
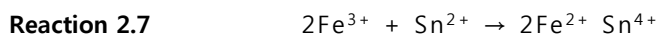
Mercury chloride ($HgCl_2$, Labbox) 5 wt% was added to oxidize the excess of Sn(II) to Sn(IV) until the solution changed to cloudy white. Problems related with interference of Sn(II) were thus avoided. The redox reaction taking place is presented in **Reaction 2.8**:

Reaction 2.8 $Sn^{2+} + 2Hg^{2+} \rightarrow Sn^{4+} + 2Hg^+$
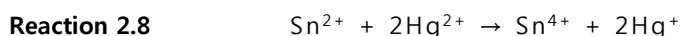
After adding a few drops of the indicator, the total iron content ([Fe$_{TOTAL}$]) was titrated with the required volume of $K_2Cr_2O_7$ (**Reaction 2.6**), The concentration of Fe(III) ([Fe(III)]) was estimated by subtraction of the amount of Fe(II) to the total amount of Fe.

Each sample was titrated three times and an averaged concentration was considered. The method has a considerable associated error due to the difficulty in identifying the exact moment of the color change.

The percentages of magnetite and maghemite in several iron oxide samples were tentatively assessed from the amounts of Fe(III) and Fe(II) measured by titration. **Table 2.7** shows the atomic ratio of cations Fe(III)/Fe(II) and the subsequent contents of maghemite (γ-Fe_2O_3) and magnetite (Fe_3O_4) calculated in the following way: the Fe(II) amount can be directly related to the amount of Fe_3O_4 (composed by a Fe(III)/Fe(II) atomic ratio = 2). Subtracting the amount of cations necessary to form Fe_3O_4, the remaining Fe(III) exits as maghemite. All the samples contained at least two third of maghemite.

Table 2.7. Results of Fe(III)/Fe(II) atomic ratio and the percentages of the two phases maghemite (γ-Fe$_2$O$_3$) and magnetite (Fe$_3$O$_4$) calculated from by iron titration for several iron oxide samples.

Sample	Fe(III)/Fe(II)	γ-Fe$_2$O$_3$ (%)	Fe$_3$O$_4$ (%)
Fe_1	8.0	75.0	25.0
Fe_2	16.0	88.2	11.8
Fe_3	8.6	77.0	23.0
Fe_4	8.2	75.0	25.0

In the light of these results, we considered that our samples were composed by a mixture of maghemite and magnetite and they were identified as *iron oxide nanoparticles* (IONPs) or the chemical formula of maghemite (Fe$_2$O$_3$), for being the majority. The concentration of iron oxide in the analyzed dispersions was calculated considering both maghemite and magnetite contributions to the whole amount of Fe.

Transmission electron microscopy (TEM)

The shape and size of two representative batches of the synthesized IONPs (samples Fe_1 and Fe_2) were studied by TEM, and the hydrodynamic diameter ($\Phi_{Hyd.}$) by DLS. Dilute dispersions of iron oxide nanoparticles in hexane were used in both characterization techniques. **Table 2.8** lists the resulting measured values. All the prepared IONPs presented diameters of *ca.* 5-6 nm obtained by TEM (Φ_{TEM}), while values of 8-9 nm for hydrodynamic diameters were estimated from DLS. The hydrodynamic diameter, which includes both the magnetic core (considered as the Φ_{TEM}) and the organic shell, was in all cases larger than the diameter estimated by TEM. Assuming that the oleic acid is a molecule with a length of ~ 2 nm, and forms a monolayer on the IONPs surface, the following expression can be approximately applied to the fabricated particles:[28]

Equation 2.6 $\Phi_{Hyd.} = \Phi_{TEM} + \sim 4$ nm

In **Figure 2.20a** and **Figure 2.20b,** TEM images of particles of the two batches are shown. Particles were spherical and they exhibited a high degree of monodispersity.

Table 2.8. Mean particle diameters from the TEM images (Φ_{TEM}) and hydrodynamnic diameter measured by DLS ($\Phi_{Hyd.}$).

Sample	Φ_{TEM} (nm)	Polydispersity in size (%)	$\Phi_{Hyd.}$ (nm), by intensity
Fe_1	6.4	18.8	8.7
Fe_2	5.3	17.6	8.0
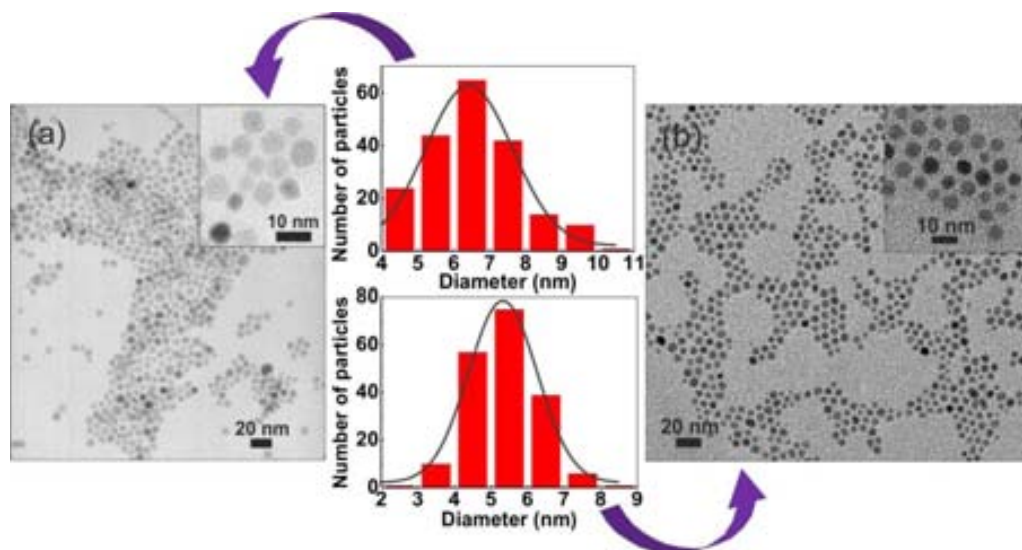
Figure 2.20. TEM images of two IONPs samples dispersed hexane: (a) Fe_1 and (b) Fe_2.

X-Ray diffraction (XRD) and selected area electron diffraction (SAED)

XRD and SAED patterns of a representative batch of iron oxide nanoparticles are presented in **Figure 2.21a** and **Figure 2.21b,** respectively. For XRD, an aliquot of the particles dispersion was deposited on a glass support. The hexane solvent was evaporated at ambient conditions. SAED pattern was captured from the electron beam irradiation of a TEM grid containing the particles. Results obtained in both cases were in agreement with the reference pattern for magnetite (ICDD PDF019-0629), but also for maghemite (ICDD PDF039-1346). The differentiation between these two phases has been object of many studies[29] and there is not yet a reliable standard technique to distinguish them when they are as nanoparticles of less than 10 nm.
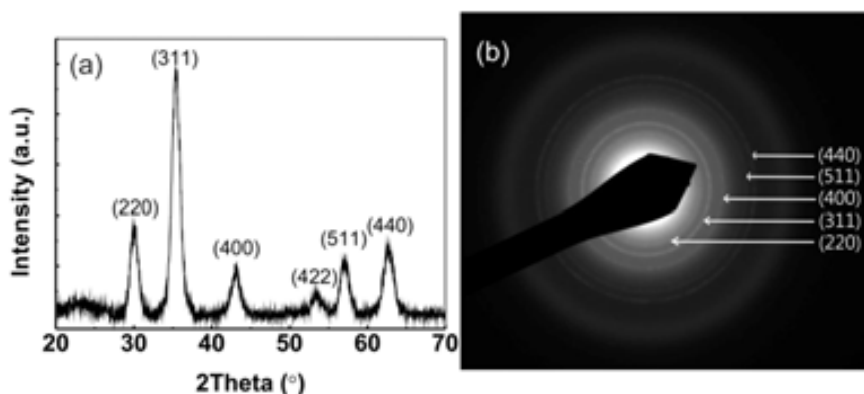
Figure 2.21. (a) X-ray diffraction and (b) SAED patterns of a representative sample of iron oxide nanoparticles.

Fourier transformed infrared spectroscopy (FTIR)

FTIR was used to detect the chemical bonds established between the surface of the iron oxide nanoparticles and the surfactant molecules. The FTIR characterization were performed with pellets made by mixing an aliquot of the particles dispersion with KBr (for IR-Spectroscopy,

Fluka) in an agatha mortar, letting the hexane to evaporate at ambient conditions. The mixture was pressed under ~ 10 bar for 2 min. **Figure 2.22** displays the IONPs, raw oleic acid (OA) and oleylamine (OAm) spectra. The recorded IONPs profile showed a strong peak at 583 cm^{-1}, characteristic of the stretching vibration in the Fe-O bonds, and a broad band between 3000 and 3600 cm^{-1} that came from the O-H stretching modes of free adsorbed water. While the spectrum of free OA presented and intense peak at 1710 cm^{-1} due to the C=O carbonyl group, the IONPs spectrum had not this signal. Besides, the particles showed two peaks at 1407 (symmetric mode) and 1572 cm^{-1} (asymmetric mode) revealing the presence of carboxylate groups adsorbed on the nanoparticles surface. Both surfactants had sharp peaks at 2855 and 2925 cm^{-1} attributed to CH$_2$ symmetric and asymmetric stretching vibrations of the alkyl chains, respectively. No signs of OAm adsorption were found by FTIR. Thus, we conclude that only OA was chemically bonded to the IONPs surface and OAm was removed during the cleaning procedure. The amount of OA chemisorbed on the nanoparticles was assumed to be around 17 wt%, in concordance with the experimental value given by O. Pascu's *et al.*[30]
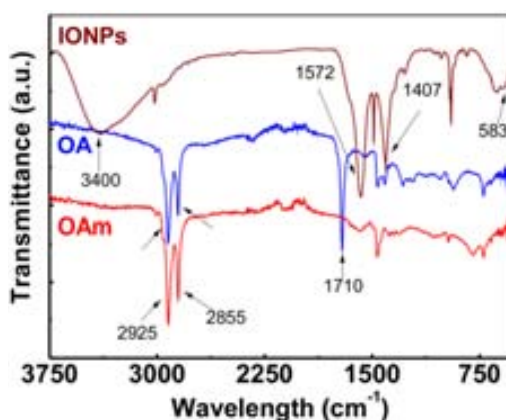
Figure 2.22. Infrared spectra of the iron oxide nanoparticles (IONPs) and the free surfactants oleic acid (OA) and oleylamine (OAm).

M(H) and Zero field cooling-field cooling (ZFC-FC) curves

Regarding the magnetic properties of these particles, different key parameters were acquired from magnetometry (SQUID) measurements: the saturation magnetization (M$_s$, emu/g), the coercitivity (H$_c$, Oe) and the superparamagnetic blocking temperature (T$_B$, K). To make the measurements, a previously dried cotton piece was introduced and compacted in a gelatin capsule and impregnated with the proper volume of an IONPs dispersion to have ~ 0.5 mg of the magnetic material. The analysis was performed once the solvent evaporated. To refer M$_s$ to the amount of magnetic material, the weight of the oleic acid coating the nanoparticles was subtracted from the total weight.

Figure 2.23a collects several magnetization curves at different temperatures obtained for sample Fe_2. The particles were superparamagnetic at room temperature, i.e., with absence of hysteresis loop in the coercivity, while they behaved as ferrimagnets at 5 K (see the inset in the

figure) with Hc = 100.7 Oe. M_s at 300 K was registered as 93 emu/g, while the values for bulk magnetite and maghemite are 92 emu/g[31] and 73-74 emu/g[32] respectively. The obtaining of such a high experimental value was related to the associated error in the iron oxide titration.

The superparamagnetic nature of the particles at room temperature was also confirmed by the Zero field cooling-field cooling (ZFC-FC) magnetization curve. **Figure 2.23b** shows the ZFC-FC curve for sample Fe_2. ZFC magnetization increased with the temperature until reaching a maximum value at which the blocking temperature (T_B) was registered. Above this parameter, the thermal energy is higher than the magnetic anisotropy energy and the magnetic material enter into the superparamegnetic zone from the ferrimagnetic one. FC curve showed a decreasing magnetization with temperature. The sharp peak representing the maximum in the ZFC and the FC curve, which separates from the ZFC one just above the blocking temperature, confirms that the system had a narrow particle size distribution.
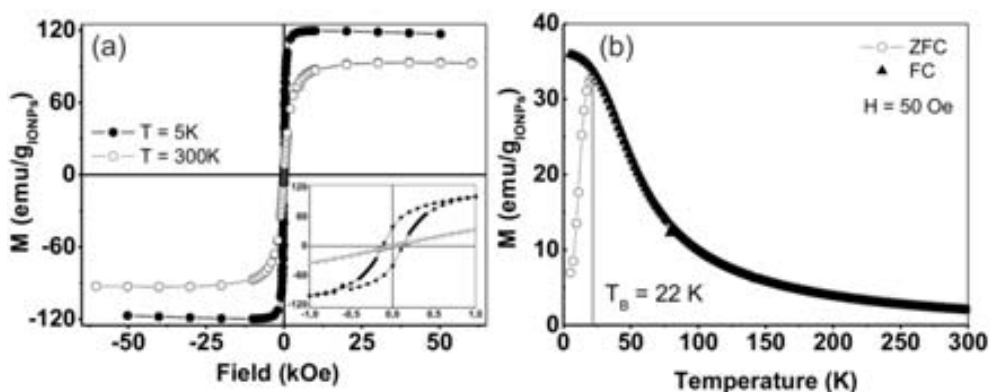
Figure 2.23. Curves of: (a) magnetization, and (b) ZFC-FC of sample Fe_2 at 50 Oe.

2.5.2. Synthesis of iron oxide-silica nanoparticles

The synthesized iron oxide nanoparticles were used as the nucleation sites for the fabrication of silica composites under supercritical conditions, following the same steps described in **Section 2.4.1**. Typically, the preparation of the sol in acetone was done by magnetically stirring the mixture for 10 min. TMOS/H_2O/acetone/IONPs/hexane were used as reagents, with a mass composition of 0.92/0.22/95.6/0.04/3.19 wt% (**Step 1**). These amounts were extracted from Elena Taboada's thesis[17] to produce core-shell IONPs-silica spherical and monodispersed particles with diameters smaller than 200 nm (**Table 2.9**). The magnetic particles dispersed in hexane were added to the solution of TMOS in acetone and water. The preparation of a stable colloidal dispersion of the IONPs in the silica sol was crucial to obtain nanoparticles with the desired quality. Among other factors, the order in which the reagents were added was previously found to be a key parameter to achieve colloidal stabilization. The most suitable sequence was established as follows: acetone as a solvent, then TMOS is added followed of water (added dropwise) and finally the suspension of IONPs in hexane. To allow the TMOS to nucleate on the iron oxide nanoparticles, the sol was prepared the day before to the

supercritical treatment. Next, the sol was introduced in the Pyrex vessel showed in **Figure 2.11** and it was fitted into the supercritical reactor of **Figure 2.6a** (**step 2**). Next, the drying in the supercritical medium was performed (**step 3**). The main stages, illustrated in **Figure 2.24**, are labeled in the same manner as in **Section 2.4.1**. Five experiments were performed and the resulting samples are named as AP_{Fe}(aerogel particles with IONPs)_number of experiment.

Table 2.9. Concentrations in acetone and volumes of reactants used to prepare IONPs-silica nanoparticles (AP_{Fe}). *The mass of silica (m_{SiO2}) was assumed as the sol-gel reaction of TMOS proceeds with a 100% mass yield.

Sample	[TMOS] (M)	V_{TMOS} (mL)	[H₂O] (M)	V_{H2O} (mL)	$V_{acetone}$ (mL)	m_{SiO2}^*/ m_{IONPs}	$V_{acetone}$ /V_{hexane}
AP_{Fe} samples	0.05	3.73	0.10	0.90	493	10	60
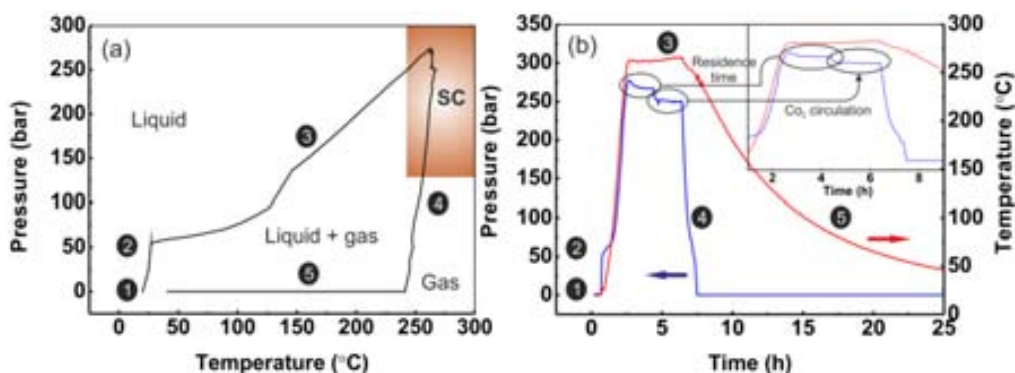
Figure 2.24. For the synthesis of AP_{Fe}, graphs of: (a) pressure vs. temperature cycle., and (b) evolution of pressure and temperature with time. The brown shadow area in (a) corresponds to the supercritical state for any CO_2/acetone mixture.

Aliquots of some sols were kept for further characterization.

IONPs were coated by organic molecules that made them stable in nonpolar solvents but unstable in polar solvents. Thus, by increasing the amount of acetone, the stability of the iron oxide dispersion decreases and the cluster size of the magnetic particles grow. Since the diameter and the magnetic response of the core-shell particles are determined by the magnetic cluster size, the possibility to modulate the $V_{acetone}$/V_{hexane} ratio confers control not only over the stability of the sol, but also over the characteristics of the composite particles. To prove the relation between the volume ratio of solvents and the magnetic clusters size, several sols of INOPs with different $V_{acetone}$/V_{hexane} ratios were prepared and the hydrodynamic diameters measured by DLS. The sols were made in 20 mL vials with constant concentrations of TMOS (0.025 M, 0.074 mL) and water (0.05 M, 0.018 mL). The SiO_2/IONPs mass ratio was also maintained equal to 10 in all the solutions. To do this, a volume of 0.149 mL of the IONPs dispersion of 20 mg/mL (calculated by iron titration) was needed. The volume ratio of acetone and hexane was varied following the next expressions:

Equation 2.7   Volume ratio $\frac{\text{acetone}}{\text{hexane}} = \frac{V_{\text{acetone}}}{V_{\text{hexane}}+0.149}$

Equation 2.8 $V_{\text{acetone}}+V_{\text{hexane}}+0.074+0.018+0.149=20$ ml

The DLS measurements were done just after preparing the sols. **Table 2.10** gives the obtained results and **Figure 2.25** shows the magnetic cluster size vs. the acetone/hexane volume ratio, showing that the larger the solvents volume ratio, the bigger the cluster. Nevertheless, high reproducibility in the cluster size is difficult to obtain because of the many other factors that have influence over this value, such as the reaction time or the stirring rate.

Table 2.10. Hydodynamic diameter ($\Phi_{\text{Hyd.}}$), polydispersity index and Z_{average} of sols with different acetone/hexane volume ratios.

$V_{\text{acetone}}/V_{\text{hexane}}$	$\Phi_{\text{Hyd.}}$ (nm), by volume	PdI	Z_{average} (nm)
5	45	0.105	53
20	58	0.117	71
30	71	0.187	92
50	86	0.145	104
90	101	0.203	127
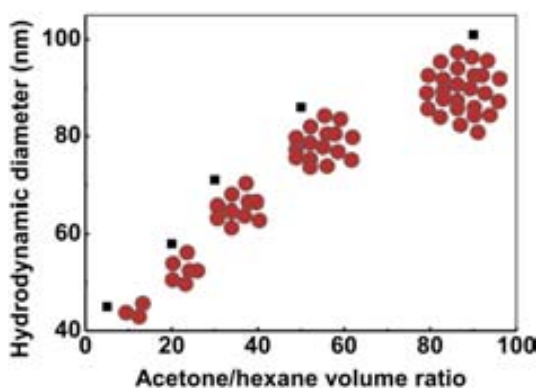
Figure 2.25. Hydrodynamic diameter of IONPs clusters vs. acetone/hexane volume ratios in the sols.

2.5.3. Results and discussion

2.5.3.1. Size and morphology of iron oxide-silica nanoparticles

Aerogel-like iron oxide-silica nanoparticles (AP$_{\text{Fe}}$) were obtained as dry, light and brown powders with a spongy texture. The powder was found located all over the autoclave and the Pyrex vessel walls. Around 1 g of material was obtained in each synthesis. The powder was easily dispersed and stabilized in water (**Figure 2.26a**) at a maximum concentration of 1 mg/mL. Moreover, the particles were homogeneously attracted by an external magnetic field, as it can be observed in **Figure 2.26b**.
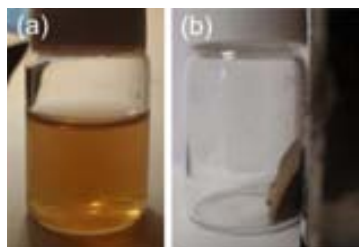
Figure 2.26. Photograph of an AP_{Fe} characteristic sample: (a) stabilized in water at *ca.* 0.5 mg/mL, and (b) being attracted by a magnet (0.5 T).

The mass yield was calculated following **Equation 2.9**:

$$\textbf{Equation 2.9} \qquad \text{Yield (\%)} = \frac{\text{mass}_{AP_{Fe}}}{\text{nominal 100\% mass}} * 100 = \frac{\text{mass}_{AP_{Fe}}}{\text{mol}_{TMOS} * MW_{SiO_2} + \text{mass}_{IONPs}}$$

Masses of SiO_2 and IONPs were obtained by elemental analysis with inductively coupled plasma combined with mass spectrometry (ICP-MS). With this technique, that was employed with samples AP_{Fe}_3 and AP_{Fe}_5, the concentration of Si and Fe in the composite particles was obtained. Previous to measurements, around 2 mg of each sample was digested twice with a mixture of HNO_3 and HF inside a microwave at 150 ºC. The IONPs mass was found to be around 7-8%. Measured SiO_2/Fe_2O_3 mass ratios were close to the initial value of 10, indicating that the loss of IONPs during the nanoparticles preparation process was low. The mass yield values calculated for AP_{Fe}_3 and AP_{Fe}_5 wherein both cases *ca.* 60%.

The morphological features of AP_{Fe} samples are listed in **Table 2.11**. Composite particle size values measured by TEM ranged from 60 to near 200 nm, with a narrow size distribution. The hydrodynamic diameter of the nanoparticles was acquired in 0.5 mg/mL dispersions in EtOH or MeOH, resulting in values between 400 and 550 nm. These high values of the diameter indicate certain aggregation of the particles when dispersed in the liquid media. The size of the magnetic core was estimated by TEM to be around 20 nm in diameter for the smallest particles and 55 nm for the largest ones. The magnetic cluster size of the prepared sols prior to the supercritical treatment of samples AP_{Fe}_1 and AP_{Fe}_4 was also analyzed by DLS. The obtained diameter values were larger than the ones resulting from TEM observations. An explanation of this comes from a possible disaggregation of the clusters inside the autoclave when being in contact with the less polar solvent mixture CO_2 + acetone.

Figure 2.27 schematizes the core-shell structure of the particles and identifies the different compounds constituting them, as well as the sizes given in **Table 2.11**.

Table 2.11. Results for synthesized IONPs-SiO$_2$ nanoparticles. *This value corresponds the material collected in three batches.

Sample	AP$_{Fe_}$1	AP$_{Fe_}$2	AP$_{Fe_}$3	AP$_{Fe_}$4	AP$_{Fe_}$5
Mass (g)	0.7	1.2	3.3*	1.3	0.9
Mass yield (%)	-	-	59	-	59
mass$_{SiO2}$/mass$_{IONPs}$	-	-	7.2	-	9.2
IONPs mass (%)	-	-	10	-	8.1
Φ_{TEM} (nm)	98	60	65	184	177
Polydispersity in size (%)	13	32	19	11	12
$\Phi_{Hyd.}$ (nm), by Intensity	446	409	742	513	548
Φ_{TEM} of IONPs cores (nm)	23	21	24	59	52
$\Phi_{Hyd.}$ of IONPs cores by volume (nm)	80	-	-	92	-
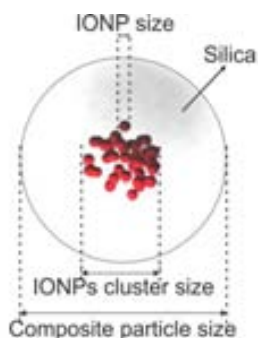
Figure 2.27. Scheme detailing the morphology of composite AP$_{Fe}$ particles.

Transmission and scanning transmission microscopy (TEM, SEM)

The spherical shape of the composite particles and their high monodispersity was shown in the TEM observations (**Figure 2.28a** and **Figure 2.28b**). The grids for TEM analysis were prepared from dispersions of the particles in EtOH or acetone. The core-shell structure is evidenced in the high magnification images shown in the insets. Besides, the absence of necking is revealed in the images and tagged by an orange arrow.
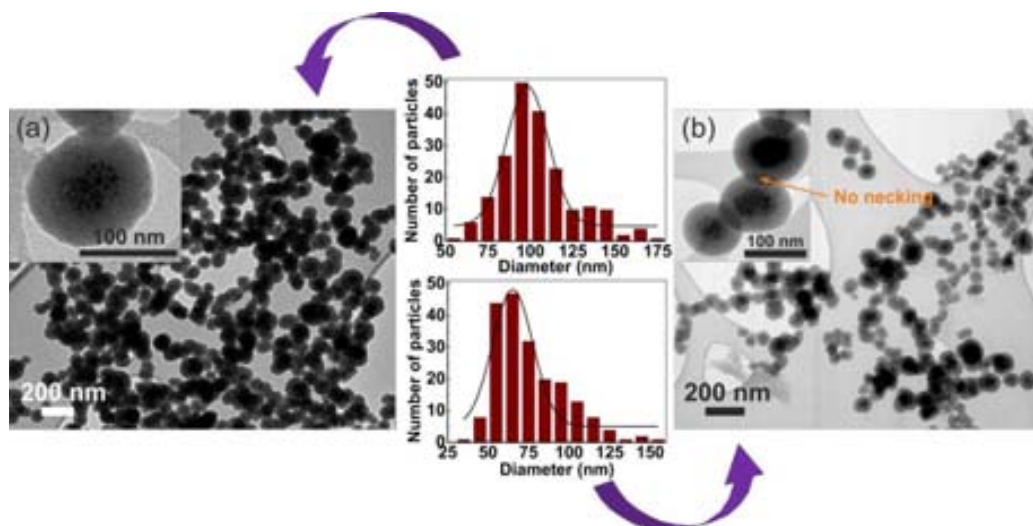
Figure 2.28. TEM images and particles size distribution of samples: (a) AP_{Fe}_1 and (b) AP_{Fe}_3. The orange arrow marks a zone where two particles are superposed evidencing lack of necking.

2.5.3.2. Textural properties of iron oxide-silica nanoparticles

Nitrogen adsorption/desorption isotherms (BET method)

The properties of the core-shell particles in terms of texture were analyzed by adsorption/desorption isotherms. Prior to measurements, samples were degasified at 300 ºC for 24 h under reduced pressure (< 10^{-8} bar). **Figure 2.29** shows the low temperature adsorption/desorption isotherm of sample AP_{Fe}_3, which corresponds to type I, typical of a microporous materials. Isotherms with these features were also found for pure silica particles (see **Section 2.4.3.2**), evidencing the existence of intraparticle microporosity and interparticle mesoporosity.
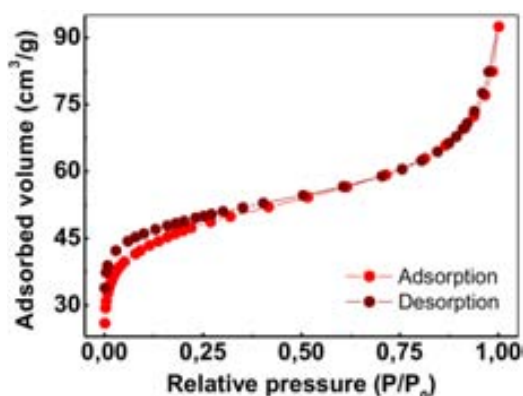
Figure 2.29. Low temperature N_2 adsorption/desorption isotherm of AP_{Fe}_3.

Table 2.12 lists the values of some textural parameters for the composite particles. Surface area values ranging from 160 to 256 m^2/g were obtained. The microporosity percentages were in the range of ≤ 50% and ≥ 70% and pore volumes were between 0.1-0.2 cm^3/g.

Table 2.12. For AP_{Fe} samples, data of porosity obtained by BET.

Sample	S_{BET} (m^2/g)	Micropore area (%)	Mean V_{pore} (cm^3/g)	Pore size$_{intraparticle}$ (nm)	Mean pore size (nm)
$AP_{Fe\_}1$	160	36	0.19	1.8	4.7
$AP_{Fe\_}3$	160	50	0.13	1.8	3.2
$AP_{Fe\_}4$	256	81	0.12	1.6	1.9
$AP_{Fe\_}5$	210	72	0.12	1.6	2.3

The textural properties of the core-shell (AP_{Fe}) and the pristine silica (AP) particles were compared. The surface area of composite particles can be given referred to either the total mass of sample or the mass of silica. Since the magnetic core is considered nonporous, data referred to silica mass was recalculated for composite samples. Thus, the mass of IONPs in AP_{Fe} was subtracted from the overall mass. The expression in **Equation 2.10** was used to estimate the surface area:

Equation 2.10 $\qquad S_{BET}\left(\dfrac{m^2}{g_{SiO_2}}\right) = S_{BET}\left(\dfrac{m^2}{g_{AP_{Fe}}}\right) * \dfrac{1\,g_{AP_{Fe}}}{(1-g_{IONPs})g_{SiO_2}}$

where the mass of SiO_2 and IONPs were obtained by ICP-MS. This formula was only applied for samples $AP_{Fe\_}3$ and $AP_{Fe\_}5$ due to the absence of data from this technique for the rest of AP_{Fe} samples.

Table 2.13 shows the porosity data of AP and AP_{Fe} referred to silica mass. Using this approach, similar values of surface area were found for both systems, with values between 150 and 230 m^2/g. The intraparticle mean pore size values were also comparable, with values near 2 nm (1.5-1.7 nm). These results indicated that the textural characteristics of the silica prepared by the described method in supercritical media were not affected by the presence of iron oxide nanoparticles and both AP_{Fe} and AP materials presented analogous porous structures.

Table 2.13. Surface area and intraparticle pore size of AP_{Fe} referred to the mass of silica and AP samples.

Sample	S_{BET} (m^2/g$_{SiO2}$)	Pore size$_{intraparticle}$ $_{SiO2}$ (nm)
$AP_{Fe\_}3$	172	1.7
$AP_{Fe\_}5$	228	1.5
AP_1	205	1.7
AP_2	146	1.6

2.5.3.3. Magnetic properties of iron oxide-silica nanoparticles

To analyze the magnetic properties of the composite particles has special relevance for exploiting those characteristics in biomedical applications. Magnetization values can be referred to the total composite mass or to the mass of constituent magnetic material (IONPs). In this work, the shown curves are assigned to the mass of composite material, but important data on

magnetization is reported being referred in both to the composite particles (AP_{Fe}) and only to the magnetic materials (IONPs). Samples were prepared by introducing in a gelatin capsule around 10 mg of the composite powder and compacted with dried cotton.

M(H) and Zero field cooling-field cooling (ZFC-FC) curves

Figure 2.30a graphs the magnetization data, M(H), vs. the applied magnetic field (H) of sample AP_{Fe}_3 at 5 K and room temperature (RT). A small coercivity can be appreciated in the inset, as well as a small M_R/M_S ratio (0.2), being M_R the remanent magnetization, characteristic of soft magnetic materials. As expected for a superparamagnetic system, the curve does not show coercivity at room temperature. Moreover, the saturation magnetization is lower at this condition than at 5 K; this is a common behavior already observed for the pristine IONPs. In particular, the studied sample has a M_S = 6.2 emu/g_{APFe} and 63.0 emu/g_{IONPs} at RT, a value that is below those for bulk magnetite (92 emu/g[31]) and maghemite (73-74 emu/g[32]).

ZFC-FC curve shown in **Figure 2.30b** has a maximum of the ZFC data that defines the blocking temperature (T_B = 59 K) and FC values decay when the temperature increases. This is the typical profile of a superparamagnetic material. The facts that this peak is not very sharp and that the FC curve does not separate from the ZFC one just below the T_B indicate a wide magnetic cluster size distribution in the composite particles.
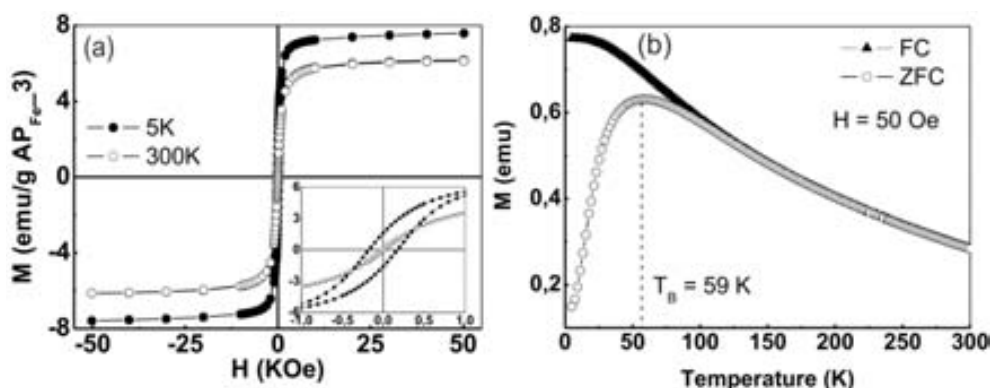
Figure 2.30. For sample AP_{Fe}_3, curves of: (a) magnetization vs. external applied field, M(H), at room temperature and 5 K and (b) ZFC-FC at 50 Oe. Inset: zoom at low magnetic field showing the coercive field at 5 K and the lack of it at 300 K.

2.6. STRUCTURAL CHARACTERIZATION OF SILICA-BASED MATERIALS

Fourier transformed infrared spectroscopy (FTIR)

The three silica-based materials: aerogel monolith (AM), aerogel-like sub-micron particles (AP) and core-shell IONPs-SiO_2 nanoparticles (AP_{Fe}), were characterized by FTIR to detect the distinctive functional groups of the silica. The measurements were performed in pellets made by grinding the samples in a concentration of ca. 0.5 wt% with KBr in an agatha mortar. The mixture is left under ~ 10 bar for 2 min. **Figure 2.31** shows the spectra of some representative

samples of AM, AP and AP_{Fe}. The three systems presented the same infrared spectrum. They showed the typical absorption signals of silica as a strong band at 1107, a shoulder at 971 and intense peaks at 805 and 475 cm^{-1}, which correspond to Si-O-Si asymmetric, Si-OH and Si-O-Si symmetric stretching modes and O-Si-O bending, respectively. Moreover, O-H st. modes at 3446 and 1636 cm^{-1} were associated to the free and the adsorbed water, respectively. The small peaks at 2956 and 2855 cm^{-1} belonged to C-H st. modes and the one at 1459 cm^{-1} to O-CH$_3$ vibrations.[33,34,35] Those signals could indicate both the presence of solvent traces or the uncompleted hydrolization of silicon precursor (TMOS). Since the high temperatures used in the drying process are enough to evaporate the MeOH, we considered the second explanation more reasonable. The absence of extra peaks from IONPs in the AP_{Fe} spectrum was related to the small amount of the magnetic material in comparison with silica (see **Table 2.11**). The quantity of Fe-O or Fe-O-Si bonds was much lower than the amount of Si-O bonds and the high intensity of this last one hinder the visibility of the less intense peaks.
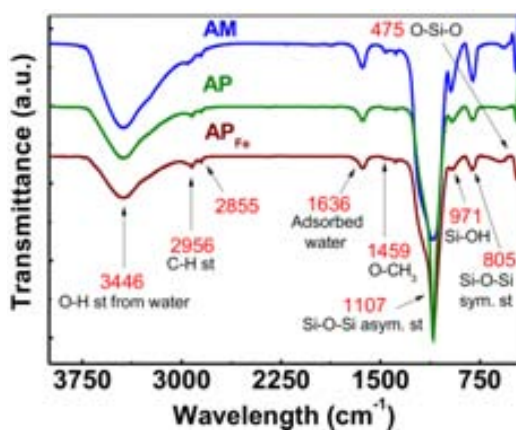
Figure 2.31. Infrared spectra of representative samples of AP_{Fe}, AP and AM.

Thermal gravimetric analysis (TGA)

TGA was performed to get information about the relative mass composition of the silica-based materials, especially to know the amount of adsorbed water, which is important in the design of drug carriers. The silicon atoms at the surface of amorphous silica try to maintain their tetrahedral coordination by two ways: the formation of silanol groups that are covalently attached to the surface or the establishment of hydrogen bonds between the oxygen and the surrounding water. The second process involves a weaker bonding energy than the previous one. These differences were evidenced in the TGA. The dehydration of a typical silica material is initiated at *ca.* 120 ºC, but for porous silicas the loosing of water molecules can be extended up to 300 ºC. In the range between 300 and 500 ºC, the condensation of vicinal -OH groups takes place forming new siloxane bonds (Si-O-Si). The sintering of the material happens at temperatures above 600 ºC, which causes the densification of the porous structure and consequently a considerable decrease in the specific surface area. This process also favors further dehydroxilation, and hence the enhancement of the hydrophobicity, of the silica surface.

For the TGA measurements, 5-10 mg of each sample were weighed and heated from room temperature to 700 ºC at 10 ºC/min under a N_2 atmosphere. The thermogravimetric profiles and the weight loss of three representative samples of the silica-based materials are represented in **Figure 2.32** and **Table 2.14**, respectively. Note that, while the particulates systems showed certain amount of physisorbed water and vicinal OH groups, AM did not present significant weight loss below 460 ºC (1 wt%) suffering only condensation processes from isolated hydroxyl groups. From these results we concluded that silica AP particles constituted the material with the highest degree of hydration, followed by the composite AP_{Fe} particles, while the aerogel AM monolith had an insignificant amount of physically adsorbed water.
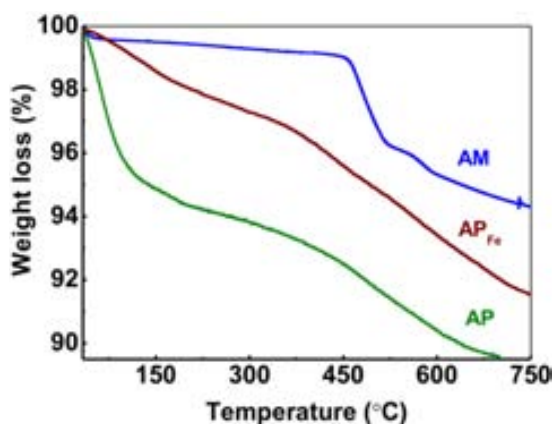
Figure 2.32. Thermal gravimetric analysis of representative samples of AP_{Fe}, AP and AM.

Table 2.14. Weight losses of the silica-based materials at different range of temperature obtained by TGA.

Sample	Chemical specie		
	Physically adsorbed H_2O	**Vicinal OH**	**Isolated OH**
AP_{Fe}	2 wt% (0-185 ºC)	1.2 wt% (185-370 ºC)	2 wt% (370-520 ºC)
AP	5 wt% (0-120 ºC)	2 wt% (120-420 ºC)	3 wt% (420-630 ºC)
AM	-	-	4 wt% (460-700 ºC)

X-ray diffraction (XRD)

The crystalline or amorphous nature of the silica-based materials was determined by PXRD. **Figure 2.33** displays the X-Ray diffractograms of characteristic samples of IONPs, composite nanoparticles, silica sub-micron particles and the aerogel monolith. The presence of amorphous silica in the three studied products was indicated by a broad band between 5 and 27 º. The peaks of IONPs in the AP_{Fe} sample appeared at 30, 35, 43, 53, 57 and 63 º and they can be indexed to either magnetite or maghemite, according to referenced patterns mentioned in **Section 2.4.1**.
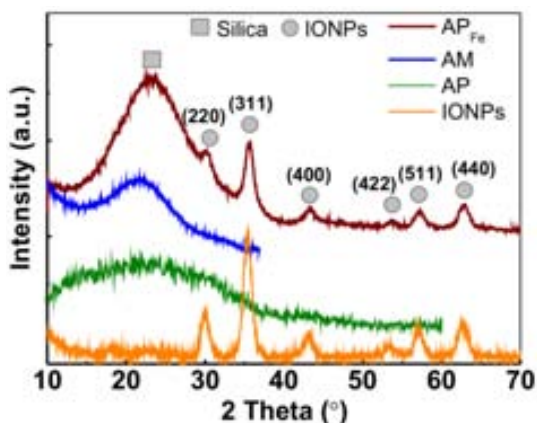
Figure 2.33. X-Ray diffractogram of representative samples of IONPs, AP_{Fe}, AP and AM.

2.7. CONCLUSIONS

Three different silica-based materials were synthesized combining sol-gel chemistry and supercritical fluids technology: silica aerogels, silica sub-micron particles and iron oxide-silica nanoparticles. All of them presented intrinsic porosity without the need of using porogenic agents during the synthetic procedure. The objective of fabricating these materials was to obtain non toxic and biocompatible matrices to host pharmaceutical ingredients for drug delivery applications. The products were amorphous and hydrophilic, which are relevant characteristics for the bioapplicability of silica. Composite magnetic nanoparticles are in addition promising theranostic devices acting as efficient contrast agents. The particulate systems, as dry and light powders, were prepared in a one-pot and one-step process. The main conclusions obtained for each material can be summarized as follows:

Silica aerogels

Highly porous and transparent aerogel monoliths were obtained with low densities (0.1 g/cm^3). BET surface areas were in most cases higher than 400 m^2/g and pore sizes fitted in the meso zone with values in the range of 7-12 nm. Although hydrophilic, aerogel monoliths showed negligible amounts of adsorbed water by TGA.

Silica particles

Around 300 nm in size microporous spheres with narrow size distributions (9-12 %) were synthesized. The particles were stable in colloidal dispersion of polar solvents. BET surface areas ranged from 150 to 200 m^2/g and intraparticle pore sizes were found below 2 nm. When analyzed by TGA, around 5 wt% of adsorbed water was encountered.

Iron oxide-silica nanoparticles

The particles were spherical in shape and colloidally stable in polar solvents. They were composed by inner cores of iron oxide clusters and external silica shells with tunable particle sizes ranging from 60 and 185 nm (suitable for parenteral administration). Superparamagnetic

properties were assessed for the nanospheres. BET surface areas were found between 160 and 250 m^2/g with intraparticle pore sizes in the micro regime (< 2 nm). TGA experiments resulted in ~ 2 wt% of adsorbed water.

2.8. REFERENCES

[1] Vansant, E.F., Van Der Voort, P., Vranchen, K.C. Characterization and chemical modification of the silica surface. *Elsevier*. Belgium, **1995**.

[2] Iller, R.K. The Chemistry of Silica. *Wiley*: New York, **1979**.

[3] Brinker, C.J., Scherer, G.W. Sol-gel science. *Academinc Press*: San Diego, **1990**.

[4] Rouquerol, J., Avnir, D., Fairbridge, C.W., Everett, D.H., Haynes, J.H., Pernicone, N., Ramsay, J.D.F., Sing, K.S.W., Unger, K.K. Recommendations for the characterization of porous solids. *Pure* & *Appl. Chern.*, **1994**, *66*, 1739-1758.

[5] Brunauer, S., Deming. L.S., Deming, W.S., Teller, E., *J. Am. Chem. Soc.*, **1940**, *62*, 1723-1732.

[6] Sing, K.S.W., Everett, D.H., Haul, R.A.W., Moscou, L., Pierotti, R.A., Rouquerol, J., Siemieniewska, T. Reporting physisorption data for gas/solid systems with special reference to the determination of surface area and porosity. *Pure* & *Appl. Chern.*, **1985**, *57*, 603-619.

[7] Brunauer, S., Emmet, P.H., Teller, B. Adsorption of Gases in Multimolecular Layers. Adsorption of gases in multimolecular layers. *J. Am. Chem. Soc.*, **1938**, *60*, 309-319.

[8] Hüsing, N., Schubert, U. Aerogels-airy materials: Chemistry, structure, and properties. *Angew. Chem. Int. Ed.*, **1998**, *37*, 22-45.

[9] Pierre, A.C., Pajonk, G.M. Chemistry of aerogels and their applications. *Chem. Rev.* **2002**, *102*, 4243-4265.

[10] Schmidt, M., Schwertfeger, F. Applications for silica aerogel products. *J. Non-Cryst. Solids*. **1998**, *225*, 364-368.

[11] Smirnova, I., Mamic, J., Arlt, W. Adsorption of drug in silica aerogels. *Langmuir*, **2003**, *19*, 8521-8525.

[12] Smirnova, I., Suttiruengwong, S., Arlt, W. Feasibility study of hydrophilic and hydrophobic silica aerogels as drug delivery systems. *J. Non-Cryst. Solids*. **2004**, *350*, 54-60.

[13] Wang, J., Uma, S., Klabunde, K.J. Visible light photocatalysis in transition metal incorporated titania-silica aerogels. *Appl. Catal. B.* **2004**, *48*, 151-154.

[14] Moner-Girona, M. Silica Aerogels: synthesis and characterization. PhD Thesis. Institut de Ciència de Materials de Barcelona (ICMAB-CSIC) and Universitat Autònoma de Barcelona, **2002**.

[15] Liu, J., Qin, Z., Wang, G., Hou, X., Wang, J. Critical properties of binary and ternary mixtures of hexane + methanol, hexane + carbon dioxide, methanol + carbon dioxide, and hexane + carbon dioxide + methanol. *J. Chem. Eng. Data*, **2003**, *48*, 1610-1613.

[16] Kuznetsova, T.F., Eremenko, S.I. Synthesis of aerogel-type mesoporous silica. *Colloid J.*, **2014**, *76*, 327-333.

[17] Taboada, E. Synthesis of γ-Fe$_2$O$_3$-SiO$_2$ composite nanoparticles targeting magnetic resonance imaging and magnetic hyperthermia applications. PhD Thesis. Institut de Ciència de Materials de Barcelona (ICMAB-CSIC) and Universitat Autònoma de Barcelona, **2009**.

[18] Bogush, G.H., Tracy, M.A., Zukoski IV, C.F. Preparation of monodisperse silica particles: control of size and mass fraction. *J. Non-Cryst. Solids*, **1988**, *104*, 95-106.

[19] Taboada, E., Solanas, R., Rodrı́guez, E., Weissleder, R., Roig, A. Supercritical fluid-Assisted one-pot synthesis of biocompatible core(γ-Fe$_2$O$_3$)/Shell(SiO$_2$) nanoparticles as high relaxivity T$_2$-contrast agents for magnetic resonance imaging. *Adv. Funct. Mater.*, **2009**, *19*, 2319-2324.

[20] Sun, S., Zeng, H., Robinson, D.B., Raoux, S., Rice, P.M., Wang, S.X., Li, G. Monodisperse MFe$_2$O$_4$ (M = Fe, Co, Mn) nanoparticles. *J. Am. Chem. Soc.*, **2004**, *126*, 273-279.

[21] Redl, F.X., Black, C.T., Papaefthymiou, G.C., Sandstrom, R.L., Yin, M., Zeng, H., Murray, C.B., O'Brien, S.P. Magnetic, electronic, and structural characterization of nonstoichiometric iron oxides at the nanoscale. *J. Am. Chem. Soc.*, **2004**, *126*, 14583-14599.

[22] Roca, A.G., Morales, M.P., Serna, C.J. Synthesis of monodispersed magnetite particles from different organometallic precursors. *IEEE Trans. Magn.*, **2006**, *42*, 3025-3029.

[23] Kashchiev, D. Nucleation: Theory and basic applications. Butterworth-Heinemann, **2000**.

[24] Yin, M., Willis, A., Redl, F., Turro, N.J., O'Brien, S.P. Influence of capping groups on the synthesis of γ-Fe_2O_3 nanocrystals. *J. Mater. Res.*, **2004**, *19*, 1208-1215.

[25] LaMer, V.K., Dinegar, R.H. *J. Am. Chem. Soc.*, **1950**, *72*, 4847-4848.

[26] Mondini, S., Drago, C., Ferretti, A.M., Puglisi, A., Ponti, A. Colloidal stability of iron oxide nanocrystals coated with a PEG-based tetra-catechol surfactant. *Nanotech.*, **2013**, *24*, 105702 (1-14).

[27] Zhang, l., He, R., Gu, H.-C. Oleic acid coating on the monodisperse magnetite nanoparticles. *Appl. Surf. Sci.*, **2006**, *253*, 2611-2617.

[28] Pascu, O., Carenza, E., Gich, M., Estradé, S., Peiró, F., Herranz, G., Roig, A. Surface reactivity of iron oxide nanoparticles by microwave-assisted synthesis; comparison with the termal decomposition route. *J. Phys. Chem. C*, **2012**, *116*, 15108-15116.

[29] Kima, W., Suha, C.-Y., Choa, S.-W., Roha, K.-M., Kwona, H., Songa, K., Shon, I.-J. A new method for the identification and quantification of magnetite–maghemite mixture using conventional X-ray diffraction technique. *Talanta*, **2012**, *94*, 348-352.

[30] Pascu, O., Carenza, E., Gich, M., Estradé, S., Peiró, F., Herranz, G., Roig, A. Surface reactivity of iron oxide nanoparticles by microwave-assisted synthesis; comparison with the thermal decomposition route. *J. Phys. Chem. C*, **2012**, *116*, 15108-15116.

[31] Cao, S.-W., Zhu, Y.-J., Chang, J. Fe_3O_4 polyhedral nanoparticles with a high magnetization synthesized in mixed solvent ethylene glycol–water system. *New J. Chem.*, **2008**, *32*, 1526-1530.

[32] Layek, S., Pandey, A., Pandey, A., Verma, H.C. Synthesis of γ–Fe_2O_3 nanoparticles with crystallographic and magnetic texture. *Int. J. Eng. Sci. Technol.* 2010, *2*, 33-39.

[33] Pouretedal, H.M., Kazemi, M. Characterization of modified silica aerogel using sodium silicate precursor and its application as adsorbent of Cu^{2+}, Cd^{2+}, and Pb^{2+} ions. *Int. J. Ind. Chem.*, **2012**, *3*:20, 8 pp.

[34] Rao, A.V., Kulkarni, M.M., Amalnerkar, D.P., Seth, T. Superhydrophobic silica aerogels based on methyltrimethoxysilane precursor. *J. Non-Crsyt. Solids*, **2003**, *330*, 187-195.

[35] Reynolds, J.G., Coronado, P.R., Hrubesh, L.W. Hydrophobic aerogels for oil-spill clean up-synthesis and characterization. *J. Non-Cryst. Solids*, **2001**, *292*, 127-137.

3

MOLECULAR IMPREGNATION OF SILICA-BASED MATERIALS

This chapter is devoted to the impregnation of porous silica-based materials with different functional organic molecules by dissolving them in supercritical carbon dioxide. Firstly, as a proof-of-concept, two organic photosensitizers were simultaneously *in situ* synthesized and encapsulated in the silica systems, leading to hybrid materials with high stability and enhanced properties for applications in photocatalysis. Secondly, drug carriers systems were fabricated by entrapping a model drug in the silica matrices. Details on the processes and on the characterization, in terms of organic load, structural and textural properties of the resulting materials, are presented. Special attention is dedicated to the chemical conformation and stability of the drug inside the silica matrices and to the *in vitro* release kinetics in aqueous media, which determines the potential use of the composites as drug delivery systems.

For comparison purposes, previous results obtained in the group from the impregnation in zeolites (for photosensitizers) and in an organic polymer (for the therapeutic agent) are also presented. Differences in the porous structure, polarity and release profiles are emphasized.

3.1. ENCAPSULATION OF ORGANIC CATIONS

One of the most interesting applications of porous materials is related to their ability of hosting molecules and other chemical entities. Zeolites, carbon nanotubes, ordered mesoporous silicas (OMSs), organic polymers and other materials with induced or intrinsic porosity can act as platforms to anchor different molecules. The encapsulation of some compounds in nanoporous matrices contributes to stabilize those substances from a chemical, crystallographic or physical point of view,[1,2,3] due to the capability of host materials to adsorb and interact with atoms, ions and molecules in restricted spaces. Among the available methods of encapsulation, the use of supercritical fluids (SCFs) to perform absorption and/or impregnation in porous matrices offers several advantages compared to the use of common solvents. In addition to the avoidance of using toxic and contaminant organic solvents, some important advantages are:

- Less energy cost in drying process.
- Prevention of pore collapse when solvent is being extracted from the porous system, due to the null surface tension of SCFs. This point is of special relevance for aerogel-like systems.
- Homogeneous surface functionalization because of the low viscosity of compressed fluids, which can diffuse easily through, even into the smallest pores.

The purpose of this work was to use the porous materials previously synthesized as described in **Chapter 2** as platforms to be impregnated with therapeutic agents for drug delivery applications. However, first trials on the encapsulation process were performed using organic photosensitizers known by the group. We chose silica aerogels (AM) and porous silica submicron particles (AP) as suitable matrices to encapsulate organic molecules, in particular cationic dyes, by dissolving them in supercritical carbon dioxide (scCO$_2$). Two kinds of chromophores, a pyrylium and a trytyl cation, were chemisorbed in the inner surface of the studied matrices,. The solvent power and diffusivity of scCO$_2$ played key roles. Results obtained with aerogel-like matrices were compared to those attained for an aluminosilicate support, a faujasite-type zeolite (ZY). The knowledge acquired with these experiments served as the basis to perform the impregnation with drugs as well as to demonstrate the versatility of the encapsulation method.

3.1.1. Organic cations for catalytic applications

The encapsulation of chromophores and cationic organic dyes within nanoporous matrices is a particular example of host-guest synthesis. The obtained hybrid nanocomposites have applications as solid-state dye lasers,[4,5] aerogel-platform gas sensors[6] and in photocatalysis, among others.[7,8,9,10,11,12] Using opaque solids as supports to carry out photochemical reactions lead to inherent disadvantages associated with the interaction of light with solids (scattering, diffraction and reflection). The use of highly transparent mesoporous silica aerogel structures could bring added value to materials with intended applications in photocatalysis. The photosensitizers selected in this work were 2,4,6-triphenylpyrylium (Ph$_3$Py$^+$) and dimethoxytrityl ((CH$_3$O)$_2$Ph$_3$C$^+$) cations. **Figure 3.1** shows the chemical structure of both species. These salts have

a relatively high oxidation power and have been reported to be good electron transfer photosensitizers for photochemical reactions involving aromatics, dienes or alkenes and epoxides, and for treating air and water pollutants using solar light.[13,14] Unfortunately, they have a poor stability in aqueous media.[15,16] For this reason, the intravoid space of nanoporous matrices is specially suited to incorporate and stabilize these guests. The resulting host-guest assemblies can act as easily recoverable heterogeneous photocatalysts.
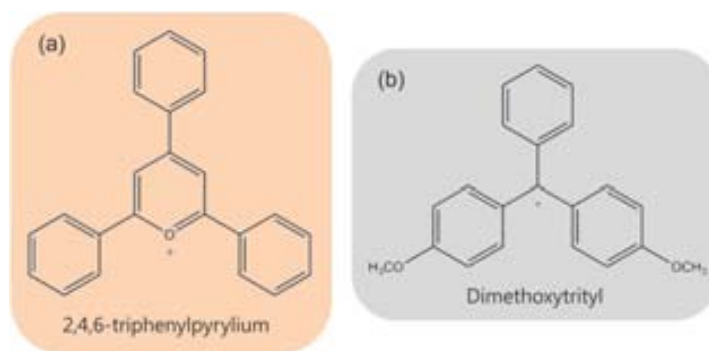
Figure 3.1. Chemical structures of: (a) 2,4,6-triphenylpyrylium, and (b) dimethoxytrityl cations.

3.1.2. Method of cations impregnation

The precursor used for Ph_3Py^+ impregnation was the diketone 1,3,5-triphenyl-2-pentene-1,5-dione, synthesized in our laboratory.[17] The two organic precursors used as the building blocks for $(CH_3O)_2Ph_3C^+$ encapsulation were benzaldehyde and anisole (≥ 98.0 wt% and ≥ 99.0 w% respectively, Fluka) in a 1:2 molar ratio. Commercially available 2,4,6-triphenylpyryl tetrafluoroborate (Ph_3PyBF_4, c-Py$^+$, Aldrich) and trityl tetrafluoroborate (Ph_3CBF_4, c-C$^+$, Aldrich) were used as references for comparisons with encapsulated products. All these substances were used as received.

Supercritical impregnation experiments were performed in the batch mode in the high pressure equipment shown in **Figure 3.2a**. In a typical experiment, liquefied CO_2 (99.995 wt%, Carburos Metálicos, Spain) was compressed by a syringe pump and conducted to the reactor. The autoclave was first charged with *ca.* 0.5 g of each matrix in the form of small pieces (AM) or powder (AP and ZY), and the precursors of the guest material in a proportion of 20 wt% with respect to the matrix (total weight 0.3 g). The three materials were enclosed in 0.45 μm pore size filter paper, thus avoiding direct contact of the matrices with the solutes, and hanged from the thermopar bar inside the reactor (**Figure 3.2b**). The cations formation proceeds in two steps: (1) diffusion and (2) condensation, separated in time.[11,12] The first step consisted in diffusing the starting reagents inside the matrix nanochannels at a pressure of 150 bar and a relatively low temperature (60 ºC), thus minimizing the formation of the bulky cation, which otherwise could block the channels in the early stages of the process. This stage was followed by a condensation step at higher temperature (130-150 ºC), serving to activate the reaction of the precursors inside the acid matrix. During the reaction, the autoclave was stirred at 400 rpm. Finally, the system was

depressurized and left to cool down to room temperature. Pressurization and depressurization cycles were carried out avoiding the formation of liquid CO_2 in the autoclave, which could damage the fragile porous structure of aerogels. Zeolite samples recovered at this stage were gently rinsed with dichloromethane (DCM). Monolithic samples were cleaned with a flow of nitrogen. The resulting products were labeled as *cation@matrix*. Some materials were further cleaned with a flow of continuous scCO$_2$ at 200 bar and 80 ºC for 3 h. The resulting samples were labeled as *[cation@matrix]$_{SC}$*.

Figure 3.2. (a) 100 mL supercritical reactor used for the organic cations impregnation, and (b) paper packets containing the matrices hanged from the thermopar bar.

The porous structure of faujasite-type zeolites presents cuasi-spherical cavities of 1.3 nm in diameter that are accessible though small channels (0.74 nm in height) arranged in a tridirectional ordered structure.[18] This porous structure is schematized in **Figure 3.3**. Since the selected cations have larger dimensions than the channels, but they fit into the cavities, a called *ship-in-a-bottle* reaction in supercritical CO_2 takes place. It basically consists in dissolving the cation precursors in the compressed fluid, diffusing them through the channels until reaching the cavities and increasing the temperature to promote the chemical reaction. Thus, the encapsulation procedure not only implies the entrapping of the cations inside the matrices, but also it is the synthetic method of the guest molecules.
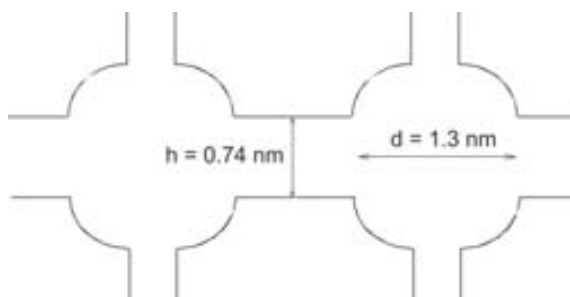
Figure 3.3. Basic scheme of the porous structure of faujasite-type zeolites. h stands for the diameter of the channels and d makes reference to the diameter of the cuasi-spherical cavities.

3.1.3. Results and discussion

Some of the characteristics of the resulting materials are shown in **Table 3.1**. The chemical reaction necessary to form the cations was triggered by the weak acid sites of the inner pores of either the silica aerogel AM or the aerogel-like spheres AP (silanols, pKa = 8) (**Figure 3.4a**) or the aluminosilicate (**Figure 3.4b**). The formation of the pyrylium cation was accomplished in two steps: first the dehydration and then the cyclisation of the diketone. The reaction used for the preparation of the dimethoxytrityl cation occurred between benzaldehyde and anisole.

The resulting hybrid nanocomposites presented a characteristic coloration which may be used as a first visual indication of the degree of success of the reactions (**Table 3.1**).

Table 3.1. Characteristics of the obtained loaded materials AM AP and ZY.

Sample	Impregnated cation	Sample color	Loading (%)
Py$^+$@AM	Pyrylium	Orange	8.6
C$^+$@AM	Trityl	Yellow	1.5
Py$^+$@AP	Pyrylium	Yellow	5.7
[Py$^+$@AP]$_{SC}$	Pyrylium	Pale yellow	5.3
C$^+$@AP	Trityl	Pale yellow	3.4
[Py$^+$@ZY]$_{SC}$	Pyrylium	Yellow	5.9
[C$^+$@ZY]$_{SC}$	Trityl	Ochre	7.0

The precursors of the guest molecules were colorless, and only after cation formation a color appeared. It was associated with absorption in the visible range. While the matrices were initially either transparent (AM in **Figure 3.5a**) or white (AP and ZY in **Figure 3.5d** and **g**, respectively), the adsorption of the cation was noticeably visible from the resulting yellow-orange color (**Figure 3.5b**, **c**, **e** and **f** for impregnated aerogels and **Figure 3.5h**, **i** for impregnated zeolites).[19,20] The pyrylium impregnated AM sample (Py$^+$@AM) exhibited a uniform color, as it is observed in **Figure 3.5b**. This uniformity indicated a homogeneous diffusion of the precursor throughout the porous sample.
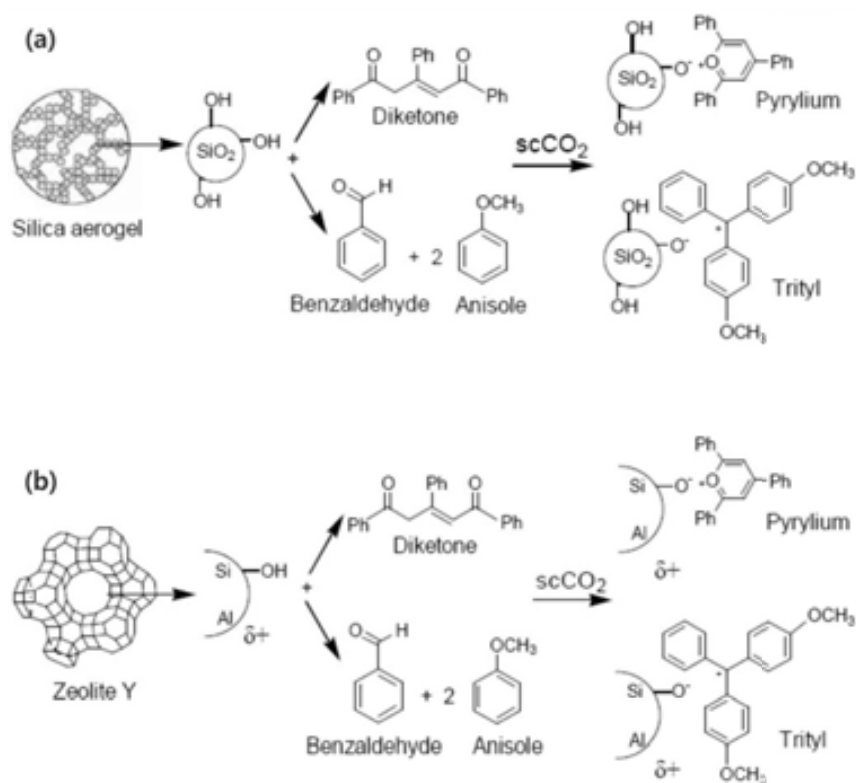
Figure 3.4. Schematic representation of the encapsulation reactions performed in the different matrices: (a) AM or AP, and (b) zeolite Y.

Figure 3.5. Optical images of: (a) pristine monolithic aerogel (AM), and impregnated samples (b) Py$^+$@AM and (c) C$^+$@AM; (d) pristine aerogel particles (AP), and impregnated samples (e) [Py$^+$@AP]$_{SC}$ and (f) C$^+$@AP; and (g) pristine zeolite Y, and impregnated samples (h) [Py$^+$@ZY]$_{SC}$ and (i) [C$^+$@ZY]$_{SC}$.

3.1.3.1. Morphological and structural characterization of the impregnated materials

The resulting hybrid nanocomposites preserved the same shape than that of the raw matrices. Thus, the silica aerogel AM remained in monolithic form and the powders AP and ZY appeared as powdered solids after the supercritical treatment, demonstrating that the encapsulation process assisted by scCO$_2$ did not change the morphological properties of the starting materials.

Fourier transformed infrared spectroscopy (FTIR)

The success of cations encapsulation was evaluated by infrared spectroscopy. **Figure 3.6a** and **Figure 3.6b** show the spectra of the commercial chromophores and the impregnated matrices for pyrylium and trityl cations, respectively. The typical bands of Ph$_3$Py$^+$ appeared between 1550 and 1650 cm^{-1} for the commercial compound[21] (sample c-Py$^+$ in **Figure 3.6a**) and at the same wave length for the encapsulated products. The lack of the C=O vibration bands at 1680-1650 cm^{-1}, characteristic of the diketone precursor, revealed a high degree of purity for samples impregnated with pyrylium cations and indicated the success in the impregnation process for this chromphore. Peaks at 1489 and 1445 cm^{-1} in the FTIR spectrum of commercial Ph$_3$CBF$_4$ (sample c-C$^+$ in **Figure 3.6b**) were attributed to C-C stretches in the phenyl ring and a signal at 1384 cm^{-1} was assigned to C-Ph stretching.[22] This latter signal did not appear in any of the building blocks used and therefore was especially useful to monitor the presence of the trityl cation. The most intense peaks for the trityl-impregnated products corresponded to the C-C ring stretching mode in the (CH$_3$O)$_2$Ph$_3$C$^+$ cation and were found between 1495-1500 and 1440-1450 cm^{-1}. However the band due to the C-Ph bond at 1384-1381 cm^{-1} was the most representative one (**Figure 3.6b**). In the light of these results, it can be assumed that the preparation of the (CH$_3$O)$_2$Ph$_3$C$^+$ cation was successfully achieved.
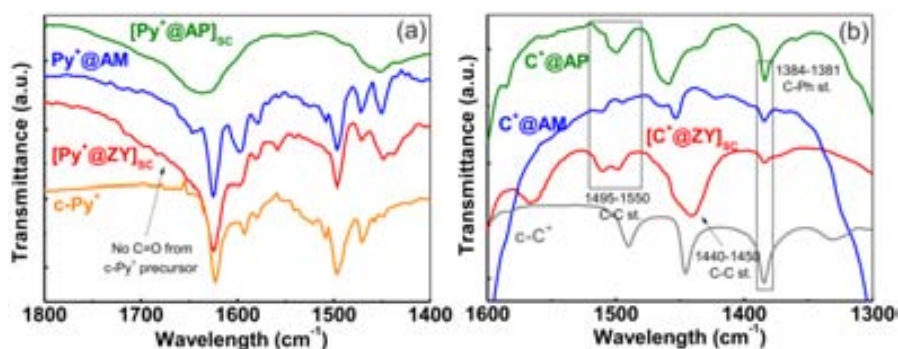
Figure 3.6. FTIR spectra of pristine matrices and commercial cations of: (a) pyrylium, and (b) trityl impregnated matrices

Thermal gravimetric analysis (TGA)

Mass loadings regarding the encapsulation of the organic cations in the different matrices were obtained by TGA. Thermal gravimetric profiles of the pristine matrices and commercial cations are shown in **Figure 3.7a** and **Figure 3.7b**, respectively. AP and ZY profiles show the evaporation of adsorbed water at temperatures lower than 150 °C, presenting an initial weight loss of ~ 5-10

wt% (**Figure 3.7a**). In the temperature range of 150-400 °C, the weight loss of untreated monolithic aerogel was insignificant, while for particulate aerogel and zeolite matrices, although minor, it was measurable (*ca.* 0.5-1 wt%). Aerogel matrices also lost weight at temperatures higher than 450-500 °C, which was attributed to material densification, and the reaction between silanol groups with the associated loss of water. Decomposition of commercial Ph_3PyBF_4 salt occurred at temperatures between 240 and 325 °C and the maximum slope was found at 300 °C. On the other hand, Ph_3CBF_4 decomposed with a profile characterized by a pronounced weight loss (~ 75 wt%) between ~ 190 and 320 °C (**Figure 3.7b**). For the impregnated samples in the form of particulate powders (**Figure 3.7c** and **Figure 3.7d**), the first mass decay was observed at temperatures lower than 180 °C due to the loss of water, while the decay at temperatures higher than 200 °C was associated with the loss of the embedded organic cation. Pyrylium cation when entrapped in aerogel-like (AM or AP) and zeolite matrices decomposed in the temperature ranges of 250-400 °C (with the maximum slope at 350 °C) and 325-500 °C (maximum slope at 425 °C), respectively as it can be seen in **Figure 3.7c**. This result indicates that the Ph_3Py^+ cation inside the nanopores presents higher thermal stability than in the Ph_3PyBF_4 salt. The trityl cation, once impregnated in the different systems, thermally decomposed (**Figure 3.7d**) in a temperature range only slightly superior (~ 250-400 °C) to that of the commercial product. Thus, organic loads were acquired by measuring the weight losses in the appropriate temperature ranges for each cation@matrix pair (**Table 3.1**). In general, higher loadings were obtained for the pyrylium than for the trityl cation. Note that the formation of those substances into the matrices proceed in different ways: while the pyrylium cation is prepared through dehydration and cyclisation of one precursor (diketone), the synthesis of trityl cation involves two building blocks and the formation of a C-C bond (**Figure 3.4**).
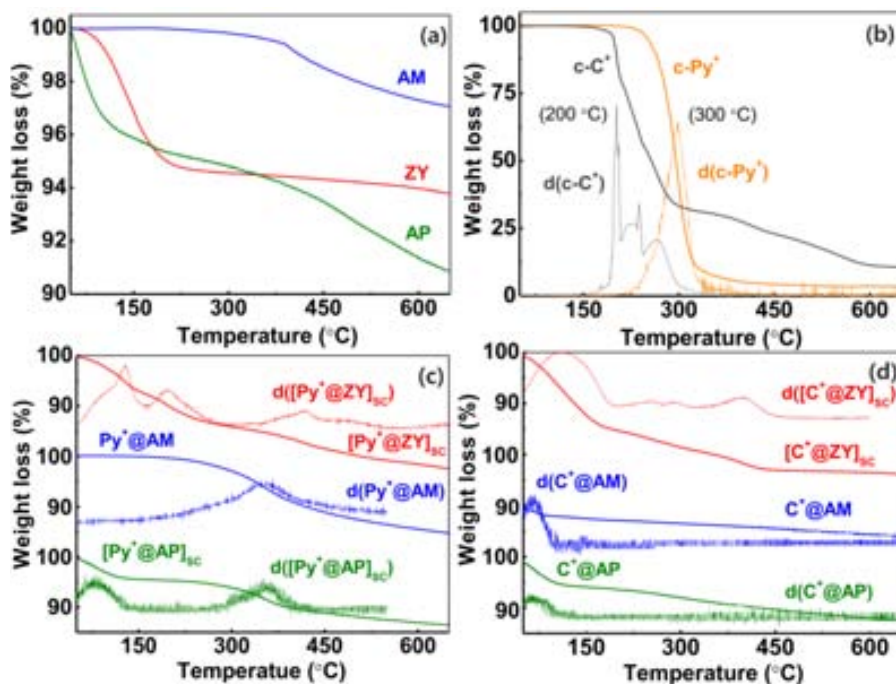
Figure 3.7. TGA curves of: (a) pristine matrices, (b) commercial salt of the organic cations; and hybrid composites obtained after impregnation with: (c) pyrylium, and (d) trityl cations. Curves labeled as *d(cation@matrix)* are the derivatives of the respective TGA curves.

3.1.3.2. Textural properties of the impregnated materials

Nitrogen adsorption/desorption isotherms (BET method)

The specific surface areas were measured before and after processing the matrices with the pyrylium cation. A significant decrease for materials with the organic molecules absorbed into the pores was expected. Prior to measurements, samples were degassed under a reduced pressure (< 10^{-8} bar). The conditions used were 300 ºC for 24 h for aerogel particles, 100 ºC for 24 h for aerogel monoliths and 150 ºC for 48 h for zeolites. The aerogel monolith and particles had surface area values of 475 and 205 m^2/g, respectively, as it was detailed in **Chapter 2**. AP sample can be considered as an intermediate material between zeolites and aerogel monoliths, since it has an intraparticle pore size of 1.5-2 nm, similar to that of zeolites, but also has some other characteristics, such as the non-ordered pore structure, closer to monolithic silica aerogels. For the calcined zeolite (ZY), the measured surface area was 700 m^2/g.

After impregnation of the AM and the zeolite with pyrylium cations, their specific surface areas were only slightly diminished to values of 410 and 500 m^2/g, respectively. Contrarily, a drastic decrease of *ca.* 80% resulted for the impregnated aerogel-like particles, pointing towards the blocking of the channels, probably due to reduced pore interconnectivity in this matrix with respect to the aerogel monolith and zeolite.

Although this analysis was not performed for trityl impregnated samples, a similar behavior is expected.

3.1.3.3. Complementary characterization towards the applicability in photocatalysis

Diffuse reflectance UV-Vis spectroscopy

The measurements were carried out entrapping the powdered samples between two microscope glass slides and fixing them with adhesive tape. The monolithic materials were directly stuck to the surface of one microscope glass slide. It is important that those plates do not absorb light in the wavelength range of operation, as well as taking care of not letting the adhesive tape interfere with the light beam. All the matrices used were quite transparent to UV-Vis radiation above *ca.* 250-300 nm. **Figure 3.8a** shows the diffuse reflectance spectra in the UV-Vis range of the commercial Ph_3PyBF_4 salt and the matrices loaded with Py^+. The solid spectrum of commercial Ph_3PyBF_4 displayed a broad band between 320 and 530 nm. For all the prepared pyrylium samples, a similar absorption band between 330 and 500 nm was found, which suggests cation formation. Analogously, **Figure 3.8b** shows the diffuse reflectance spectra of the commercial Ph_3CBF_4 salt, as well as the matrices loaded with C^+. The spectrum of the commercial product is characterized by a broad absorption band from 320 to 530 nm. For the trityl-impregnated aerogel, the absorption in the range 352-525 nm was weak, which was related to the relatively low impregnated amount (see **Table 3.1**). On the other hand, the diffuse reflectance UV-Vis spectrum of sample $[C^+@ZY]_{SC}$ showed two separated maxima at 417 and 506 nm, characteristic of substituted trityl cations with optical asymmetry.
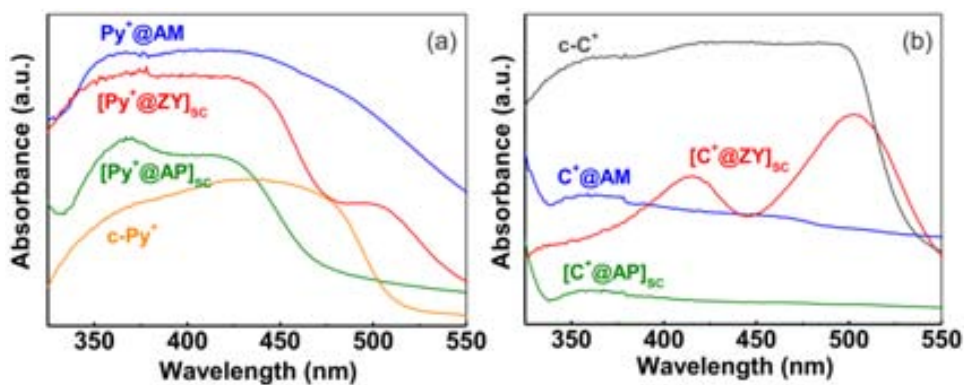
Figure 3.8. Diffuse reflectance UV-Vis spectra of: (a) pyrylium product and the matrices impregnated with Py^+, and (b) commercial trityl product and the matrices impregnated with C^+.

Fluorescence spectroscopy

Room temperature emission fluorescence microscopy was used to investigate the fluorescence of the AM and ZY impregnated samples upon excitation at 420 nm. The products were directly placed on the microscope glass slides. Control experiments with the pristine matrices did not show any significant fluorescence. The emission spectra of the matrices with entrapped pyrylium cations (samples $Py^+@AM$ and $[Py^+@ZY]_{SC}$) are presented in **Figure 3.9a**. In particular, pyrylium

salts in solution have a fluorescence band with a maximum at 470-480 nm.[23,24] This value is similar to that found for the prepared solid pyrylium samples, which clearly showed a strong fluorescence band centered close to 500 nm. In contrast to pyrylium, trityl cations exhibited a much weaker fluorescence[25,26] and low intensity emission spectra were registered for the matrices with entrapped trityl cations (not shown). For [C⁺@ZY]$_{SC}$ and C⁺@AM, fluorescence microscopy indicated that samples were also fluorescent in the blue region (**Figure 3.9b**). It is remarkable that fluorescent optical images showed a homogeneous distribution of dyes in the matrices, even in the large pieces of the aerogel monolith.
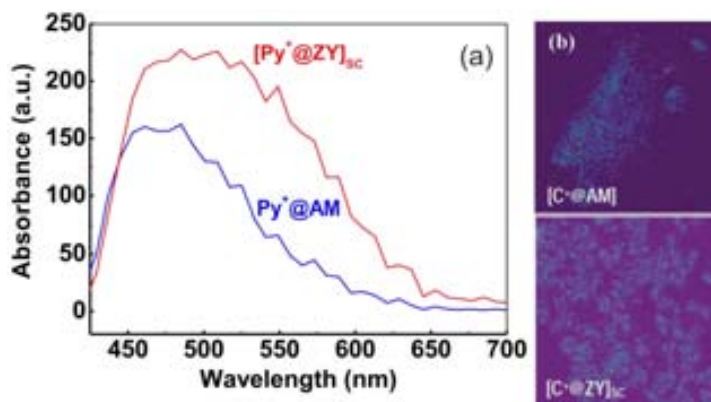
Figure 3.9. Fluorescence data upon 420 nm excitation: (a) emission spectra of encapsulated pyrylium, and (b) fluorescence images of encapsulated trityl.

Leaching behavior in water by UV-Vis spectrophotometry

The synthesized composite materials have a great number of potential applications involving the presence of water, for instance, as heterogenous catalytic platforms for contaminated waters. For such applications, it is important to know the possible leaching of the encapsulated substances from the nanoporous matrices in water. An experimental procedure was designed to elucidate the leaching behavior of the impregnated cations, which allowed controlling their stability in water at the same time. The impregnated matrices were immersed in distilled water (pH = 6.5) for a total period of 12 days. Approximately 3-5 mg of each sample was placed into a glass beaker with 4 mL of water and kept in a lab exposed to natural light. After the first 24 h, 1.5 mL of the liquid was analyzed by UV-Vis spectrophotometry. On the 5th day, a second 1.5 mL aliquot was extracted and the absorption measurement repeated. Then, the impregnated matrices were covered with a further 5 mL of fresh water and one more UV-Vis monitoring was performed at day 12. Importantly, after this relatively long period of time, the materials still maintained their characteristic yellow/orange color of the impregnated products, indicating that both leaching and degradation of the cation were minor. The UV-Vis spectra of the triphenylpyrylium and trityl salts in organic solution are characterized by the presence of a broad band between 370-480 nm, generated by two independent chromophores,[27,28] while their precursors have appreciable absorption at wavelengths between 200 and 350 nm. Preliminary tests have showed that both

cations were unstable in water at neutral pH, being transformed in low molecular weight degradation products exempted of color.

0 gathers the results obtained after following the designed leaching protocol. After 5 days of water inmersion, the spectra of the as-prepared aerogel samples showed an appreciable absorption between 225 and 325 nm whatever the encapsulated compound (either pyrylium or trityl cations in **0a**, **c** and **0b**, **d**, respectively). However, they did not present any significant amount of organic compounds in the refreshed water added afterwards and measured on day 12. On the other hand, the supercritically-washed samples $[Py^+@AP]_{SC}$, $[Py^+@ZY]_{SC}$ and $[C^+@ZY]_{SC}$ (**0c, e** and **f**) did not undergo any significant leaching during the time period of analysis, indicating that the washing procedure was effective at eliminating the residual reagents and unbounded chromophore molecules and that the remaining impregnated material was stable and strongly interacting with the matrix.

In **Figure 3.10a** and **Figure 3.10b** the leaching behavior in water of the three studied matrices charged with either pyrylium or trityl cation is compared. Some leaching was only observed for samples that were not previously washed with $scCO_2$. Even in these cases, the desorption of material only occurred in the first stage, suggesting that the leaching was originated from impregnated organics located on the most external part of the matrices where the cation was less stabilized than in the most internal nanopores. It has been previously reported that simple deposition of these cations on the external surface of silica does not prevent hydrolysis.[29] In our case, cation leaching behavior was probably diffusion controlled through the nanopores, since the UV-Vis absorption at day 1 was much lower than at day 5. For all the studied matrices, the impregnated cations showed higher hydrolysis stability when encapsulated than the non-encapsulated ones.
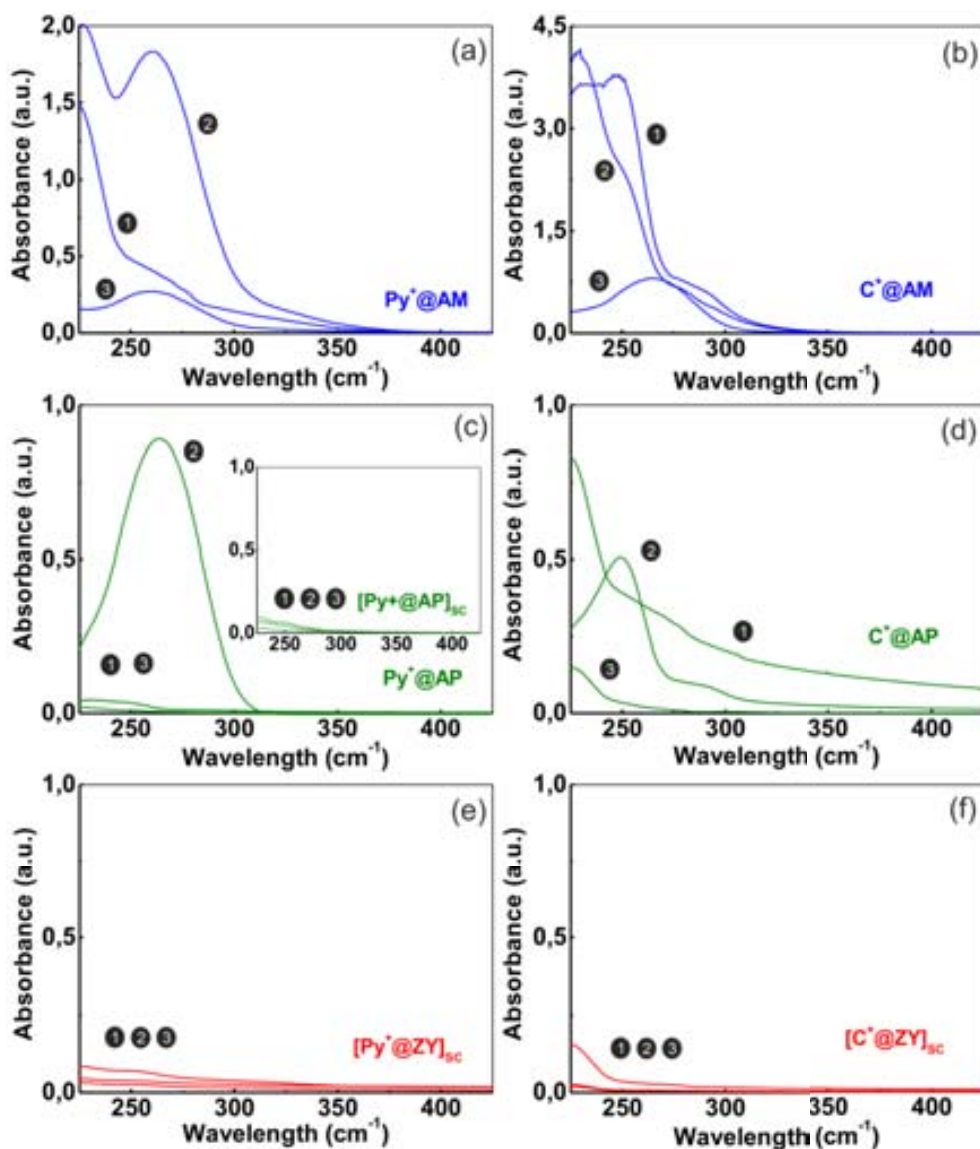
Figure 3.10. Leaching behavior in water of the prepared samples measured by UV-Vis spectroscopy: (a), (c) and (e) matrices impregnated with pyrylium cation; and (b), (d) and (f) matrices impregnated with trityl cation. The numeric notation is referred to the time of aliquot measurements: after ❶ 1 day, after ❷ 5 days and after ❸ 12 days with refreshed mother liquid.
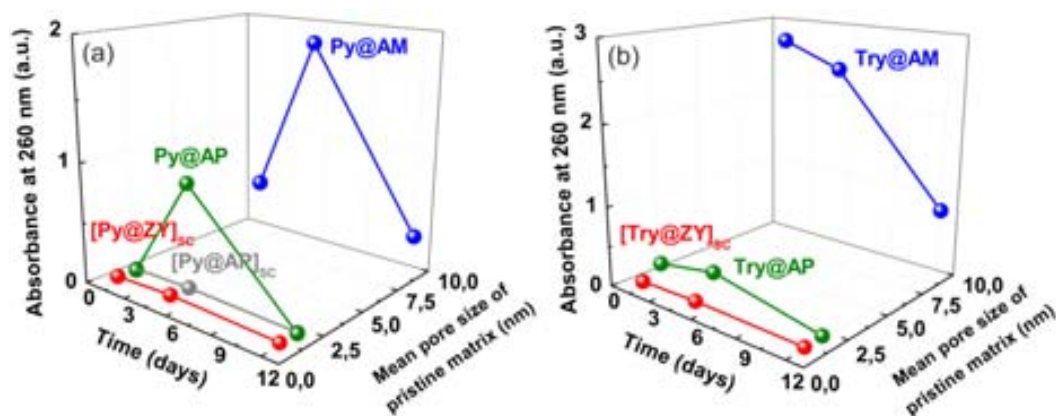
Figure 3.10. Leaching behavior of (a) pyrylium impregnated, and (b) trityl impregnated samples. Axis Y indicates the average pore diameter of the raw matrices calculated by BET ($4V_{pore}/S_{BET}$), corresponding to ~ 1.2 for zeolites, ~ 1.8 for aerogel particles and ~ 7 for aerogel monoliths.

3.2. ENCAPSULATION OF TRIFLUSAL AS MODEL DRUG

The development of drug carriers as controlled drug delivery systems have been deeply explored during the last few decades,[30] because they can solve several common problems in the pharmaceutical industry. Compared to traditional pharmaceutical formulations, these new materials with engineered biodistribution profiles diminish side effects, insufficient drug concentration at target sites, rapid metabolization or drug degradation related problems. Among the studied systems, nanoparticulate materials have been proved to enhance the *in vivo* efficiency[31,32,33] of active agents by facilitating prolonged circulation after administration, by increasing bioavailability and by enhancing the percentage of unaltered drug in the pathological area. In this category, hydrophilic silica offers some advantages when contrasted to polymer-based materials: stability under various thermal and chemical conditions, non aggregation related to lipophilic nature upon intravenous administration[34] and biocompatibility.[35,36,37] While many of the marketed polymeric drug delivery carriers are adequate for the sustained release of water-soluble drugs, porous silica particles are mostly applied to obtain an immediate optimal drug dosage of poorly water-soluble compounds at the desired target site.[38] Another challenge for SiO_2 drug delivery systems is to warrant the full preservation of the drug activity during its storage and administration period.

We selected a poorly water-soluble drug as model active agent (*Triflusal*) to be encapsulated into the pores of the three silica-based materials previously synthesized (**Chapter 2**): AP_{Fe}, AP and AM. See **Section 3.2.1** below for main characteristics of Triflusal. Using hydrophilic silica as the host matrix we expect to improve both the dissolution profile and to increase the preservation of the Triflusal. Besides, composites AP_{Fe} can actuate not only in therapeutics, but also in diagnosis (MRI). In the impregnation procedure, supercritical CO_2 was the solvent for the therapeutic agent. The unique properties of this fluid have been advantageously exploited in processes involving poorly water-soluble drugs, since a higher solubility of hydrophobic compounds in $scCO_2$ is

usually found. Besides, the avoidance of organic solvents, the intrinsic sterility of $scCO_2$ and the fact that the final product is in a dry form and is produced in confined autoclaves are also of particular interest for pharmaceutical products manufacturing.[39] Results attained for these systems were compared to those obtained for a hydrophobic matrix made of polymethyl metacrylate (PMMA) in terms of drug loading, stabilization and release profile.

A generic $scCO_2$ method for the impregnation of both inorganic and polymeric matrices with Trf is proposed to create potential drug delivery systems.

3.2.1. Properties of triflusal

Triflusal (Trf), 2-acetyloxy-4-trifluoromethyl benzoic acid, is defined as a drug practically insoluble in water by the European Pharmacopoeia and with an estimated log P (log octanol/water partition coefficient) of 2.09.[40] Triflusal is an antiplatelet agent that irreversibly acetylates cyclooxygenase isoform 1 and, therefore, inhibits thromboxane biosynthesis.[41] The main metabolite of Trf is the 2-hydroxy-4-trifluoromethyl benzoic acid (HTB) that also possesses anti-aggregation activity. Trf has a structural analogy to aspirin, with a trifluoromethyl group in the C_4 position of the aromatic ring. Although both drugs are widely used, Trf has less risk of producing hemorrhagic complications due to its lower acidic nature (**Figure 3.11a** and **Figure 3.11b**). At the same time, care must be taken to ensure that the drug does not extensively hydrolyze before it can be absorbed. Therefore, the pharmaceutical industry is promoting the development of alternative forms of Trf administration trying to overcome two main problems: its low solubility and its high instability at alkaline pH. The use of micelles in the pharmaceutical formulae has been the most investigated approach to enhance Trf water dissolution and to protect the active agent from degradation by alkaline hydrolysis.[42] Moreover, the use of a polymeric delivery system based on a copolymer of an acrylic derivative of triflusal has been commercialized.[43] Here, nanoporous silica-based carriers are introduced as a proposal to substitute the commonly used organic systems.
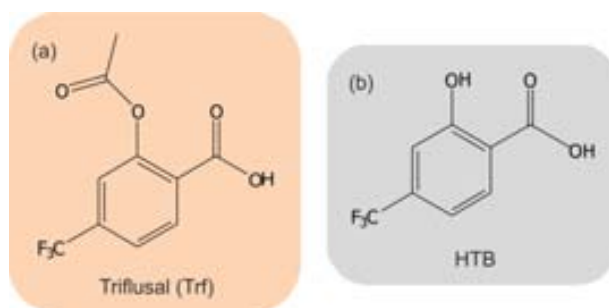
Figure 3.11. Chemical structures of: (a) 2-acetyloxy-4-trifluoromethyl benzoic acid (Trf), and (b) 2-hydroxy-4-trifluoromethyl benzoic acid (HTB).

3.2.2. Method of drug impregnation

The silica matrices were first dehydrated by heating them in a tubular oven (Carbolite 3216) at 300 °C (particulate systems) and 100 °C (AM) for 2 h under a flow of nitrogen. This step was supposed to guarantee the availability of the total surface area by desorbing the whole amount of water.

Impregnation process in $scCO_2$ was performed in the high pressure equipment presented in **Figure 3.12a**. Experiments were carried out in the batch mode. The autoclave (100 mL) was charged with Triflusal (kindly donated by Uriach S.A.) and the matrix in a weight ratio of *ca.* 1:2. The aerogel monolith was micronized in pieces between 2 and 5 mm. Each matrix was then separately wrapped with a 0.45 µm pore filter paper, and placed inside the reactor maintaining a physical separation from the drug of 2-3 cm. In order to get this separation, a cylindrical steel grid was used from which the paper-wrapped matrices were hanged (**Figure 3.12b**). The reactor was then filled with pressurized CO_2 up to 200 bar and heated at 45 °C. These conditions were previously found as the most appropriate ones for the drug dissolution.[44]

In all the experiments, the amount of commercial Trf was added in excess ensuring saturation of the $scCO_2$ phase. In a typical run, the autoclave was magnetically stirred at 300 rpm during 6 h for the silica matrices and 24 h for the PMMA. PMMA was purchased from Bonar Polymers (UK) with a molecular weight of ~ 350,000 g/mol in the form of beads of 0.5-1 µm in diameter. Experiments performed at longer running times did not lead to higher load of Trf, indicating that maximum loading was likely reached under chosen working conditions. Nonporous PMMA needed longer reaction time to induce the swelling previous to impregnation. For silica samples, pressurization and depressurization were carried out slowly and stepwise to avoid the formation of liquid CO_2 in the autoclave, which could damage their fragile porous aerogel structure. This impregnation methodology is reproducible and it has been demonstrated by repeating the experiments at least three times and obtaining similar results. Moreover, it allows the impregnation of various materials at the same time, in our case Trf was encapsulated in all the silica aerogel-like matrices in the same experiment. The resulting materials from the impregnation of the AP_{Fe}, AP, AM and PMMA matrices are labeled as *Trf@AP$_{Fe}$*, *Trf@AP*, *Trf@AM* and *Trf@PMMA* respectively.
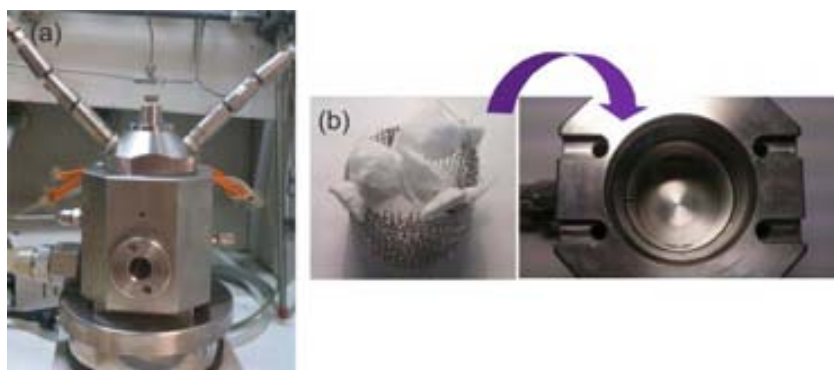
Figure 3.12. Equipment for the impregnation of matrices with drugs: (a) 100 mL autoclave, and (b) silica samples wrapped in paper bags hanged from a steel grid.

3.2.3. Results and discussion

Table 3.2 shows different characteristics of the studied matrices. Inorganic SiO_2 matrices have an inherent pore volume available to be loaded. AM has the largest surface area (*ca.* 430 m^2/g) and pore volume and mean pore size (0.75 cm^3/g and 6.8 nm respectively). AP_{Fe} and AP have intraparticle pore sizes near 2 nm which are comparable to that of the size of the studied drug, with a total pore volume around 0.1 cm^3/g and S_{BET} values of 160-200 m^2/g. For nonporous PMMA, impregnation must be preceded by polymer swelling. Contrasting to acetyl salicylic acid, the presence of an additional hydrophobic trifluoromethyl group in the Trf molecule renders a pronounced effect in the interaction of Trf with scCO$_2$ and thus on its solubility. The Trf solubility in this solvent at the working temperature and pressure was found to be in the order of $3 \cdot 10^{-2}$ mole fraction, a relatively high value for a scCO$_2$/solute system.[45] Trf molecules most likely stabilize forming dimmers in both crystalline and solution states, as determined by comparison with other structurally similar carboxylic acid compounds.[44,46,47,48,49] On the other hand, HTB tends to form intramolecular H-bonds (see **Figure 3.13**).

Table 3.2. Characteristics of the matrices and drug load impregnation values by HPLC.

Matrix	AP_{Fe}	AP	AM	PMMA
Φ_{TEM} (nm)	65	303	-	500-1000
Polydispersity in size (%)	19	9	-	20
S_{BET} (m^2/g)	160	205	430	0.07
Mean V_{pore} (cm^3/g)	0.1	0.1	0.7	-
Mean pore size (nm)	-	-	6.8	-
Pore size$_{intraptle.}$ (nm)	1.8	1.7	-	-
Drug loading (%)	4.1	3.3	17	16
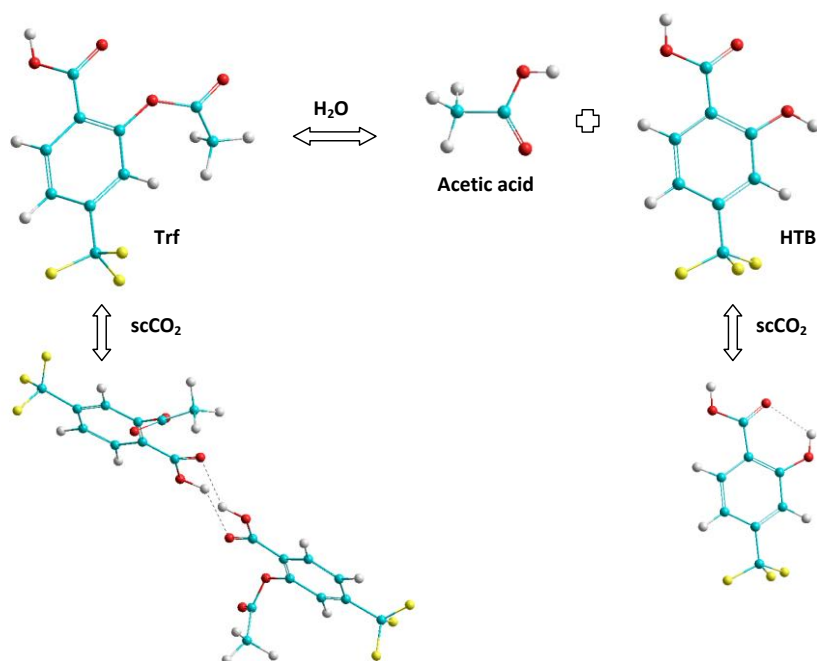
Figure 3.13. Proposed 3D-comformations of Trf and HTB metabolite and equilibrium conformations via H-bonds of the molecules dissolved in scCO$_2$.

3.2.3.1. Drug loading in the drug impregnated materials

High performance liquid chromatography (HPLC)

The percentage of drug loaded in each matrix was determined by following a HPLC procedure. Accurately weighed samples of 3-5 mg were treated with 50 mL of either acetone (99.5 wt%, Fluka) for PMMA or 20 mL of ultrapure water (Millipore, Milfdford, MA, USA) for aerogel-like systems. These last ones were also submitted to magnetic stirring at 150 rpm during 2 h. Those treatments were expected to completely extract and dissolve the drug contained in the matrices. In the case of the hydrophobic polymer, the solvent was evaporated under a nitrogen flow and the dry residue was re-dissolved in 20 mL of mobile phase, which consisted of 25 mM acetic acid/acetate aqueous solution (pH = 5)/MeOH in a volume ratio of 40/60. Acetic acetate and ammonium acetate were used to prepare the aqueous phase (Merck, a.r.). MeOH (HPLC-grade) was purchased from Merck. 20 µL of the resulting solution for each material were injected into the chromatograph at a flow rate of 1 mL/min. Since both Trf and HTB resulted in separated peaks with different retention times (**Figure 3.14**), the HPLC method was also used to evaluate the progress of Trf hydrolisis. Both species were spectrophotometrically detected at 280 nm. The stationary phase where the components separated was a Synergy Hydro-RP C18 column from Phenomenex (150 mm x 4.6 mm i.d. particles size 4 µm, 80 Å). In all cases, three independent replicates were carried out and the following mean values were obtained: 4.1 ± 0.2, 3.3 ± 0.2, 17 ± 2 and 16 ± 1 wt% for samples Trf@AP$_{Fe}$, Trf@AP, Trf@AM and Trf@PMMA, respectively. To calculate the amount of impregnated drug both the Trf and the HTB contributions were

considered. For the silica matrices, drug load could be correlated with the pore volume available (**Table 3.2**). AM matrix had the highest value of pore volume and size (in the mesopore zone), and, thus, the highest impregnation capacity. AP_{Fe} and AP samples had similar values of mean pore volume and intraparticle micropore sizes, leading in similar drug payloads although slightly higher for the composite nanospheres.

3.2.3.2. Drug stability in the drug impregnated materials

In this study we were interested in analyzing not only drug loading, but also drug stability. Therefore, the amounts of Trf and HTB were evaluated separately by chromatographically monitoring the decomposition of Trf in water and in 10 mM HCl (pH = 2.0) and 10 mM $Na_2HPO_4/NaH_2PO_4 \cdot 2H_2O$ (pH = 7.4) solutions. Such conditions simulated the pH-conditions of either stomach or blood plasma, respectively. Hydrochloric acid (37 wt%) was purchased from Merck. Dibasic sodium phosphate (Na_2HPO_4) and dihydrated monobasic sodium phosphate ($NaH_2PO_4 \cdot 2H_2O$) were acquired from Merck (a.r.). Ultrapure water was used for the preparation of all the solutions.

As shown in **Figure 3.15a**, Trf hydrolysis was faster in water and basic media than in acid medium. In water and at pH = 7.4, the degradation of Trf to HTB was completed in 10 days, while for acid solutions the process lasted for 1 month. The transformation into HTB of impregnated Trf for the different matrices was studied after 6 months of samples preparation. Samples were stored under ambient conditions (21 °C and 60-65% relative humidity). The percentage of both species was calculated from the corresponding chromatographic peaks at the initial stages of the release. Those values were considered to mirror the degree of hydrolysis of the encapsulated drug, and were related to the percentage of drug degradation during preparation and storage. As **Figure 3.15b** shows, the hydrolysis degree ranged from *ca.* 18% in Trf@AM to more than 50% in Trf@PMMA. Intermediate values of approximately 30% were found for Trf@AP_{Fe} and Trf@AP. It is noteworthy that the highest value of HTB among the prepared drug delivery system was found for the most hydrophobic matrix, the PMMA, being Trf better preserved inside the hydrophilic aerogel-like matrices. This behavior was attributed to the acidity provided to the adsorbed water by the SiO_2 system, which in turn stabilized Trf molecules against hydrolysis. Trf is a drug with a relatively high stability in acid media.[49] After impregnation, the PMMA matrix would have an internal porosity induced by CO_2 swelling.[45] This feature allowed the incorporation of neutral water to the matrix, which led to a high hydrolysis degree of the Trf drug. Hence, for those drugs susceptible of hydrolysis, the use of aerogel matrices as drug delivery carriers have the additional advantage of contributing more efficiently to drug preservation than when using hydrophobic polymeric microparticles. Comparing Trf stability in the three silica matrices, it was found that the mesoporous aerogel monolith was more effective than the microporous particles. We argue that this finding could be related to two different geometrical conformations adopted by the Trf molecule inside of the pores, as explained later in the structural analysis.
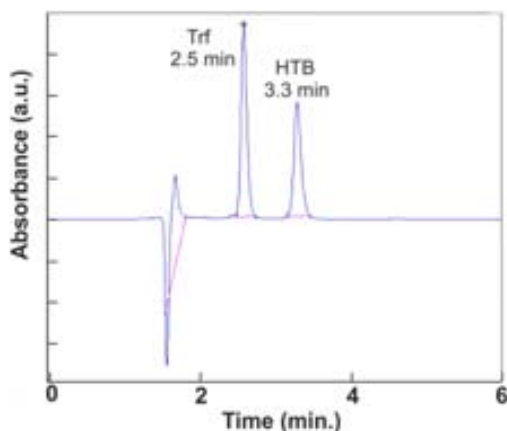
Figure 3.14. Representative chromatogram of a raw Trf sample in aqueous medium. The retention times for both Trf and HTB at the used chromatographic conditions are shown.
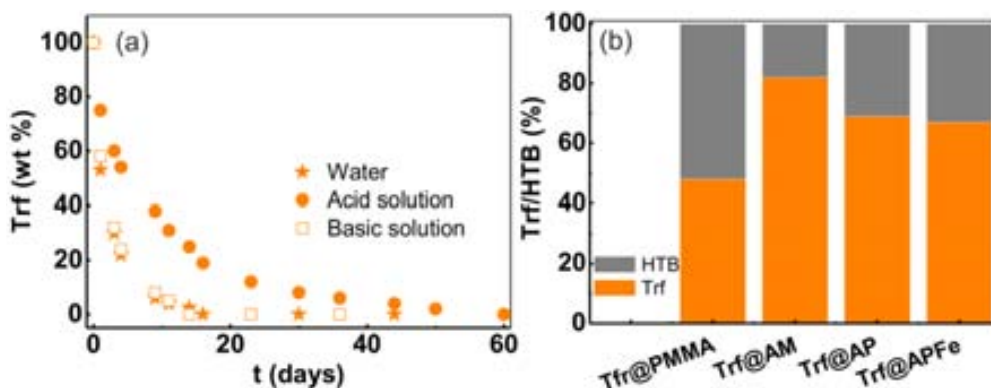
Figure 3.15. Hydrolysis of triflusal: (a) time evolution of Trf crystals dissolved in aqueous solutions (pH = 7), 10 mM HCl (pH = 2) and 10 mM $Na_2HPO_4/NaH_2PO_4 \cdot 2H_2O$ (pH = 7.4), and (b) percentage of Trf and HTB inside the studied matrices after 6 months of storage (21 ºC and 60-65% relative humidity).

3.2.3.3. Structural analysis of the drug impregnated materials

Fourier transformed infrared spectroscopy (FTIR)

The presence of the drug and the chemical interactions with the host matrices were monitored by FTIR spectroscopy. **Figure 3.16** depicts the spectra of the raw Trf and HTB and of the impregnated materials in the useful region of solid Trf (1800-1500 cm^{-1}). The spectra of the silica matrices can be found in **Chapter 2**. The spectrum of triflusal contains a band at *ca.* 1510 cm^{-1} corresponding to the benzene ring, and two bands at 1770 (band **1**) and 1685 cm^{-1} (band **2**) that belong to the carbonyls (C=O) **(Figure 3.13)**. This second band is shifted to lower wavenumbers in Trf crystals than the regular carbonyl range, 1730-1740 cm^{-1}, due to both conjugation with C=C in the attached benzene ring and Trf-Trf dimmer formation with the consequent weakening of the C=O bond. The main characteristic peak of HTB is associated to the carbonyl group and appears at 1671 cm^{-1}. The presence of Trf in the impregnated matrices was checked by the band **1** (1770 cm^{-1}) in **Figure 3.16**. This signal was more evident in Trf@PMMA and Trf@AM samples than in the particulate systems, thus indicating the higher loads achieved in the first cases. For

Trf@AM, the 1770 cm^{-1} band appears together with an additional carbonyl mode at 1752 cm^{-1} (band **4**) that is attributed to carboxylic acid species formed via cleavage of the ester and decomposition of Trf into HTB (see **Figure 3.13**). In Trf@PMMA, the band **4** is imbibed by the C=O band of the ester in the polymer. In both samples, the C=O band **1** at 1770 cm^{-1} is not shifted between the crystalline and impregnated forms of Trf, indicating an equivalent structure. However, the C=O band **2** at 1685 cm^{-1} in the crystalline Trf was shifted to the high wavenumber region of 1700-1720 cm^{-1} (band **3**) in PMMA and AM impregnated matrices. This indicated breakage of the self association in Trf molecules and formation of H-bonding with the ester or OH groups existing in PMMA or SiO$_2$ matrices, respectively. Amorphous silica particles present a large number of silanol groups on their surfaces, which may be able to form hydrogen bonds with carboxylic groups of drug molecules. It has been suggested the formation of a six-membered hydrogen bonding intermediate through the reaction of OH in the SiO$_2$ with carboxylic acid containing compounds via adsorbed H$_2$O.[46] The intermediate can transform to a carboxylate (COO$^-$) ion by transference of the acidic H. However, carboxylate peaks at *ca.* 1580-1590 cm^{-1} did not appear in any of the impregnated materials, thus suggesting that the acid-base reaction between OH in SiO$_2$ and the carbonyl acid of the drug did not take place. In the particulate materials neither the formation of H-bonds with the surface nor the carboxylate salt was observed by FTIR. In sample Trf@AP$_{Fe}$, the shift on the C=O band **2** was not detectable, indicating that Trf molecules were likely placed in the pores in a similar conformation that in the solid crystal, *i.e.*, forming dimmers. Bands for Trf@AP were not defined enough to be well analyzed due to low loading.
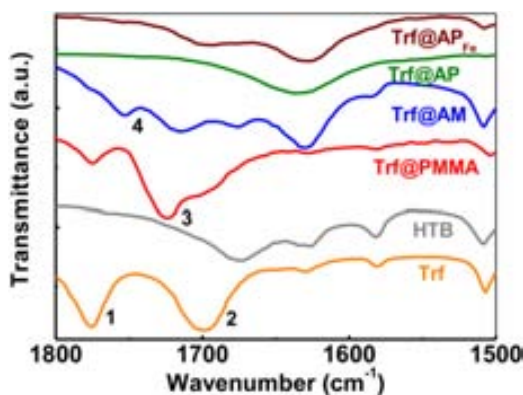
Figure 3.16. Infrared spectra of the impregnated matrices, and Trf and HTB crystals. The different C=O bands are identified as **1** (C=O of the ester in the Trf molecule), **2** (C=O of the carboxylic group in the Trf molecule), **3** (C=O of the ester group in the PMMA matrix), and 4 (C=O of the carboxylic group of the acetic acid).

X-Ray diffraction (XRD)

XRD was used to assess the occurrence or the absence of a crystalline arrangement for the impregnated drug. The aerogel monolith sample was analyzed by microdiffraction. **Figure** 3.17 presents the recorded spectra. Non-encapsulated Trf could be readily identified by its two most intense peaks at 2θ = 19 and 26º, while HTB displayed two intense peaks at 2θ = 17 and 24º

(**Figure 3.17a**). XRD patterns of the impregnated matrices did not show diffraction peaks of the Trf (or HTB) crystalline form, in which only the amorphous broad bands of PMMA (2θ = 10-30º) and silica (centered at 2θ = 22º) and the characteristics (2 2 0) and (3 1 1) peaks of magnetite at 2θ = 30 and 36º were clearly observed in **Figure** 3.17**b**. This indicates that the drug did not crystallize during the supercritical processing, an especially relevant result for the potential bioapplications of these hybrid materials.
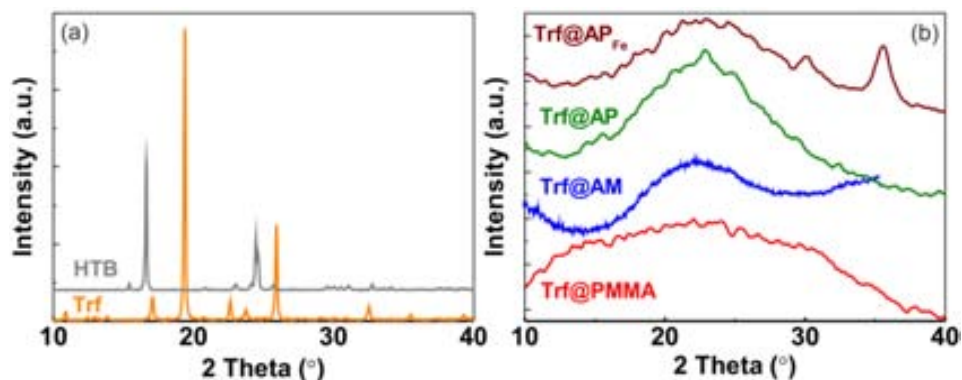
Figure 3.17. X-ray diffractograms of: (a) the therapeutic agent and its metabolite and (b) the impregnated matrices.

Differential scanning calorimetry (DSC)

DSC analysis was complementarily used to further confirm the desirable absence of drug crystals. Around 5-10 mg of the samples were accurately weighed and heated from room temperature to 180 ºC for the crystalline Trf and to 300 ºC for the impregnated matrices in a differential scanning calorimeter. Raw triflusal has a melting point of 118 ºC. The glass transition of the PMMA appears at around 125 ºC. Within the studied temperature interval (up to 450 ºC), thermal transitions are inexistent for silica matrices. The melting peak of Trf was not observed in any of the four samples. As an example, **Figure 3.18a** and **Figure 3.18b** show the DSC curves of Trf@PMMA and Trf@AM, which corresponds to samples loaded with the highest drug percentages (*ca.* 16-17 wt%).
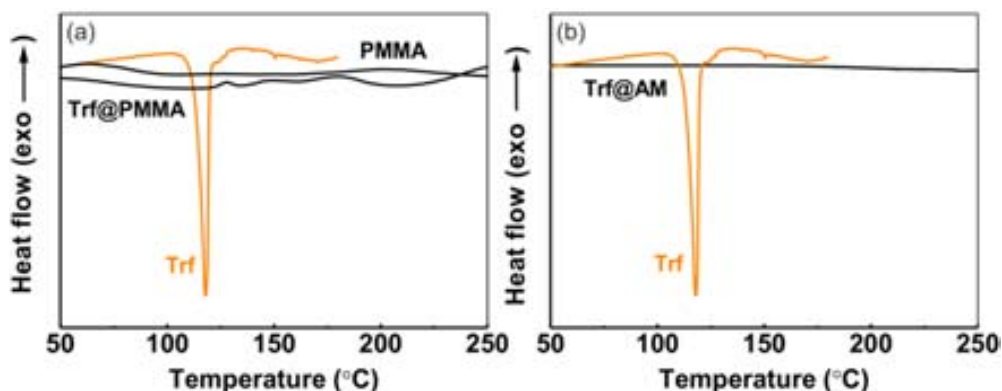
Figure 3.18. Differential scanning calorimetry thermographs of Trf crystals and impregnated: (a) PMMA, and (b) AM matrices.

Thus, XRD and DSC results indicated that Trf was most likely dispersed inside the matrices at a molecular level.

3.2.3.4. Proposed conformation of triflusal molecules in the silica-based matrices

The differences in the molecular conformation of drug impregnated molecules for monolithic or particulate aerogel matrices could be related to their different pore size (**Table 3.2**). For AM, the formation of hydrogen bonding between the matrix and the drug did not have any esteric impediment, since most of the pores were between 5 and 50 nm and the length of the Trf molecule in this configuration is of ~ 1.13 nm. On the other hand, steric impediments and polar repulsions, caused by close contact between the hydrophobic CF_3 group in the Trf and the hydrophilic adsorbed water on SiO_2 pore walls, are expected in the small pores of AP_{Fe} and AP. Consequently, impregnation in the form of dimmers was likely favored (**Figure 3.19**). Moreover, hydrogen bonding of Trf molecules with the surface of AM stabilizes the drug against hydrolysis more efficiently than the dimmers occurring in the aerogel-like particles, obtaining a higher degree of hydrolysis in the impregnated AP_{Fe} and AP (see **Figure 3.15b**).
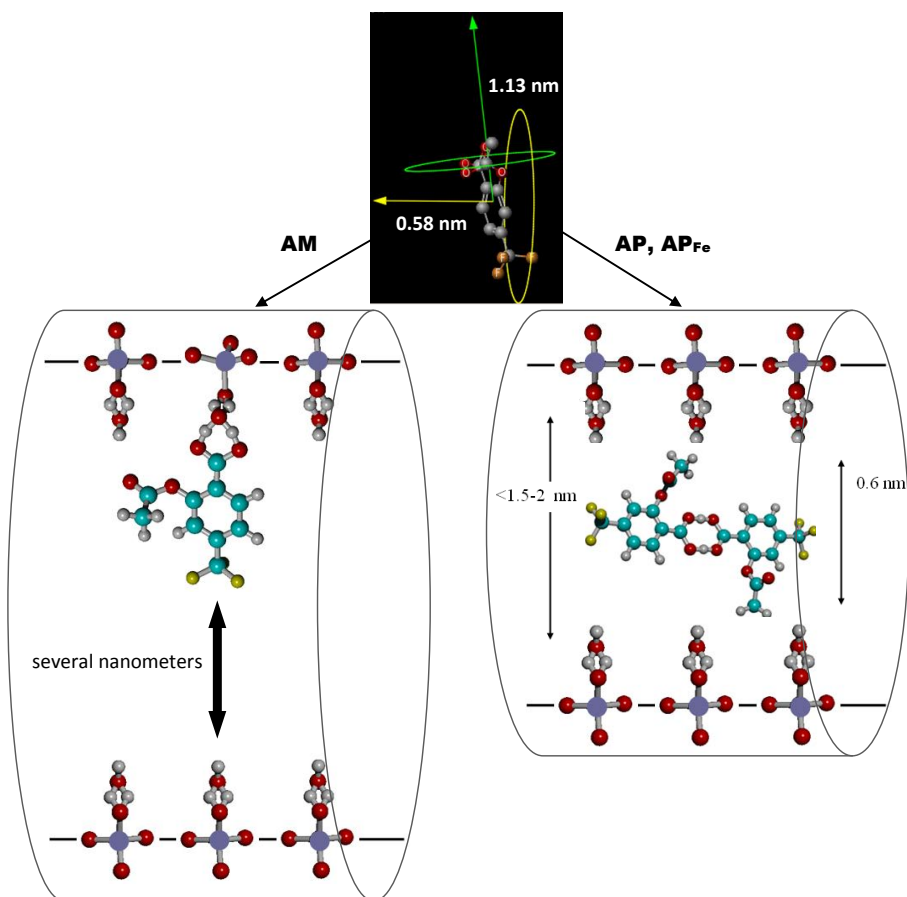
Figure 3.19. Proposed conformations of triflusal molecules inside the aerogel pores (AM) forming H-bonds with the water adsorbed at the pore surface and triflusal molecules forming dimmers inside the smaller pores of the particles (AP, AP_{Fe}). Simulations were performed with the HyperChem 8.03 software.

The Van der Waals-surface-bounded molecular volume of triflusal was calculated using QSAR (quantitative structure-activity relationship) module together with Hyperchem 8.03 program.[50] The calculated volume of the Trf molecule was 619 Å^3, while the volume of the dimmer was 1138 Å^3. Thus, the occupied pore volume by Trf molecules is the 40-50% of the total mesopore volume in the aerogel (**Table 3.2**). However, the molecular Van der Waals volume only counts the volume occupied by single molecules, without considering molecular packing or conformational structures. Similarly, using a value of 60 Å^2 for the area occupied by an adsorbed Trf molecule, the covered surface was estimated to be around 300 m^2/g that means more than 50% of the BET surface area in the pristine matrix, indicating the formation of an adsorbed monolayer of Trf. During the adsorption process, a monolayer of the adsorbate with liquid-like density is formed. As a result, these molecules present mobility and their conformation change, being the real volume occupied by each Trf molecule higher than the estimated Van der Waals value. Hence, the empty mesopore volume after impregnation could be even smaller than the calculated 50-60%. Total coverage was not achieved because the pore size distribution also plays an important role in adsorption. It has been demonstrated that this phenomena occurs more efficiently in large mesopores than in the smaller ones due to better diffusion and less steric impediments.[51] It should be taken into account that smaller pores contribute more largely to surface area. Hence, and since crystallization was avoided, it is likely that the maximum possible loading was achieved. Indeed, by modifying processing conditions, such as pressure or reaction time, the achieved loading was not varied.

3.2.3.5. Drug release profiles

High performance liquid chromatography (HPLC)

Release kinetics were followed under gastric (pH = 2) and plasmatic (pH = 7.4) pH-conditions. In these experiments, a given amount of sample (~ 5 mg) was placed in each vessel containing 25 mL (AP_{Fe} sample), 12.5 mL (AP sample) and 100 mL (AM and PMMA samples) of 10 mM HCl (pH = 2) or 10 mM $Na_2HPO_4/NaH_2PO_4 \cdot 2H_2O$ (pH = 7.4) solutions. Stirring rate was fixed at 60 rpm and temperature at 37 ºC. The kinetic curves were monitored chromatographically to obtain the corresponding delivery profiles. The experiments were repeated three times for silica matrices and an error range was obtained from the standard deviation in each case. **Table 3.3** shows the drug release data of the studied matrices. Drug dissolution profiles, involving both Trf and HTB contributions, at acid pH of the impregnated matrices are shown in **Figure 3.20a**. For silica aerogel spheres (Trf@AP), the drug release occurred almost instantaneously and the 97 wt% of the drug was dissolved completely in 1 min. The behavior of Trf@AP_{Fe} was very similar to that of the Trf@AP, being the 90 wt% of Trf + HTB released in the first minute. The drug delivery profile of the monolithic aerogel Trf@AM was different, around 70 wt% of the drug was dissolved during the first 5 min and a progressive release of the remaining 30 wt% occurred during the next 2 h. Reasons of prolonged released could be related to both the different conformation of the drug inside the pores (**Figure 3.19**) and to the longer diffusion channels that the molecules

follow to reach the bulk solution in the monolithic aerogels. The slowest release kinetics was obtained with the impregnated PMMA. In this case, the delivery of Trf from the sample to gastric-pH medium lasted several days having only the 18 wt% released in the first 60 min. Slightly slower dissolution rates were measured in experiments performed at pH 7.4 (**Figure 3.20b**), but the same general tendency as in acid solutions was observed. Particulate materials have the 56 wt% and 77 w% of the drug delivered in the first minute and the 69 wt% and 87 wt% in 30 min (for Trf@AP and Trf@AP$_{Fe}$, respectively). The monolith Trf@AM showed a similar release profile with the 32 wt% of the drug delivered in 1 min. The fast drug release observed when the materials were submerged in acid solution is explained by a favored hydrolysis of the ester group when a high concentration of H$^+$ is present. Once more, for sample Trf@PMMA a sustained release lasting more than 1 month was observed (only the 4.5 wt% of the drug is discharged after 60 min) and almost instantaneous release for the rest of the samples.
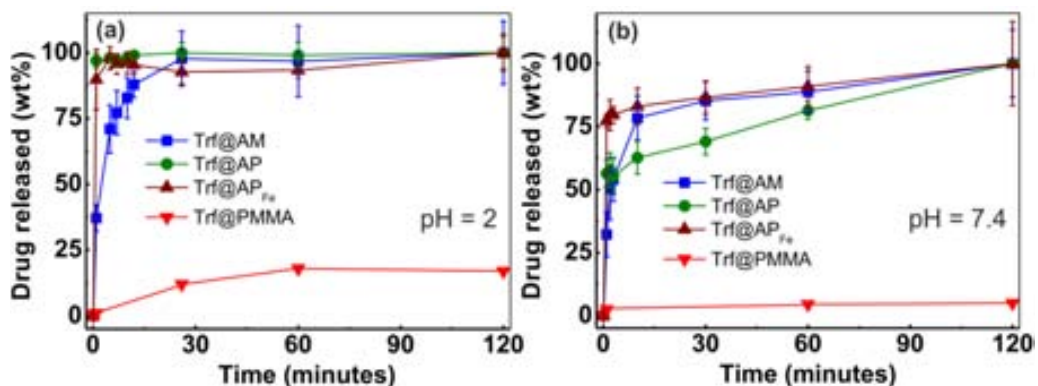
Figure 3.20. Overall drug release profiles (Trf + HTB) obtained for the investigated materials at the two studied conditions: (a) acid pH, and (b) basic Ph. Error bars correspond to the standard deviation of three replicates. Solid lines are included as a guide to the eye.

Table 3.3. Drug release in the impregnated matrices obtained by HPLC in acidic and basic aqueous media.

Sample	Medium pH	Drug release (± 5 wt%)				
		1 min.	5 min.	30 min.	60 min.	120 min.
Trf@AP	2	97	98	99	99	100
Trf@AP$_{Fe}$		90	98	93	93	100
Trf@AM		37	70	98	96	100
Trf@PMMA		1.0	3.0	13	18	18
Trf@AP	7.4	56	58	69	81	100
Trf@AP$_{Fe}$		77	81	87	91	100
Trf@AM		32	61	85	89	100
Trf@PMMA		2.5	3.0	3.0	4.5	5.0

The release behavior of the drug in the silica matrices attends to the phenomenon typically referred as "burst effect", which consists on an initial release of the drug to the concomitant medium just upon placement in it, before the release reaches a stable profile. Although this

situation has been identified as a limitation to create long-term controlled release devices, this rapid delivery at the initial stage may be desirable in several cases. For instance, in the treatment of wounds or applied to triggered and pulsatile releases.[52] During this thesis, some effort has been made to understand the Trf + HTB release mechanism from the silica-based materials. In particular, the experimental data has been fitted to different mathematical models describing the physical phenomena which govern the process. Those models are explained in **Chapter 4**.

3.3. CONCLUSIONS

The combination of inorganic nanoporous host and functional organic molecules render hybrid materials with enhanced properties towards different applications. Encapsulation within the matrices by dissolving, and in some cases also synthesizing, the substances of interest in supercritical carbon dioxide opens interesting possibilities for materials processing. From a general point of view, $scCO_2$ technology can be used for upscaling the production of complex high purity nanoproducts at a reasonable cost and with positive green chemistry implications. Here, we have successfully synthesized and impregnated photoactive cations and a model drug in silica-based matrices (**Chapter 2**) by $scCO_2$, yielding hybrid nanocomposite materials with good stability. Those systems were designed to be applied in photocatalysis and drug delivery and they were compared with more conventional materials used in these fields, such as zeolites and polymeric PMMA matrices respectively:

- Pyrylyum and trytil cations entrapped in silica materials (aerogel monolith and aerogel-like particles) and in zeolites present high photostability and a favorable polar environment for photoinduced electron transfer. Moreover, the high surface area and adsorbent capacity provided by the mesopores in the AM are expected to increase the efficiency of light activated processes. Cations supported in the mesoporous aerogel underwent some initial hydrolysis, while when encapsulated into the microporous zeolite, were totally stable. However, this transparent matrix enhances their intrinsic photocatalytic activity due to the absence of both solvent and light diffusion restrictions. On the other hand, the accessibility of organics to be oxidized to the encapsulated photocatalyst may be difficult in microporous zeolite matrices.

- Triflusal, an antithrombotic agent, was chosen as a model compound to be impregnated in both hydrophobic PMMA beads and hydrophilic SiO_2-based materials (magnetic aerogel-like nanospheres, sub-micron arogel-like particles and aerogel monoliths). The $scCO_2$ loading procedure allowed a homogeneous impregnation of the drug inside of the matrices in percentages of the order of 16 wt% for PMMA and aerogel monolith and 3-4 wt% for particles. The drug was distributed at a molecular level and no crystals or amorphous forms of the drug were detected. Carboxylic H-bonding was determined to be the most feasible conformation for triflusal adsorbed in PMMA and aerogel monolith matrices. In contrast, due to steric reasons dimmer was the most likely conformation of the Trf molecules inside the aerogel particles. An *in vitro* release study in aqueous media demonstrated a sustained

release lasting for several days in Trf@PMMA, in which the induction of polymer swelling was required previous to drug dissolution. On the contrary, the experiments for aerogel matrices showed that more than 80 wt% of triflusal was dissolved within the first minutes. Although these systems could not be used for prolonged release, they could be highly attractive for enhancing the bioavailability of poorly water-soluble drugs in intravenous or gastric conditions. The molecular dispersion of Trf in the SiO_2 aerogel-like matrices was relatively stable against hydrolysis for at least six months when stored under ambient conditions while when entrapped in PMMA gradually changed to the HTB metabolite.

3.4.　REFERENCES

[1] Di Nunzio, M.R., Agostoni, V., Cohen, B., Gref, R., Douhal, A. A "Ship in a Bottle" Strategy to load a hydrophilic anticancer drug in porous metal organic framework nanoparticles: efficient encapsulation, matrix stabilization, and photodelivery. *J. Med. Chem.*, **2014**, *57*, 411–420.

[2] Jarvis, K.L., Barnes, T.J., Prestidge, C.A. Surface chemistry of porous silicon and implications for drug encapsulation and delivery applications. *Adv. Colloid Interface Sci.*, **2012**, *175*, 25-38.

[3] Zoua, X., Wonga, K.-L., Thomasa, S., Metzgerc, T.H., Valtcheva, V., Mintova, S. Platinum clusters confined in FAU–LTA hierarchical porous composite with a core-shell structure. *Catal. Today*, **2011**, *168*, 140-146.

[4] Shulz-Ekloff, G., Wöhrle, D., Van Duffel, B., Schoonheydt, R.A. Chromophores in porous silicas and minerals: preparation and optical properties. Microporous *Mesoporous Mater.*, **2002**, *51*, 91-138.

[5] García, O., Sastre, R., Del Agua, D., Costela, A., García-Moreno, I., Roig, A. Efficient optical materials based on fluorinated-polymeric silica aerogels. *Chem. Phys. Lett.*, **2006**, *427*, 375-378.

[6] Plata, D.L., Briones, Y.J., Wolfe, R.L., Carroll, M.K., Bakrania, S.D., Mandel, S.G., Anderson, A.M. Aerogel-platform optical sensors for oxygen gas. *J. Non-Cryst. Solids*, **2004**, *350*, 326-335.

[7] Corma, A., Garcia, H., Sastre, G., Viruela, P.M. Activation of molecules in confined spaces: an approach to zeolite-guest supramolecular systems. *J. Phys. Chem. B*, **1997**, *101*, 4575-4582.

[8] Dutta, P.K., Kim, Y. Photochemical processes in zeolites: new developments. *Curr. Opin. Solid State Mater. Sci.*, **2003**, *7*, 483-490.

[9] Corma, A., Garcia, H. Zeolite-based photocatalysts. *Chem. Commun.*, **2004**, 1443-1459.

[10] Corma, A., Fornés, V., García, H., Miranda, M.A., Sabater, M. Highly efficient photoinduced electron transfer with 2,4,6-triphenylpyrylium cation incorporated inside extra large pore zeotype. MCM-41 *J. Am. Chem. Soc.*, **1994**, *116*, 9767-9768.

[11] López-Periago, A.M., Fraile, J., García-González, C.A., Domingo, C. Impregnation of a triphenylpyrylium cation into zeolite cavities using supercritical CO$_2$. *J. Supercrit. Fluids*, **2009**, *50*, 305-312.

[12] López-Periago, A.M., García-González, C.A., Saurina, J., Domingo, C. Preparation of trityl cations in faujasite micropores through supercritical CO$_2$ impregnation. *Microporous Mesoporous Mater.*, **2010**, *132*, 357-362.

[13] Sanjuán, A., Aguirre, G., Alvaro, M., García, H. 2,4,6_Triphenylpyrylium ion encapsulated in Y zeolite as photocatalyst. A co-operative contribution of the zeolite host to the photodegradation of 4-chlorophenoxyacetic acid using solar light. *Appl. Catal. B*, **1998**, *15*, 247-257.

[14] Miranda, M.A., Garcia, H. 2,4,6-Triphenylpyrylium Tetrafluoroborate as an electron-transfer photosensitizer *Chem. Rev.*, **1994**, *94*, 1063-1089.

[15] Williams, A. The hydrolysis of pyrylium salts. Kinetic evidence for hemiacetal intermediates. *J. Am. Chem. Soc.*, **1971**, *93*, 2733-2737.

[16] Toncheva, V.D., Velichkova, R.S. Photostability of trityl salts with different anions under argon. *Makromol. Chem.*, **1983**, *184*, 2231-2239.

[17] Kharchenko, V.G., Pchelintseva, N.V. Unsaturated 1,5-diketones and their halogen-substituted derivatives-Preparation and use in the synthesis of heterocycles. *Chem. Heterocycl. Compd.*, **1996**, *32*, 1113-1130.

[18] Lercher, J.A., Jentys, A. in *Handbook of Porous Solids*, ed. F. Schüth, K. Sing and J. Weitkamp, Wiley-VCH, Weinheim, **2002**, *vol. 2*, ch. 4, pp. 1097.

[19] Saunders, R.M., Schwarz, H.P., Stewart, J.C. Spectrophotometric assay of the triphenylmethyl group. *Anal. Chem.*, **1967**, *39*, 550-551.

[20] Shchepinov, M.S., Korshun, V.A. Recent applications of bifunctional trityl groups. *Chem. Soc. Rev.*, **2003**, *32*, 170-180.

[21] Infrared Spectra of Adsorbed Molecules, ed. L. H. Little, Willmer Brothers, Ltd. New York, **1996**.

[22] Eide, O.K., Ystenes, M., Stovneng, J.A., Eilertsen, J.L. Investigation of ion pair formation in the triphenylmethyl chloride–trimethyl aluminium system, as a model for the activation of olefin polymerization catalyst *Vib. Spectrosc.*, **2007**, *43*, 210-216.

[23] Chen, Y., Wu, S.K. A study of the photophysical properties of 2,4,6-triphenyl pyrylium salts with rigid and non-rigid structures. *J. Photochem. Photobiol. A*, **1997**, *102*, 203-206.

[24] Atienzar, P., Corma, A., García, H., Serra, J.M. High-throughput characterisation of materials by photoluminescence spectroscopy. *Chem.-Eur. J.*, **2004**, *10*, 6043-6047.

[25] Cano, M., Coznes, F.L., García, H., Martí, V., Scaiano, J.C. Intrazeolite photochemistry. 13. photophysical properties of bulky 2,4,6-triphenylpyrylium and tritylium cations within large- and extra-large-pore zeolites. *J. Phys. Chem.*, **1996**, *100*, 18152-18157.

[26] Adolph, S., Spange, S., Zimmermann, Y. Catalytic activities of various moderately strong solid acids and their correlation with surface polarity parameters. *J. Phys. Chem. B*, **2000**, *104*, 6429-6438.

[27] Fakis, M., Tsigaridas, G., Polyzos, I., Giannetas, V., Persephonis, P., Spiliopoulos, I., Mikroyannidis, J. Intensity dependent nonlinear absorption of pyrylium chromophores. *Chem. Phys. Lett.*, **2001**, *342*, 155-161.

[28] Duxbury, D.F. The photochemistry and photophysics of triphenylmethane dyes in solid and liquid media. *Chem. Rev.*, **1993**, *93*, 381-433.

[29] Miranda, M.A., Amat, A.M., Arques, A. Stability and performance of silica gel-supported triphenylpyrylium cation as heterogeneous photocatalyst. *Catal. Today*, **2002**, *76*, 113-119.

[30] Bhise, N.S., Ribas, J., Manoharana, V., Zhang, Y.S., Polini, A., Massa, S., Dokmeci, M.R., Khademhosseini, A. Organ-on-a-chip platforms for studying drug delivery systems. *J. Controlled Release*, **2014**, 190, 82-93.

[31] Torchilin, V.P. Multifunctional nanocarriers. *Adv. Drug Deliv. Rev.*, **2006**, *58*, 1532-1535.

[32] Sahoo, S.K., Labhasetwar, V. Nanotech approaches to drug delivery and imaging. *Drug Discov. Today*, **2003**, *8*, 1112-1120.

[33] Peer, D., Karp, J.M., Hong, S., Farokhzad, O.C., Margalit, R., Langer, R. Nanocarriers as an emerging platform for cancer therapy. *Nat. Nanotechnol.*, **2007**, *2*, 751-760.

[34] Lee, J.E., Lee, N., Kim, T., Kim, J., Hyeon, T. Multifunctional mesoporous silica nanocomposite nanoparticles for theranostic applications. *Acc. Chem. Res.*, **2011**, *44*, 893-902.

[35] Gupta, K., Gupta, M. Synthesis and surface engineering of iron oxide nanoparticles for biomedical applications. *Biomaterials*, **2005**, *26*, 3995-4021.

[36] Radin, S., El-Bassyouni, G., Vresilovic, E., Schepers, E., Ducheyne, P. *In vivo* tissue response to resorbable silica xerogels as controlled-release materials. *Biomaterials*, **2005**, *26*, 1043-1052.

[37] Wu, S., Lin, Y., Hung, Y., Chou, Y., Hsu, Y., Chang, C., Mou, C. Multifunctional mesoporous silica nanoparticles for intracellular labeling and animal magnetic resonance imaging studies. *ChemBioChem*, **2008**, *9*, 53-57.

[38] Qian, K.K., Bogner, R.H., Application of mesoporous silicon dioxide and silicate in oral amorphous drug delivery systems, *J. Pharm. Sci.*, **2012**, *101*, 444-463.

[39] Schutz, E. Supercritical fluids and applications-a patent review. *Chem. Eng. Technol.*, **2007**, *30*, 685-688.

[40] US Environmental Agency's EPISuiteTM v4.10.

[41] Murdoch, D., Plosker, G.L. Triflusal: a review of its use in cerebral infarction and myocardial infarction, and as thromboprophylaxis in atrial fibrillation. *Drugs*, **2006**, *66*, 671-692.

[42] Ferrit, M., Del Valle, C., Martínez, F. The study of the influence of surfactant charge on alkaline hydrolysis reactions of acetylsalicylic acid (ASA) and triflusal (TFR) using spectrophotometric methods. *Eur. J. Pharm. Sci.*, **2007**, *31*, 211-220.

[43] Rodríguez, G., Fernández-Gutiérrez, M., Parra, J., López-Bravo, A., Honduvilla, N.G., Buján, J., Molina, M., Duocastella, L., San Román, J. Bioactive polymeric systems with platelet antiaggregating activity for the coating of vascular devices. *Biomacromolecules*, **2010**, *11*, 2740-2747.

[44] Andanson, J.M., López-Periago, A., García-González, C.A., Domingo, C., Kazarian, S.G. Spectroscopic analysis of triflusal impregnated into PMMA from supercritical CO_2 solution. *Vib. Spectrosc.*, **2009**, *49*, 183-189.

[45] López-Periago, A., Argemí, A., Andanson, J.M., Fernández, V., García-González, C.A., Kazarian, S.G., Saurina, J., Domingo, C. Impregnation of a biocompatible poly-mer aided by supercritical CO_2: evaluation of drug stability and drug–matrix interactions. *J. Supercrit. Fluids*, **2008**, *48*, 56-63.

[46] Gupta, M.K., Vanwert, A., Bogner, R.H. Formation of physically stable amorphous drugs by milling with Neusilin. *J. Pharm. Sci.*, **2003**, *92*, 536-551.

[47] Domingo, C., Berends, E., Van Rosmalen, G.M. Precipitation of ultrafine organic crystals from the rapid expansion of supercritical solutions over a capillary and a frit nozzle. *J. Supercrit. Fluids*, **1997**, *10*, 39-55.

[48] Kazarian, S.G., Martirosyan, G.G. Spectroscopy of polymer/drug formulations, processed with supercritical fluids: in situ ATR-IR and Raman study of impregnation, of ibuprofen into PVP. *Int. J. Pharm.*, **2002**, *232*, 81-90.

[49] Argemi, A., Lopez-Periago, A., Domingo, C., Saurina, J. Spectroscopic and chromatographic characterization of triflusal delivery systems prepared by using supercritical impregnation technologies. *J. Pharm. Biomed. Anal.*, **2008**, *46*, 456-462.

[50] HyperChem (Molecular Modeling System), Hypercube, Inc., Gainesville, FL, USA, **2007** http://www.hyperchem.com/.

[51] I. Smirnova, S. Suttiruengwong, W. Artl. Feasibility study of hydrophilic and hydrophobic silica aerogels as drug delivery systems. *J. Non-Cryst. Solids*, **2004**, *350*, 54-60.

[52] Huang, X. Brazel, C.S. On the importance and mechanisms of burst release in matrix-controlled drug delivery systems. *J. Control. Release*, **2001**, *73*, 121-136.

4

POLYMER COATING OF SILICA-BASED PARTICLES
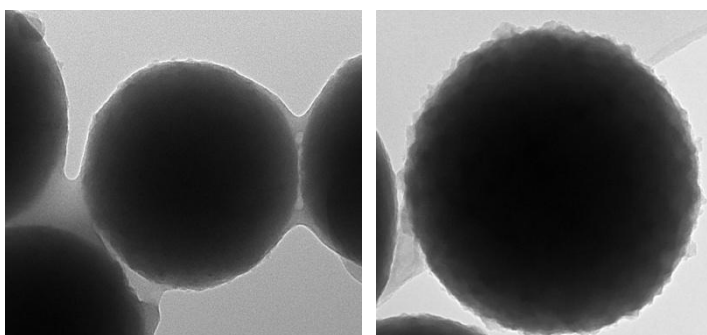
The polymer coating of silica sub-micron particles and iron oxide-silica nanospheres envisaging enhanced properties of the hybrid products for biomedical applications is tackled in this chapter. Two different biopolymers were grafted on the surface of drug-loaded silica-based particles: Eudragit® RL 100 and polyethyleneimine to sustain the drug release and to confer improved features for potential uses biomedicine, respectively. Both coatings involved the presence of compressed CO_2, which served as an antisolvent or as reaction medium and catalyst for the polymer. Employed methods and pertinent characterization showing the success of the coating processes are here presented. The morphological properties and thermal stability of the resulting materials were also studied. Moreover, *in vitro* drug delivery in aqueous media and drug stability were analyzed and the obtained results compared with those found for an organic polymeric matrix. Based on the results obtained by fitting the data to different mathematical models, a diffusion-controlled mechanism is proposed for the release of the drug in our materials.

4.1. POLYMER COATING OF PARTICLES FOR BIOMEDICINE

The coating of micro and nanoparticles with polymers is nowadays a widely used technique for powder processing in the pharmaceutical industry.[1,2] There are many different biocompatible polymers that can potentially be used in the preparation of pharmaceutical systems. They include both naturally derived and synthetic materials.[3,4,5] Natural polymers encompass hydrophilic carbohydrates (dextran, starch), hydrophilic proteins (albumin, arginylglycylaspartic acid), and hydrophobic lipids[6,7] and phospholipids.[8] Regarding synthetic polymers, the most widely used are polyethylene glycol (PEG), polyvinyl alcohol (PVA), polyethyleneimine (PEI), and poly-L-lactic acid (PLA). Fats and waxes can also be used for encapsulation. Particles modification with these polymers provides organic linkers on the surface and, thus, a wide range of surface properties to suit various processes. The most common organic linkers are amine (NH_2, NHR, NR_2), carboxylic acid (COOH), aldehyde (CHO), and thiol (SH) groups. In addition, polymer coating can modify several physicochemical characteristics of the original material, such as, hydrophilicity, appearance, mechanical strength or degradation rate. Polymer encapsulation of particles can also result in more uniform particle size distributions, smoother surfaces, and enhanced flowability. Regarding the chemical characteristics, it aids to protect unstable ingredients from external degradation factors, such as moisture, air, or light, and can enhance compatibility and wettability.

Many different techniques can be used to coat the surface of small particles, among others we can mention, dip coating, spray coating, sputtering, and layer-by-layer assembly.[9] Dip coating involves soaking the powder in a polymer solution. Spray coating comprises spraying micro-droplets of a polymer solution directly onto the particles surface. A very thin coating can be obtained by using the more recently developed layer-by-layer assembly technology, in which oppositely charged polymers and drugs can be sequentially deposited.[10] However, when using processes based on solution chemistry, individual particles coating is difficult to achieve mainly due to particles aggregation. Besides, high temperatures are commonly used to evaporate the solvents.[11,12,13] Alternatively, replacement of organic solvents with compressed CO_2 results in an environmental friendly option with a near-zero waste production.[14,15] As already mentioned in this thesis, CO_2 is an ideal processing medium, because of its relatively mild critical conditions (31.1 °C and 73.8 bar) and generally recognized as safe (GRAS) status. The applicability of compressed CO_2 to coating depends primarily on the solubility of the coating material in this fluid.[16,17] In general, compressed CO_2 has a limited solvent strength for many polymers of interest. Hence, most of the work performed in coating using compressed CO_2 has been carried out by antisolvent methods.[18,19] CO_2 antisolvent approaches have often been successfully applied to the coating of micrometric organic and inorganic particles,[20,21,22] although only in some particular cases they are used for the coating of nanometric particles. As an example, it was used for the surface modification of superparamagnetic 10-15 nm iron oxide particles.[23,24]

4.2. POLYMER COATING OF SILICA-BASED PARTICLES FOR DRUG DELIVERY

In the particular case of controlled drug delivery systems, encapsulation is used to modulate the release rate of an active pharmaceutical ingredient into the organism. Many of the commercial polymeric drug delivery carriers are adequate for the sustained release of water-soluble drugs. For low water-solubility substances, polymeric systems could also exhibit a good response but often they release the drug very slowly due to its high hydrophobicity. As an alternative, the relevance in controlled drug delivery of inorganic materials such as silica, titania, or magnetic iron oxide particles, either alone or combined with polymers in hybrid matrices, is increasing.[25,26,27] Inorganic porous particles are mostly applied to obtain an immediate drug dosage of poorly water-soluble compounds at the desired target site.

In **Chapter 3**, supercritical carbon dioxide was used to prepare impregnated drug delivery systems involving a practically water-insoluble and highly unstable at neutral and alkaline pH drug (triflusal). Those systems were based in aerogel-like silica matrices[28] (**Chapter 2**). Here, we have extended our background in the processing with supercritical and compressed CO_2 using its antisolvent power to address the precipitation of the polymer Eudragit® RL 100 on the surface of AP_{Fe} and AP particles. The particles used were either as synthesized or previously impregnated with Trf. Results showed that polymer coating of particles was achieved in both cases.

4.2.1. Eudragit® RL 100 for sustained drug release

Eudragit® RL 100 is a commercial copolymer of acrylate and methyl methacrylate with a low content of methacrylic acid ester and quaternary ammonium groups. It is hydrophobic and water insoluble, but has a relatively high permeability due to the presence of ammonium groups as salts. **Figure 4.1** shows its chemical structure. Since it presents suitable characteristics to be applied in drugs dispersions,[29,30,31] it is commonly used in the design of drug controlled-release formulations, *i.e.* for coating of tablets or in transdermal patches.[32]
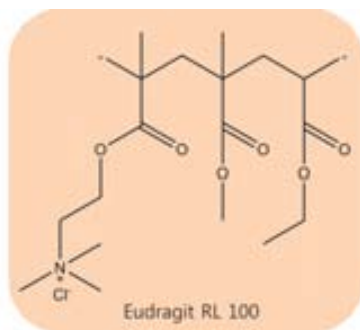
Figure 4.1. Chemical structure of Eudragit® RL 100.

The *in vitro* release studies of Trf-impregnated silica matrices demonstrated that the 80 wt% of the drug was dissolved in the media within the first minutes, while a sustained released prolonged for several days was attained in the PMMA polymeric systems. In the light of these

results, a sustained release at intermediate times was sought by coating the silica-based particles with Eudragit® RL 100. As found in release studies, the deposited coating acted as a drug-release barrier, resulting in delivery rates that were in between those attained with uncoated particles and the PMMA matrix. Moreover, drug stability in water increased in the hybrid matrices with respect to the rest of studied systems.

4.2.2. Eudragit® RL 100 coating of silica-based particles

Two experimental approaches were used for particles encapsulation in Eudragit® RL 100 depending on the particles size. Both methods were based on the precipitation of the polymer from an acetone solution when brought in contact with compressed CO_2.

The semicontinuous precipitation compressed antisolvent (PCA) technique was used to coat the smallest AP_{Fe} particles, and the batch gas antisolvent (GAS) method was employed for AP.

4.2.2.1. Semicontinuous precipitation compressed antisolvent (PCA)

A set of experiments, aiming at coating of the smallest iron oxide-silica particles (AP_{Fe}, 65 nm), was performed using the PCA semicontinuous approach. The used equipment works in a semicontinuous co-current mode, in which the CO_2 antisolvent and the liquid solution are separately fed to the top of the precipitator and are continuously discharged from the bottom. The temperature inside the chamber is controlled by heating jackets.[33] A more detailed description is provided in **Chapter 7**. In this technique, an acetone solution involving dispersed silica-based nanoparticles (previously impregnated with triflsual or not), the polymer dissolved, and in some cases triflusal was sprayed into a continuous feed of CO_2. When Trf was added to the solution, the mixture was left to soak overnight under mild conditions of stirring. The mixture was sonicated during 15 min before pumping. The high pressure autoclave was first heated at 30 ºC and filled with CO_2 at a pressure of 90 bar, and, then, the acetone suspension was sprayed into the vessel at a flow rate of 1.5-2.0 mL/min. A capillary nozzle (180 μm diameter) was used. Liquid CO_2 was continuously pumped to the vessel at a rate of 15-25 g/min during acetone injection and, afterwards, for 1 h to wash the obtained product. The coated material was recovered on a 5 μm filter overtopped by two membranes of 0.22 μm placed at the bottom of the autoclave. More than ten experiments were performed adjusting the AP_{Fe}, polymer and Trf concentrations obtaining similar results. Samples were called *Eud_Trf@AP_{Fe}* or *Eud_Trf_AP_{Fe}* for pre-impregnated and non pre-impregnated particles respectively. **Table 4.1** gathers the concentrations of the materials in the liquid phase for two representative experiments.

Table 4.1. Concentrations of AP_{Fe}, the polymer and triflusal in acetone for PCA experiments.

Sample	[AP_{Fe}] (mg/ml)	[Eudragit® RL 100] (mg/ml)	[triflusal] (mg/ml)
Eud_Trf@AP_{Fe}	4.0	8.0	-
Eud_Trf_AP_{Fe}	5.0	20	6.5

4.2.2.2. Batch gas antisolvent (GAS)

Other experiments were performed in a GAS home-made batch apparatus, consisting of a 0.5 L autoclave that at the bottom has a membrane filter of 0.22 µm placed on the top of a stainless steel frit (5 µm mesh). The setup is provided by a stirrer that plunges into the solution, thus maintaining the particles in suspension. The pumped CO_2 is dispersed into the solution through an eight turbine holes and the temperature is controlled by heating jackets[34] (see **Chapter 7** for more details). In the batch approach, compressed CO_2 was introduced into the vessel that contained the acetone suspension of 300 nm AP particles with the polymer and the drug dissolved. In a typical GAS experiment, AP and triflusal were weighed in a mass ratio of 1.0/1.4 (*ca.* 0.25 g of Trf) and mixed with 40 mL of acetone. The obtained mixture was soaked overnight under mild conditions of stirring, previous to Eudragit addition, which was done in a silica/polymer mass ratio of 1.0/0.8. The temperature of the vessel was maintained at 26 ºC during the polymer precipitation step. Compressed CO_2 was added resulting in a gradual increase of the pressure in the chamber up to 100 bar. After 1 h, the exit valve was opened, and the product was washed at 30 ºC with a fresh flow of CO_2. Two experiments were carried out in the same conditions obtaining analogous results. Samples recovered were labeled as *Eud_Trf_AP*.

4.2.3. Results and discussion

The antisolvent process is based on solute precipitation occurring when compressed CO_2 and an organic liquid phase that contains the solute come into contact.[35,36] The interdiffusion of the organic solvent and CO_2 creates conditions of solute supersaturation in the organic phase, since the newly formed CO_2-solvent mixture exhibits lower solubilization ability than that of the pure solvent. Besides the precipitation of a single specie, the formation of complex mixtures can also be carried out through CO_2 antisolvent coprecipitation of two or more solutes dissolved in the liquid phase.[37] In the process used in this work, aerogel-like particles were dispersed in a liquid solution containing the dissolved polymer. The CO_2 addition provoked the precipitation of the polymer embedding the inorganic particles and forming the hybrid products.

The used experimental conditions are shown in **Table 4.2** together with some products characteristics. The mass composition of the products was calculated by TGA in the case of the polymer and the silica-based particles and by HPLC for triflusal. Under working conditions, the yield was typically below 50 wt%, likely due to the high solubility of Trf and Eudragit in acetone. The yield was also reduced because of the nanometric size of the inorganic particles that could easily bypass the used filter at the bottom of the reactor. Moreover, Trf has a relatively high solubility in compressed and supercritical CO_2 (a mole fraction of $3 \cdot 10^{-2}$ at 200 bar and 35 ºC).[38] Experiments were performed at a temperature lower than the critical temperature of CO_2 to reduce drug solubility in the solvent mixture and to prevent polymer swelling in the liquid phase. Organic compounds solubility in CO_2 + solvent mixtures increase generally with temperature,[35,39] thus processing at low temperature reduced the risk of losing the drug by dissolution. Regarding

the mixing behavior of the solvent and CO_2, 3D simulation has shown that the mixing plume do not differ notably in the interval from 25 to 45 °C, since convection and not diffusion is the mechanism that dominates mass transfer.[35]

Batch GAS approach was applied to modify the surface of the 300 nm AP particles. The feasibility of this precipitation-on-slurry technique has been demonstrated previously for micrometric particles.[34] This approach was selected preferably to the semicontinuous PCA mode to coat the largest silica particles that are difficult to pump avoiding sedimentation. The PCA approach could be applied only for the coating of the 65 nm AP_{Fe} particles, avoiding flow instabilities and nozzle plugging occurring when pumping large particles. For the Trf pre-impregnated samples, it was observed that the drug loading was reduced after antisolvent processing, likely due to partial dissolution of the drug in both the compressed CO_2 and in the liquid phase. Trying to reduce this problem, GAS experiments were performed starting from a pristine AP sample that was soaked overnight with a solution of Trf in acetone (Eud_Trf_AP). The soaking step was thought as a way to infiltrate the drug into the silica pores.[40] Using the PCA approach, samples were prepared either directly from a triflusal pre-impregnated sample, $Trf@AP_{Fe}$, (Eud_Trf@AP_{Fe}) or by first soaking pristine AP_{Fe} nanoparticles in acetone with Trf overnight (Eud_Trf_AP_{Fe}).

Table 4.2. Composition of the processed slurry and recovered powder, in regard to polymer, silica matrix, and triflusal drug, for the antisolvent experiments.

Sample	Matrix composition before coating		Slurry composition	Composition of as-recovered samples (wt%)		
	Silica particles	Trf (wt%)	Silica/Eudragit/Trf mass ratio	Silica	Eudragit	Trf
Eud_Trf@AP$_{Fe}$	Trf@AP$_{Fe}$	4.1	1.0/0.5/-	43	56	1
Eud_Trf_AP$_{Fe}$	AP$_{Fe}$	-	1.0/4.0/1.3	47	51	2
Eud_Trf_AP	AP	-	1.0/0.8/1.4	60	39	1

4.2.3.1. Morphological characterization of Eudragit-coated particles

Scanning and transmission electron microscopy (SEM, TEM)

When performing the PCA experiments, part of the polymer was stuck to the filter as a cake due to the continuous flow. The rest of the product was recovered from the reactor as a free-flowing powder. **Figure 4.2a** shows a SEM image of the filter cake product of a representative sample, in which aggregates of nanoparticles were entrapped in the polymeric matrix. SEM (**Figure 4.2b**) characterization of the as-recovered flowing powder demonstrated that it consisted of small agglomerated entities immersed in a continuous polymer film. The product can be further dispersed by rinsing it with a minimum amount of a proper solvent (acetone, ethanol, or methanol) to eliminate the excess of polymer, as it is shown in the TEM image of **Figure 4.2c**. Washing the polymer excess with a liquid solvent was not strictly necessary for controlled drug delivery applications; however, it was considered desirable to reduce particle aggregation while

still having a polymer coating. The presence of Eudragit after dispersing the powder in liquid media was confirmed by TEM observations, as it is marked in the image, but also by FTIR and TGA measurements.
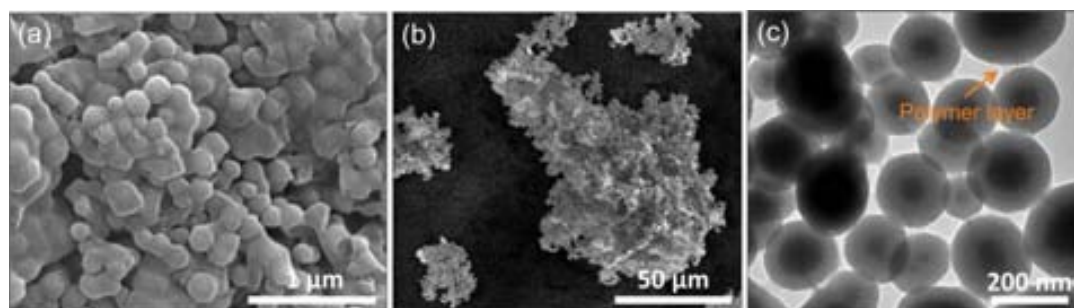
Figure 4.2. For a representative sample processed by the PCA method, SEM images of: (a) the cake portion of the product, and (b) some pieces of the as-recovered sample; and (c) TEM image of the sample, after being dispersed in MeOH. The arrow marks the polymeric layer covering the nanoparticles.

Bare AP_{Fe} and AP particles were spherical, non-aggregated and they presented narrow size distributions. Besides, the first ones showed a characteristic core-shell structure form their composite nature (see **Chapter 2**). After the PCA coating process, the as-recovered Eud_Trf@AP_{Fe} and Eud_Trf_AP_{Fe} particles were clearly embedded in a continuous mass of polymer, as shown in **Figure 4.3a** and **Figure 4.3b**, respectively. The core-shell structure is easily distinguishable in the image insets of those figures. The thickness of the polymer film could be reduced by rinsing the sample with methanol (**Figure 4.3c** and **Figure 4.3d**), thus producing almost individually coated particles. The presence of the polymer after rinsing was not easily seen in the images, and only a thin layer of the organic material connecting the particles was visible (**Figure 4.3d**).

A similar behavior to that explained for Eudragit-coated AP_{Fe} samples was observed for the Eud_Trf_AP sample. GAS precipitation produced particles embedded in a polymer mass (**Figure 4.4a**). The polymer layer is clearly seen in the inset of this image. After partial elimination of Eudragit with methanol, the particles looked like being individually coated (**Figure 4.4b**). In the TEM images, the polymer is not easily observed surrounding the rinsed particles, but some techniques showed its presence, as it is presented below.
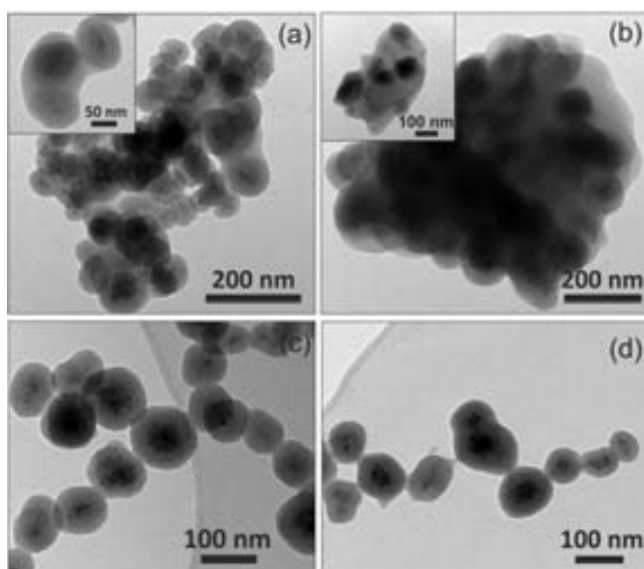
Figure 4.3. TEM images of: sample Eud_Trf@AP$_{Fe}$ (a) as-recovered, and (c) rinsed with MeOH and of sample Eud_Trf_AP$_{Fe}$ (b) as-recovered, and (d) rinsed with MeOH.
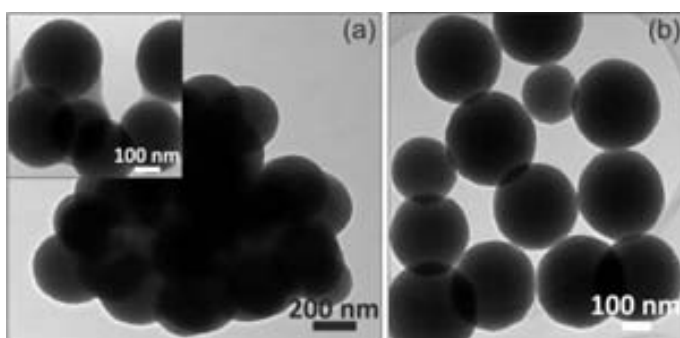
Figure 4.4. TEM images of the flowing Eud_Trf_AP powder: (a) as-recovered, and (b) after rinsing it with MeOH.

4.2.3.2. Structural characterization of Eudragit-coated particles

Fourier transformed infrared spectroscopy (FTIR)

FTIR spectroscopy was used to monitor the presence of the different components in the precipitated products involving Trf drug, silica matrix, and Eudragit polymer as a coating agent. The spectra of the different products obtained by the antisolvent route are shown in **Figure 4.5**. The as-recovered samples were rinsed with methanol before analysis. The most distinctive band in the spectrum of Eudragit was the C=O vibration appearing at *ca.* 1725 cm^{-1}. Moreover, the spectra of the polymer exhibited the characteristic bands of the asymmetric and symmetric alkyl stretching modes at 2990 and 2950 cm^{-1}, respectively. The corresponding absorbance of bending vibrations appeared as a shoulder around 1480 cm^{-1} and as two peaks at *ca.* 1445 and 1385 cm^{-1}. The spectra of the studied silica matrices are shown in **Chapter 2** and presented three main bands: at 900-1200 cm^{-1}, 1620-1630 cm^{-1} and 3600-3100 cm^{-1}. They correspond to O-Si-O bonds in the SiO$_4$ tetrahedrons, bending frequency of molecular water adsorbed in the silica and free

O-H stretching vibrations, respectively. The useful FTIR region of solid Trf/HTB contained bands at 1770 and 1685 cm^{-1} corresponding to the carbonyls (C=O). The presence of Trf in the coated matrices was difficult to assess, due to the low percentage of drug in the samples. However, for some samples, the Trf could be tentatively monitored by the C=O band of the ester appearing at a frequency near 1770 cm^{-1}, as a shoulder of the more intense carbonyl band associated to the polymer occurring at a slightly higher frequency (1725 cm^{-1}).
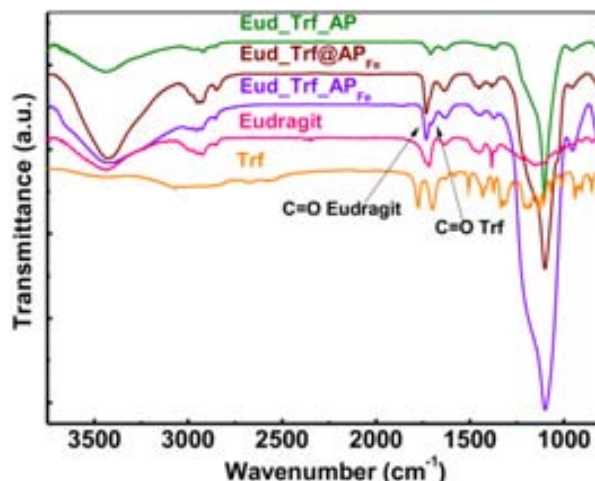
Figure 4.5. FTIR spectroscopic analysis of the Eudragit-coated products (indicating the C=O carbonyl functionality for the polymer and, tentatively, also for the drug), and of pristine Eudragit and Triflusal.

Thermal gravimetric analysis (TGA)

The quantification of the organic and inorganic phases was performed by sample heating in TGA measurements. The thermogravimetric curve obtained for solid Eudragit indicated that the polymer decomposed in the temperature interval of 350-430 °C (**Figure 4.6a**). The lost of Trf occurred in the range 150-350 °C. However, the amount of Trf in the samples was too small to be quantified. The remaining weight after heating up to 450 °C was assigned to the inorganic phase. **Figure 4.6b** shows the thermogravimetric profiles of the coated materials. In the Eud_Trf_AP sample, the percentage value of the residue at 450 °C corresponded to *ca.* 60 wt% of the total composite mass, while in the PCA precipitated products, this percentage was reduced to values of less than 50 wt%. After rinsing the Eud_Trf@AP$_{Fe}$ sample with methanol, the percentage of polymer was reduced to values of 10-20 wt%.
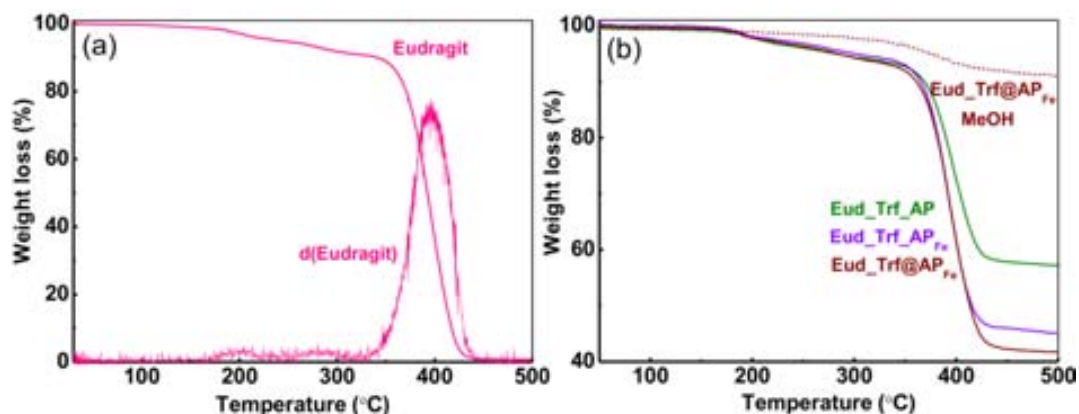
Figure 4.6. Thermal analysis of: (a) the solid Eudragit polymer, and (b) the as-recovered powders of the studied experiments, and sample Eud_Trf@AP$_{Fe}$ also after rinsing it with methanol (Eud_Trf@AP$_{Fe}$ MeOH). Curve labeled as *d(Eudragit)* is the derivative of the respective TGA curve.

4.2.3.3. Drug stability in Eudragit-coated particles

The preservation of the non hydrolyzed Trf inside the Eudragit-coated matrices during preparation and storage was studied and compared with the pure drug and the Trf in silica samples before Eudragit coating and with Trf@PMMA. The transformation was evaluated after 6 months of storing the samples under ambient conditions, *i.e.*, 21 °C and 60-65 % relative humidity.[28] The amount of either Trf or HTB was determined from the corresponding chromatographic peaks at the initial stages of the release in water using a HPLC equipment. The experimental protocol is described in **Chapter 3**. **Figure 4.7** shows that the Trf transformation for the different samples was of more than 50% for the PMMA-based matrix to less than 8% for the Eudragit-coated AP$_{Fe}$ particles. An intermediate situation was observed for the uncoated Trf@AP$_{Fe}$ and Trf@AP materials, which showed hydrolysis degrees of ~ 30%. The Eudragit-coated AP sample showed a similar behavior but with a slightly lower hydrolysis of around 20%. As studied in **Chapter 3**, hydrophilic silica matrices preserved the water-sensitive drug more efficiently than the PMMA beads due to the acidity that silica provides to the adsorbed water. After impregnation in CO_2, the PMMA matrix has an internal porosity[38] that allowed the water diffusion leading to an increase in the hydrolysis degree of Trf. For the inorganic particles, the coating with Eudragit likely avoided the diffusion of water into the material, minimizing the subsequent hydrolyzation of the drug.
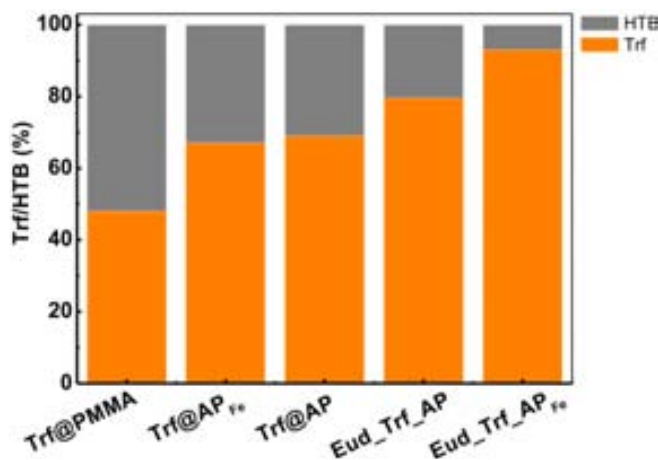
Figure 4.7. Percentage of Trf and HTB in the studied silica-based particles before and after Eudragit-coating after 6 months of storage (21 °C and 60-65% relative humidity) and in Trf@PMMA.

4.2.3.4. Drug release profiles of Eudragit-coated particles

The percentage of drug loaded in the as-recovered powders was determined by HPLC (see **Table 4.1**). Obtained values were in the order of 1 wt% for Eud_Trf@AP$_{Fe}$ and Eud_Trf_AP samples and of 2 wt% for Eud_Trf_AP$_{Fe}$. The release kinetics of samples Eud_Trf_AP$_{Fe}$ and Eud_Trf_AP were followed under gastric and under blood stream pH-conditions for the coated-composite nanoparticles (**Figure 4.8a** and **Figure 4.8b** respectively) and they were compared with the results obtained for the uncoated AP$_{Fe}$ particles. The drug release curves of sample Trf@PMMA are also shown in the figures for comparison. When oral administration, the carboxylic acid of the Trf molecule is protonated at the acid stomach pH, and the drug is completely absorbed before reaching the intestine. Although uncoated Trf@AP$_{Fe}$ nanospheres released the drug almost instantaneously in both pH, the release profile was slightly faster in acid (more than the 95 wt% was dissolved in 5 minutes) than in basic medium (around the 80 wt% was released in the first 5 minutes). In contrast, the slowest release kinetics was obtained for the sample Trf@PMMA with a drug delivery lasting for several days and having only the 18 wt% released in the first 60 min at acid and the 4.5 wt% at basic conditions. The measured drug delivery profiles of the coated samples Eud_Trf_AP$_{Fe}$ and Eud_Trf_AP were intermediate between those of Trf@AP$_{Fe}$ (fastest kinetics) and Trf@PMMA (slowest kinetics). For Eudargit-coated particles, *ca.* 25 wt% of the drug was dissolved during the first 10 min., and a progressive release of the remaining 75 wt% occurred during the next 5-8 h in acid pH. For instance, at 60 min, the released percentages were around 70 and 55 wt% for Eud_Trf_AP$_{Fe}$ and Eud_Trf_AP samples, respectively (**Table 4.3**). The coated AP$_{Fe}$ particles showed a similar behavior in basic pH releasing around the 25 wt% of the drug in the first 10 minutes and the 65 wt% in 60 minutes. According to literature, the drug dissolution profile of pure Trf is characterized by a fast kinetics with complete drug dissolution in a period of ~ 25 min. for both gastric and blood stream pH-conditions.[41] This kinetics profile was considered comparable to that of the uncoated particles.

Reasons of prolonged released in the coated systems were related to the necessity of swelling the polymer before diffusion and the long diffusion channels that the drug molecules have to follow to reach the bulk solution.
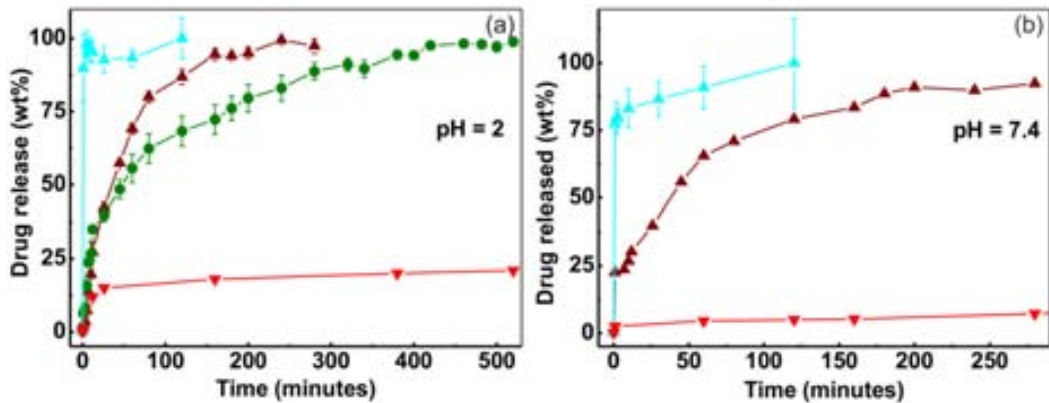
Figure 4.8. Drug delivery profiles for Trf pre-impregnated AP_{Fe} (Trf@AP_{Fe}), and PMMA (Trf@PMMA) samples, and Eudragit-coated powders Eud_Trf_AP_{Fe} and Eud_Trf_AP in: (a) acid pH, and (b) basic pH. Error bars correspond to the standard deviation of three replicates. Solid lines are included as a guide to the eye.

Table 4.3. Drug release in the pre-impregnated and Eudragit-coated samples obtained by HPLC in acidic (pH =2) and basic (pH = 7.4) aqueous media.

Sample	Medium pH	Drug release (wt%)				
		5 min.	60 min.	120 min.	280 min.	520 min.
Trf@AP_{Fe}	2	98	93	100	-	-
Eud_Trf_AP_{Fe}		7.0	69	87	97	-
Eud_Trf_AP		16	56	68	89	100
Trf@PMMA		3.0	18	18	19	21
Trf@AP_{Fe}	7.4	81	91	100	-	-
Eud_Trf_AP_{Fe}		22	65	79	92	-
Trf@PMMA		3.0	4.5	5.0	7.2	9.1

To better understand the mechanism of the drug delivery from the Eudragit-coated silica particles, the release data was fitted in the light of two different models.

The first one, the Korsmeyer-Peppas model,[42,43] is a simple semi-empirical model which follows **Equation 4.1** and includes the possibility of a burst effect:

Equation 4.1 $$\frac{M_t}{M_\infty} = at^n + b$$

where M_t represents the amount of the drug released at time t; M_∞, the total amount of drug released over a long period of time (it is considered equivalent to the drug loading); a, the kinetics constant that is related to structural and geometrical characteristics of the carrier; t, the elapsed time; n, the release exponent, indicative of the drug release mechanism; and b, the

parameter that introduces the burst effect. This model is commonly used to describe the drug release from polymeric systems and when the kinetics of the process is unknown.

The second model is the Baker-Lonsdale[43] that interprets the diffusion of the drug from a spherical matrix, being adjusted to the expression shown in **Equation 4.2**:

Equation 4.2 $$f_i = \frac{3}{2}\left[1 - \left(1 - \frac{M_t}{M_\infty}\right)^{2/3}\right] - \frac{M_t}{M_\infty} = kt$$

where M_t is the drug released amount at time t and M_∞ is the amount of drug released at an infinite time. For a heterogeneous system with structural features that influence the drug discharge mechanism, k can be written as depicted in the **Equation 4.3**:

Equation 4.3 $$k = \frac{3D_f K C_{fs}}{r_0^2 \tau}$$

being D_f the diffusion coefficient, K the drug specific volume, C_{fs} the drug solubility in the liquid surrounding the matrix, r_0 the radius of the spherical matrix, and τ the tortuosity factor of the system. The use of this approach requires the total drug loading to be greater than its solubility in the matrix.

The drug dissolution data in both acid and basic pH for samples Eud_Trf_AP$_{Fe}$ and Eud_Trf_AP were fitted to **Equation 4.1**, and when needed also to **Equation 4.2**. For **Equation 4.1**, only the first 60% of the cumulative release points was considered, as the Korsmeyer-Peppas model demands. Correlation coefficients (R^2) were used to evaluate the quality of the fit.

In **Table 4.4**, the correlation coefficients, "n" values and kinetic constants resulting from fitting the curves with the Korsmeyer-Peppas equation are presented. On the basis of this model, reasonable values of R^2 were obtained for the drug release performed at pH = 2, especially for the case of the Eudragit-coated AP$_{Fe}$ nanoparticles. In addition, the n exponents were determined to be equal to 0.42 and 0.49 and the kinetic constants to 0.92 and 0.55 for encapsulated AP$_{Fe}$ and AP particles, respectively (**Figure 4.9a** and **Figure 4.9b**). According to these results, the drug was released by a Fickian diffusion mechanism in Eud_Trf_AP$_{Fe}$ sample. The release from sample Eud_Trf_AP did not seem to be governed by a Fick's law[44] but could be described by anomalous transport, as Peppas *et al.* determined for spherical polymeric matrices.[45] The release data of Eud_Trf_AP in acid medium was also fitted to the Baker-Lonsdale equation, obtaining a correlation coefficient value of 0.9888 (**Figure 4.9c**).

The release data of Eud-coated AP$_{Fe}$ nanospheres in pH = 7.4 were fitted to the same equations obtaining the best fit for the Korsmeyer-Peppas model (**Table 4.4**, **Figure 4.10a**). Those results suggested also an anomalous transport of the drug when released from AP$_{Fe}$ in basic medium. **Figure 4.10b** shows the curve fitted to the Baker-Lonsdale equation, and the improved R^2 resulted with a value of 0.9910 indicating a diffusion drug release mechanism from the composite nanospheres.

However, it is worth mentioning that the application to these models was not satisfactory for the non coated Trf-loaded particles (**Chapter 3**) even for Korsmeyer Peppas model. We interpret this as the drug delivery systems we fabricated show a faster release than the most common mathematical models contemplates.

Table 4.4. For samples Eud_Trf_AP$_{Fe}$ and Eud_Trf_AP, release parameters estimated from the fits of the experimental data in acid and basic media to the Korsmeyer-Peppas model.

Sample	Medium pH	R^2	n	a (h^{-n})
Eud_Trf_AP$_{Fe}$	2	0.9965	0.42	0.92
Eud_Trf_AP		0.9838	0.49	0.55
Eud_Trf_AP$_{Fe}$	7.4	0.9878	0.48	0.63
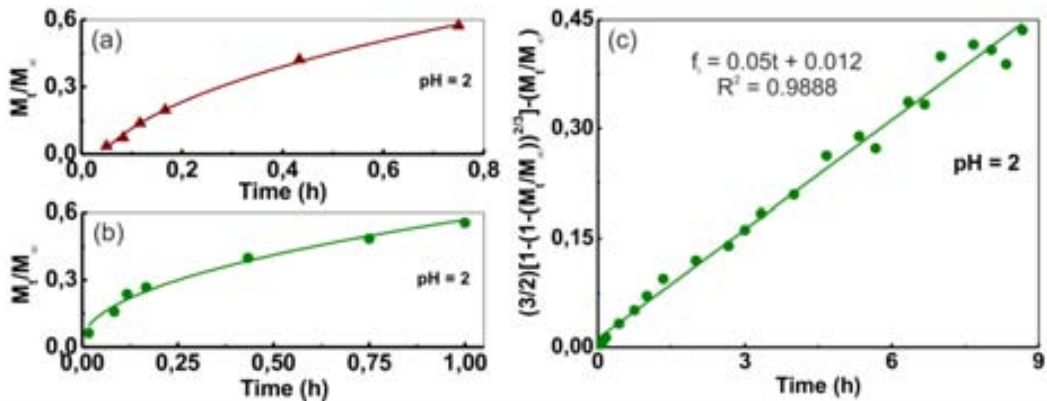
Figure 4.9. For pH = 2, drug release data fitted with the Korsmeyer-Peppas equation for the following: (a) Eud_Trf_AP$_{Fe}$ and (b) Eud_Trf_AP samples, and with the Baker-Lonsdale equation for (c) Eud_Trf_AP. Symbols correspond to experimental data and solid lines to fitted profiles.
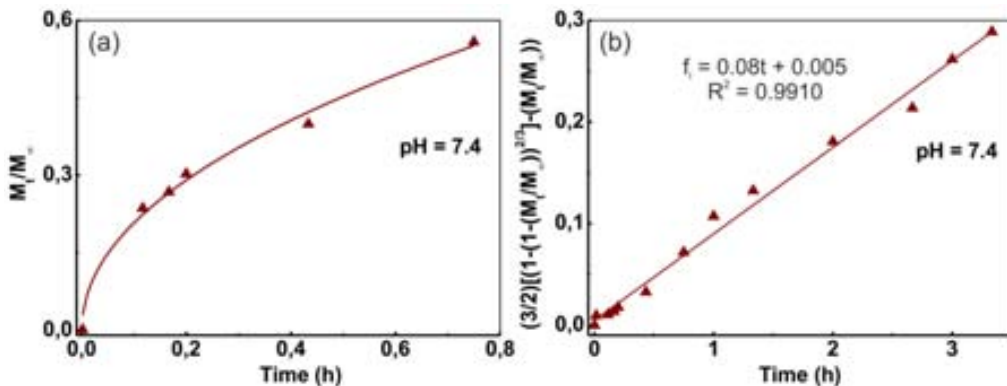
Figure 4.10. For sample Eud_Trf_AP$_{Fe}$ and pH = 7.4, drug release data fitted with: the (a) Korsmeyer-Peppas, and the (b) Baker-Lonsdale equations. Symbols correspond to experimental data and solid lines to fitted profiles.

4.3. GRAFTING OF POLYETHYLENEIMINE ON SILICA-BASED PARTICLES

4.3.1. Polyethyleneimine for biomedical applications

Polyethyleneimine (PEI) is a hydrophilic polymer composed by repeating units of ethyleneimine monomers (**Figure 4.11**). The uses of polyethyleneimine go from a wide variety of applications in different industrial processes[46] to the pharmaceutical industry. Regarding biomedical applications, drug surface modification by coating with PEI is a common method to prevent burst release.[47] PEI has also been used for the coating of stents to reduce inflammation and thrombogenicity.[48] Moreover, PEI with amine linkers creates ionic interactions with protein molecules forming protein-polymer conjugates. PEI modified systems are utilized for prolonging the *in vivo* circulation half-live of therapeutic proteins, for reducing proteolysis, for avoiding chemical modification and denaturation during storage and administration, or for delivering targeted payloads of therapeutical proteins into specific tissues.
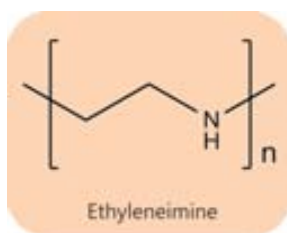
Figure 4.11. Chemical structure of the polyethyleneimine monomer (ethyleneimine).

Even though, the most generalized application of PEI involves *in vivo* gene delivery.[49,50] The transfer of DNA or siRNA into eukaryotic cells is considered a highly promising approach for the treatment of a wide spectrum of hereditary disorders. Many clinical trials have been performed with viral vectors for gene delivery, but the potential risks of undesired immune and toxic side reactions have raised some concerns.[51] As an alternative, non-viral vectors, such as cationic polymers, can be used as effective transfection reagents. Particularly for PEI, the large number of secondary amine groups in its cationic structure facilitates interaction with the negatively charged phosphate backbone of DNA. Indeed, PEI-coated magnetic nanoparticles was the first reported example of *in vitro* nanoparticle-mediated non-viral gene delivery.[52,53] Silica fine powders have also been widely used for this purpose.[54,55] It has been shown that PEI coating enhances the cellular uptake of mesoporous silica and iron oxide particles and allows safe delivery of siRNA and DNA constructs.[56,57] In addition, *in situ* polymerization of aziridine in the presence of silica particles suspended in a liquid has been shown to form densely packed hyperbranched PEI grafted on the silica surface.[58]

The main objective of this section has been to develop an alternative PEI coating method for small silica-based particles. Thin coatings of polymeric PEI were deposited on the surface of both AP_{Fe} and AP particles, either pristine or previously impregnated with Trf, using compressed CO_2. The possibilities of small particles coating by the *in situ* polymerization of ethyleneimine (or

aziridine) in the absence of liquid solvents are here demonstrated. By employing compressed CO_2, the process is carried out at lower temperatures and shorter reaction times than the conventional liquid-solvent processes.[15,59] Aspects of composition and polymer molecular weight, coverage, thermal stability, and morphological parameters of the synthesized hybrid products are discussed, together with a comparative study of the zeta potential. Besides, *in vitro* HPLC characterization showed that the hydrophilic PEI coating did not significantly modify the drug release kinetics.

4.3.2. Polyethyleneimine coating of silica-based particles

Silica-based AP_{Fe} and AP particles were coated with PEI by two different methods: a novel CO_2-assisted approach, and, for comparative purposes, a conventional liquid-solvent process. Importantly, using compressed CO_2, particles coated with low molecular weight PEI were obtained. Besides, washing steps were avoided when using this approach in contrast with the standard one.

4.3.2.1. *In situ* synthesis of polyethyleneimine

The *in situ* synthesis of PEI on the particles silica surface was carried out in a high-pressure reactor of 100 mL running in the batch mode.[15] The equipment is described in **Chapter 7**. The vessel was charged with about 0.2 g of powder enclosed in a cylindrical cartridge made of 0.45 µm pore filter paper. The cartridge was placed in the upper part of the autoclave using a stainless steel platform. Around 0.7 mL of liquid ethyleneimine (kindly donated by Menadiona S.A.) was added at the bottom of the reactor, avoiding solid-liquid contact. To promote the polymerization of the monomer, the vessel was pressurized to 50 bar with CO_2 at room temperature and left to react for 30 min. Low-molecular weight chains of PEI that were not strongly bonded to the silica surface were eliminated during depressurization. A dry sample was recovered after depressurization. $Trf@AP_{Fe}$, AP and Trf@AP particles were coated following this procedure, and the obtained materials were labeled as $PEI_{CO2}\_Trf@AP_{Fe}$, AP_PEI_{CO2} and $PEI_{CO2}\_Trf@AP$, respectively. A similar control experiment was performed without the addition of the solid powder. The polymer recovered from this experiment was called PEI_{CO2}.

This is a new process for the grafting of low-molecular weight PEI chains on silica-based particles surface. It is based on the use of compressed CO_2 as the initiator of the ring opening polymerization of the ethyleneimine monomer (**Figure 4.12**). According to literature, a covalent bond is formed between the silica and the produced PEI.[58,60]

Figure 4.12. Chemical structure of ethyleneimine monomer that forms polyethyleneimine in compressed CO_2.

4.3.2.2. Standard polyethyleneimine noncovalent coating

AP_{Fe} and AP particles were coated with commercial PEI, following a standard soaking procedure[59] and the obtained samples were labeled as *PEI_AP_{Fe}* and *PEI_AP*, respectively. This procedure consisted of first dispersing 50 mg of the silica-based particles in 5 mL of ethanol containing commercial PEI at a concentration of 2.5 mg/mL. The suspension was then sonicated for 15 min. and magnetically stirred for 30 more min. The particles were centrifuged to eliminate the liquid phase and washed three times with 10 mL of ethanol, following the protocol of first sonication for 5 min. and then centrifugation at 5000 rpm for 20 min.

4.3.3. Results and discussion

4.3.3.1. Mechanism of polyethyleneimine polymerization

PEI is a water soluble cationic polymer that can take both linear and branched forms.[61] The random branched structure is commonly produced by acid-catalyzed polymerization of aziridine monomers in aqueous or alcoholic solution.[62,63] The polymerization is activated by aziridine protonation, followed of nucleophilic attack by a second aziridine molecule as it is schematized in **Figure 4.13a**. The ring opening polymerization can be also initiated by a Lewis acid, such as CO_2 (**Figure 4.13b**).[64] For unsubstituted aziridine, CO_2 is not chemically incorporated to the polymer chain, but it is adsorbed in the formed homopolymer.[65] Unsubstituted aziridine reversibly generates the corresponding carbamic acid derivative in equilibrium with the corresponding ammonium carbamate.[66] The CO_2 sorbed into the synthesized PEI polymer is easily eliminated at temperatures of 80-100 °C.[67]

Currently, the used methods to graft hyperbranched polyamines on inorganic surfaces need the use of organic solvents, catalysts, high temperatures, and/or long reaction times.[62,63] The present work tackles the possibility of simultaneous ethyleneimine polymerization and PEI grafting on the surface of silica-based submicron and nanoparticles using compressed CO_2. The process takes place at low pressure and temperature and in the absence of any organic solvent.
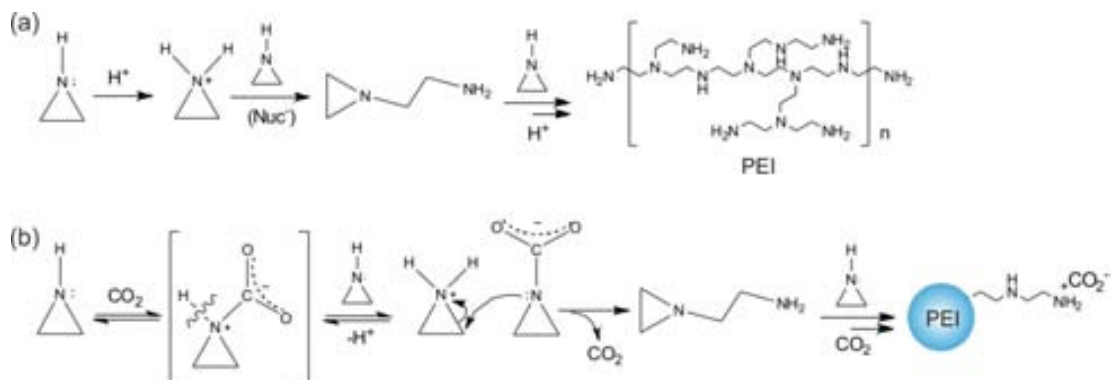
Figure 4.13. Schematic representation of different mechanisms established for the formation of hyperbranched PEI from aziridine under: (a) acid and (b) CO_2 catalysis.

4.3.3.2. Morphological characterization of polyethyleneimine-coated particles

Transmission electron microscopy (TEM)

The PEI-coated AP particles had a similar morphology than before the encapsulation treatment, but they were individually coated by the polymer, as it can be clearly observed in **Figure 4.14a** and **Figure 4.14b** for representative samples of coating with PEI synthesized in compressed CO_2 (PEI_{CO2}) and commercial PEI (PEI), respectively. A thin polymer layer can be seen around the particles whatever the coating method. This layer is marked with arrows in the images (insets of **Figure 4.14a** and **Figure 4.14b**). The polymer coating was harder to identify by TEM observations in the case of the AP_{Fe} nanoparticles. The surface of the pristine composite spheres was already rough at high a magnification (**Figure 4.14c** and **Figure 4.14d**). However, the presence of the polymer on the silica surface was confirmed for both types of particles by ξ-potential measurements shown below in **Table 4.5**.
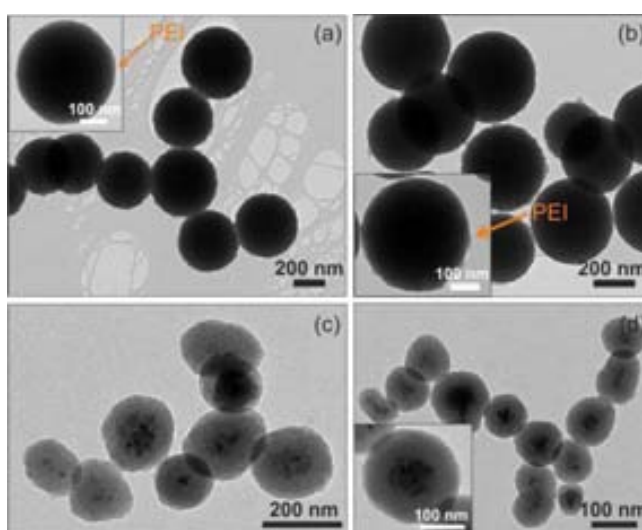
Figure 4.14. TEM images of coated particles: (a) PEI_{CO2}_AP, (b) PEI_AP, (c) PEI_{CO2}_Trf@AP_{Fe}, and (d) PEI_AP_{Fe}. Arrows point the polymer layer.

As described earlier, the pristine silica-based particles have an aerogel-like porous structure with surface areas of around 200 m^2/g, mean pore volumes of about 0.1 cm^3/g and intraparticle pore sizes of 1.6-1.8 nm. Small molecules as triflsual can fit into the internal pores of the particles, but hyperbranched PEI chains are expected to be predominantly accommodated on the external surface due to molecular size impediments.[68] Some important differences regarding PEI_{CO2} and PEI configuration on the particles surface are related with the preparation mode (**Figure 4.15**).

Strong covalent links between the branched PEI_{CO2} and the supports have been described for *in situ* polymerization of aziridine in the presence of silica (**Figure 4.15a**).[15,69,70] However, for the high molecular mass PEI, which was here added to a particles suspension as a hyperbranched polymer, the most probable configuration is the one resulting from its electrostatic adsorption on the silica surface (**Figure 4.15b**).
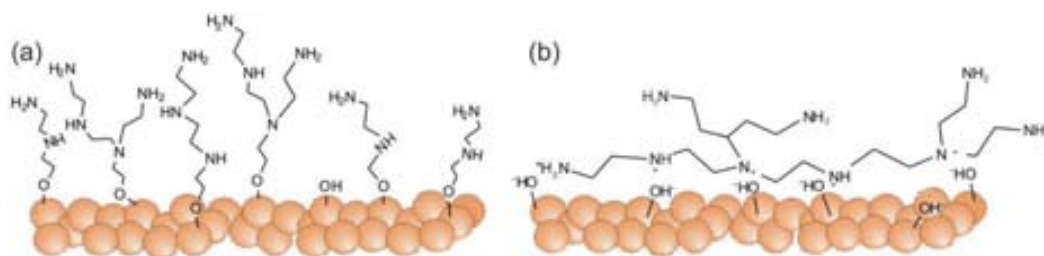
Figure 4.15. Schematic representation of different possible configurations of PEI on the surface of silica particles: (a) PEI_{CO_2} grafted on the silanol groups, and (b) PEI deposited by electrostatic interactions.

4.3.3.3. Structural characterization and size determination of polyethyleneimine-coated particles

Fourier transformed infrared spectroscopy (FTIR)

FTIR spectroscopy was used to monitor the presence of the different components in the PEI composites. Representative spectra in the range of 3000-1500 cm^{-1} of the polymers and the polymer-coated particles in compressed CO_2 or by the conventional method are shown in **Figure 4.16a** and **Figure 4.16b**, respectively. Below 1500 cm^{-1}, intense absorption bands appear in the 900-1200 cm^{-1} region, corresponding to Si-O-Si vibrations in the aerogel skeleton that complicate the observation of organic functional peaks. The band at 1620-1630 cm^{-1} was due to the bending frequency of molecular water adsorbed into the particles. The useful FTIR region of solid Trf contained bands at about 1770 and 1685 cm^{-1} from the carbonyl groups of Trf and the hydrolyzed form, respectively. However, the presence of the pre-impregnated drug in the coated AP_{Fe} nanospheres was difficult to assess using FTIR analysis, due to the low percentage of the drug in the composite samples.

The spectra of the PEI_{CO_2} and PEI polymer exhibited the characteristic bands of the asymmetric (~ 2920 cm^{-1}) and symmetric alkyl stretching modes (~ 2850 cm^{-1}). The most distinctive band for PEI_{CO_2} was the C=O vibration appearing at about 1714 cm^{-1} and assigned to carbamate formed by interaction with CO_2 during *in situ* polymerization. This band was clearly observed for PEI_{CO_2}-coated particles as a sharp peak except in the case of sample PEI_{CO_2}_Trf@AP, where it appeared as a shoulder of the broad band from adsorbed water. The spectrum of commercial PEI did not present the C=O band at 1774 cm^{-1}. The presence of the polymer when using the conventional coating method was difficult to confirm by FTIR due to overlapping of its characteristic peaks with signals present in the pristine matrices. Other techniques were used for this purpose, for instance TGA or measurements of the ξ-potential.
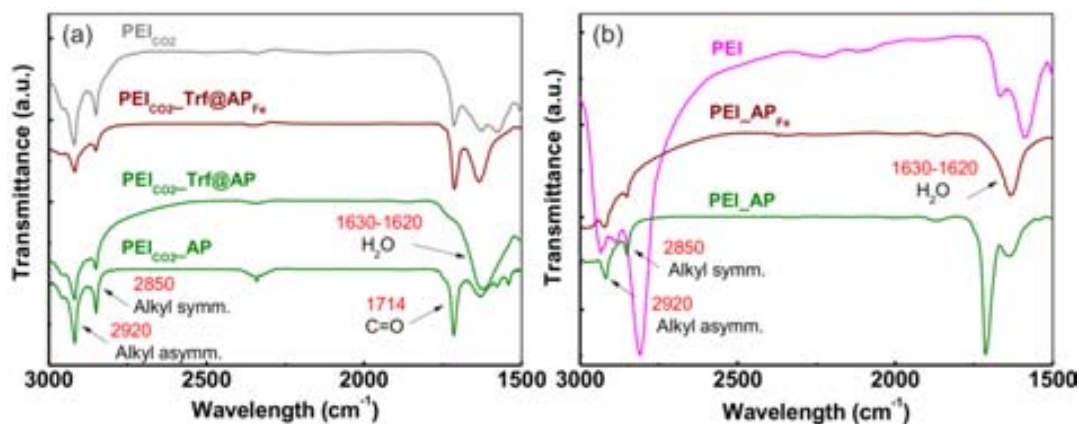
Figure 4.16. FTIR spectra in the range 3000-1500 cm^{-1} of: (a) the synthesized PEI$_{CO2}$ and the PEI$_{CO2}$-coated particles, and (b) commercial PEI and PEI-coated particles.

Thermal gravimetric analysis (TGA)

The mass composition of the PEI-coated particles was assessed by TGA. PEI featured a three-step weight decay in the temperature interval of 50-450 °C (**Figure 4.17a**). Up to 150 °C, the weight loss was assigned to water and CO$_2$ elimination for *in situ* prepared PEI$_{CO2}$ (25 wt%), and to water evaporation for commercial PEI (5 wt%). PEI began to decompose above 150 °C and up to 375 °C the weight loss is gradual, with values of 30 and 50 wt% for PEI$_{CO2}$ and PEI, respectively. When the temperature was increased above 375 °C, the degradation rate increased for both polymers, indicating that a different decomposition process took place.

At 500 °C, both studied PEI polymers were completely decomposed and removed as volatile species. TGA analysis indicated that samples consisting of PEI$_{CO2}$ or PEI deposited on the surface of the silica-based particles decomposed in a similar temperature range (*ca.*, 150-500 °C in **Figure 4.17b**) than pristine polymers. For samples containing particles, a plateau in the weight loss is not reached, even at temperatures of 500 °C, due to material densification.[71,72,73] The first derivative graphs are depicted in the figures to indicate the temperature intervals used for weight lost calculations. Among other data, **Table 4.5** shows the mass of deposited polymer for the coated samples calculated using TGA data. The accuracy of this method has previously been confirmed in similar PEI-silica composite samples and contrasted with values obtained by elemental analysis.[15,74] PEI coated particles in compressed CO$_2$ showed a larger polymer amount than particles processed by the conventional method.

For Trf pre-impregnated samples, the drug incorporated was estimated from TGA weight loss measured in the 150 °C-350 °C range (**Figure 4.17c** and **Figure 4.17d**). The estimated drug percentages were 3.3 and 2.1 wt% for Trf@AP$_{Fe}$ and Trf@AP, respectively. The amount calculated for the PEI phase was found to be 5-10 wt%.
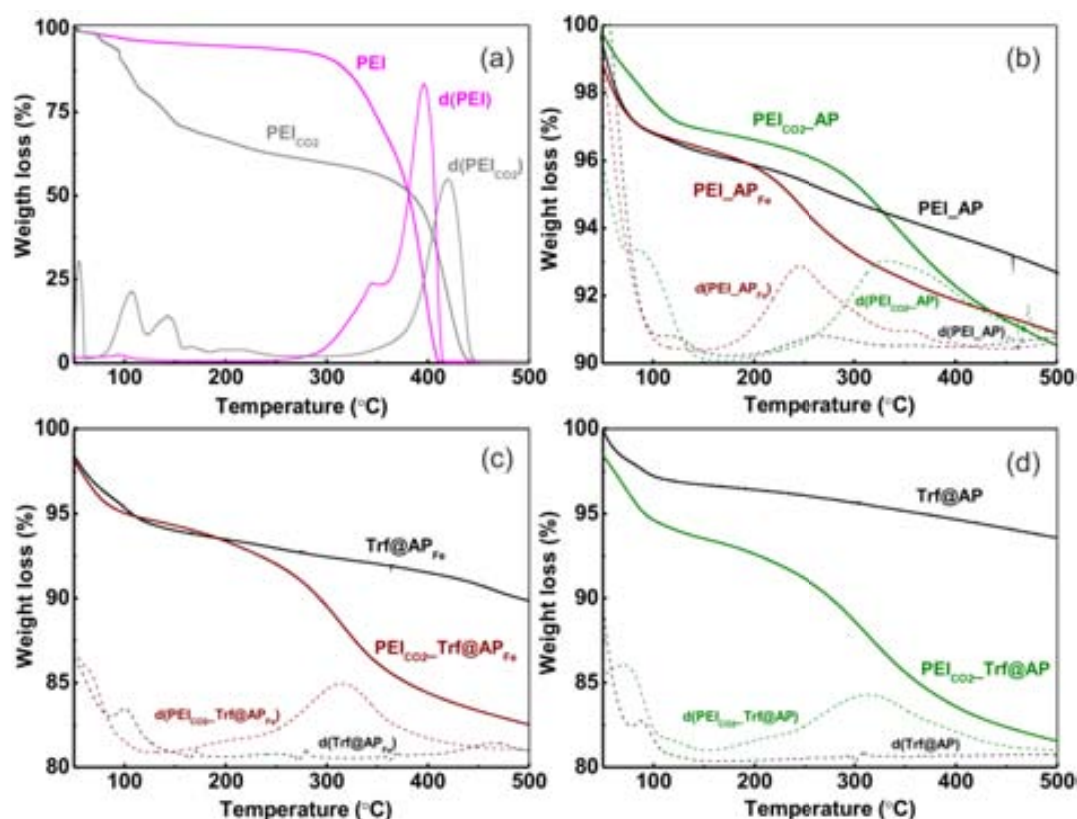
Figure 4.17. TGA profiles of: (a) raw polymers, (b) PEI and PEI_{CO2}-coated particles, and Trf pre-impregnated and coated (c) AP_{Fe} nanospheres and (d) AP particles. $d(xx)$ profiles correspond to the first derivative curves.

Table 4.5. PEI weight percentage from TGA data, ξ-potential and hydrodynamic diameter measured by DLS in water at 25°C.

Sample	PEI (wt%)	Drug (wt%)	ξ-potential (mV)	$\Phi_{Hyd.}$ (nm), by intensity
AP_{Fe}	-	-	-40	416
$PEI_{CO2}\_Trf@AP_{Fe}$	8.5	3.3	54	418
PEI_AP_{Fe}	5.5	-	33	239
AP	-	-	-55	575
PEI_{CO2}_AP	6.5	-	58	771
$PEI_{CO2}\_Trf@AP$	10	2.1	60	739
PEI_AP	3.7	-	45	603

ξ-potential and hydrodynamic diameter measurements (DLS)

Important features of PEI are its high cationic charge density and the presence of reactive amine linkers. This characteristic overcomes one of the main drawbacks of the most extensively used PEG coating, which is the difficulty to further functionalize it with active biomolecules. Hence, PEI-based systems are widely used for gene delivery thanks to their ability to complex with DNA, to facilitate endosomal release via the "proton sponge effect", and to guide intracellular

trafficking of their cargo into the nucleus. In the literature, it is shown that a positive net charge and, thus, a positive zeta potential, is necessary to allow complexes entering into the cells.[75]

The ξ-potential of the raw and the PEI-coated samples was determined by measuring dispersions of the particles in water at 0.1 mg/mL and 25 °C. The silica surface of the silica-based systems had a negative zeta potential of -40 and -55 mV for AP_{Fe} and AP samples, respectively. The coating with cationic PEI led to a sharp increase in the zeta potential, resulting in positive values of +30 to +60 mV for both Trf free and Trf pre-impregnated samples (**Table 4.5**).

Data on the mean cluster hydrodynamic size, measured by dynamic light scattering of the same dispersions in water used for zeta potential studies, is also shown in **Table 4.5**. Cluster size was not increased by coating with commercial PEI following the standard procedure, and even a deagglomerating effect was observed PEI_AP_{Fe} nanoparticles. However, the hydrodynamic diameter of the clusters increased after PEI coating by using the CO_2-based procedure, reflecting the relatively high amount of deposited PEI_{CO2} (**Figure 4.17b**). As it was observed in the TEM images for the PEI_{CO2}-coated particles, the polymer can joint several particles together to form clusters, thus, increasing the measured particle size (see **Figure 4.14a**).

4.3.3.4. Molecular weight and structure of the *in situ* synthesized polyethyleneimine

High- and low-molecular weight polymers have different properties when considering their biomedical applications.[76,77,78] While high-molecular weight PEI (25-50 kDa) is effective for complexing and delivering nucleic acids, these systems repeatedly produce cytotoxicity due to the damage of cells, lysosomes, and mitochondrial membranes.[79,80] Decreasing PEI molecular weight to medium values (5-10 kDa) reduces cellular toxicity, while the effectiveness of nucleic acid delivery is maintained. Finally, despite being inefficient at transfecting nucleotides, coating with low-molecular weight PEI (0.6-1.8 kDa) is useful for several drug delivery applications.

Thus, the synthesis of PEI with reduced molecular weights is of special relevance when seeking biomedical applications.

Static light scattering (SLS) and time-of-flight mass spectrometry with a matrix-assisted laser desorption/ionization source (MALDI-TOF)

SLS and MALDI-TOF were both used to determine the molecular weight of the synthesized PEI_{CO2} polymer.

For PEI polymers, the average molecular weight achieved following the conventional liquid synthesis mode is typically within the range of 20-50 kDa.[81] The commercial PEI used in this work has a molecular weight of 25 kDa, as determined by light scattering. The molecular weight of a PEI_{CO2} sample was first determined using a SLS method, similarly to the approach used to determine the molecular weight of the commercial product. Four concentrations of the polymer dissolved in deionized water were prepared. To determine the absolute molecular weight, a Debye plot was generated from the light scattering measurements performed for the solvent and

polymer solutions. The estimated value was in the order of 8 ± 2 kDa, which corresponds to a PEI of low molecular weight. To contrast the results, the PEI_{CO2} sample was also characterized by using a MALDI-TOF equipment. Significant amounts of 0.2-1 kDa chains were detected by this technique (**Figure 4.18**), indicating a low molecular weight for the synthesized PEI_{CO2} polymer, in agreement with the results obtained by SLS. Slight discrepancies on the absolute mass estimated using different characterization techniques are typical for such a low-molecular weight polymers, shifting the molecular weight distribution to lower masses for MALDI-TOF analysis.[82] The maximum peak intensity was centered at 132-304 Da, corresponding to 3 (129 Da)-7 (301 Da) repeating units (CH_2CH_2NH) in the protonated PEI molecule.
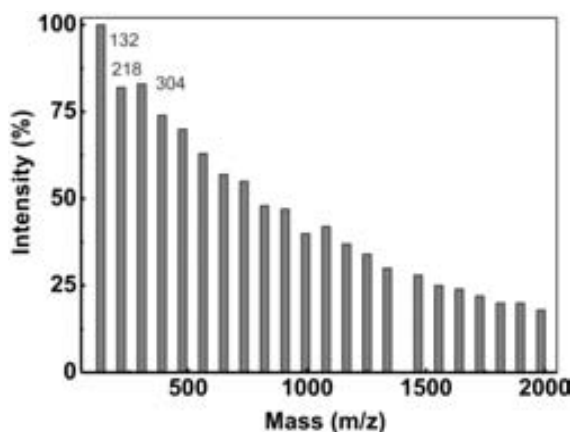
Figure 4.18. MALDI-TOF mass spectrum of the synthesized PEI$_{CO2}$ polymer.

The process of PEI polymerization in aqueous or alcoholic solutions occurs in a homogeneous mixture due to the high solubility of the monomer, the polymer, and the acid initiator in the continuous liquid phase. Solubilization of the polymer during polymerization results in the formation of high-molecular weight PEI. In contrast, because of the limited solubility of most polymers in compressed CO_2, low-molecular weight systems are frequently obtained in supercritical and compressed CO_2 in the absence of surfactants.[83] Since aziridine undergoes exothermic polymerization in contact with CO_2,[84] the ring opening polymerization carried out in the compressed fluid occurs at high reaction rates. The quick heat release vaporized the monomer resulting in a visually observed vapor cloud, occurring at ~ 50 bar under working conditions. Hence, the process featured an initially homogeneous vapor phase reaction, where monomer and initiator (in this case, the Lewis acid CO_2) are homogeneously mixed. During polymerization, the system became rapidly heterogeneous once the growing oligomeric chains reach a critical molar mass that exceeds the solubility limit in the compressed CO_2 vapor phase. Polymer precipitation would reduce significantly the molecular weight of the recovered PEI$_{CO2}$. In addition, polymer chains grafted on silica surface are expected to have a still lower molecular weight than the value found by SLS for PEI_{CO2} (*ca.*, 8 kDa), due to factors related to strong steric hindrance occurring between the pendant polymer chains.[85] The high density of chains grafted

onto the silica particles would interfere with the propagation of the hyperbranched tree-like structure, resulting in the decrease of the apparent molecular weight.[86,87]

The molecular weight values estimated in this work for the *in situ* synthesized PEI_{CO_2} polymers are in the medium-low values, thus, resulting in compounds with a reduced cytotoxicity and biological potential applicability.

Powder X-ray diffraction (PXRD)

PXRD analysis of synthesized PEI_{CO_2} showed a broad band between 7 and 35° and centered around 20° (**Figure 4.19**). This indicated that the polymer had an amorphous structure, which suggested a highly branched configuration.
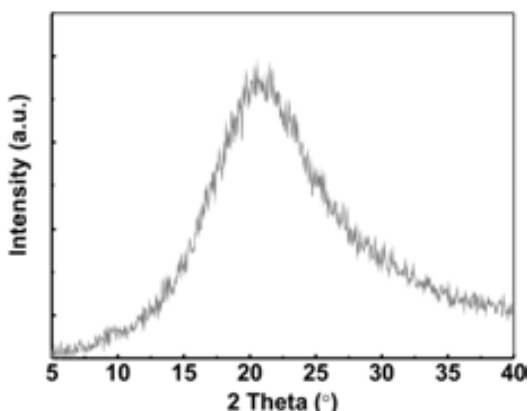
Figure 4.19. X-ray diffractiogram of PEI_{CO_2}.

Differential scanning calorimetry (DSC)

Amorphous PEI_{CO_2} synthesized in CO_2 exhibited a glass transition step between 50 °C and 90 °C as exhibited in **Figure 4.20**, similar to the one described for the 25 kDa commercial PEI centered at about 65 °C.[88]
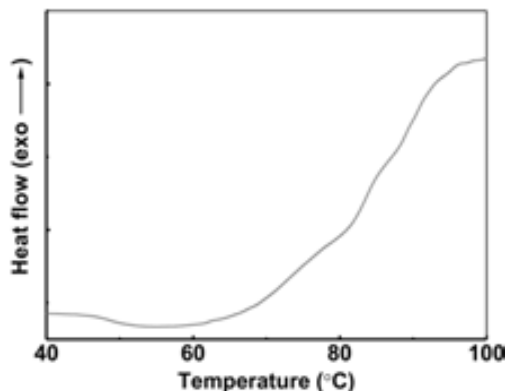
Figure 4.20. Differential scanning calorimetry thermograph of PEI_{CO_2}.

4.3.3.5. Drug release of polyethyleneimine-coated partcicles

Uncoated Trf@AP$_{Fe}$ and coated Trf@AP$_{Fe}$_PEI$_{CO2}$ samples were analyzed by HPLC to assess the influence of the coating in the drug release profile in both acid and basic pH-conditions, as shown in **Figure 4.21**. The percentage of Trf incorporated in each pre-impregnated sample was also determined by HPLC. Values obtained were 2.1 and 1.9 wt% for Trf@AP$_{Fe}$ and PEI$_{CO2}$_Trf@AP$_{Fe}$ samples, respectively; which means only a 9.5 % of drug loss during the coating process in CO$_2$. Impregnated Trf values measured using the HPLC approach were slightly lower than the values estimated by TGA, but nevertheless comparable. Release profiles were not significantly modified by polymer encapsulation when measured in either stomach (pH = 2 in **Figure 4.21a**) or blood plasma (pH = 7.4 in **Figure 4.21b**) pH-simulated fluids.[89] For coated and uncoated composite nanospheres, the drug release occurred very fast and the 95 wt% of the drug was dissolved within the first 30 min. Nevertheless, a slightly accelerated drug delivery was found for the PEI-coated nanoparticles than that for the uncoated ones, which was attributed to the water solubility of the polyethyleneimine layer.
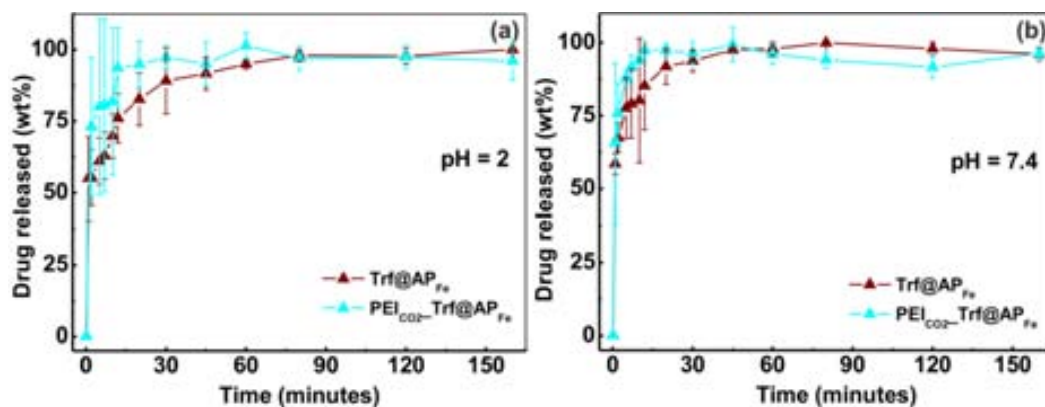
Figure 4.21. Drug delivery profiles obtained for uncoated and coated Trf@AP$_{Fe}$ nanoparticles in aqueous media of: (a) pH = 2, and (b) pH = 7.4.

4.4. CONCLUSIONS

The surface modification of silica-based particles by polymer coating was successfully performed by using compressed CO$_2$ as processing medium. Two different polymers were selected regarding the design of drug carriers; for controlled release (Eudragit® RL 100), and multiple applicabilities in biomedicine (polyethyleneimine).

- Compressed CO$_2$ antisolvent route was here presented as a versatile approach for coating fine particles and preparing hybrid composites made of silica particles, a polymeric coating, and an active pharmaceutical ingredient. For sub-micron sized particles (300 nm), the coating was based on mixing an acetone slurry of aerogel nanoparticles and dissolved polymer with pressurized CO$_2$ in a batch antisolvent mode (GAS method). A semicontinuous antisolvent mode (PCA method) could be applied to encapsulate nanometric particles (65 nm). The

coating was performed without any prefunctionalization of the surface of the silica particles, although, in some cases, they were supercritically pre-impregnated with the therapeutic agent. Our results showed that sub-micron and nanometric porous silica particles were successfully coated by the polymer Eudragit forming loose agglomerates while simultaneously incorporating the drug. While, at both pH = 2 and pH = 7.4, triflusal-loaded particles released almost 100 wt% of the drug in the first 5 min, coating with Eudragit enabled a significant reduction to less than 25 wt% in the first 10 min and prolonging further the release to several hours. In addition, the kinetics of the release was shown to obey the Baker-Lonsdale model indicating a diffusion-controlled delivery of the drug for the sample obtained using the GAS and the PCA methods at acid and basic pH, respectively. The data of the sample prepared by PCA at pH = 2 fitted to the Korsmeyer-Peppas model, exhibiting a Fickian diffusional mechanism.

Compressed CO_2 antisolvent processes are environmentally friendly techniques for fine particles encapsulation/coating with diverse solutes, which have applications as high-added-value pharmaceutical products in relation with their surface chemistry and delivery characteristics.

- PEI-coated silica fine powder was here shown as a versatile delivery system, which can facilitate cellular uptake to increase drug delivery payload, and also be utilized to improve nucleic acids delivery for therapeutic use. PEI was grafted to silica-based particles surface through covalent bonding by using a novel solventless compressed CO_2 procedure, starting with the ring opening polymerization of aziridine. The achieved covalent grafting confers a high thermal and chemical stability. Moreover, the low molecular weight of PEI prepared following the *in situ* polymer synthesis (*ca.*, 8 kDa by SLS) should result in a toxicity decrease of the PEI-coated particles. Owing to the relatively low pressure used in the PEI synthesis procedure, drug pre-impregnated systems could be coated with PEI, avoiding drug degradation, losses of the loaded drug and the modification of pre-designed release profiles.

4.5. REFERENCES

[1] Gombotz, W.R., Pettit, D.K. Biodegradable Polymers for Protein and Peptide Drug Delivery. Bioconjugate *Chem.*, **1995**, *6*, 332-351.

[2] Hughes, G.A. Nanostructure-mediated drug delivery. *Nanomed. Nanotechnol. Biol. Med.*, **2005**, *1*, 22-30.

[3] Yan, F.Y., Gross, K.A., Simon, G.P., Berndt, C.C. Peel-strength behavior of bilayer thermal-sprayed polymer coatings. *J. Appl. Polym. Sci.*, **2003**, *88*, 214-226.

[4] Skirtach, A.G., Volodkin, D.V., Möhwald, H. Bio-interfaces interaction of PLL/HA thick films with nanoparticles and microcapsules. *Chem. Phys. Chem.*, **2010**, *11*, 822-829.

[5] Leyton, P., Domingo, C., Sanchez-Cortes, S., Campos-Vallette, M., Garcia-Ramos, J.V. Surface enhanced vibrational (IR and Raman) spectroscopy in the design of chemosensors based on ester functionalized p-tert-butylcalix[4]arene hosts. *Langmuir*, **2005**, *21*, 11814-11820.

[6] Gomes, J.F.P.S., Rocha, S., Do Carmo Pereira, M., Peres, I., Moreno, S., Toca-Herrera, J., Coelho, M.A.N. Lipid/particle assemblies based on maltodextrin-gum arabic core as bio-carriers. *Colloids Surf., B*, **2010**, *76*, 449-455.

[7] Vezzù, K., Campolmi, C., Bertucco, A. Production of lipid microparticles magnetically active by a supercritical fluid-based process. *Int. J. Chem. Eng.*, **2009**, *781247*, 9 pp.

[8] Sarkar, P.P., Mahato, M., Kamilya, T., Chaudhuri, A., Talapatra, G.B. On the origin of iron-oxide nanoparticle formation using phospholipid membrane template. *Colloids Surf., B*, **2010**, *79*, 384-389.

[9] Caruso, F. Nanoengineering of particle surfaces. *Adv. Mater.*, **2001**, *13*, 11-22.

[10] Ariga, K., Hill, J.P., Ji, Q. Layer-by-layer assembly as a versatile bottom-up nanofabrication technique for exploratory research and realistic application. *Phys. Chem. Chem. Phys.*, **2007**, *9*, 2319-2340.

[11] Domingo, C., Saurina, J. An overview of the analytical characterization of nanostructured drug delivery systems: towards green and sustainable pharmaceuticals. *Anal. Chim. Acta*, **2012**, *744*, 8-22.

[12] Fan, J., Chen, S., Gao, Y. Coating of gold nanoparticles with peptide molecules via a peptide elongation approach. *Colloids Surf., B*, **2013**, *28*, 199-207.

[13] Ebrahiminezhad, A., Ghasemi, Y., Rasoul-Amini, S., Barar, J., Davaran, S. Preparation of novel magnetic fluorescent nanoparticles using amino acids. *Colloids Surf., B*, **2013**, *102*, 534-539.

[14] Cooper, A.I. Polymer synthesis and processing using supercritical carbon dioxide. *J. Mater. Chem.*, **2000**, *10*, 207-234.

[15] López-Aranguren, P., Vega, L.F., Domingo, C. A new method using compressed CO_2 for the *in situ* functionalization of mesoporous silica with hyperbranched polymers. *Chem. Commun.*, **2013**, *49*, 11776-11778.

[16] Roy, C., Vega-González, A., García-González, C.A., Tassaing, T., Domingo, C., Subra-Paternault, P. Assessment of $scCO_2$ techniques for surface modification of micro- and nanoparticles: process design methodology based on solubility. *J. Supercrit. Fluids*, **2010,** *54*, 362-368.

[17] Domingo, C., Vega, A., Fanovich, M.A., Elvira, C., Subra, P. Behavior of poly(methyl methacrylate)-based systems in supercritical CO_2 and CO_2 plus cosolvent: solubility measurements and process assessment. *J. Appl. Polym. Sci.*, **2003**, *90*, 3652-3659.

[18] Seremeta, K.P., Chiappetta, D.A., Sosnik, A. Poly(ε-caprolactone). Eudragit® RS 100 and poly(ε-caprolactone)/Eudragit® RS 100 blend submicron particles for the sustained release of the antiretroviral efavirenz. *Colloids Surf., B*, **2013**, *102*, 441-449.

[19] Cansell, F., Aymonier, C. Design of functional nanostructured materials using supercritical fluids. *J. Supercrit. Fluids*, **2009**, *47*, 508-516.

[20] García-González, C.A., Vega-González, A., López-Periago, A.M., Subra-Paternault, P., Domingo, C. Composite fibrous biomaterials for tissue engineering obtained using a supercritical CO_2 antisolvent process. *Acta. Biomater.*, **2009**, *5*, 1094-1103.

[21] Wang, Y., Dave, R.N., Pfeffer, R. Polymer coating/encapsulation of nanoparticles using a supercritical anti-solvent process. *J. Supercrit. Fluids*, **2004**, *28*, 85-99.

[22] Wang, Y., Pfeffer, R., Dave, R.N. Polymer encapsulation of fine particles by a supercritical antisolvent process. *AIChE J.*, **2005**, *51*, 440-455.

[23] Chen, A.-Z., Kang, Y.-Q., Pu, X.-M., Yin, G.-F., Li, Y., Hu, J.-Y. Development of Fe_3O_4-poly(L-lactide) magnetic microparticles in supercritical CO_2. *J. Colloid Interface Sci.*, **2009**, *330*, 317-322.

[24] Adami, R., Reverchon, E. Composite polymer-Fe_3O_4 microparticles for biomedical applications, produced by supercritical assisted atomization. *Powder Technol.*, **2012**, *218*, 102-108.

[25] Roca, A.G., Costo, R., Rebolledo, A.F., Veintemillas-Verdaguer, S., Tartaj, P., González-Carreño, T., Morales, M.P., Serna, C.J. Progress in the preparation of magnetic nanoparticles for applications in biomedicine. *J. Phys. D Appl. Phys.*, **2009**, *42*, 224002, 11pp.

[26] Sanchez, C., Belleville, P., Popall, M., Nicole, L. Applications of advanced hybrid organic-inorganic nanomaterials: from laboratory to market. *Chem. Soc. Rev.*, **2011**, *40*, 696-753.

[27] Murakami, T., Tsuchida, K., Recent advances in inorganic nanoparticle-based drug delivery systems. *Mini-Rev. Med. Chem.*, **2008**, *8*, 175-183.

[28] Murillo-Cremaes, N., López-Periago, A.M., Saurina, J., Roig, A., Domingo, C. Nanostructured silica-based drug delivery vehicles for hydrophobic and moisture sensitive drugs. *J. Supercrit. Fluids*, **2013**, *73*, 34-42.

[29] Murillo-Cremaes, N., Subra-Paternault, P., Domingo, C., Roig, A. Preparation and study of naproxen in silica and lipid/polymer hybrid composites. *RSC Adv.*, **2014**, *4*, 7084-7093.

[30] Momoh, M.A., Kenechukwu, F.C., Adedokun, M.O., Odo, C.E., Attama, A.A. Pharmacodynamics of diclofenac from novel Eudragit entrapped microspheres. *Drug Deliv.*, **2014**, *21*, 193-203.

[31] Pignatello, R., Bucolo, C., Spedalieri, G., Maltese, A., Puglisi, G. Flurbiprofen-loaded acrylate polymer nanosuspensions for ophthalmic application. *Biomaterials*, **2002**, *23*, 3247-3255.

[32] Mundada, A.S., Avari, J.G. Novel biomaterial for transdermal application: in vitro and in vivo characterization. *Drug Deliv.*, **2011**, *18*, 424-431.

[33] Duarte, A.R.C., Roy, C., Vega-González, A., Duarte, A.M.M., Subra-Paternault, P. Preparation of acetazolamide composite microparticles by supercritical anti-solvent techniques. *Int. J. Pharm.*, **2007**, *332*, 132-139.

[34] Subra-Paternault, P., Vrel, D., Roy, C. Coprecipitation on slurry to prepare drug-silica-polymer formulations by compressed antisolvent. *J. Supercrit. Fluids*, **2012**, *63*, 69-80.

[35] Erriguible, A., Laugier, S., Laté, M., Subra-Paternault, P. Effect of pressure and non-isothermal injection on re-crystallization by CO_2 antisolvent: solubility measurements, simulation of mixing and experiments. *J. Supercrit. Fluids*, **2013**, *76*, 115-125.

[36] Kikic, I., De Zordi, N., Moneghini, M., Solinas, D. Solubility estimation of drugs in ternary systems of interest for the antisolvent precipitation processes. *J. Supercrit. Fluids*, **2010**, *55*, 616-622.

[37] Yeo, S.-D., Kiran, E. Formation of polymer particles with supercritical fluids: a review. *J. Supercrit. Fluids*, **2005**, *34*, 287-308.

[38] López-Periago, A.M., Argemí, A., Andanson, J.M., Fernández, V., García-González, C.A., Kazarian, S.G., Saurina, J., Domingo, C. Impregnation of a biocompatible polymer aided by supercritical CO_2: evaluation of drug stability and drug-matrix interactions. *J. Supercrit. Fluids*, **2009**, *48*, 56-63.

[39] Revelli, A.L., Laugier, S., Erriguible, A., Subra-Paternault, P. High pressure solubility of naproxen, nicotinamide and their mixture in acetone with supercritical CO_2 as anti-solvent. *Fluid Phase Eq.*, **2014**, *373*, 29-33.

[40] Xu, Y., Qu, F., Wang, Y., Lin, H., Wu, X., Jin, Y. Construction of a novel pH-sensitive drug release system from mesoporous silica tablets coated with Eudragit. *Solid State Sci.*, **2011**, *13*, 641-646.

[41] Argemí, A., López-Periago, A., Domingo, C., Saurina, J. Spectroscopic and chromatographic characterization of triflusal delivery systems prepared by using supercritical impregnation technologies. *J. Pharm. Biomed. Anal.*, **2008,** *46*, 456-462.

[42] Kim, H., Fassihi, R. Application of binary polymer system in drug release rate modulation. 2. Influence of formulation variables and hydrodynamic conditions on release kinetics. *J. Pharm. Sci.*, **1997**, *86*, 323-328.

[43] Costa, P., Sousa Lobo, J.M. Modeling and comparison of dissolution profiles. *Eur. J. Pharm. Sci.*, **2001**, *13*, 123-133.

[44] Guo, R., Li, L.-L., Yang, H., Zhang, M.-J., Fang, C.-J., Zhang, T.-L., Zhang, Y.B., Cui, G.-H., Peng, S.-Q., Feng, W., Yan, C.-H. Tuning kinetics of controlled-release in disulfide-linked MSN-folate conjugates with different fabrications procedures. *Mater. Lett.*, **2012**, *66*, 79-82.

[45] Siepmann, J., Peppas, N.A. Modelling of drug release from delivery systems based on hydroxypropyl methylcellulose (HPMC). *Adv. Drug Deliv. Rev.*, **2001**, *48*, 139-157.

[46] Davidson, R.L., Sittig, M. Water-soluble resins. *Van Nostrand Reinhold Inc.*: New York, **1968**.

[47] Huang, X., Brazel, C.S. On the importance and mechanisms of burst release in matrix-controlled drug delivery systems. *J. Control. Release*, **2001**, *73*, 121-136.

[48] Acharya, G., Park, K. Mechanisms of controlled drug release from drug-eluting stents. *Adv. Drug Deliv. Rev.*, **2006**, *58*, 387-401.

[49] Kircheis, R., Wightman, L., Wagner, E. Design and gene delivery activity of modified polyethylenimines. *Adv. Drug Deliv. Rev.*, **2001**, *53*, 341-358.

[50] Pack, D.W., Hoffman, A.S., Pun, S., Stayton, P.S. Design and development of polymers for gene delivery. *Nat. Rev. Drug Discov.*, **2005**, *4*, 581-593.

[51] Kunath, K., Von Harpe, A., Fischer, D., Petersen, H., Bickelb, U., Voigtc, K., Kissel, T. Low-molecular-weight polyethylenimine as a non-viral vector for DNA delivery: comparison of physicochemical properties, transfection efficiency and in vivo distribution with high-molecular-weight polyethylenimine. *J. Control. Release*, **2003**, *89*, 113-125.

[52] Scherer, F., Anton, M., Schillinger, U., Henke, J., Bergemann, C., Krüger, A., Gänsbacher, B., Plank, C. Magnetofection: enhancing and targeting gene delivery by magnetic force in vitro and *in vivo*. *Gene Ther.*, **2002**, *9*, 102-109.

[53] Veiseh, O., Gunn, J.W., Zhang, M. Design and fabrication of magnetic nanoparticles for targeted drug delivery and imaging. Adv. Drug Deliv. Rev., **2010**, 62, 284-304.

[54] Steitza, B., Hofmanna, H., Kamaub, S.W., Hassab, P.O., Hottigerb, M.O., Von Rechenbergc, B., Hofmann-Amtenbrinkd, M., Petri-Fink, A. Characterization of PEI-coated superparamagnetic iron oxide nanoparticles for transfection: Size distribution, colloidal properties and DNA interaction. *J. Magn. Magn. Mater.*, **2007**, *311*, 300-305.

[55] McBain, S.C., Yiu, H.H.P., Dobson, J. Magnetic nanoparticles for gene and drug delivery. *Int. J. Nanomed.*, **2008**, *3*, 169-180.

[56] Xia, T., Kovochich, M., Liong, M., Meng, H., Kabehie, S., George, S., Zink, J.I., Nel, A.E. Polyethyleneimine coating enhances the cellular uptake of mesoporous silica nanoparticles and allows safe delivery of siRNA and DNA constructs. *ACS Nano*, **2009**, *3*, 3273-3286.

[57] Calatayud, M.P., Sanz, B., Raffa, V., Riggio, C., Ibarra, M.R., Goya, G.F. The effect of surface charge of functionalized Fe3O4 nanoparticles on protein adsorption and cell uptake. *Biomaterials*, **2014**, *35*, 6389-6399.

[58] Kim, C.O., Cho, S.J., Park, J.W. Hyperbranching polymerization of aziridine on silica solid substrates leading to a surface of highly dense reactive amine groups. *J. Colloid Interf. Sci.*, **200**3, *260*, 374-378.

[59] Meng, H., Xue, M., Xia, T., Ji, Z., Tarn, D.Y., Zink, J.I., Nel, A.E. Use of Size and a Copolymer design feature to Improve the biodistribution and the enhanced permeability and retention effect of doxorubicin-loaded mesoporous silica nanoparticles in a murine xenograft tumor model. *ACS Nano*, **2011**, *5*, 4131-4144.

[60] Hicks, J.C., Drese, J.H., Fauth, D.J., Gray, M.L., Qi, G., Jones, C.W. Designing adsorbents for CO_2 capture from flue gas-hyperbranched aminosilicas capable of capturing CO_2 reversibly. *J. Am. Chem. Soc.*, **2008**, *130*, 2902-2903.

[61] Kircheis, R., Wightman, L., Wagner, E. Design and gene delivery activity of modified polyethylenimines. *Adv. Drug Deliv. Rev.*, **2001**, *53*, 341-358.

[62] Minakata, S., Okada, Y., Oderaotoshi, Y., Komatsu, M. Lewis base catalyzed ring opening of aziridines with silylated nucleophiles. *Org. Lett.*, **2005**, *7*, 3509-3512.

[63] Kubisa, P., Penczek, S. Cationic activated monomer polymerization of heterocyclic monomers. *Prog. Polym. Sci.*, **1999**, *24*, 1409-1437.

[64] Sakakura, T., Choi, J.-C., Yasuda, H. Transformation of carbon dioxide. *Chem. Rev.*, **2007**, *107*, 2365-2387.

[65] Soga, K., Hosoda, S., Ikeda, S. Copolymerization of carbon dioxide and Ethyleneimine. *Macromol. Chem. Phys.*, **1974**, *175*, 3309-3314.

[66] Dell'Amico, D.B., Calderazzo, F., Labella, L., Marchetti, F., Pampaloni, G. Converting carbon dioxide into carbamato derivatives. *Chem. Rev.*, **2003**, *103*, 3857-3897.

[67] Schladt, M., Filburn, T.P., Helble, J.J. Supported amine sorbents under temperature swing absorption for CO2 and moisture capture. *Ind. Eng. Chem. Res.*, **2007**, *46*, 1590-1597.

[68] Reynhardt, J.P., Yang, Y., Sayari, A., Alper, H. Polyamidoamine dendrimers prepared inside the channels of pore-expanded periodic mesoporous silica. *Adv. Funct. Mater.*, **2005**, *15*, 1641-1646.

[69] Buchman, Y.K., Lellouche, E., Zigdon, S., Bechor, M., Michaeli, S., Lellouche, J.-P. Silica nanoparticles and polyethyleneimine (PEI)-mediated functionalization: a new method of PEI covalent attachment for siRNA delivery applications. *Bioconjugate Chem.*, **2013**, *24*, 2076-2087.

[70] Drese, J.H., Choi, S., Lively, R.P., Koros, W.J., Fauth, D.J., Gray, M.L., Jones, C.W. Adv. Funct. Synthesis-structure-property relationships for hyperbranched aminosilica CO$_2$ adsorbents. *Adv. Funct. Mater.*, **2009**, *19*, 3821-3832.

[71] Jaroniec, C.P., Gilpin, R.K., Jaroniec, M., Adsorption and thermogravimetric studies of silica-based amide bonded phases. *J. Phys. Chem. B*, **1997**, *101*, 6861-6866.

[72] Scott, R.P.W., Traiman, S. Solute-solvent interactions on the surface of silica gel III. Multilayer adsorption of water on the surface of silica gel. *J. Chromatogr.*, **1980**, *196*, 193-205.

[73] Pena, M.L., Della Rocca, V., Rey, F., Corma, A., Coluccia, S., Marchase, L. Elucidating the local environment of Ti(IV) actives sites in Ti-MCM-48: a comparison between silylated and calcined catalysts. *Micropor. Mesopor.*, **2001**, *44*, 345-356.

[74] Hicks, J.C. Organic/inorganic hybrid amine and sulfonic acid tethered silica materials: synthesis, characterization and application. PhD Thesis. Georgia Institute of Technology, **2007**.

[75] Nomura, T., Nakjima, S., Kawabata, K., Yamashita, F., Takakura, Y., Hashida, M. Intratumoral pharmacokinetics and in vivo gene expression of naked plasmid DNA and its cationic liposome complexes after direct gene transfer. *Cancer Res.*, **1997**, *57*, 2681-2686.

[76] Fischer, D., Bieber, T., Li, Y., Elsasser, H.-P., Kissel, T. A novel non-viral vector for DNA delivery based on low molecular weight, branched polyethyleneimine: effect of molecular weight on transfection efficiency and cytotoxicity. *Pharm. Res.*, **1999**, *16*, 1273-1279.

[77] Neu, M., Fischer, D., Kissel, T., Recent advances in rational gene transfer vector design based on poly(ethylene imine) and its derivatives. *J. Gene. Med.*, **2005**, *7*, 992-1009.

[78] Huang, X., Heo, M.S., Yoo, J.-W., Choi, J.-S., Kim, I., Hyperbranched aliphatic polyether esters by ring-opening polymerization of epoxidized 2-hydroxyethyl methacrylate. *J. Polym. Sci., Part A: Polym. Chem.*, **2014**, *52*, 1643-1651.

[79] Shao, W., Paul, A., Abbasi, S., Chahal, P.S., Mena, J.A., Montes, J., Kamen, A., Prakash, S., A novel polyethyleneimine-coated adenoassociated virus-like particle formulation for efficient siRNA delivery in breast cancer therapy: preparation and in vitro analysis. *Int. J. Nanomed.*, **2012**, *7*, 1575-1586.

[80] Clemens, D.L., Lee, B.-Y., Xue, M., Thomas, C.R., Meng, H., Ferris, D., Nel, A.E., Zink, J.I., Horwitz, M.A. Targeted intracellular delivery of antituberculosis drugs to Mycobacterium tuberculosis-infected macrophages via functionalized mesoporous silica nanoparticles. *Antimicr. Agents Chemother.*, **2012**, *56*, 2535-2545.

[81] Von Harpe, A., Petersen, H., Li, Y., Kissel, T. Characterization of commercially available and synthesized polyethylenimines for gene delivery. *J. Control. Release*, **2000**, *69*, 309-322.

[82] Rivera-Tirado, E., Wesdemiotisa, C. Characterization of polyethylenimine by electrospray ionization and matrix-assisted laser desorption/ionization. *J. Mass. Spectrom.*, **2011**, *46*, 876-883.

[83] Rindfleisch, F., DiNoia, T.P., McHugh, M.A., Solubility of polymers and copolymers in supercritical CO_2. *J. Phys. Chem.*, **1996**, *100*, 15581-5587.

[84] Dermer, A. Ethylenimine and Other Aziridines: Chemistry and Applications. *Academic Press, Inc.*: UK, **1969**.

[85] Khan, M., Huck, W.T.S. Hyperbranched polyglycidol on Si/SiO_2 surfaces via surface initiated polymerization. *Macromolecules*, **2003**, *36*, 5088-5093.

[86] Kaneko, Y., Imai, Y., Shirai, K., Yamauchi, T., Tsubokawa, N. Preparation and properties of hyperbranched poly(amidoamine) grafted onto a colloidal silica surface. *Colloids Surf. A: Physicochem. Eng. Aspects*, **2006**, *289*, 212-218.

[87] Yu, Y., Rong, M.Z., Zhang, M.Q. Grafting of hyperbranched aromatic polyamide onto silica nanoparticles *Polymer*, **2010**, *51*, 492-499.

[88] Mady, M.M., Mohammed, W.A., El-Guendy, N.M., Elsayed, A.A. Interaction of DNA and polyethylenimine: Fourier-transform infrared (FTIR) and differential scanning calorimetry (DSC) studies. *Int. J. Phys. Sci.*, **2011**, *6*, 7328-7334.

[89] Ghoroi, C., Gurumurthy, L., McDaniel, D.J., Jallo, L.J., Davé, R.N. Multi-faceted characterization of pharmaceutical powders to discern the influence of surface modification. *Powder Technol.*, **2013**, *236*, 63-74.

5

PRELIMINARY BIOLOGICAL EVALUATION OF THE SILICA-BASED MATERIALS FOR BIOMEDICAL APPLICATIONS
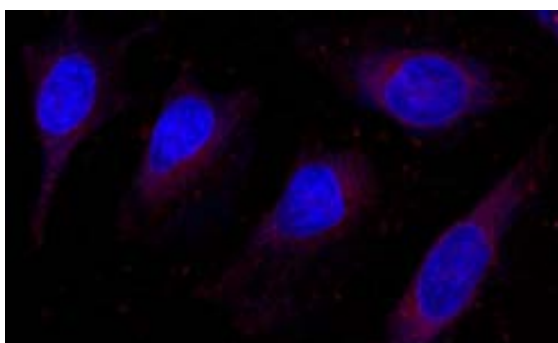
During the last decades, silica-based materials have been one of the most explored systems aiming at several applications within biomedicine. They have shown promising properties for their use as drug delivery systems and cell tracking among others, therefore promoting a vast production of silica-based products with numerous shapes, microstructure and surface functionality to target specific requirements. However, their behavior in biological environments is still under discussion and more efforts have to be devoted in understanding their interaction with biological systems.

This chapter deals with the preliminary study of the silica-based materials described in **Chapter 2** as potential drug carriers, in terms of degradability, colloidal stability in biological media, cytotoxicity and cellular uptake. Strategies of silica surface functionalization with the goal of overcoming problems encounter in bioapplications are also shown.

5.1. DEGRADATION OF SILICA-BASED MATERIALS IN BIOLOGICAL MEDIA

When designing materials for its use in medicine, an important feature to be studied is their biodegradability, meaning the capability of being degraded by biological agents. An extremely fast degradation in biological media should be avoided in order to allow the systems to develop its function, but a very low degradation rate leading to the accumulation of the product in the organism may induce undesired side effects.[1,2] Thereby, a compromise between a sufficient biological half-life and an efficient biodegradability must be accomplished by the materials used for *in vivo* applications.

Although silica is considered an inert and stable material in aqueous media, it is known that amorphous silica can readily be dissolved in highly alkaline media (pH > 11) through the Si-O bond cleavage to form silicic acid ($Si(OH)_4$).[3,4] Moreover, this process has also been observed in basic and acid environments.[5,6,7] A special mention is here devoted to porous silica materials, both monolithic and particulate, which have dissolution rates strongly depending on the surface area and pore structure.[8,9,10]

Herein, the dissolution of the silica-based particles and silica aerogels, at both stomach and blood stream-pH conditions, was monitored along the time. Briefly, around 75 mg of samples AP_{Fe}, AP (previously calcinated at 300 ºC for 24h) and AM were weighed twice and placed on lab beakers. Then, they were covered with 150 mL of 10 mM HCl (pH = 2.0, as the stomach) or 10 mM $Na_2HPO_4/NaH_2PO_4 \cdot 2H_2O$ (pH = 7.4, as the blood stream) solutions previously heated at 37 ºC. Magnetic stirring at 60 rpm was applied during the experiments. Aliquots of 3 mL were withdrawn at different times during 30 days and the equivalent volume of fresh solution was added to the beakers. The aliquots were filtered with a 0.45 µm filter (VWR International) and the filtered solution was analyzed by ICP-MS giving the concentration of Si dissolved in the media from the solids. **Table 5.1** gathers the textural characteristics of the silica materials, which are important to explain the degradation experiments.

Table 5.1. Textural properties and particle diameter of the silica-based systems.

Sample	S_{BET} (m^2/g)	Mean pore size (nm)	Φ_{TEM} (nm)
AP_{Fe}	210	2.3	177
AP	205	2.3	303
AG	429	6.8	-

The weight amount of SiO_2 remaining in the solutions at pH = 2 and pH = 7.4 as a function of time is represented in **Figure 5.1**. The particles AP_{Fe} and AP remained highly stable in acid medium showing negligible silica dissolution (98 wt% of remaining silica was found at 30 days in both samples). In contrast, the aerogel monolith (AG) presented a certain degree of dissolution. This difference was attributed to the higher surface area available to be wetted by the liquid medium in the AG monolith compared to the microporous particles. As expected, a faster

dissolution rate was observed for all the silica-based materials at basic pH. Hence, the degradation profiles in the phosphate buffer solution were characterized by a fast silica dissolution rate during the first 8 h, followed by a plateau in the case of particles and a slow and progressive further dissolution for the aerogel sample. The fact that the silica particles, AP, where the least dissolved, even below the composite nanospheres, could be explained by the calcination process performed, which caused the dehydration of the silica and forming a dense network structure that hinders its degradation.[11] Again, the monolith presents the largest solubility at pH = 7.4 due to its high porosity.
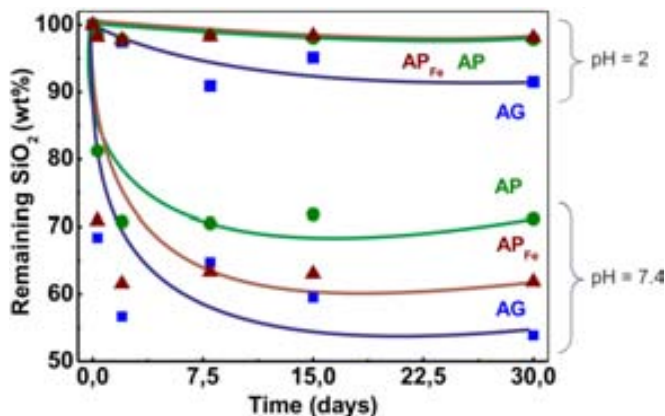
Figure 5.1. Remaining SiO_2 *vs.* time for monolith and particulate silica-based matrices immersed in aqueous media at acid and basic pH (37 ºC, 60 rpm). Solid lines serve as a guide to the eye.

5.2. COLLOIDAL STABILITY OF SILICA-BASED PARTICLES

Aggregation of nanoparticles can significantly change when they are transferred into biological systems. Here, the colloidal behavior of our silica-based particles was studied in different biological media and pH ranges regarding cluster size and surface charge, ξ-potential measurements.

Particles aggregation in biological media

Both types of particles, AP_{Fe} and AP, were analyzed by DLS after being dispersed at a concentration of 0.4 mg/mL in different biological fluids: phosphate buffered saline (PBS), minimum essential medium (MEMα) enriched with 10 % of fetal bovine serum (FBS), all purchased from Life Technologies (Invitrogen). For comparison purposes, the measurements were also performed in EtOH and water. Hydrodynamic diameters were determined based on the average of the intensity-weighted particle size distribution of three measurements.

Figure 5.2a and **Figure 5.2b** show the size distribution of AP_{Fe} and AP in different liquid media, respectively. It is worth to note that AP_{Fe} nanoparticles exhibited an increased stabilization when the fluid was supplemented with serum, presenting the smallest $\Phi_{Hyd.}$ when dispersed in MEMα + FBS (480 nm). This value was even lower than the one found when particles were dispersed in

EtOH (550 nm). However, without proteins, the nanoparticles readily aggregated reaching hydrodynamic diameters of near 1 μm in MEMα and up to more than 2 μm in water and PBS, showing in addition broader size distributions. AP particles showed similar behavior in all the fluids, with cluster sizes between 570 and 640 nm, except in PBS, where they tended to form aggregates of around 1 μm with a broad size distribution.

In contrast with the results found by other research groups,[12,13] particles studied in this thesis deagglomerated or at least they did not show larger aggregates when dispersed in supplemented media. We argue that a specific type of protein or biomolecule is preferentially adsorbed on the silica surface over the rest and thus reducing the interaction with other particles and stabilizing the colloidal system. The tendency of the particles to stabilize with the enrichment in proteins of the fluid is clearly shown in **Figure 5.3**.

Precipitation of particles was not observed in any of the studied systems.
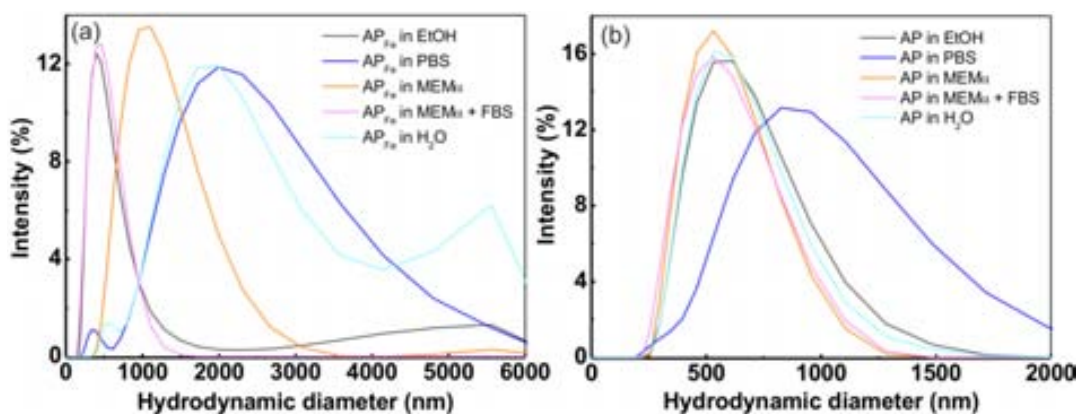
Figure 5.2. DLS intensity-weighted size distributions for: (a) AP$_{Fe}$, and (b) AP particles in biological media, EtOH and water.
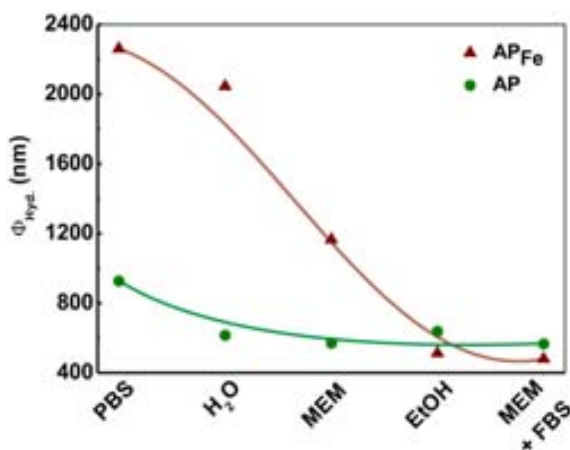
Figure 5.3. Hydrodynamic cluster diameters of particles AP$_{Fe}$ and AP in biological media, EtOH and water. Solid lines serve as a guide to the eye.

For sample AP_{Fe}, the zeta potential was also measured by DLS. The obtained results are summarized in **Table 5.2** as the average of three measurements with the Φ_{Hyd} data. The charge of the composite nanospheres increased from -40 mV in water to near -20 mV in both PBS and complete cell culture medium. Despite of having similar zeta potentials, nanoparticles were much more stable in MEMα + FBS than in PBS. We explain this finding as an additional indication of the adsorption of a specific protein on the particles surface, which would stabilize the colloidal systems by combining electrostatic repulsions and steric impediments.[14]

Table 5.2. ξ-potential and hydrodynamic diameter measured by DLS in water, PBS and MEMα + FBS at 25ºC for AP_{Fe} nanoparticles,.

Medium	ξ-potential (mV)	$\Phi_{Hyd.}$ (nm), by Intensity
H_2O	-40	2045
PBS	-17	2261
MEMα + FBS	-20	480

Nanoparticles aggregation as a function of pH

The size of the AP_{Fe} nanoparticles agglomerates in water as a function of pH was also investigated. The hydrodynamic diameters were measured by DLS between pH = 1.8 and 11.8 at 25 ºC. In **Figure 5.4** the obtained results are plotted as $\Phi_{Hyd.}$ *vs.* pH. It was observed that large aggregates were formed in acidic conditions, probably due to an inhomogeneous distribution of the charge, while the minimum aggregate size is observed between pH = 6 and 8 that are considered physiological conditions. Particle size slightly increased at basic pH values.
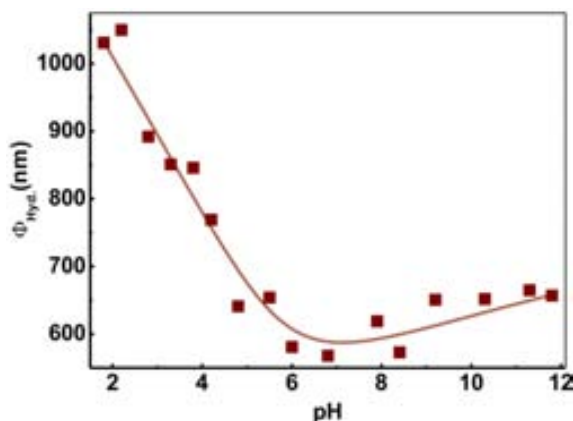
Figure 5.4. Evolution of the cluster size as a function of pH measured by DLS for AP_{Fe},.

5.3. CYTOTOXICITY EVALUATION OF IRON OXIDE-SILICA NANOPARTICLES

Cytotoxicity is defined as the quality of being toxic to cells. Cells exposed to a cytotoxic compound can respond in a number of ways altering their normal functioning. Regarding nanomaterials, especially nanoparticles, the new interactions that would appear between those

materials and biological functional units within cells must be studied. In addition, they depend on many factors such as cell line, chemical nature, size, shape and porosity of the nanomaterials, as well as the time of incubation. The analysis of toxicity at the nanoscale is nowadays an emerging discipline that is still in its infancy. Although living organisms are more complex than cells, cytotoxicity studies in cell cultures are considered the first necessary step to establish how toxic a material is.

A revision of the bibliography of toxicity for silica nanoparticles reports contradictory findings. Several authors have found that those particles are non toxic and biocompatible for both healthy and cancer cell lines.[15,16,17,18,19,20] However, other research groups have reported harmful effects in different cell lines.[20,21,22,23,24] The severity of this toxicity is conditioned by the size, shape, porosity and concentration[25] of the particles, but also by the density of silanol groups (Si-OH) on the surface accessible to the cells.[21] Hence, a specific study on each material of interest should be performed.

In this work, the cell viability when exposed to composite AP_{Fe} nanoparticles was evaluated with the MTT assay by Dr. Maria Milla. The cell line of choice was the human cervical cancer cells (HeLa) obtained from American Type Culture Collection (ATCC, Manassas, VA). Particles $AP_{Fe\_}3$ and $AP_{Fe\_}5$, with mean diameters of 65 and 177 nm, respectively, were used at concentration of 25, 50 and 100 µg/ml. Basically, the cells were detached from growth flask by using treatment with 0.25 % (w/v) trypsin-EDTA (incubation for 1 min.), re-suspended in MEMα medium supplemented with 10 % FBS and 2 mM GlutaMax, all purchased from Life Technologies (Invitrogen), and pelleted by centrifugation at 1400 rpm for 5 min. For cells growth, they were plated at a concentration of $5 \cdot 10^4$ cells/mL in a 96 well-plate and incubated for 24 h at 37 ºC and an atmosphere of 5 % CO_2. The following day, the media was replaced by the particles dispersions in fresh supplemented medium, which were just prepared in sterile conditions, and the plate was incubated as before for another 13 h. Next, MTT reactive (Bio-Medica) was added up to 10 % (v/v) and the plate was incubated for 1 h and read in a micro plate reader (Victor3, Perkin Elmer) at 450 and 620 nm as reference. Three wells were treated for every sample and the results were expressed as: mean ± SD.

Figure 5.5 presents the cell viability in presence of the composite particles at the selected concentrations. Surprisingly, materials can be considered toxic when the cell viability is lower than 90 %[26] and it is indicated in the figure with a dashed line. AP_{Fe} nanoparticles were in all cases toxic for the cells at the used conditions. However, when the time of incubation was reduced to 1 h, the cell viability was not affected and the 100 % of the cell survive to the particles exposition (shown in **Section 5.6.3**). It was also observed that the cell viability decreased while the particles size increased. Obviously, the particles concentration have an influence on the toxicity degree: the cells were less affected at 25 µg/mL than at 50 or 100 µg/mL. Those are preliminary results and more tests should be performed at different incubation times and

concentrations to know the optimal conditions at which HeLa cells would be treated with the AP_{Fe} nanospheres.

No previous sterilization of the nanoparticles or antibiotic to the culture medium was used.
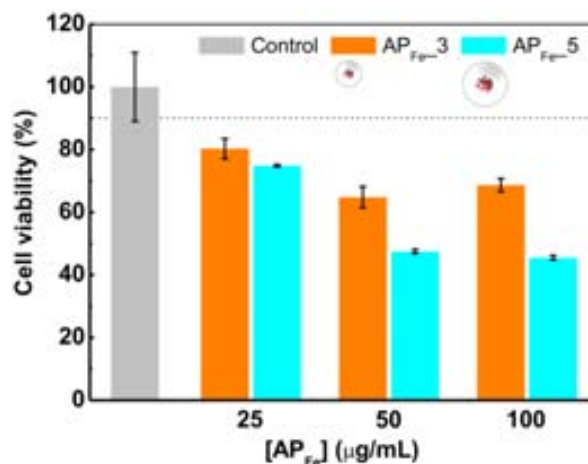
Figure 5.5. HeLa cells viability in the presence of particles of AP_{Fe}_3 and AP_{Fe}_5. Error bars were calculated from the deviation standard of the results obtained in three wells. The dashed line at 90 % of cell viability is a guide for the eye.

5.4. POLYETHYLENE GLYCOL COATING OF SILICA-BASED PARTICLES

One of the most common strategies to enhance the particles biocompatibility and colloidal stability is the coating with polyethylene glycol (PEG), a nontoxic polymer that provides steric hindrance when attached to the particles improving their dispersion. Besides, it is well recognized that PEG prevents nonspecific adsorption of proteins[27,28] and uptake by the reticuloendothelial system (RES), rendering a long circulation time in the blood-stream for the *PEGylated*-materials,[29,30,31] which is highly desirable for *in vivo* applications. For these reasons, the modifications of particles surface using PEG have been widely used in fields such as drug delivery systems or biosensing technology.[32]

PEG is a simple linear polymer soluble in water. The chemical structure of PEG is illustrated in **Figure 5.6**.
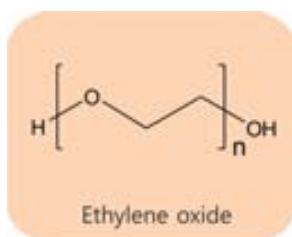
Figure 5.6. Chemical structure of the polyethylene glycol.

In this work, AP_{Fe} and AP particles were coated with a diacid derivative of PEG: polyethylene glycol bis(carboxymethyl) ether (PEG-(COOH)$_2$). The chemical structure of this PEG derivative is

shown in **Figure 5.7**. The obtained materials were fully characterized confirming satisfactory results on their PEGgylation.

Figure 5.7. Chemical structure of the polyethylene glycol bis(carboxymethyl) ether.

5.4.1. Method of silica-based particles coating with polyethylene glycol

To coat both AP_{Fe} and AP silica-based particles, a mixture of ~ 50 mg of the particles, 2.8 mL of polyethylene glycol bis(carboxymethyl) ether (PEG-$(COOH)_2$, Sigma-Aldrich) and 120 mL of H_2O was prepared, sonicated for 30 min. and magnetically stirred during 24 h at 300 rpm. The particles were then precipitated by centrifuging at 5000 rpm for 20 min. and three washes with 200 mL of fresh water, following the protocol of first sonication for 5 min. and then centrifugation at 5000 rpm for 20 min. The samples obtained are labeled as PEG_AP_{Fe} and PEG_AP for composite AP_{Fe} and AP particles coated with PEG, respectively.

5.4.2. Size and morphology of polyethylene glycol-coated particles

Transmission electron microscopy (TEM)

The PEG-coated particles dispersed in EtOH were observed by TEM to confirm the presence of the polymer. **Figure 5.8** shows a TEM image of the sample PEG_AP where a thin layer of polymer on the particles surface can be seen.

Figure 5.8. TEM image of the PEG_AP particles. The arrow points the polymer.

5.4.3. Structural characterization of polyethylene glycol-coated particles

Fourier transformed infrared spectroscopy (FTIR)

The successful polymer grafting on the surface of the silica-based particles was confirmed by using FTIR. In **Figure 5.9**, the spectra of PEG_AP$_{Fe}$ and PEG_AP and the commercial polymer PEG-(COOH)$_2$ in the useful wavelength range of 300-1300 cm^{-1} are presented. The polymer showed different characteristics peaks at 1349, 1457 and 1741 cm^{-1} that were attributed to the hydroxyl (O-H), alkyl (CH$_2$) and carbonyl groups (C=O) vibrations, respectively. For both PEG-covered particles, the signals corresponding to O-H appeared slightly shifted to lower wavelengths, while the peaks due to the alkyl groups were tentatively observed as shoulder around 1405 and 1485 cm^{-1} (dashed circles in **Figure 5.9**). The coated particles were repeatedly washed with large amounts of water before measurements to rinse off the PEG polymer physically adsorbed on the silica surface. Thereby, the C=O signal appeared shifted to 1701 (PEG_AP$_{Fe}$) and 1713 cm^{-1} (PEG_AP), suggesting the formation of a covalent bond between the silica surface and the polymer.[33,34]
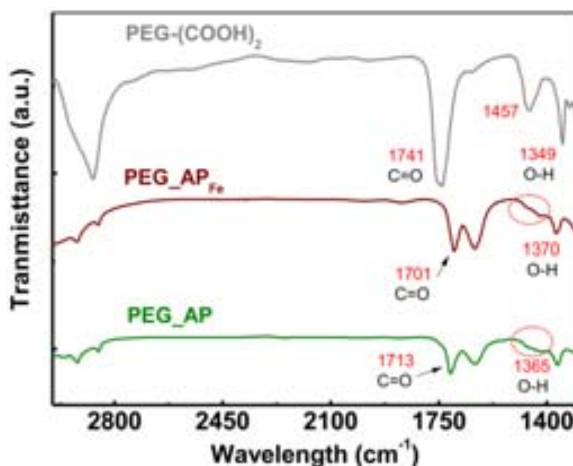
Figure 5.9. FTIR spectra in the range 3000-1300 cm^{-1} of the PEG-coated particles, and commercial PEG-(COOH)$_2$. Dashed circles mark the signal of alkyl CH$_2$ groups appearing as shoulder.

Thermal gravimetric analysis (TGA)

The amount of PEG covering the particles surface as well as the thermal stability of the hybrid materials was assessed by TGA measurements. It is reported that a synthesized PEG-COOH polymer looses physically adsorbed water in the temperature range from 0 to 150 ºC and then decomposed up to 410 ºC.[33] The TGA profile of the commercial PEG-(COOH)$_2$ used in this work indicates that the polymer mainly decomposed in the range of 260-440 ºC, losing the 92 wt% of the total weight (**Figure 5.10a**). For the PEGylated AP$_{Fe}$ nanoparticles, the weight loss attributed to the polymer is shifted to higher temperatures: from 280 up to 475 ºC, indicating the presence of chemical bonds that confer thermal stability to polymer in the hybrid material (**Figure 5.10b**).

For sample PEG_AP, the polymer decomposition was assigned to the weight loss in the region from 290 to 390 °C (**Figure 5.10b**). In **Table 5.3**, the polymer percentages estimated for the coated particles are shown.
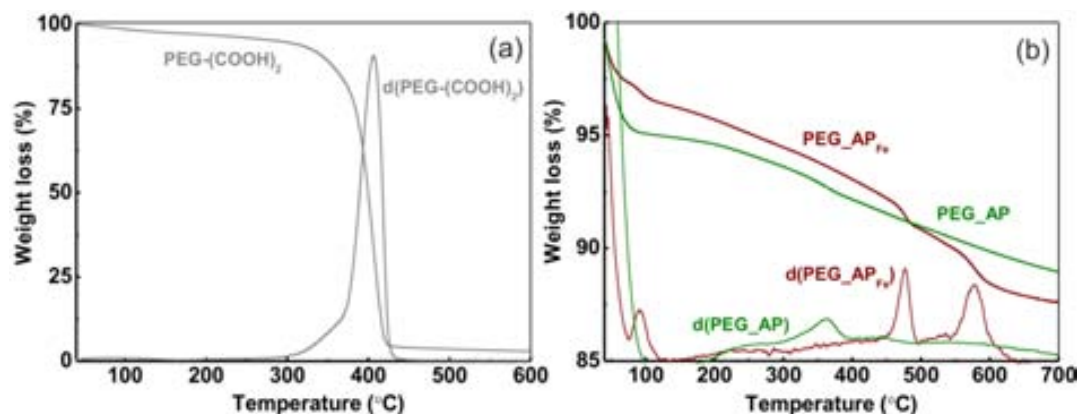
Figure 5.10. TGA profiles of: (a) raw PEG-(COOH)$_2$, and (b) PEG-coated AP$_{Fe}$ and AP particles. *d(xx)* profiles correspond to the first derivative curves.

Table 5.3. Estimated PEG weight percentage from TGA data, together with ξ-potential and hydrodynamic diameter measured by DLS in water at 25°C for the PEG-coated samples.

Sample	PEG (wt%)	ξ-potential (mV)	$\Phi_{Hyd.}$ (nm), by Intensity
AP$_{Fe}$	-	-40	304
PEG_AP$_{Fe}$	3.2	-20	319
AP	-	-65	627
PEG_AP	1.4	-25	573

The samples were characterized by DLS to know the influence of the polymer coating on the colloidal stability of the particles. Dispersions in water at 0.1 mg/mL were used for the measurements. The PEG functionalization of the silica surface changed the zeta potential of the silica-based particles in water from highly negative (≤ -40 mV) to less negative (≥ -25 mV), as it is listed in Table 5.3. Nevertheless, the colloidal stability of the dispersions was maintained after the coating, exhibiting similar hydrodynamic diameters than the pristine materials and no sedimentation was observed during hours.

5.5. CELL INTERNALIZATION OF IRON OXIDE-SILICA NANOPARTICLES

The cellular uptake of the composite AP$_{Fe}$ nanoparticles was preliminarily studied by confocal microcopy. First, the nanoparticles were successfully labeled with a fluorescent dye by chemically modifying the silica surface. The presented work was done in collaboration with Elif Ertem from the Ècole Polythecnique Fèderale de Laussanne (EPFL), who was in charge of marking the silica surface of the particles with the fluorescent molecule.

5.5.1. Method of fluorescence-labeling of iron-oxide silica nanoparticles

The labeling of AP_{Fe} nanospheres with a fluorescent compound was performed in two steps: first, the modification of the silica surface with amino groups (NH_2) was carried out using an aminosilane and second, the covalent grafting with a fluorophore was performed. The experimental procedures followed are next explained.

Amino group functionalization

Briefly, 68 mg of AP_{Fe} particles were dispersed in 136 mL of EtOH and sonicated for 30 min. Then, 170 µL of (3-aminopropyl)triethoxysilane (APTES, Sigma-Aldrich) were added and the mixture was magnetically stirred at 80 °C under reflux during 7 h. The particles were washed three times with EtOH using magnetic decantation. The obtained amine-functionalized particles are labeled as *AP_{Fe}-NH₂* and schematized in **Figure 5.11**.
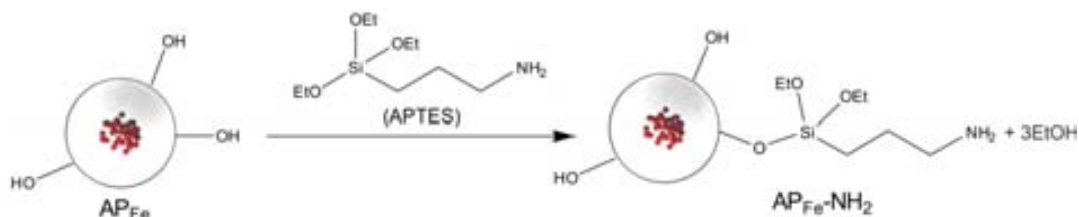
Figure 5.11. Schematic representation of amino functionalization of AP_{Fe} nanoparticles.

Fluorescence-labeling

0.5 mg of succinimidyl ester of the BODIPY® 630/650-X dye (BODIPY® 630/650-X NHS ester, Invitrogen) were dissolved in 1 mL of dymethylformamide (DMF, Sigma-Aldrich). This dye contains the amine-reactive group n-hydroxysuccinimide (NHS), which would form amide groups (R-CO-NH-R′) on the silica surface by undergoing chemical conjugation with the amines. In another flask, 8 mg of AP_{Fe}-NH₂ particles were dispersed in 1 mL of water + 6 mL of PBS (pH = 8.9, Ambion Life Technologies). Then, the solution was left to react under magnetic stirring at room temperature and dark conditions for 3 h. The resultant samples are named as *AP_{Fe}-BODIPY*. **Figure 5.12** presents a schematic representation of the dye linked to the particles surface.
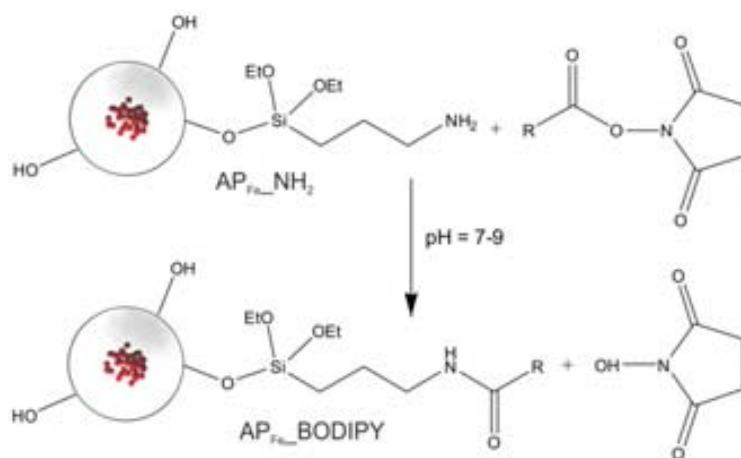
Figure 5.12. Schematic representation of the synthesis of the fluorescent AP_{Fe} nanoparticles.

5.5.2. Internalization of iron oxide-silica nanoparticles in HeLa cells

The cellular uptake and distribution of the composite nanoparticles as well as the possible changes in cell structure in presence of particles was monitored by confocal microcopy by Dr. Maria Milla. Prior to their observation, HeLa cells were seeded as previously explained and the particles were incubated for 1 h at 0.1 mg/mL and washed twice with PBS. Then, the cells were stained with 10 µg/mL Hoechst (cell nucleus) at room temperature for 5 min. and washed twice with PBS. Three dimensional reconstructions were processed with Imaris sorftware. For comparison, the same protocol for cell incubation was followed with the particles up to 13 h.

Figure 5.13 shows upper views of confocal microscopy for the cells after 1 h of AP_{Fe}-BODIPY nanoparticles incubation. The cell nucleus appeared in blue while the particles showed red color after exciting the culture sample at 405 and 640 nm, respectively. As seen in the images, the nanospheres were distributed in the cytoplasm, mainly accumulated in the perinuclear region, but without penetrating the nucleus (**Figure 5.13a**). Moreover, small amounts of particles were identified outside the cells as bright red spots that may be big aggregates unable to be uptaken by the cells. Regarding cell damage, several authors have found that apoptosis (a mechanism of cell death) occurs accompanied by ultrastructural changes, like volume reduction of nucleus and cytoplasm and abnormal cell membranes.[35,36] After the particles incubation, cells did not exhibit signs of apoptosis having their previous characteristic shape with the nuclear and cell membranes remaining continuous and the cytoplasm with a similar volume (**Figure 5.13b**). Those findings indicated that the cells were not affected by the presence of the nanoparticles up to 1 h. The lack of cell alteration is clear when comparing the images with the upper views of confocal microscopy for the control cells (**Figure 5.14a** and **Figure 5.14b**), which had cell membranes and nucleus with comparable shapes to those found for the AP_{Fe}-BODIPY incubation.

Figure 5.13. Confocal microscopy upper views for HeLa cells after 1 h incubation (37 °C, 5 % CO_2) of AP_{Fe}-BODIPY nanoparticles at: (a) low, and (b) high magnification. Nucleus stained with Hoechst and AP_{Fe}-BODIPY showed blue and red color respectively.
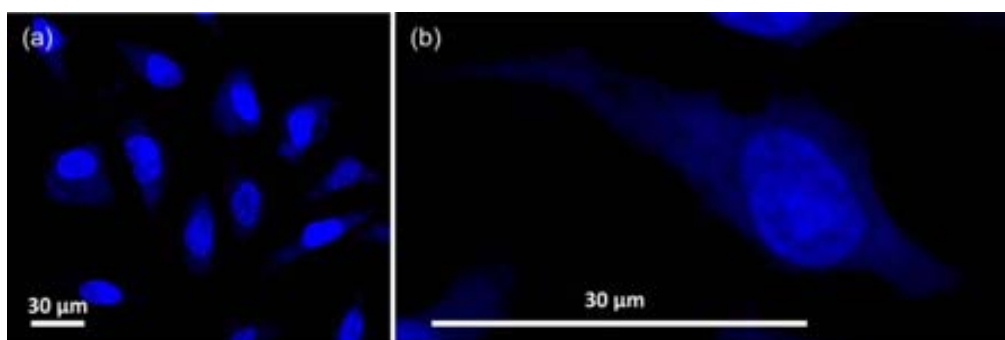
Figure 5.14. Confocal microscopy upper views for control HeLa cells after 1 h incubation (37 °C, 5 % CO_2) at: (a) low, and (b) high magnification. Nucleus stained with Hoechst showed blue color.

When cells were treated with AP_{Fe}-BODIPY nanoparticles for 13 h, cellular uptake increased considerably with respect to the incubation for 1 h (**Figure 5.15a)**. However, the cells suffered apoptosis showing nucleus of shrinkage volume and half-moon appearance, which is also a characteristic feature of this process[36] (**Figure 5.15b**). These results were in agreement with the low cell viability that was previously described above (see **Section 5.3**).
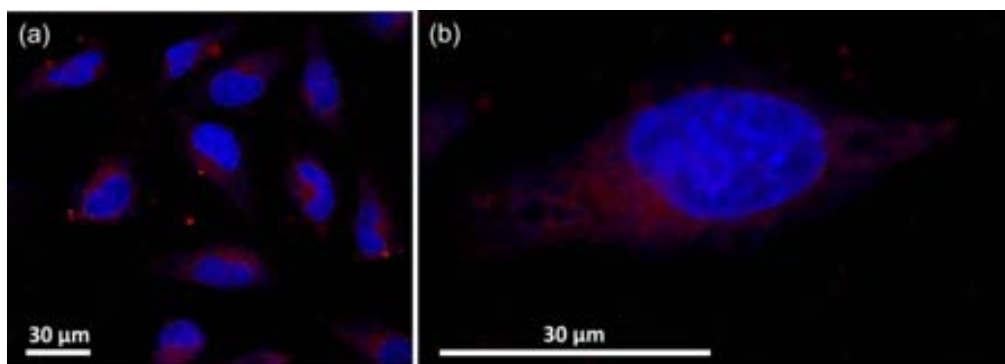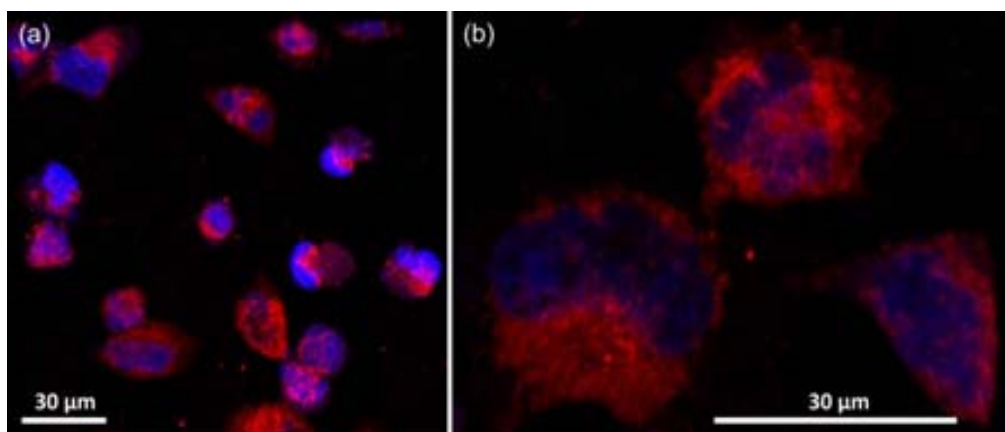
Figure 5.15. Confocal microscopy upper views for HeLa cells after 13 h incubation (37 ºC, 5 % CO_2) of AP_{Fe} nanoparticles at: (a) low, and (b) high magnification. Nucleus stained with Hoechst and AP_{Fe}-BODIPY showed blue and red color respectively.

5.6. DECORATION OF IRON OXIDE-SILICA NANOPARTICLES WITH GOLD NANOPARTICLES AND CELL INTERNALIZATION

Knowing that the surface of the nanoparticles plays an important role on the cellular uptake efficiency, AP_{Fe}-NH_2 nanoparticles were decorated with two types of functionalized gold nanoparticles and the resulting materials were internalized in cells and studied by different techniques. The gold particles were in turn functionalized as *Janus particles* (*JPs*). Those JPs present two distinguished surfaces/chemistries on the two sides, usually made of non-miscible materials, such as hydrophobic *versus* hydrophilic or positive *versus* negative charge. **Figure 5.16** shows a schematic representation of several examples of Janus particles.

Figure 5.16. Schematic representation of some possible Janus particles. Red and yellow colors represent the different domains.[38]
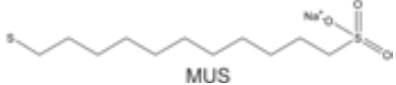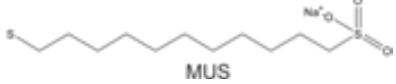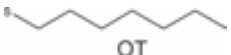
Actually, many fundamental biological structures show simple Janus motives. For instance, cell membranes are bilayers assembled from phospholipids, which are amphiphilic molecules with Janus geometry.[37] Due to their asymmetric structures, JPs possess vastly different physical and biochemical properties, which is especially interesting for applying this kind of materials to biomedicine.[38] In this work, two kinds of Janus gold nanoparticles (all hydrophilic and striped-like hydrophilic and hydrophobic) were attached to the surface of the previously functionalized AP_{Fe}-NH_2 and incubated with cells to study the influence of the surface polarity in the cellular uptake and distribution. The results were compared with those found for pristine AP_{Fe} particles. This was a project done in collaboration with Elif Ertem in Prof. Francesco Stellacci group from the EPFL, who synthesized and partially characterized the iron oxide-silica nanoparticles decorated with the gold ones.

5.6.1. Method of gold-decoration of iron oxide-silica nanoparticles

Two types of ligand-coated gold nanoparticles of 3-4 nm in diameter were first synthesized. Particles were coated with 11-mercapto-1-undecanesulphonate (MUS) and a 2:1 molar mixture of MUS and 1-octanethiol (OT). They are labeled as *MUS_Au* and *MUS-OT_Au*, respectively. **Table 5.4** shows a schematic representation of the capped particles and the chemical structures of the organic ligands together with the concentration of ligand obtained by TGA. Note that the MUS-

OT_Au nanoparticles were functionalized in a striped-like arrangement with the hydrophilic (cationic) MUS and hydrophobic OT ligands. MUS_Au and MUS-OT_Au nanoparticles were further functionalized with NHS groups and finally linked to the AP_{Fe}-NH_2 particles. The followed experimental procedures are next explained, and the resultant materials characterization is displayed.

Table 5.4. For ligand-coated gold nanoparticles, scheme of the particles, chemical structure and amount of the organic ligands.

Sample	Particle scheme	Organic ligand	Organic ligands amount (wt%)
MUS_Au		MUS	21.4
MUS-OT_Au		MUS	21.6
		OT	

N-hydroxysuccinimide functionalization of ligand-coated gold nanoparticles

Basically, 3 mg of ligand-coated gold nanoparticles were dissolved in 2.5 mL of water. In another flask, 2 mg of *n*-hydroxysuccinimidyl 11-mercaptoundecanoate (SH-$(CH_2)_{10}$-COO-NHS, Prochimia Surfaces) were dissolved with 2-3 drops of DMF and added to the previous solution. After 15 min. of magnetic stirring, the particles were cleaned with a Sephadex column and washed with water. The particles obtained are labeled as *MUS_Au-NHS* and *MUS-OT_Au-NHS* for the MUS and MUS-OT functionalized gold nanoparticles, respectively. This process consisted in a ligand exchange reaction. Since the time of this reaction was very short, only the most reactive parts of the nanoparticles underwent ligand exchange with molecule SH-$(CH_2)_{10}$-COO-NHS. Those parts, that in our case were the MUS ligands, are commonly expressed as *poles* and the ligand exchange involving them is known as *pole functionalization*.

Synthesis of gold-decorated iron-oxide silica nanoparticles

Briefly, 50 mg of AP_{Fe}-NH_2 particles were dispersed in 20 mL of water with 5-6 drops of 1 M HCl (Sigma-Aldrich). Then, 70 mL of PBS (pH = 8.9) were added to the dispersion. The mixture was sonicated for 10 min. Then, 8.4 mg of MUS_Au-NHS or MUS-OT_Au-NHS dispersed in 6.5 mL of water were added and the mixture was magnetically stirred overnight at room temperature and dark conditions. The collected particles are called *MUS_AP$_{Fe}$* and *MUS-OT_AP$_{Fe}$* for the MUS and MUS-OT functionalized NHS-gold nanoparticles, respectively. The produced particles are schematically represented in **Figure 5.17**.
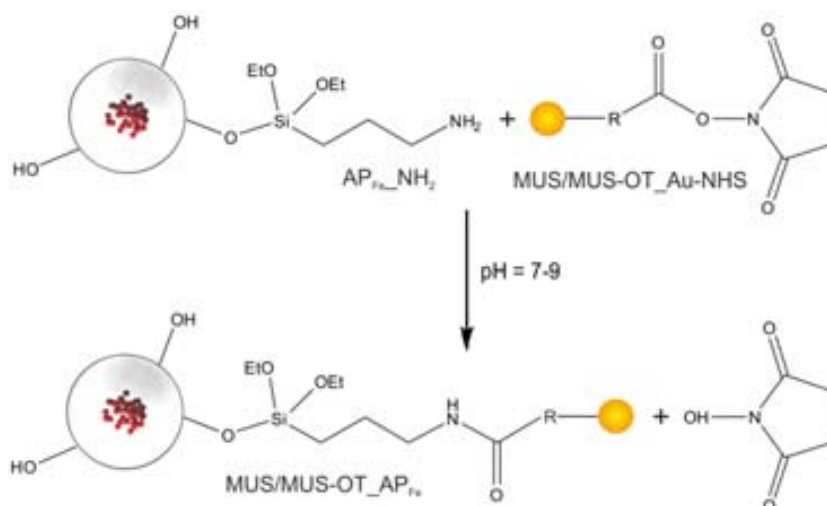
Figure 5.17. Schematic representation of the synthesis of the gold-decorated AP_{Fe} nanoparticles. (●) stands for both types of ligand-capped gold nanoparticles: MUS_Au (●) or MUS-OT_Au (●)

The hybrid structure of the synthesized gold-decorated AP_{Fe} particles was studied by **TEM** and energy dispersive X-ray (**EDX**) emission spectroscopy.

Figure 5.18 shows the TEM images of the core-shell particles capped with the two types of gold nanoparticles (GNPs), in which it was clearly appreciated that the silica surface was homogenously covered with gold nanospheres.
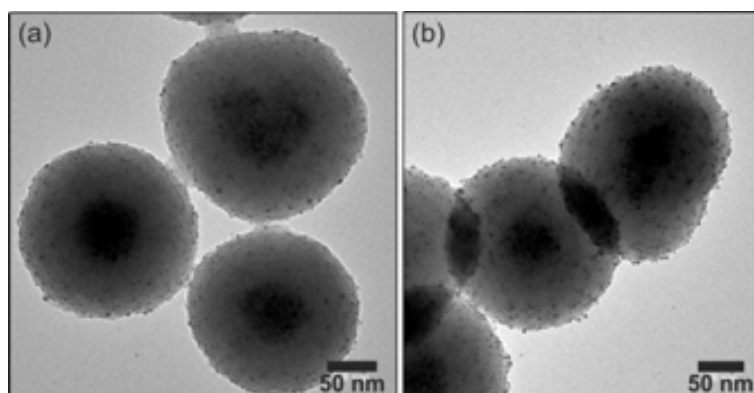
Figure 5.18. TEM images of gold-decorated AP_{Fe} nanoparticles with: (a) MUS_Au, and (b) MUS-OT_Au.

An elemental mapping analysis from the EDX spectra evidenced the presence and the spatial location of the three different materials composing both the MUS_AP_{Fe} and $MUS\text{-}OT\_AP_{Fe}$ nanoparticles (**Figure 5.19**). While the Si was forming the whole spheres (green dots), the Au appeared covering them (blue dots) and the Fe was confined inside the silica forming the particles core (red dots).
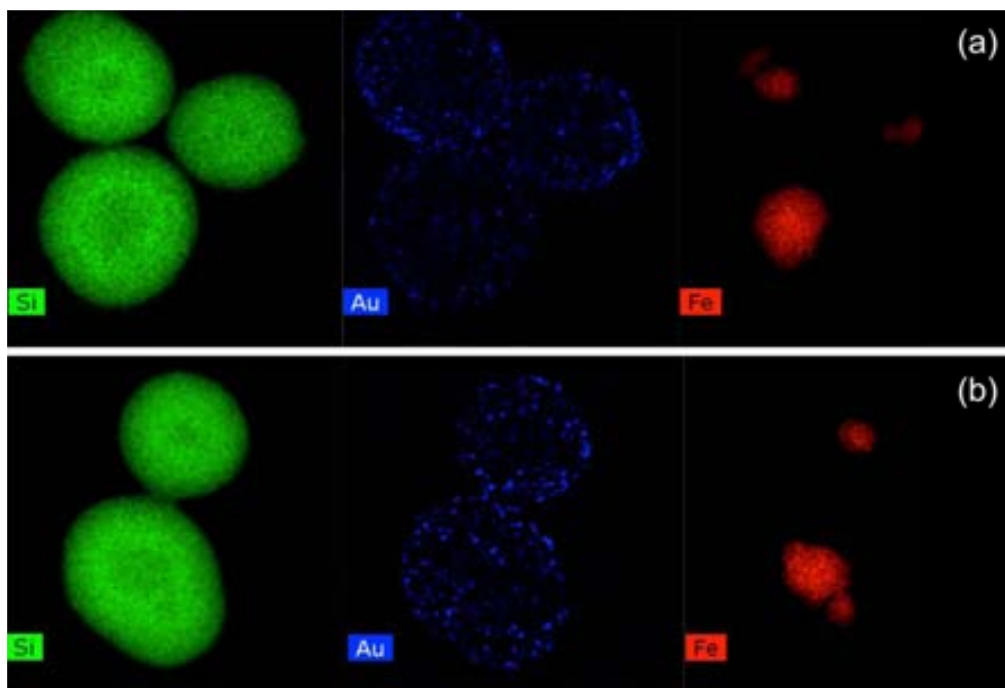
Figure 5.19. Elemental mapping of EDX spectra for: (a) MUS_Au, and (b) MUS-OT_Au.

The shape and size of the clusters formed by the Au-coated AP_{Fe} particles in culture medium were analyzed by **Cryo-TEM** and **DLS**, respectively. In order to prepare the samples for Cryo-TEM, a drop of particles dispersed in supplemented MEMα medium at 0.1 mg/mL was deposited onto a Quantifoil® grid, and rapidly quenched into liquid ethane. During the imaging, the temperature was kept at -140 °C. The vitrified aggregates were considered to be in "native state". The same dispersions were used for the DLS measurements.

The three types of particles All MUS_AP_{Fe} (**Figure 5.20a**, **d**), MUS-OT_AP_{Fe} (**Figure 5.20b**, **e**) and AP_{Fe} (**Figure 5.20c**, **f**) formed elongated and spherical-like aggregates with a broad size distribution: groups of particles from two or three up to 30-40 particles were observed. This polydispersity in size was confirmed by the broad peaks obtained by DLS (**Figure 5.21).** The hydrodynamic diameter of the aggregates was between *ca.* 550 and 600 nm for all samples.
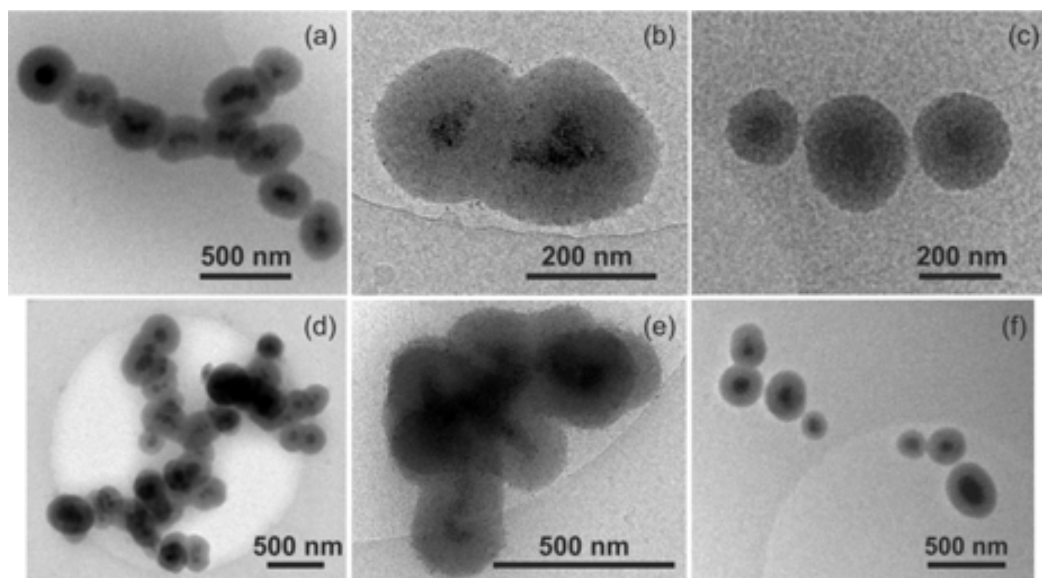
Figure 5.20. Cryo-TEM images for MEMα supplemented medium with 10 % FBS and 2 mM Glutamax of: (a, d) MUS_AP$_{Fe}$, (b, e) MUS-OT_AP$_{Fe}$, and (c, f) AP$_{Fe}$ particles.
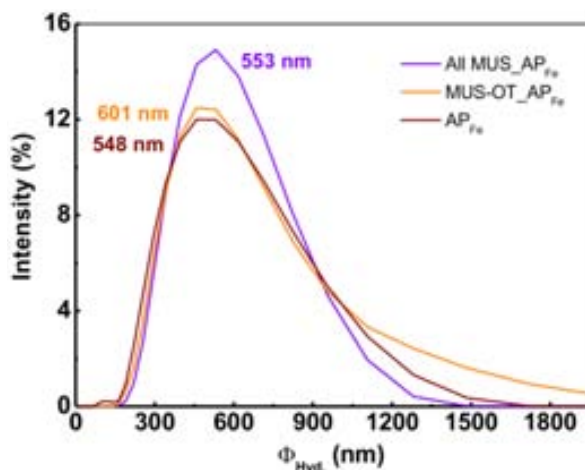
Figure 5.21. DLS intensity-weighted size distributions of the gold-coated AP$_{Fe}$ and the pristine AP$_{Fe}$ particles in MEMα supplemented medium with 10 % FBS and 2 mM Glutamax.

5.6.2. Internalization of gold-decorated iron oxide-silica nanoparticles in HeLa cells

Endocytosis is the most common route by which cells uptake macromolecules, particulate substances, and, in specialized cases, even other cells. In this process, the material to be ingested is progressively enclosed by a portion of the cell membrane, which first invaginates and then internalizes to form an endocytic vesicle (endosome) containing the ingested material.[39] It is an energy consuming process and we referred to it as "active" in contrast to "passive" non endocytic mechanisms.

Although the MUS-OT_Au particles were found to be internalized by cells following an endocytosis-independent pathway, nanoscale objects typically penetrate the cell membrane by endocytic mechanisms.[40] Herein, the presence of the ligand-capped gold nanoparticles onto the surface of the AP_{Fe} particles is not expected to influence the cellular uptake mechanism due the size-limiting parameter: the composite particles are too large to be internalized by cells trough passive pathways. However, since the efficiency of endocytosis in terms of particles loading is mediated, among other, by surface parameters such as surface charge or functional groups,[41,42] the two types of gold-decorated AP_{Fe} particles likely show different results between them in terms of cell uptake and when compared with the pristine material.

The gold-coated and the uncoated particles were incubated in presence of HeLa cells for 1 h at 0.1 mg/mL in the complete culture medium and washed three times with PBS. Following the protocol already explained for detaching the cells from the flask, a pellet was obtained after centrifuging at 1400 rpm for 5 min.

The amount of particles uptaken by the cells was obtained by SQUID magnetometry and TEM images were acquired to visualize the particles inside the cells. High resolution-TEM (HRTEM) was also used to investigate the formation of endosomal membranes around the cell internalized particles.

Determination of the cellular uptake by SQUID magnetometry

Prior to measurements, the cell population in the obtained pellets was counted with optical microscopy, after trypan-blue (Sigma-Aldrich) staining, by selecting three different frames. To acquire a measurable magnetic signal, the cell population had to be around $2*10^6$ cells. Then, the cell pellets were re-suspended in 50 μL of supplemented MEMα culture medium and transferred to a polycarbonate capsule. Next, the capsules were dried overnight in a vacuum hood at *ca.* 0.5 bar and 60 ºC in order to ensure the absence of diamagnetism coming from water. A control sample (cells treated in the same conditions) and particles All MUS_AP_{Fe} and AP_{Fe} were also measured. The as-prepared samples were inserted in the SQUID magnetometer sample holder.

Figure 5.22 and **Figure 5.23** exhibit the magnetization curves for the gold-decorated AP_{Fe} and pristine AP_{Fe} particles both in powder and in the cell pellets. Raw cells had insignificant magnetization (not shown). The particles loading in the cells was determined by measuring the remanent magnetization (M_R) applying the **Equation 5.1**. In the formula, the M_R obtained for the two types of gold-decorated particles in cells were divided by the M_R of the All MUS_AP_{Fe} powder, thus considering the same signal for the solids gold-coated samples. The magnetization of the raw composite particles in cells was compared with the as-recovered powder.

Equation 5.1　　　　$\dfrac{M_{Rparticles+cells} \text{ (emu/cell)}}{M_{Rparticles} \text{ (emu/g}_{particles})} * 10^{12} = \dfrac{m_{particles}}{cell} \text{ (pg/cell)}$

The obtained results are summarized in **Table 5.5**. In contrast with the results found for the functionalized gold nanoparticles,[43] the most internalized particles were the hydrophilic All

MUS_AP$_{Fe}$ ones. The cell uptake for the raw particles was in between. Furthermore, it was concluded that, for the prepared materials, the influence of the surface polarity and charge in the cellular uptake was not determinant and the particles diameter was the main factor affecting this process. Thereby, the particles forming the largest aggregates showed the lowest capability of being engulfed by the cells.

Table 5.5. Amount of particles internalized in HeLa cells for the gold-decorated AP$_{Fe}$ and AP$_{Fe}$ particles.

Particles	m$_{particle}$ (pg/cell)
All MUS_AP$_{Fe}$	18.0
MUS-OT_AP$_{Fe}$	11.7
AP$_{Fe}$	15.5
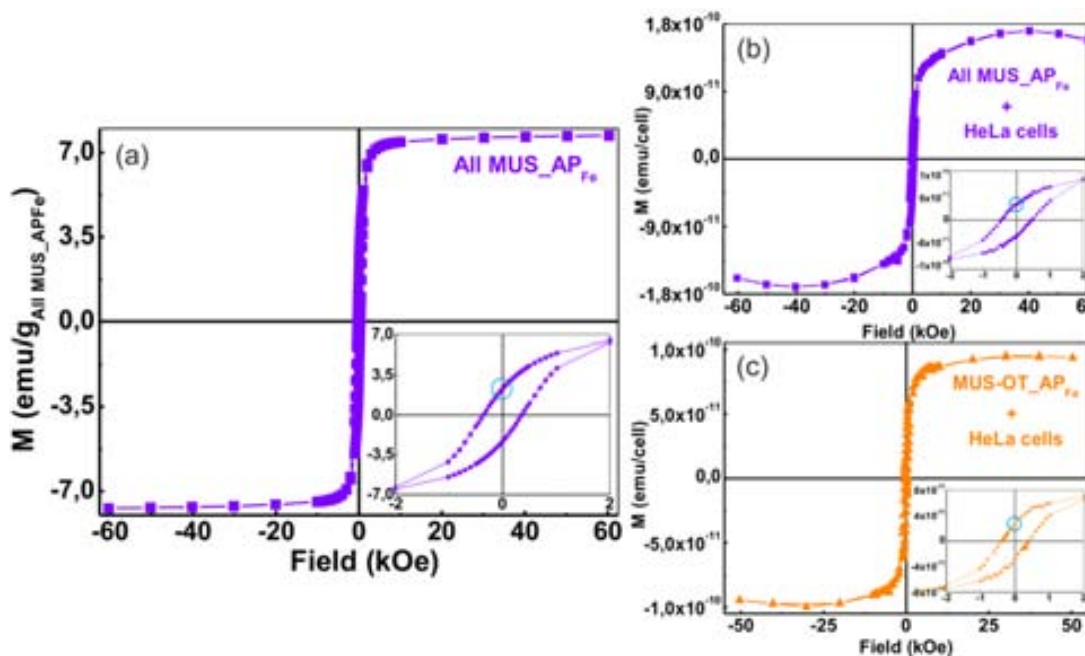
Figure 5.22. Curves of magnetization for: (a) All MUS_AP$_{Fe}$, and the cell pellets containing, (b) All MUS_AP$_{Fe}$ and (c) MUS-OT_AP$_{Fe}$.
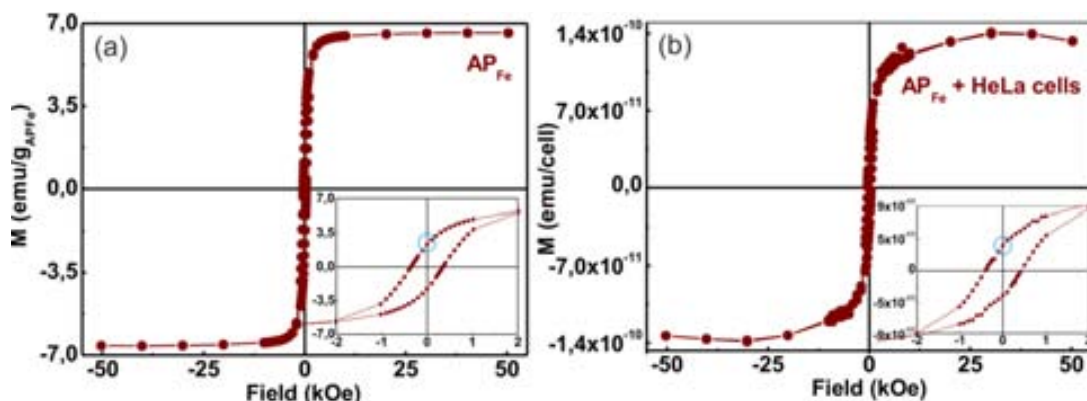
Figure 5.23. Curves of magnetization for: (a) AP$_{Fe}$, and (b) the cell pellet containing AP$_{Fe}$

Analysis of the cell internalized particles by TEM/HRTEM

Electronic microscopy was used not just for localizing particles into cells, but also for checking the cells structure after the treatment. Before performing the observation, chemical fixation was needed to preserve and stabilize the soft structure of the cells. This process followed a pre-designed protocol and it was done by the technicians at the *Microscopy Service* of the Universitat Autònoma de Barcelona (UAB): after discarding the supernatant, the pellets were redispersed in 1.5 mL of the fixation medium (glutaraldehyde 2 % in cacodylate buffer at 0.1 M) and incubated at 4 ºC for at least 2 h. After this process, a post-fixation step carried out at the same time staining with OsO_4 1 % at 4 ºC for 2 h. Then, the cells were dehydrated in alcohol series and embedded in Epon resin. Ultrathin sections (70 nm in thickness) were cut with a diamond knife, placed on non-coated 200 mesh copper grids and contrasted with conventional uranyl acetate solution for 30 min.

The cells observed by TEM after the incubation with the particles All MUS_AP_{Fe} (**Figure 5.24b**), MUS-OT_AP_{Fe} (**Figure 5.24c**) and AP_{Fe} (**Figure 5.24d**) presented neither size nor structural differences when compared with the control cells in **Figure 5.24a**. The cell and nuclear membranes remained continuous after the particles treatment and there was not evidence of apoptotic bodies.

In all cases, nanoparticles appeared internalized into the cells as bright and spherical dots and only in some cases the core-shell structure could be distinguished, as in the AP_{Fe} sample in the purple inset of **Figure 5.24d**. The particles were distributed in the cytoplasm and they did not enter into the nucleus. Only few nanoparticles were found outside the cells.
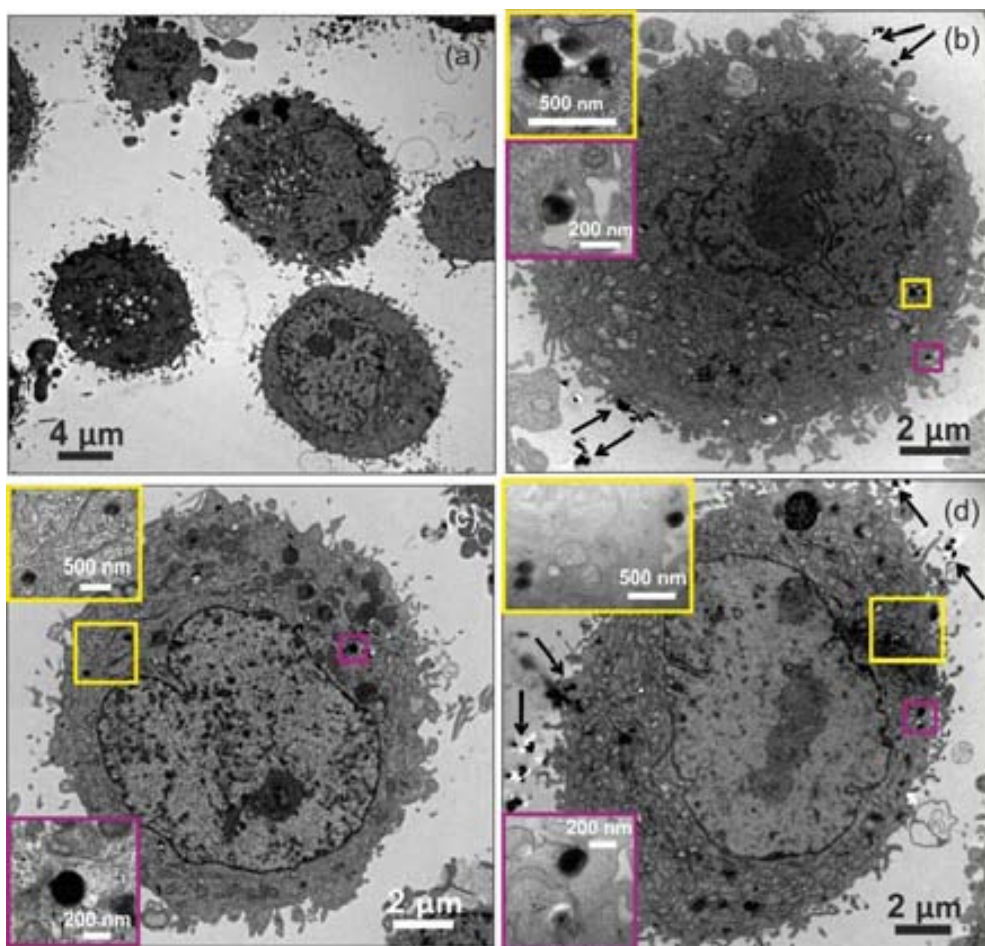
Figure 5.24. TEM images of HeLa cells: (a) as control and after 1 h incubation (37 °C, 5 % CO$_2$) of (b) All MUS_AP$_{Fe}$, (c) MUS-OT_AP$_{Fe}$ and (d) AP$_{Fe}$ nanoparticles. Black arrows mark the particles inside or outside the cells. Insets: larger magnification with enhances contrast between the nanospheres and the organic matter of the cells.

The particles structure was clearly observed by HRTEM and, more importantly, the particles seemed to be confined in an area delimited by a membrane. This finding may indicate the presence of endosomes surrounding the particles. **Figure 5.25a** shows the All MUS_AP$_{Fe}$ particle inside one cell where the vesicle is not clear. A group of the same particles in the cytoplasm of a cell is exhibited in the high magnification image of **Figure 5.25b**, where the membrane could be recognized. Increasing the magnification to capture the image of one particle (**Figure 5.25c**), the membrane was more easily identified. Similarly, the same aspects were monitored for the MUS-OT_AP$_{Fe}$ (**Figure 5.25d, e and f**) and AP$_{Fe}$ (**Figure 5.25g, h and i**) particles. For these samples, it is possible to distinguish even the two flat sheets forming the lipid bilayer of the cell membrane at high magnification.

The fact that not all the particles were internalized and surrounded by a membrane suggested that nanospheres could escape from the endosomes. This process has found to be related with the surface functionalization of silica systems.[42]
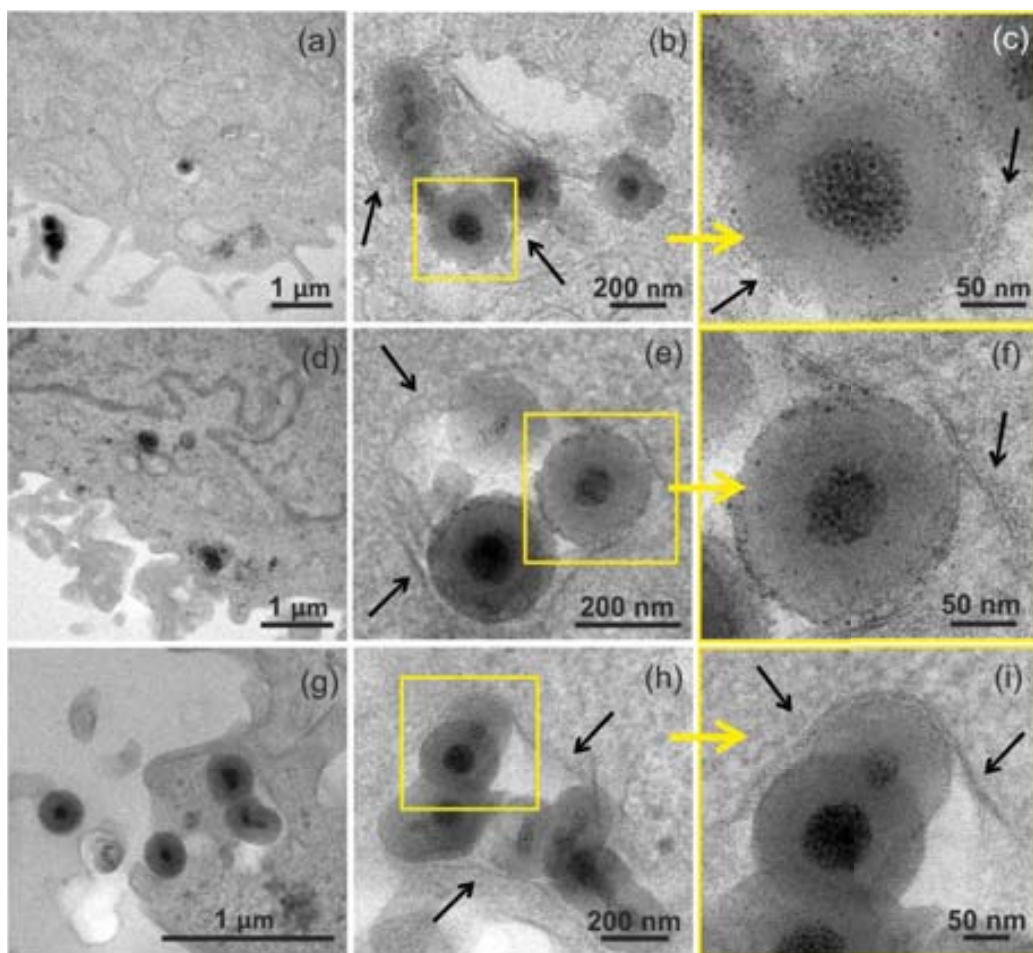
Figure 5.25. HRTEM images of HeLa cells after 1 h incubation (37 °C, 5 % CO_2) of: (a, b, c) MUS_AP$_{Fe}$, (d, e, f) MUS-OT_AP$_{Fe}$ and (g, h, i) AP$_{Fe}$ nanoparticles. Black arrows mark the possible endosomal membranes. Yellow arrows indicate the images in each yellow square at larger magnification.

By electronic microscopy, it was also checked that, in general, both the gold-functionalized and the pristine AP$_{Fe}$ nanoparticles were uptaken by the cells as independent entities or as small groups of 2-4 particles. The largest aggregates were not engulfed by the cells.

5.6.3. Cytoxicity evaluation of gold-decorated iron oxide-silica nanoparticles

Cell viability was evaluated for both the gold-coated and pristine composite particles. MTT tests were performed by Maria Milla, as previously explained, after incubation at 0.1 mg/mL during 1 h (37 °C, 5 % CO_2) in HeLa cell cultures.

The results obtained are represented in **Figure 5.26**. All the particles were non toxic to the cells showing cell viabilities around or over 100 %.

Note that raw AP_{Fe} nanoparticles at a concentration of 0.1 mg/mL were cytotoxic when incubation was done for 13 h (see **Figure 5.5**) but they were non toxic after 1 h of treatment.
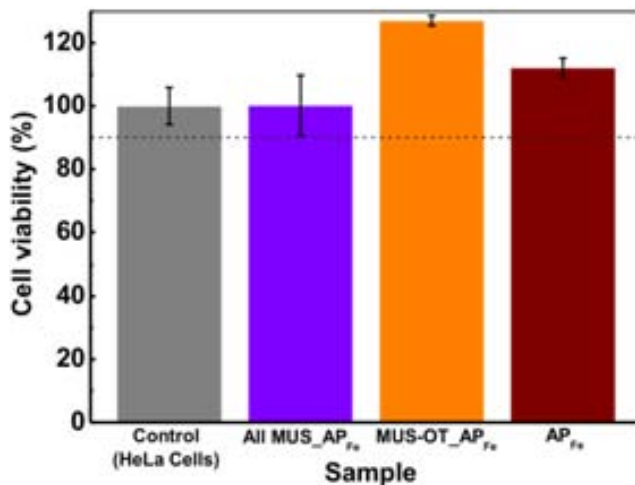
Figure 5.26. HeLa cells viability in the presence of particles gold-coated and AP_{Fe} nanparticles. Error bars were calculated from the deviation standard of the results obtained in three wells. The dashed line at 90 % of cell viability is a guide for the eye.

5.7. CONCLUSIONS

Preliminary biological assessment of the three types of silica-based materials synthesized in this thesis was studied. Several physicochemical properties such as colloidal stability in different media or surface functionalization of the silica-based particles were explored. In addition, cytotoxicity tests and cells internalization of pristine and both fluorescently-labeled and gold-decorated iron oxide-silica nanoparticles were studied. The main results and conclusions found are summarized as follows:

- As many colloidal systems, AP and AP_{Fe} particles aggregated in liquid media. However, those materials presented the highest colloidal stability when dispersed in supplemented culture medium, while the largest aggregates were found in PBS. This trend was especially visible for the AP_{Fe} nanospheres forming clusters smaller than 500 nm in serum supplemented biological medium, but aggregates larger than 2 μm in the saline solution. Stabilization due to both electrostatic repulsions and steric impediments due to a specific protein adsorption on the silica surface was attributed to this finding. When dispersed in pure water, composite particles exhibited the highest stabilization at physiological conditions (neutral pH) and the largest clusters in acid pH.

- Silica submicron particles (AP) and composite nanoparticles (AP_{Fe}) presented negligible degradation at stomach pH-simulated medium (pH = 2) but partial silica dissolution at blood stream pH-conditions (pH = 7.4) occurred in two days. The highly porous aerogel monolith (AM) is the most degraded, with amounts of remaining SiO_2 of ~ 90 wt% for acid pH and ~ 50 wt% for basic medium up to 30 days.

- AP_{Fe} nanoparticles were non toxic to the cells at a concentration of 0.1 mg/mL for 1 h of incubation. In contrast, they were cytotoxic when the incubation time increased to 13 h even at low concentrations (0.025 and 0.05 mg/mL).

- The chemical versatility of the silica and its importance in biomedical applications was checked by functionalizing particle surfaces. Besides the particles coating with PEG, the silica surface of the composite nanoparticles was modified with amino groups to which fluorescent molecules or two types of ligand-coated gold nanoparticles were attached. For 1 h of incubation at a concentration of 0.1 mg/mL, the cell uptake was around 15 and 18 pg/cell for the pristine AP_{Fe} nanospheres and one type of gold-decorated AP_{Fe}, respectively. The composite material distributed in the cytoplasm as individual particles or small groups of them without damaging the cells structure. The endocytic cell uptake mechanism could be tentatively assessed by identifying endosomal vesicles with HRTEM. For these particles, that were 177 nm in size, endocytosis was likely surface charge-independent being the particles size the dominant factor for internalizing the external material into cells.

However, in regards of their bioapplications, more research is needed to better understand the mechanism through the nanospheres colloidally stabilized in presence of serum or in order to find the optimal conditions of concentration and incubation time without inducing cytoxicity.

In conclusion, the composite iron oxide-silica nanoparticles are a promising system to be used in biomedical applications, especially in drug delivery. Oral and direct cellular internalization were suitable routes of administration, while the aggregation in liquid media limited the potential intravenous injection. In those cases, disaggregation strategies need to be explored. Moreover, the particles surface was easily modified to produce multifunctional materials targeting specific requirements. The magnetic counterpart gives the particles theranostic properties (MRI) and presumably allows guidance by applying an external magnetic gradient.

5.8. REFERENCES

[1] Shen, D., Yang, J., Li, X., Zhou, L., Zhang, R., Li, W., Chen, L., Wang, R., Zhang, F., Zhao, D. Biphase stratification approach to three-dimensional dendritic biodegradable mesoporous silica nanospheres. *Nano Lett.*, **2014**, *14*, 923-932.

[2] Mitchell, K.K.P., Liberman, A., Kummel, A.C., Trogler, W.C. Iron(III)-doped, silica nanoshells: a biodegradable form of silica. *J. Am. Chem. Soc.*, **2012**, *134*, 13997-14003.

[3] Legrand, A.P. The surface properties of silicas. West Sussex: *Wiley*, **1998**.

[4] Mavredaki, E., Stathoulopoulou, A., Neofotistou, E., Demandis, K.D. Environmentally benign chemical additives in the treatment and chemical cleaning of process water systems: implications for green chemical technology. *Desalination*, **2007**, *210*, 257-265.

[5] Cypryk, M. Rubinsztajn, S., Chojnowski, J. Disproportionation of oligodimethylsiloxanols in the presence of a protic adic in dioxane. *J. Organomet. Chem.*, **1993**, *446*, 91-97.

[6] Rubinsztajn, S., Cypryk, M., Chojnowski, J. Behavior of oligo(dimethylsiloxanols) in the presence of protic acids in an acid-Base inert solvent. kinetics of the competition of disproportionation, ester formation, and condensation. *Macromolecules*, **1993**, *26*, 5389-5395.

[7] Cypryk, M., Apeloig, Y. Machnism of the acid-catalyzed Si-O bond cleavage in siloxanes and siloxanols. A theoretical study. *Organometallics*, **2002**, *21*, 2165-2175.

[8] Andersson, J., Rosenholm, J., Areva, S., Lindén, M. Influences of material characteristics on ibuprofen drug loading and release profiles from ordered micro- and mesoporous silica matrices. *Mater. Chem.*, **2004**, *16*, 4160-4167.

[9] Kortesuo, P., Ahola, M., Karlsson, S., Kangasniemi, I., Yli-Urpo, A., Kiesvaara, J. Silica xerogel as an implantable carrier for controlled drug delivery evaluation of drug distribution and tissue efects after implantation. *Biomaterials*, **2000**, *21*, 193-198.

[10] Falaize, S., Radin, S., Ducheyne, P. *In vitro* behavior of silica-based xerogels intended as controlled release carrier. *J. Am. Ceram. Soc.*, **1999**, *82*, 969-976.

[11] Li, X., Zhang, L., Dong, X., Liang, J., Shi, J. Preparation of mesoporous calcium doped silica spheres with narrow size dispersion and their drug loading and degradation behavior *Microporous Mesoporous Mater.*, **2007**, *102*, 151–158.

[12] Drescher, D., Zeise, I., Traub, H., Guttmann, P., Seifert, S., Büchner, T., Jakubowski, N., Schneider, G., Kneipp, J. In situ characterization of SiO_2 nanoparticle biointeractions using bright silica. *Adv. Funct. Mater.*, **2014**, *24*, 3765-3775.

[13] Wang, J., Shen, Y., Bai, L., Lv, D., Zhang, A., Miao, F., Tang, M., Zhang, J. Mesoporous silica shell alleviates cytotoxicity and inflammation induced by colloidal silica particles. *Colloids Surf. B*, **2014**, *116*, 334-342.

[14] Yu, S.-M., Laromaine, A., Roig, A. Enhanced stability of superparamagnetic iron oxide nanoparticles in biological media using a pH adjusted-BSA adsorption protocol. *J. Nanopart. Res.*, **2014**, *16*: 2484, 1-15.

[15] Meng, H., Liong, M., Xia, T., Li, Z., Ji, Z., Zink, J.I., Nel, A.E. Engineered design of mesoporous silica nanoparticles to deliver doxorubicin and p-glycoprotein siRNA to overcome drug resistance in a cancer cell line. *ACS Nano*, **2010**, *4*, 4539-4550

[16] Lu, J., Liong, M., Li, Z., Zink, J.I., Tamanoi, F. Biocompatibility, biodistribution, and drug-delivery efficiency of mesoporous silica nanoparticles for cancer therapy in animals. *Small*, **2010**, *6*, 1794-1805.

[17] Barbé, C., Bartlett, J., Kong, L., Finnie, k., Lin, H.Q., Larkin, M., Calleja, S., Bush, A., Calleja, G. Silica particles: a novel drug-delivery system. *Adv. Mater.*, **2004**, *16*, 1959-1966.

[18] Lu, J., Liong, M., Zink,, J.I., Tamanoi, F. Mesoporous silica nanoparticles as a delivery system for hydrophobic anticancer drugs. *Small*, **2007**, *3*, 1341-1346.

[19] Radu, D.R., Lai, C.-Y., Jeftinija, K., Rowe, E.W., Jeftinija, S., Lin, V.S.-Y. Polyamidoamine dendrimer-capped mesoporous silica nanosphere-based gene transfection reagent. *J. Am. Chem. Soc.*, **2004**, *126*, 13216-13217.

[20] Hudson, S.P., Padera, R.F., Langer, R., Kohane, D.S. The biocompatibility of mesoporous silicates. *Biomaterials*, **2008**, *29*, 4045-4055.

[21] Slowing, I.I., Wu, C.-W., Vivero-Escoto, J.L., Lin, V.S.-Y. Mesoporous silica nanoparticles for reducing hemolytic activity towards mammalian red blood cells. *Small*, **2009**, *5*, 57-62.

[22] McCarthy, J., Inkielewicz-Stępniak, I., Corbalan, J.J., Radomski, M.W. Mechanisms of toxicity of amorphous silica nanoparticles on human lung submucosal cells in vitro: protective effects of fisetin. *Chem. Res. Toxicol.*, **2012**, *25*, 2227–2235.

[23] Xu, Z., Chou, L., and Sun, J. Effects of SiO_2 nanoparticles on HFL-I activating ROS-mediated apoptosis via p53 pathway. *J. Appl. Toxicol.*, **2012**, *32*, 358–364.

[24] Yu, K.O., Grabinski, C.M., Schrand, A.M., Murdock, R.C., Wang, W., Gu, B., Schlager, J.J., Hussain, S.M. Toxicity of amorphous silica nanoparticles in mouse keratinocytes. J. *Nanopart. Res.*, **2009**, *11*, 15-24.

[25] Lin, Y.-S., Haynes, C.L. Impacts of Mesoporous silica nanoparticle size, pore ordering, and pore integrity on hemolytic activity. *J. Am. Chem. Soc.*, **2010**, *132*, 4834-4842.

[26] Lewinski, N., Colvin, V., Drezeck, R. Cytotoxicity of nanoparticles. *Small*, **2008**, *4*, 26-49.

[27] Gref, R., Luck, M., Quellec, P., Marchand, M., Dellacheire Harnisch, S., Blunk, T., Muller, R.H. "Stealth" corona-core nanoparticles surface-modified by polyethylene glycol (PEG): influences of the corona (peg chain length and surface density) and of the core of the composition on phagocytic uptake and plasma protein adsorption. *Colloids Surf. B*, **2000**, *18*, 301-313.

[28] Orts-Gil, G., Natte, K., Thiermann, R., Girod, M., Rades, S., Kalbe, H., Thünemann, A.F., Maskos, M., Österle, W. On the role of surface composition and curvature on biointerface formation and colloidal stability of nanoparticles in a protein-rich model system. *Colloids Surf B: Biointerfaces*, **2013**, *108*, 110-119.

[29] He, Q., Zhang, Z., Gao, F., Li, Y., Shi, J. In vivo biodistribution and urinary excretion of mesoporous silica nanoparticles: effects of particle size and PEGylation. *Small*, **2011**, *7*, 271-280.

[30] Torchilin, V.P. Recent advances with liposomes as pharmaceutical carriers. *Nat. Rev. Drug Discov.*, **2005**, *4*, 145-160.

[31] Antonietti, M., Forster, S. Vesicles and liposomes: a self-assembly principle beyond lipids. *Adv. Mater.*, **2003**, *15*, 1323-1333.

[32] Harris, M. Poly(ethylene) glycol chemistry: biotechnical and biomedical applications. New York: *Plenum Press*, **1992**.

[33] Feng, L., Wang, Y., Wang, N., Ma, Y. Preparation of poly(ethylene glycol)-grafted silica nanoparticles using a facile esterification condensation method. *Polym. Bull.*, **2009**, *63*, 313-327.

[34] Xu, H., Yan, F., Monson, E.E., Kopelman, R. Room-temperature preparation and characterization of poly(ethylene glycol)-coated silica nanoparticles for biomedical applications. *J. Biomed. Mater. Res.*, **2003**, *66*, 870-879.

[35] Morgan, M., Thorburn, J., Pandolfi, P.P., Thorburn, A. Nuclear and cytoplasmic shuttling of TRADD induces apoptosis via diVerent mechanisms. *J. Cell Biol.*, **2002**, *157*, 975-984.

[36] Taatjes, D.J., Sobel, B.E., Budd, R.C. Morphological and cytochemical determination of cell death by apoptosis. *Histochem. Cell Biol.*, **2008**, *129*, 33-43.

[37] Jiang, S., Granick, S. Janus particle, synthesis, self-assembly and applications. *The Royal Society of Chemistry*: Cambridge, **2012**.

[38] Walther, A., Müller, A.H.E. Janus Particles: Synthesis, self-assembly, physical properties, and applications. *Chem. Rev.*, **2013**, *113*, 5194–5261.

[39] Alberts, B., Johnson, A., Lewis, J., Raff, M., Roberts, K., Walter, P. Molecular Biology of the Cell. 4th Edition. *Garland Science*: New York, **2002**.

[40] Verma. A., Uzun, O., Hu, Y., Hu, Y., Han, H.-S., Watson, N., Chen, S., Irvine, D.J., Stellacci, F. Surface-structure-regulated cell-membrane penetration by monolayer-protected nanoparticles. *Nat. Mater.*, **2008**, *7*, 588-595.

[41] Nel, A.E., Mädler, L., Velegol, D., Xia, T., Hoek, E.M.V., Somasundaran, P., Klaessig, F., Castranova, V., Thompson, M. Understanding biophysicochemical interactions at the nano-bio interface. *Natur. Mater.*, **2009**, *8*, 543-557.

[42] Slowing, I., Trewyn, B.G., Lin, V.S.-Y. Effect of surface functionalization of MCM-41-type mesoporous silica nanoparticles on the endocytosis by human cancer cells. *J. Am. Chem. Soc.*, **2006**, *128*, 14792-14793.

[43] Jewell, C.M., Jung, J.-M., Atukorale, P.U., Carney, R.P., Stellacci, F., Irvine, D.J. Oligonucleotide delivery by cell-Penetrating "striped" nanoparticles. *Angew. Chem. Int. Ed.*, **2011**, *50*, 12312-12315.

6

CONCLUSIONS AND FUTURE WORK
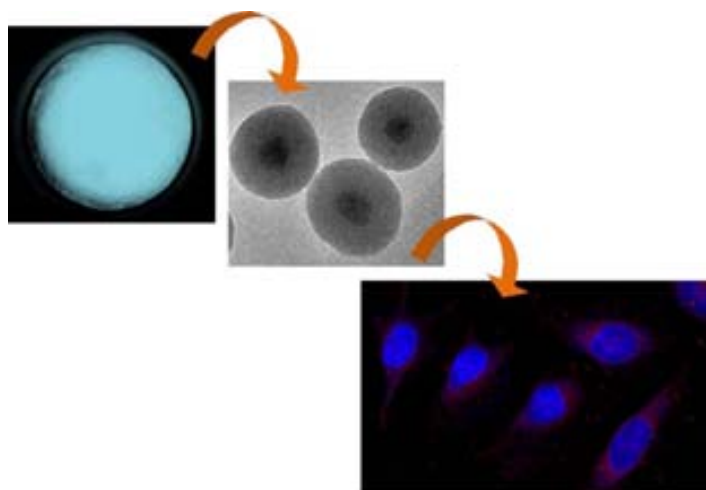
In this chapter the general conclusions and some suggestions for future studies to continue the work developed in the present thesis are summarized.

6.1. GENERAL CONCLUSIONS

The main goals achieved during this PhD thesis are described in the following four sections:

1- An approach for the synthesis of porous silica-based nanoparticles combining sol-gel chemistry with the supercritical fluids technology, without using porogenic agents, was validated by the fabrication of two different types of materials: core(iron oxide)-shell(silica) nanoparticles and sub-micron silica particles. Those products were aimed to fulfill the required properties to be further charged with a therapeutic agent and functionalized for controlled drug delivery applications.

The systems showed spherical morphology, tunable sizes and narrow size distributions. The particles were obtained as dried powder and they were easily dispersible in water and other polar solvents until a maximum concentration of 1 mg/mL. Their textural properties were characterized by the presence of micropores interconnected in an open framework. Iron oxide-silica nanoparticles exhibited superparamagnetic properties with high saturation magnetization.

The obtained results indicated that iron oxide-silica nanoparticles had suitable structural and magnetic properties for their use as theranostic devices, both as drug carriers and contrast agents for magnetic resonance imaging (MRI). Silica particles would be restricted to oral administration of therapeutics because of a size-limitation.

2- A therapeutic agent for thrombosis treatment (Triflusal) was homogenously encapsulated and stabilized in molecular form within the silica-based materials by dissolution in supercritical carbon dioxide, thus avoiding the use of toxic organic solvents. Drug stability to moisture when entrapped in the silica-based materials and the *in vitro* drug release profiles in aqueous media at different pHs were studied. The obtained results were compared with those acquired for an organic polymeric system (PMMA beads).

Triflusal loadings were found to be around 16 wt% for aerogels and PMMA beads and 3-4 wt% in the particulate materials. Importantly, higher drug stabilization against moisture was found when impregnated in the hydrophilic silica matrices when compared to data obtained for the hydrophobic polymer. Triflusal release showed different profiles depending on the porous structure and the chemical nature of the matrices: a fast delivery with more than 80 wt% of the drug dissolved within the first minute was found for silicas, while a sustained release lasting for several days was observed for PMMA.

Summarizing, the combined use of porous inorganic matrices as host materials, functional organic molecules as guests and the supercritical fluids technology renders hybrid materials with improved properties towards different purposes. Silica-based materials behaved as drug carriers for the potential enhancement of the bioavailability of poorly-water soluble therapeutics.

3- The silica-based particles were functionalized with biopolymers by modifying the silica surface in presence of compressed fluids, which acted as antisolvent or reaction media for the polymers Eudragit® RL 100 and polyethyleneimine, respectively. Three different coating methods were assayed depending on the particle size and the type of coating agent used. Eudragit covering of the triflusal-loaded nanoparticles was proved as an efficient mechanism to sustain the drug release in aqueous media at different pHs, while protecting the cargo from hydrolysis. PEI grafted on the particles surface potentially enhances the cellular uptake without varying the drug release behavior.

Results presented a sustain triflusal release for both silica and iron oxide-silica particles when functionalized with Eudragit: less than 25 wt% of the drug was dissolved in the first ten minutes and the remaining amount showed a prolonged release during several hours. When fitting the obtained data to some mathematical models, the drug delivery mechanism was found to be governed by diffusion in all cases.

Polymerization of aziridine to form PEI on the surface of silica-based particles was assessed using a rapid approach in compressed CO_2. Interestingly, the formed PEI was characterized by its low molecular weight, which leads on a toxicity decrease of the PEI-coated particles. Since PEI-functionalization is known to facilitate cellular uptake, an effective and direct release of the therapeutic cargo into cells would be favored for the PEI-coated silica-based particles.

In conclusion, chemically stable complex materials have been fabricated by coating the silica-based particles with biopolymers. Eudragit-encapsulated particles were established as adequate products for controlled drug delivery and PEI-coated particles showed appropriate features for their use in biomedicine.

4- In order to better understand some perspectives and limitations of the use of silica-based materials in biomedicine, several physicochemical characteristics of these materials were explored. Cytotoxicity and cell internalization were also preliminarily tested. Finally, further modification of the silica surface was performed to provide the particles with extra functionalities. The main results and conclusions are:

 - Although particles aggregated in water forming clusters larger than 2 μm in size, they tend to stabilize in serum supplemented biological medium resulting in aggregates below 500 nm in size.

- Particles degraded in basic aqueous medium (pH = 7.4) around 30-40 wt % in two days, but they remained stable in acid conditions (pH = 2).

- Iron oxide-silica nanoparticles were biocompatible at a concentration of 0.1 mg/mL for 1 h of incubation in HeLa cells, but they were cytotoxic after 13 h of incubation.

- The chemical versatility of the silica was utilized to fluorescently-label the iron oxide-silica nanoparticles. Moreover, ligand-capped gold nanoparticles were chemically bonded to the

silica surface and HeLa cells uptake was evaluated at a concentration of 0.1 mg/mL for 1 h of incubation. Pristine and gold-decorated particles were internalized up to 15 pg/cell and 18 pg/mL, respectively.

When considering biomedical uses of our silica-based materials, the obtained results so far evidence that more research would be needed to refine the optimal conditions of application. Still, iron oxide-silica nanoparticles are promising theranostic materials especially for drug delivery and MRI imaging, which could be intravenously administered if disaggregation studies are better explored. We have further demonstrated that silica is a versatile material that can be chemically exploitable to fabricate complex materials. This has been done by decorating silica particles with gold nanoparticles or by attaching functional molecules (polyethylene glycol, BODIPY® dye, ...).

6.2. FUTURE WORK

In view of future research, the results obtained in this thesis allow for further experimentation in several directions, enumerated following.

Regarding drug delivery, other active pharmaceutical ingredients with higher therapeutic value than Triflusal could be impregnated in the silica-based particles. Drugs for chemotherapy could be good candidates for this purpose. Nevertheless, it has to be taken into account that the therapeutic agents of choice should have a sufficient solubility in supercritical CO_2[1] or in compressed mixtures co-solvent/CO_2.

To increase drug payload and diversification of the type of therapeutics, the fabrication of mesoporous nanoparticles that could host more quantity and larger molecules could be tackled by using porogenic agents in combination with the use of supercritical fluids. Preservation of the colloidal stability of the initial sol in presence of a surfactant would be a key point to be solved for applying such approach.

Achieving a target drug release commonly requires functionalization of the materials surface. In this sense, it would be interesting to functionalize the particles with specific ligands (folate receptors, antigens, ...) that could target the tissue for which the drug has been designed. This conjugation would likely help particles disaggregation in aqueous media, thus facilitating their potential intravenous administration.

Degradation kinetics of the silica-based particles in water, basal and serum supplemented biological media could be evaluated and compared. This study would clarify the role of the adsorbed proteins on the silica dissolution at physiological pH.

Interestingly, results are expected by exploring the internalization of PEI-coated iron oxide-silica nanoparticles in HeLa cells and comparing with the results observed for the pristine and the gold-decorated nanoparticles. An increase in the cellular uptake is expected for the materials encapsulated in positively charged PEI.[2] These experiments could be accompanied with

cytotoxicity evaluations by MTT tests, which are expected to reflect an enhanced biocompatibility of the functionalized nanoparticles with respect to the uncoated ones.

Biocompatibility of porous silica nanoparticles to red blood cells has found to be shape-dependent increasing with the aspect ratio of the particles.[3] Since our methodology permits to obtain worm-shaped nanostructures (results not shown), analysis of the hemolytic activity of nanoworms and nanospheres would be relevant for potential intravenous administration.

1. Gupta, R.B., Shim, J.-J. Solubility in supercritical carbon dioxide. *CRC Press*, New York, **2006**.
2. Calatayud, M.P., Sanz, B., Raffa, V., Riggio, C., Ibarra, M.R., Goya, G.F. The effect of surface charge of functionalized Fe_3O_4 nanoparticles on protein adsorption and cell uptake. *Biomaterials*, **2014**, *35*, 6389-6399.
3. Yu, T., Malugin, A., Ghandehari, H. Impact of silica nanoparticle design on cellular toxicity and hemolytic activity. *ACS Nano*, **2011**, *5*, 5717-5728.

7

ANNEXES

This section briefly introduces basic concepts on the techniques used and gives technical information on the employed facilities.

7.1. CENTRIFUGES

Iron oxide nanoparticles and PEI and PEG-coated particles were purified by redipsersion in the appropriate solvents and precipitation in an Eppendorf Centrifuge 5804.

Cell pellets were obtained by using an Eppendorf Centrifuge 5702 at the Institut de Biologia i Biomedicina (IBB).

7.2. CONFOCAL MICROSCOPY

With confocal microscopy the emitting light of fluorescent materials can be visualized as an image.

For chromophore-impregnated materials, a Fluorescence data was obtained using a Leica TCS SP5 AOBS confocal laser microscope was used while, for fluorescently-labeled composite AP_{Fe} nanoparticles, images were taken with a Zeiss SLM 700 confocal microscope at the Universitat Autònoma de Barcelona (Medicine Faculty).

7.3. DIFFERENTIAL SCANNING CALORIMETRY (DSC)

DSC allows the detection of thermal-induced transitions of materials such as melts, glass transitions, phase changes, and curing. A sample of known mass is heated or cooled and the changes in its heat capacity are tracked as changes in the heat flow in a nitrogen atmosphere.

DSC data were acquired using a Perkin Elmer DSC8500 LAB SYS (N5340501) differential scanning calorimeter equipped with a Liquid N_2 controller CRYOFILL (N534004).

7.4. DIFFUSE-REFLECTANCE SPECTROSCOPY

Reflectance spectroscopy is very closely related to UV-Vis spectroscopy, in that both of these techniques use visible light to excite valence electrons to empty orbitals. The difference in these techniques is that diffuse-reflectance measures the relative change in the amount of reflected light off of a surface.

The diffuse-reflectance measurements of chromphore-impregnated materials were performed at the Universitat de Barcelona (Departament de Química Analítica) with a Perkin-Elmer Lambda 19 UV/Vis/NIR spectrophotometer.

7.5. DINAMIC LIGHT SCATTERING (DLS)

The hydrodynamic diameter of micro and nanoparticles in a liquid medium can be determined by DLS. Particles dispersed in a liquid constantly collide with solvent molecules and move randomly in different directions with different speeds (Brownian motion). A laser irradiates the sample and the beam is scattered by particles in Brownian motion. The detector measures the rate at which the intensity of the scattered light changes in time due to particle movement

(smaller particles induce more rapid fluctuations of light than larger particles). The intensity fluctuation of the scattered light is related to the size distribution of particles by instrument calculations (correlation function) obtaining an intensity of scattered light *vs.* size curve. The fundamental size distribution generated by DLS in intensity distribution can be converted to a volume distribution that can also be further converted to a number distribution.

DLS experiments were performed using a Zetasizer Nano ZS instrument (Malvern Instruments) with a He/Ne 633 nm laser.

7.6. FLUORESCENCE SPECTROSCOPY

Fluorescence spectroscopy provides information for both qualitative and quantitative analysis. By being irradiated with a light source (commonly of ultraviolet wavelengths), the electrons of a material are excited and promote to higher energetic levels emitting radiation at different wavelengths when returning to the ground state. The emitted light is measured as a function of the wavelength.

Fluorescence data of chromophore-impregnated samples were obtained using a Leica TCS SP5 AOBS confocal laser microscope at 420 nm.

7.7. FOURIER TRANSFORM INFRARED SPECTROSCOPY (FTIR)

FTIR is used to gather qualitative and quantitative information about the chemical structure of organic and inorganic compounds. Most molecules vibrate in the mid-infrared range (4000-400 cm^{-1}) showing specific vibration frequencies for each chemical bond. The sample is irradiated with wavelengths in the mid-infrared range and absorption is measured at each wavelength. Afterwards, the equipment converts the adsorption value at each corresponding wavelength into a spectrum by using a mathematical process Fourier transform.

FTIR spectra were recorded on a Perkin-Elmer Spectrum One spectrometer.

7.8. HIGH-PERFORMANCE LIQUID CHROMATOGRAPHY (HPLC)

The components of a mixture can be separated, identified and quantitatively analyzed by a HPLC equipment. It consists on the interaction between two different phases: the mobile phase (commonly the solvent for the analyte) and the stationary phase (a chromatographic column that contains the packing material needed to effect the separation). A high-pressure pump is used to generate a specified flow rate of the mobile phase. An injector introduces the sample into the continuously flowing mobile phase stream that carries the sample into the HPLC column. The different components elute from the column to reach the detector at different times depending on the physical or chemical interactions that they establish with both mobile and stationary phases. This time is characteristic of every compound and it is called *retention time* (t_R).

The chromatographic system consisted of an Agilent 1100 Series instrument equipped with a G1311A quaternary pump, a G1379A degasser, a G1315B diode array-detector furnished with a 13-µl-flow-cell and an Agilent Chemstation for data acquisition and analysis (Rev. A 10.02). Samples were injected with a six-port valve Rheodyne 7725 with a 20 µl sample loop.

7.9. HIGH-PRESSURE EQUIPMENT

Synthesis of silica-based materials

The silica-based materials were prepared in the Pilot Plant (**Figure 7.1**) of the Laboratory of Supercritical Fluids sited at MATGAS 2000 AIE. The equipment can operate up to 500 bar and 400 ºC. The system was equipped with two reactors: the 2 L reactor was used as the synthesis chamber while the 1 L reactor was used as the collector for the extracted solvents. The pressurization was performed injecting compressed carbon dioxide with a Lewa pump. The depressurization was automatically controlled by a flow rate control valve. The plant was controlled by a Programmable Logic Controller (PLC) through a software control. No mechanical stirring or refrigeration systems were used during the synthesis. The plant was operated by Raul Solanas, the engineer in charge of the Laboratory of Supercritical Fluids where the system is placed.

Figure 7.1. Pilot plant at MATGAS 2000 AIE used for the synthesis of silica-based materials.

Cations impregnation equipment

A high pressure equipment running in the batch mode was employed to impregnate materials with photosensitive cations (**Figure 7.2**). The system utilized a cooling unit (EX1, Lauda Ecoline) containing polyethyleneglycol and water to liquefy CO_2 and a TharDesign SP240 syringe pump to

pressurize CO_2. The tubular vessel had a volume of 100 mL (Autoclave Engineers) and it was equipped with a vertical magnetic stirrer from MagnetDrive III.

Figure 7.2. High-pressure equipment used for cations impregnation.

Drug impregnation equipment

A high pressure equipment (**Figure 7.3**). running in the batch mode provided with a cooling unit (EX1, Lauda Ecoline) containing polyethyleneglycol and water, a 70 mL autoclave (TharDesign) and a syringe pump (TharDesign SP240) was used for drug impregnation experiments.

Figure 7.3. High-pressure equipment used for drug impregnation.

Semicontinuous precipitation compressed antisolvent (PCA) equipment

The PCA apparatus worked in a semicontinuous co-current mode, in which the CO_2 anti-solvent and the liquid solution were separately fed to the top of the precipitator and were continuously discharged from the bottom. The spray chamber consisted of a high-pressure vessel (Autoclave Engineers), 5 cm i.d. × 25 cm long with sapphire windows at three different levels allowing a visual observation of both the spray and the precipitation. At the bottom of the vessel, the

precipitated powder collected onto a membrane filter of 0.22 μm placed on top of a stainless steel filter of 2 μm porosity. The CO_2 was cooled by flowing through a cold water + ethanol bath and pumped at constant flow with a reciprocating LEWA (EK3) pump. Prior to entering the precipitation chamber, it flowed through a second water bath for heating at the vessel temperature. The pressure inside the vessel was controlled downstream by a metering valve, and the temperature was controlled with heating jackets (Watlow). Acetone solutions of solutes were sprayed into the precipitation chamber by means of a reciprocating dual-piston minipump (Milton Roy LDC).

Batch gas antisolvent (GAS) equipment

A GAS high pressure apparatus working in the batch mode was used. The precipitation unit was a 0.490 L vessel equipped with a stirrer ended by a Rushton-type turbine that plunges into the solution. The CO_2, introduced by a Lewa pump, was dispersed into the solution through the eight turbine holes. The vessel temperature was controlled by heating jackets. A stainless steel filter (porosity 5 μm) overtopped by a membrane disk of 0.22 μm in porosity collects the produced particles at the vessel bottom.

7.10. INDUCTIVELY COUPLED PLASMA-MASS SPECTROMETRY (ICP-MS)

ICP-MS is used for quantitative determination of elements in solids, liquids or gases. In an ICP-MS apparatus, a high-temperature ICP source is combined with a mass spectrometer detector. The material is introduced into a high-energy argon plasma (at 7000 K) where the material is split into individual atoms that then lose electrons to become into singly charged positive ions. Most elements ionize very efficiently (> 90%) in the hot plasma. To allow their identification, the elemental ions produced are extracted into a mass spectrometer, with which the elemental composition of the material is determined.

The elemental analysis was done at the Universitat Autònoma de Barcelona (Servei d'Analisi Química) in an Agilent 7500ce ICP-MS equipment. When measuring solid samples, they were first digested with a mixture of nitric acid (HNO_3) and hydrofluoric acid (HF) in a microwaves oven. For liquid solutions, samples were directly diluted in HNO_3 (1% v/v).

7.11. LASER DOPPLER MICRO-ELECTROPHORESIS

This technique is used to calculate the zeta potential of colloidal particles in aqueous suspensions. The electrophoretic mobility is the movement of a charged particle under the influence of an applied electric field and relative to the liquid in it is suspended. Since this parameter depends on the zeta potential of the colloid, by performing an electrophoresis experiment on the sample and measuring the particles velocity, the obtained data can be related with the zeta potential.

Electrophoresis experiments were done using a cell with electrodes and the particles velocity was measured by a Laser Doppler Velocimetry (LDV) apparatus. The equipment used was a Zetasizer Nano ZS instrument (Malvern Instruments) with a He/Ne 633 nm laser.

7.12. MATRIX-ASSISTED LASER DESORPTION/ IONIZATION SOURCE (MALDI)-TIME OF FLYING (TOF)

MALDI attached to a mass spectrometry (TOF) detector is a sensitive technique for determining the mass of polymers or biomolecules. The sample is mixed with an appropriate matrix on top of a slide plate and irradiated with a short laser pulse. The matrix absorbs the ultraviolet light and converts it to heat energy. A small part of the matrix heats rapidly and vaporized, together with the sample leading to release of matrix, sample molecules, and ions of various sizes from the slide. A potential difference between the sample slide and ground attracts the ions in a particular direction with a velocity that is related to the mass to charge ratio (m/z) of the ions: ions with smaller m/z value move faster through the drift space until they reach the detector. Consequently, the time of ion flight differs according to the m/z value of each ion.

An Applied Biosystems Voyager 6214 time-of-flight mass spectrometer equipped with a MALDI-TOF was also used to estimate the molecular weight of the polyethyleneimine polymer obtained after the process in compressed CO_2.

7.13. MTT ASSAY

A colorimeter assay based on MTT (3-[4,5-dimethylthiazol-2-yl]-2,5 diphenyl tetrazolium bromide) reduction is used to determine the *in vitro* cell viability. The yellow MTT complex is reduced by metabolically active cells to generate reducing equivalents. The resulting intracellular purple formazan can be solubilized and quantified by UV-Vis spectrophotometry.

The cells incubated with the composite particles were analyzed in a Perkin Elmer Victor3 micro plate reader.

7.14. NITROGEN ADSORPTION/DESORPTION ISOTHERMS (BET EQUIPMENT)

Nitrogen adsorption/desorption isotherms are used to analyze the textural properties of different materials, mainly powders. By applying the BET method to the obtained isotherms, parameters such as surface area, pore volume or pore size of mesoporous materials are acquired. T-plot method is widely used to have information about microporous systems.

Nitrogen adsorption/desorption data were taken at 77 K using an ASAP 2000 surface area analyzer from Micromeritics Instrument Corporation.

7.15. SCANNING ELECTRON MICROSCOPY (SEM)

Electron microscopies serve to obtain information about the morphology (texture) and chemical composition of materials, some of them at the nanometric scale. In a SEM microscope, a beam of accelerated electrons is produced at the top of the microscope by an electron gun. The electron beam follows a vertical path through the microscope, which is held within a vacuum, travelling through electromagnetic fields and lenses, which focus the beam to the sample. Once the beam interacts with the sample, electrons and X-rays are ejected, collected and converted into a signal that produces the final image.

In this thesis, a QUANTA FEI 200 FEG-ESEM microscope was used to observe different materials.

Samples were previously coated with gold at the Universitat Autònoma de Barcelona (Servei de Microscòpia) with a K550 Sputter Coater (Coating Attatchment Emitech. Ashford, UK).

7.16. STATIC LIGHT SCATTERING (SLS)

SLS is used to characterize molecules in solution. In a similar way to DLS, the molecules in a sample are illuminated by a laser, with the molecules scattering the light in all directions. But, instead of measuring the time dependent fluctuations in the scattering intensity, SLS uses the time-averaged intensity of scattered light. The intensity of light scattered over a period of time, *i.e.* 10 to 30 seconds, is accumulated for a number of concentrations of the sample. This time averaging removes the inherent fluctuations in the signal, hence the term "Static Light Scattering".

A Zetasizer Nano ZS instrument (Malvern Instruments) with a He/Ne 633 nm laser was utilized to measure the molecular weight of the polyethyleneimine polymer obtained after the process in compressed CO_2.

7.17. SUPERCONDUCTIVE QUANTUM INTERFERENCE DEVICE (SQUID)

SQUID is a highly sensitive magnetometer used to measure extremely subtle magnetic fields.

The magnetization of the iron oxide and composite iron oxide-silica nanoparticles were measured at 5 and 300 K using a magnetometer Quantum Design MPMS5XL that applied magnetic fields up to 6 Tesla. Zero-field cooling, field cooling magnetization measurements as a function of temperature were performed applying a magnetic field of 50 Oe.

7.18. THERMOGRAVIMETRIC ANALYSIS (TGA)

This technique gives quantitative data on the chemical changes of a solid with temperature. The sample is placed on a support attached to a precision balance and subjected to a controlled temperature program (normally heating) in a controlled atmosphere. The equipment monitors the sample weight as a function of temperature. This gaseous atmosphere might be inert or a reactive gas.

TGA measurements were done in a NETZSCH-STA 449 F1 Jupiter equipment in a flow of nitrogen.

7.19. TRANSMISSION ELECTRON MICROSCOPY (TEM)

TEM allows performing morphological and crystalline analysis of materials in the nano level with high resolution. An electron source at the top of the microscope emits the electrons that travel through vacuum in the column of the microscope. As in SEM, TEM uses electromagnetic lenses to focus the electrons into a very thin beam. The electron beam then is transmitted through the specimen. Depending on the electronic density of the material, some of the electrons are scattered and disappear from the beam. At the bottom of the microscope the unscattered electrons hit a fluorescent screen, resulting in a "shadow image" of the specimen with its different parts displayed in varied darkness according to their density.

Different microscopes were used depending on the purpose. For low-resolution images, a 120 KV JEOL 1210 operating at 120 KV was used. At the Universitat Autònoma de Barcelona (Sevei de Microscòpia) a low-resolution 120 KV JEM 1400 opreating a 100 KV and a high-resolution 200 KV JEM 2011 operating at 200 KV were used. Cryo-TEM analysis was performed by depositing a drop of the sample dispersion onto a Quantifoil® grid, and rapidly quenching it into liquid ethane. The grid was then transferred into the JEM 2011 microscope operating where the temperature was kept under -140 °C during the cell imaging.

7.20. UV-VIS SPECTROSCOPY

UV-Vis spectroscopy is used in the quantitative determination of many compounds. It is commonly carried out in solutions. When a material is irradiated by an ultraviolet or visible light beam (400-700 nm), the valence electrons of some molecules can absorb the light and excite to higher energetic states of empty orbitals. This technique measures the relative change of transmittance of light as it passes though the medium that is equivalent to the absorbed light by a sample.

A Cary 5 Varian UV/Vis/NIR spectrophotometer was used.

7.21. X-RAY DIFFRACTION (XRD)

It is possible to identify the atomic and molecular structure of crystalline materials with XRD obtaining information about the crystalline phase and unit cell dimensions of solids. X-ray wavelengths are in the range of interatomic distances (0.1-10 nm). When X-ray radiation is directed on a sample, the X-rays are diffracted by atoms present in the material. If the atoms in the material are arranged in a regular structure, *i.e.* if the material is crystalline, these constructive interferences are produced into specific directions. During a powder XRD (PXRD) measurement the angles of incidence and detection are scanned while the sample is rotated around the beam

axis. When the intensity of detected X-rays is plotted as a function of the diffraction angle (Ɵ) an X-ray diffraction pattern is obtained, which is characteristic for the sample material.

In this thesis the XRD patterns where obtained by using different equipments:

To analyze iron oxide nanoparticles in both composite AP_{Fe} and dried IONPs particles, a Rigaku Rotaflex RU-200B using a Cu anode with $\lambda_{K\alpha1} + \lambda_{K\alpha2} = 1.5418$ Å in the 2Ɵ range of 10-90º (AP_{Fe}) and 20-70º (IONPs) was used.

To detect both the amorphous structure of silica and the drug in raw silica AP and drug-impregnated AP and AP_{Fe} particles a Siemens D-5000 with a Cu anode provided by $\lambda_{K\alpha1} + \lambda_{K\alpha2} = 1.5418$ Å in the 2Ɵ range of 5-60º was employed.

To analyze the amorphous nature of silica and the drug in raw or drug-loaded aerogels without grinding the monolithic structure a Bruker-AXS D8 Advance using a Cu anode with $\lambda_{K\alpha1} + \lambda_{K\alpha2} = 1.5418$ Å and a 0.5 mm collimator operating from 5 to 70º.

8

CURRICULUM VITAE OF THE AUTHOR AND LIST OF PUBLICATIONS

Personal information

Surnames, first name: Murillo Cremaes, Nerea.
Date and place of birth: 25/05/1984, Barcelona.
Nationality: Spanish
E-mail: nmurillocremaes@gmail.com

Languages

Spanish: Mother tongue.
English: June 2010, *First Certificate Degree*. University of Cambridge. June 2008, Intermediate level by the Official Languages School. Good level on speaking, writing and reading.
Galician: Good level, speaking and writing.
Catalan: Good level speaking and basic at writing.

Education

November 2008-currently: **PhD in Materials Science**. Intitut de Ciència de Materials de Barcelona (ICMAB-CSIC), Spain. *Dissertation title:* Multifunctional silica-based nanoparticles for biomedical applications. Supervisors: Dr. Anna Roig and Dr. Concpeción Domingo. PhD to be defended 14 November 2014.

2007-2008: **Master in Advanced Chemistry**. Universidade de Vigo, Spain. *Dissertation title*: Synthesis of multifunctional microcapsules with optical properties sensitive to environmental changes. Supervisors: Dr. Luis Liz-Marzán and Dr. Isabel Pastoriza-Santos.

2002-2007: **Bachelor in Science (Chemistry)**. Universidade de Vigo, Spain.

Honors/contracts/awards

2009-2013: **Predoctoral FPU Fellowship** from the Spanish Ministry of Education (MEC). Reference: AP2008-04133.

2008-2009: **Research contract**. Institut de Ciència de Materials de Barcelona (ICMAB-CSIC).

Full Schoolarship to attend Summer school in Nanoscale Science of Biological Interfaces
June 19th-july 1st 2010. University of California Santa Barbara (UCSB), California (EEUU).

Predoctoral stays in foreign labs

January 2012-April 2012: Chemie et biologie des membranes et des nanoobjects (CBMN UMR), Bordeaux, France. Department: Biologie et biotecnologie, Research group: *Colloïdes et lipides pour l'Insdustrie et la Nutrition*. Project: "Coating of nanostructured silica-based materials with byomolecules". Supervisor: Pascale Subra-Paternault.

Technical experience

Nanotechnology: Synthesis of gold, iron oxide, silica and iron oxide/silica nanoparticles with tunable sizes. Coating of inorganic nanoparticles with polymers. Self assembly approaches with polyelectrolytes.

Supercritical technologies: Supercritical fluids as solvents, antisolvents or reaction media..

Limited experience in **Organic chemistry**: Synthesis of chromophore molecules.

During my thesis and master period I have learnt touse several instruments commonly required in materials science research and to interpret the results obtained from different techniques.

Self user: Electronic transmission microscopy (TEM), optical microscopy, dynamic light scattering (DLS), infrared spectroscopy (FTIR/ATR), UVVIs spectroscopy, fluorimetry, high performance liquid chromatography (HPLC), differential scanning calorimetry (DSC).

With technical support: scanning electron microscopy (SEM), thermogravimetric analysis (TGA), X-ray diffraction (XRD), nuclear magnetic resonance (RMN), chemical analysis (atomic flame spectrometry, inductively coupled plasma and mass spectrometry), contact angle measurements, superconducting quantum interference device (SQUID).

Computer skills

MS Office, EndNote, OriginLab, MestreC, Spectrum Version 5.01, Zetasizer software, Matersizer 2000. Gatan digital micrograph, ImageJ, NETZSCH Proteous thermal analysis, Cary WinUV software, PerkinElmer LS 45 Fluorescence software, SciFinder, Scopus, ISI Wok, Corel Draw X6.

Publications

1. **Nerea Murillo-Cremaes**, Ana Maria López-Periago, Javier Saurina, Anna Roig*, Concepción Domingo*
A clean and effective supercritical carbon dioxide method for the host-guest synthesis and encapsulation of photoactive molecules in nanoporous matrices.
Green Chemistry, **2010**, *12*, 2196-2204. DOI: 10.1039/C004762G. Impact factor = 6.852.

2. **Nerea Murillo-Cremaes**, Ana Maria López-Periago, Javier Saurina, Anna Roig*, Concepción Domingo*
Nanostructured silica-based drug delivery vehicles for hydrophobic and moisture sensitive drugs.
J. Supercrit. Fluids, **2013**, *73*, 34-42. DOI: 10.1016/j.supflu.2012.11.006. Impact factor = 2.571.

3. **Nerea Murillo-Cremaes**, Pascale Subra-Paternault*, Concepción Domingo*, Anna Roig*
Preparation and study of naproxen in silica and lipid/polymer hybrid composites.
RSC Adv., **2014**, *4*, 7084-7093. DOI: 10.1039/C3RA46947F. Impact factor = 3.708.

4. **Nerea Murillo-Cremaes**, Pascale Subra-Paternault, Javier Saurina, Anna Roig*, Concepción Domingo*
Compressed antisolvent process for polymer-coating of drug loaded aerogel nanoparticles and study of their release behaviors.
In print *Coll. Polym. Sci*., **2014**. DOI 10.1007/s00396-014-3260-6. Impact factor = 2.410.

5. **Nerea Murillo-Cremaes**, Pedro López-Aranguren, Lourdes Fernández Vega, Anna Roig*, Concepción Domingo*.
A novel solventless coating method to covalently graft low molecular weight polyethyleneimine on silica aerogel fine particles.
J. Polym. Sci. A: Polym. Chem., **2014**, *52*, 2760-2768. DOI: 10.1002/pola.27297. Impact factor = 3.543.

Published Proceedings

1. **N. Murillo-Cremaes**, E. Taboada, C. Domingo, A. Roig*
Silica and core-shell nanospheres by supercritical fluid assisted sol-gel process
13rd *European Meeting on Supercritical Fluids. SCFs as product and process solvents in emerging applications* (2011), p.: 200. The Hague (The Netherlands) ISBN 978-2-905267-77-1.

2. **N. Murillo-Cremaes**, A. M. López-Periago, J. Saurina, A. Roig*, C. Domingo*
Functionalized aerogels and aerogels inspired materials for different applications: photoactive molecules stabilization and accelerated release of drugs
13rd *European Meeting on Supercritical Fluids. SCFs as product and process solvents in emerging applications* (2011), p.: 70. The Hague (The Netherlands), ISBN 978-2-905267-77-1.

3. **N. Murillo-Cremaes**, J. Saurina, P. Subra-Paternault, A. Roig, C. Domingo*
Preparation of magnetic silica nanoparticles as drug delivery systems by using supercritical carbon dioxide. 14th *European Meeting on Supercritical Fluids.*

Scientific conferences/congresses

During my PhD thesis I have attended five international congresses, two projects meetings, one symposium and one workshop giving a total of six oral presentations and presenting seven posters.

3rd Meeting of experts on compressed fluids technology
February 5th-6th 2009, Universidad Complutense de Madrid (Spain).
Poster: "Pyrylium salt impregnation of nanoporous materials with scCO$_2$". **Nerea Murillo-Cremaes**, Ana María López-Periago, Elena Taboada, Carlos García-González, Concepción Domingo, Anna Roig.

Meeting on **Synthesis and surface modifications of nanocolloids**
February 18th-20th 2009. Hotel Bahía, Bayona (Pontevedra, Spain). Attendee

Annual Consolider Nanoselect Project Meeting
July 14th-16th 2010. Hotel Cap Roig, Platja d'Aro (Girona, Spain).
Poster: "Use of supercritical carbon dioxide for the host-guest synthesis and encapsulation of photoactive molecules in nanoporous matrices". **Nerea Murillo-Cremaes**, Ana María López-Periago, Javier Saurina, Anna Roig, Concepción Domingo.

ESF-UB Conference in Biomedicine, Nanomedicine: Reality Now and Soon
October 23rd-28th 2010. San Feliu de Guixols (Girona, Spain). No personal attendance.
Oral presentation: "Magnetic-silica nanospheres. Application as contrast agents for MRI and as drug delivery carriers". Nerea Murillo-Cremaes, Elena Taboada, Elisenda Rodríguez, Javier Saurina, Concepción Domingo, Anna Roig.

Materials Research Symposium (MRS), Fall Meeting 2010
November 29th-december 3rd 2010. Boston (Massachusetts, USA). No personal attendance.
Oral presentation: "A clean and effective supercritical carbon dioxide method for the host-guest synthesis and encapsulation of photoactive molecules in nanoporous matrices". Nerea Murillo-Cremaes, Ana María Lopez-Periago, Xavier Saurina, Concepción Domingo, Anna Roig.
Poster: "Drug Impregnated magnetic nanospheres for biomedical applications". Nerea Murillo-Cremaes, Elena Taboada, Ana María Lopez-Periago, Xavier Saurina, Concepción Domingo, Anna Roig.

2nd International Conference on Multifunctional, Hybrid and Nanomaterials.
March 6th-10th 2011. Palais des Congrès, Estrasbourg (France).
Poster: "Use of supercritical carbon dioxide for the host-guest synthesis and encapsulation of photoactive molecules in nanoporous matrices". **Nerea Murillo-Cremaes**, Ana María López-Periago, Xavier Saurina, Anna Roig, Concepción Domingo.
Poster: "Drug impregnated magnetic nanospheres". **Nerea Murillo-Cremaes**, Javier Saurina, Concepción Domigo, Anna. Roig.

Annual Consolider Nanoselect Project Meeting
June, 12nd-15th 2011. Hotel Cap Roig, Platja d'Aro (Girona, Spain).
Oral presentation: "Drug loaded hybrid magnetic nanoparticles".
Poster: "Photoactive organic molecules grafted in nanostructured oxides using supercritical fluids". **Nerea Murillo-Cremaes**, Irene González, Ana María López-Periago, Mónica Lira-Cantu, Anna Roig, Concepción Domingo.

13th European Meeting on Supercritical Fluids
October 9th-12nd 2011. World Forum Convention Center, Den Hague (The Netherlands).
Oral presentation: "Functionalized aerogels and aerogels inspired materials for different applications: photoactive molecules stabilization and accelerated release of drugs". **Nerea Murillo-Cremaes**, Ana María López-Periago, Javier Saurina, Anna Roig, Concepción Domingo.
Poster: "Silica and core-shell nanospheres by supercritical fluid assisted sol-gel process". **Nerea Murillo-Cremaes**, Elena Taboada, Concepción Domingo, Anna Roig.

4th IBEC Symposium on Bioengineering and Nanomedicine
Octuber 18th 2011. Hospital de Bellvitge, Barcelona (Spain).
Poster: "Drug impregnated magnetic nanospheres". **Nerea Murillo-Cremaes**, Javier Saurina, Concepción Domingo, Anna Roig.

9th International Conference on the Scientific and Clinical Applications of Magnetic Carriers
May 22nd-27th 2012. Minneapolis (USA). No personal attendance.
Poster: "Drug impregnated magnetic nanospheres". Nerea Murillo-Cremaes, Javier Saurina, Concepción Domingo, Anna Roig.

International Magnifyco 2013 Workshop
February 20th-22nd 2013. Universitat de Barcelona, Barcelona (Spain).
Oral presentation: "Iron oxide-silica-polymer as tunable drug delivery systems". **Nerea Murillo-Cremaes**, Javier Saurina, Pascale Subra-Paternault, Concepción Domingo, Anna Roig.

E-MRS Spring Meeting
May 27th-31st 2013. Palais des Congrès, Estrasbourg (France).
Oral presentation: "Magnetic silica nanospheres as drug delivery systems by a supercritical fluid route". **Nerea Murillo-Cremaes**, Javier Saurina, Pascale Subra-Paternault, Concepción Domingo, Anna Roig.

XVII International Sol-Gel Conference
August 25th-30th 2013. Hotel Meliá Castilla, Madrid (Spain).
Oral presentation: "Multifunctional silica nanoparticles as drug delivery systems". **Nerea Murillo-Cremaes**, Javier Saurina, Pascale Subra-Paternault, Concepción Domingo, Anna Roig.

14th European Meeting on Supercritical Fluids
May 18th-21st 2014. Palais du Pharo, Marseille (France).
Oral presentation: "Preparation of magnetic silica nanoparticles as drug delivery systems by using supercritical carbon dioxide". **Nerea Murillo-Cremaes**, Javier Saurina, Pascale Subra-Paternault, Concepción Domingo, Anna Roig.

Courses/seminars

During my PhD thesis I have attended to six courses and three seminars presenting one poster.

X-Ray diffraction applied to materials
November 2008. Institut de Ciència de Materials de Barcelona (ICMAB-CSIC), Bellaterra (Spain).

Materials for implants
April 2009. Universitat Autònoma de Barcelona (UAB), Bellaterra (Spain).

Microscopy conferences: SEM, TEM; AFM, OM. General aspects and applications
May 25th 2009. Institut de Ciència de Materials de Barcelona (ICMAB-CSIC), Bellaterra (Spain).

Practical course on polymers and drug delivery
June 18th-28th 2009. Instituto de Ciencia y tecnología de Polímeros (ICTP-CSIC), Madrid (Spain).

RMN and EPR spectroscopic conferences. General aspects and applications
 November 23rd 2009. Institut de Ciència de Materials de Barcelona (ICMAB-CSIC), Bellaterra (Spain).

3rd Course on thermal analysis and applied calorimetry
February 8th-12nd. Superior technical college of Girona, Girona (Spain).

Application of supercritical fluids to processes respectful to the environmnet
Apirl 2010. MATGAS, Bellaterra (Spain).

Summer school in Nanoscale Science of Biological Interfaces
June 19th-july 1st 2010. University of California Santa Barbara (UCSB), California (EEUU).
Poster: "Drug impregnated core@shell magnetic nanoparticles for biomedical applications". **Nerea Murillo-Cremaes**, Elena Taboada, Javier Saurina, Ana María López-Periago, Concepción Domingo, Anna Roig.

Course **PhDs in the industry**
December 2012. Institut de Ciència de Materials de Barcelona (ICMAB-CSIC), Bellaterra (Spain).

Participation in Research Projects

Nanostructured thin films and nanoparticles: preparation, characterization and prospective for technological applications. MAT2009-08024.
Institut de Ciència de Materials de Barcelona (ICMAB-CSIC), Spain. January 2010-december 2012. PI: Benjamín Martínez.

Materiales avanzados y nanotecnologías para dispositivos y sistemas eléctricos, electrónicos y magnetoelectrónicos innovadores. NANOSELECT CSD 2007-00041
Institut de Ciència de Materials de Barcelona (ICMAB-CSIC), Spain. October 2007-september 2012. PI: Xavier Obradors.

Suport als grups de recerca de Catalunya (SGR). 2009SGR203
Institut de Ciència de Materials de Barcelona (ICMAB-CSIC), Spain. PI: Elies Molins.

Materiales bioactivos nanoestructurados para medicina regenerativa y salud preparados con tecnología de CO$_2$ supercrítico. MAT2012-35161.
Institut de Ciència de Materials de Barcelona (ICMAB-CSIC), Spain. PI: Aurelio Salerno.

Material prototipo de nanopartículas inteligentes aptas para la vehiculización de fármacos.
Institut de Ciència de Materials de Barcelona (ICMAB-CSIC), Spain. Fundación Domingo-Martínez. February 2009-february 2010. PI: Anna Roig.

Rational design of hybrid organic-inorganic interfaces: the next step towards advanced functional materials.
COST Action MP1202 (COST program). Institut de Ciència de Materials de Barcelona (ICMAB-CSIC), Spain. March 2013-March 2016. PI: Marie-Helene Delville (ICMCB-CNRS).

References

In case references were required, I will be happy to provide names of researchers able to provide them.

A clean and effective supercritical carbon dioxide method for the host–guest synthesis and encapsulation of photoactive molecules in nanoporous matrices†

Nerea Murillo-Cremaes,[a] Ana M. López-Periago,[a] Javier Saurina,[b] Anna Roig*[a] and Concepción Domingo*[a]

The present work is concerned with host–guest processes in the micro- and mesoporous restricted spaces provided by silica aerogels and aluminosilicates. A supercritical carbon dioxide ship-in-a-bottle approach was used for the synthesis of photoactive molecules (triphenylpyrylium and dimethoxyltrityl cations) inside these nanoporous matrices. The resulting hybrid nanocomposites can act as stable and recoverable heterogeneous photocatalysts, having obvious advantages with respect to the more easily degraded organic cations frequently used in homogeneous catalysis. Two aspects of green chemistry are combined in this study to produce nanoporous materials loaded with cationic photosensitizers: (i) the use of supercritical carbon dioxide as a reaction medium in one-pot and as a zero waste technology, and (ii) the use of transparent high surface area nanoporous supports that are expected to be more effective for the target photoactive applications than traditional opaque microporous matrices.

Introduction

Nanoporous inorganic oxide materials possess unique surface, structural and bulk properties that underpin their importance in various fields of application, such as ion exchange, separation, catalysis, sensors and molecular isolation or purification processes.[1,2] Nanoporous materials are also of scientific and technological importance owing to their ability to adsorb and interact with atoms, ions and molecules in restricted spaces. As a result, new synthetic pathways to fabricate functional materials can be implemented in research areas such as inclusion chemistry, host–guest synthesis, molecular manipulation and reactions at the nanoscale.[3] This work deals with the preparation of nanoporous and nanocomposite hybrid materials. In particular, we report here an environmentally improved ship-in-a-bottle approach for the synthesis of photoactive molecules inside the micro- and mesoporous spaces provided by silica aerogel matrices, which are compared with an aluminosilicate support. In fact, both aerogels[4,5] and zeolites[6,7] are among the most porous host materials known, with accessible surface areas as large as 1000 m²g⁻¹.

A particular case of a host–guest synthesis procedure is the encapsulation of chromophores and cationic organic dyes within nanoporous matrices to be used in optical applications such as solid-state dye lasers,[8,9] aerogel-platform gas sensors[10] or in photocatalysis.[11–16] In comparison to homogeneous transparent solutions, an inherent disadvantage to all photochemical reactions carried out heterogeneously using opaque solids as supports are optical phenomena associated with the interaction of light with the solids (scattering, diffraction and reflection). The use of highly transparent mesoporous silica aerogel structures could bring added value to materials for photocatalysis (Table S1, ESI†). The photosensitizers selected in this work were the 2,4,6-triphenylpyrylium (Ph_3Py^+) and the dimethoxyltrityl ((CH_3O)$_2Ph_3C^+$) cations. Both salts have a relatively high oxidation power and have been reported to be good electron transfer photosensitizers for photochemical reactions involving aromatics, dienes or alkenes and epoxides, and for treating air and water pollutants using solar light.[17,18] Unfortunately, they also have a poor stability in aqueous media.[19,20] The compartmentalized intravoid spaces of nanoporous matrices are specially suited to incorporating and stabilizing these guests. Hence, the resulting host–guest assemblies can act as easily recoverable heterogeneous photocatalysts.

The use of supercritical carbon dioxide ($scCO_2$) as a solvent to perform adsorption and impregnation processes,[21–27] materials functionalization[28–32] and chemical reactions has received considerable attention as a viable and sustainable alternative to conventional liquid solvents.[33–37] In our previous work,[15,16] the use of $scCO_2$ to impregnate organic molecules and cations into microporous solids have been reported as viable and sustainable alternatives to conventional organic solvents. The results of these previous studies, together with the work extended here to preparing photocatalytic transparent nanocomposite materials based on silica aerogels, are further discussed in light of the principles and tools of green chemistry.[38] Firstly, our one-step ship-in-a-bottle process incorporates environmental considerations by avoiding the use of persistent organic solvents and minimizing

[a] Institut de Ciència de Materials de Barcelona (ICMAB-CSIC), Campus UAB, 08193, Bellaterra, Spain.
E-mail: roig@icmab.es, conchi@icmab.es; Fax: +34 935805729; Tel: +34 935801853
[b] Department of Analytical Chemistry. University of Barcelona, Martí I Franquès 1–11, Barcelona, E-08028, Spain.
E-mail: xavi.saurina@ub.edu; Fax: +34 934021233; Tel: +34 934039778
† Electronic supplementary information (ESI) available: Raw and prepared materials characteristics comparative table. See DOI: 10.1039/c004762g

the necessity of the final washing and drying steps. The final washing step is performed with a continuous flow of scCO$_2$. The generated CO$_2$ is contaminated with residual organics; however, these organics can be easily eliminated from the exit flow by solid adsorption (f.i., using zeolites) or by decreasing the pressure, thus reducing the scCO$_2$ solvent power. Conversely, conventional processes usually require an exhaustive and time consuming Soxhlet extraction post-treatment for purification[39–41] consisting of cleaning through extraction with dichloromethane at 40–45 °C over 2–3 days followed by filtration and solvent drying under vacuum for a minimum of 24 h. Secondly, the use of scCO$_2$ as a solvent facilitates the recovery of the non-reacted raw materials by simply lowering the pressure of the system. Finally, the very low viscosity and null surface tension of scCO$_2$ greatly accelerates diffusion through the nanochannels in comparison with organic solvents.

In this work, results of the encapsulation ability and photochemical stability of the previously mentioned cations in transparent mesoporous silica aerogels were compared with those obtained for opaque zeolites. For all the studied matrices, the impregnated cations showed a higher hydrolysis stability when encapsulated than in their crystalline form. The characterization of the resulting materials was based on infrared, ultraviolet-visible and fluorescence spectroscopies, thermogravimetric analysis, surface area nitrogen adsorption and optical microscopy.

Experimental

Materials

Host nanoporous matrix preparation. Laboratory-synthesized monolithic and particulate silica aerogels (AM and AP, respectively) and a commercial microporous zeolite of the faujasite-type (ZY) were used as matrices for impregnation.

Aerogel matrices were prepared by the hydrolysis and polycondensation of tetramethylorthosilicate (TMOS, Aldrich) and high temperature supercritical drying by following reported procedures.[42,43] Typically, silica aerogel monoliths were obtained from a mixture of methanol : TMOS : water (12.25 : 1 : 4 molar ratio) in the presence of a small amount of ammonium hydroxide used as a catalyst, while a mixture of acetone : TMOS : H$_2$O (88.34 : 1 : 2 molar ratio) was used to precipitate the particulate system. In the first case, the gels were subjected to supercritical drying using a 2 L automated high pressure reactor (Autoclave Engineers). In the second, the sol obtained from the acetone solution was transferred to a 1 L Pyrex lab beaker and immediately introduced into the high pressure autoclave. In both cases, the pressure inside the reactor was increased to *ca.* 50 bar by adding CO$_2$. Next, to exceed the critical point of the mixtures (CO$_2$/methanol or CO$_2$/acetone), the temperature was increased stepwise to 220 or 250 °C, with a corresponding pressure rise to 250 or 280 bar, respectively. After 2 h at these conditions, fresh CO$_2$ was circulated over 2 h with the purpose of extracting any unreacted alkoxide precursor. The system was then depressurized and the solid material was further washed for 30 min with a flow of fresh CO$_2$ at 3 bar. Finally, the autoclave was allowed to cool down to room temperature. The material collected from the methanol solution was in the shape of transparent cylinders (AM samples) of about 0.8

× 2.4 cm and a density of 0.1 Kg m^{-3}, while the material obtained from the acetone solution was a very light, white, spongy and homogeneous powder (AP samples) composed of monodispersed spherical nanoparticles of ~ 300 nm mean diameter and 9% polydispersity.

The ZY microporous matrix was the ammonium counterion tridirectional Y zeolite (Si/Al = 1.6) supplied by Strem Chemicals. Before impregnation, the zeolite was activated by calcination in a tubular oven (Carbolite 3216) at 520 °C over 48 h under a flow of nitrogen with oxygen traces.

Guests and precursor materials. The guest compounds chosen for encapsulation were the organic cations: 2,4,6-triphenylpyrylium (Ph$_3$Py$^+$, Py$^+$) and dimethoxytrityl ((CH$_3$O)$_2$Ph$_3$C$^+$, C$^+$). The precursor used for Ph$_3$Py$^+$ impregnation was the diketone 1,3,5-triphenyl-2-pentene-1,5-dione, synthesized in our laboratory by following a reported procedure.[44] The two organic precursors used as the building blocks for (CH$_3$O)$_2$Ph$_3$C$^+$ encapsulation were benzaldehyde and anisole (Fluka) in a 1 : 2 molar ratio. Commercially available 2,4,6-triphenylpyryl tetrafluoroborate (Ph$_3$PyBF$_4$, c-Py$^+$, Aldrich) and trityl tetrafluoroborate (Ph$_3$CBF$_4$, c-C$^+$, Aldrich) were used as references for comparisons with encapsulated products.

Methods: scCO$_2$ encapsulation procedure

Supercritical impregnation experiments were performed in batch mode in high pressure equipment described elsewhere.[15,16] In a typical experiment, liquified CO$_2$ was compressed by a syringe pump and delivered to a 0.1 L reactor equipped with a vertical magnetic stirrer. The reactor was first charged with *ca.* 0.5 g of the matrix in the form of small pieces (AM) or powder (AP and ZY), and the precursors of the guest material in a proportion of 20 wt%. The matrices were enclosed in cylindrical cartridges made of 0.45 μm pore size paper, thus avoiding direct contact with the solutes. The approach followed assumes that the cation formation proceeds in two steps: (i) diffusion followed by (ii) condensation, performed separately in time.[15,16] The first step consisted of diffusing the starting reagents inside the matrix nanochannels at a pressure of 150 bar and a relatively low temperature (60 °C), thus minimizing the formation of the bulky cation, which otherwise could block the channels in the early stages of the process. This stage was followed by a condensation step at high temperature (130–150 °C), performed to activate the reaction of the precursors inside the solid acidic matrix. During the reaction, the autoclave was stirred at 400 rpm. Finally, the system was depressurized and left to cool to room temperature. Pressurization and depressurization cycles were carried out avoiding the formation of liquid CO$_2$ in the autoclave, which could damage the fragile porous structure of the aerogels.

Zeolite samples recovered at this stage were gently rinsed on the surface with dichloromethane (DCM), while monolithic samples were cleaned with a flow of high velocity N$_2$. The resulting materials were labeled as [cation@matrix]. Some materials were further cleaned with a flow of continuous scCO$_2$ at 200 bar and 80 °C for 3 h. The resulting samples were labeled as [cation@matrix]$_{SC}$.

Characterization

Loading efficiencies were evaluated by thermogravimetric analysis (TGA, Perkin-Elmer 7) under an N_2 atmosphere with a 10 °C min^{-1} heating rate. The BET specific surface area (S_a) was determined by N_2 adsorption–desorption measurements at 77 K using an ASAP 2000 Micromeritics Inc. instrument. Prior to measurements, samples were dried under a reduced pressure. The conditions used were 300 °C over 24 h for aerogel particles, 100 °C over 24 h for aerogel monoliths and 150 °C over 48 h for zeolites. Fourier transformed infrared (FTIR) spectra of the solid samples mixed with KBr were recorded on a Perkin-Elmer Spectrum One instrument. The diffuse reflectance spectra of the impregnated matrices were acquired on a UV-vis spectrophotometer (Perkin-Elmer Lambda 19 UV/VIS/NIR). Fluorescence data was obtained using a Leica TCS SP5 AOBS confocal laser microscope at 420 nm. The impregnated matrices were immersed in distilled water (pH = 6.5) for 12 d to evaluate their leaching behavior. Approximately 3–5 mg of each impregnated matrix was placed into a glass with 4 mL of water and kept in a lab exposed to natural light. After the first 24 h, 1.5 mL of the liquid was analyzed by UV-vis spectroscopy using a Cary 5 Varian UV/vis/NIR spectrophotometer. On the 5th day, a second 1.5 mL aliquot was extracted and the absorption measurement repeated. Then, the impregnated matrices were covered with a further 5 mL of fresh water and one more UV-vis monitoring was performed on day 12.

Results and discussion

The scCO$_2$ ship-in-a-bottle method used for the preparation of aerogel- or zeolite-encapsulated cations consisted of the adsorption into the nanopores of different building blocks dissolved in scCO$_2$ and their subsequent condensation to form the guest cations. In all cases, the sizes of the molecular precursors were smaller than the aerogel or the zeolite channels. Some of the characteristics of the resulting materials are shown in Table 1.

The chemical reaction necessary to form the cations was triggered by the weak acid sites (such as those of silanols, pK_a = 8) of the inner pores of either the silica aerogel (Fig. 1a) or the aluminosilicate (Fig. 1b). In the case of the zeolite, the resulting cations could only be accommodated in the 1.3 nm cavities. The formation of the pyrylium cation was accomplished by the dehydratation and cyclisation of the diketone. The reaction used for the preparation of the dimethoxytrityl cation occurred between benzaldehyde and anisole.

Table 1 Characteristics of the obtained materials (AM: aerogel monolith; AP: aerogel particles; ZY: zeolite Y)

Sample	Impregnated cation	Sample color	Loading (wt%)
[Py$^+$@AM]	Pyrylium	Orange	8.6
[C$^+$@AM]	Trityl	Yellow	1.5
[Py$^+$@AP]	Pyrylium	Yellow	5.7
[Py$^+$@AP]$_{SC}$	Pyrylium	Pale yellow	5.3
[C$^+$@AP]	Trityl	Pale yellow	3.4
[Py$^+$@ZY]$_{SC}$	Pyrylium	Yellow	5.9
[C$^+$@ZY]$_{SC}$	Trityl	Ochre	7.0

The coloration of the resulting host materials may be used as a first visual indication of the degree of success of the reaction (Table 1). The precursors of the guest molecules were colorless, and only after cation formation did a color appear that was associated with absorption in the visible range. While the matrix was initially either transparent (AM in Fig. 2a) or white (AP and ZY in Fig. 2d and g, respectively), the adsorption of the cation was noticeably visible from the resulting yellow-orange color (Fig. 2b, c, e, f for impregnated aerogels and Fig. 2h, i for impregnated zeolites).[45–46] A uniform color of the pyrylium impregnated AM material was noted (sample [Py$^+$@AM] in Fig. 2b), indicating that diffusion of the precursor was homogeneous throughout the sample.

Thermal studies (TGA)

Thermogravimetric profiles of the pristine matrices and commercial cations are shown in Fig. 3a and 3b, respectively. Aerogel and zeolite particles presented an initial weight loss of ~ 5–10 wt% at temperatures lower than 150 °C, corresponding to the evaporation of adsorbed water (Fig. 3a). In the temperature range 150–400 °C, the weight loss of untreated monolithic aerogel was insignificant, while for particulate aerogel and zeolite matrices, although minor, it was measurable (*ca.* 0.5–1 wt%). Aerogel matrices also lost weight at temperatures higher than 450–500 °C due to material densification, and the reaction between silanol groups and the concomitant loss of water. Commercial Ph$_3$PyBF$_4$ decomposed at temperatures between 240 and 325 °C and the maximum slope was found at 300 °C, while the Ph$_3$CBF$_4$ salt showed a decomposition profile characterized by a pronounced weight loss (~75 wt%) between ~ 190 and 320 °C (Fig. 3b). For the impregnated samples in the form of particulate powders (Fig. 3c, d), the first mass decay was observed at temperatures lower than 180 °C and was associated with the loss of water, while the decay at temperatures higher than 200 °C was attributed to the loss of the encapsulated organic cation. The decomposition of the pyrylium cation when entrapped in the aerogel (AM or AP) and zeolite systems occurred in the temperature ranges of 250–400 °C (maximum slope at 350 °C) and 325–500 °C (maximum slope at 425 °C), respectively (Fig. 3c). This result indicates that the Ph$_3$Py$^+$ cation inside the nanopores presents a higher thermal stability than in the Ph$_3$PyBF$_4$ salt. On the other hand, the trityl cation, once impregnated in the different matrices, thermally decomposed (Fig. 3d) in a temperature range only slightly superior (~ 250–400 °C) to that of the commercial product.

Weight losses measured in the appropriate temperature range for each [cation@matrix] pair were used to estimate the load of formed organic cation (Table 1). As a general trend, higher loadings were obtained for the pyrylium than for the trityl cation. Note that the formation of the pyrylium cation proceeds through the dehydration and cyclisation of one precursor (diketone), while the preparation of the trityl cation involves two building blocks and the formation of a C–C bond (Fig. 1).

Surface area

The specific surface areas were measured before and after processing the matrices with the pyrylium cation. The aerogel monolith and particles had surface area values of 475 and
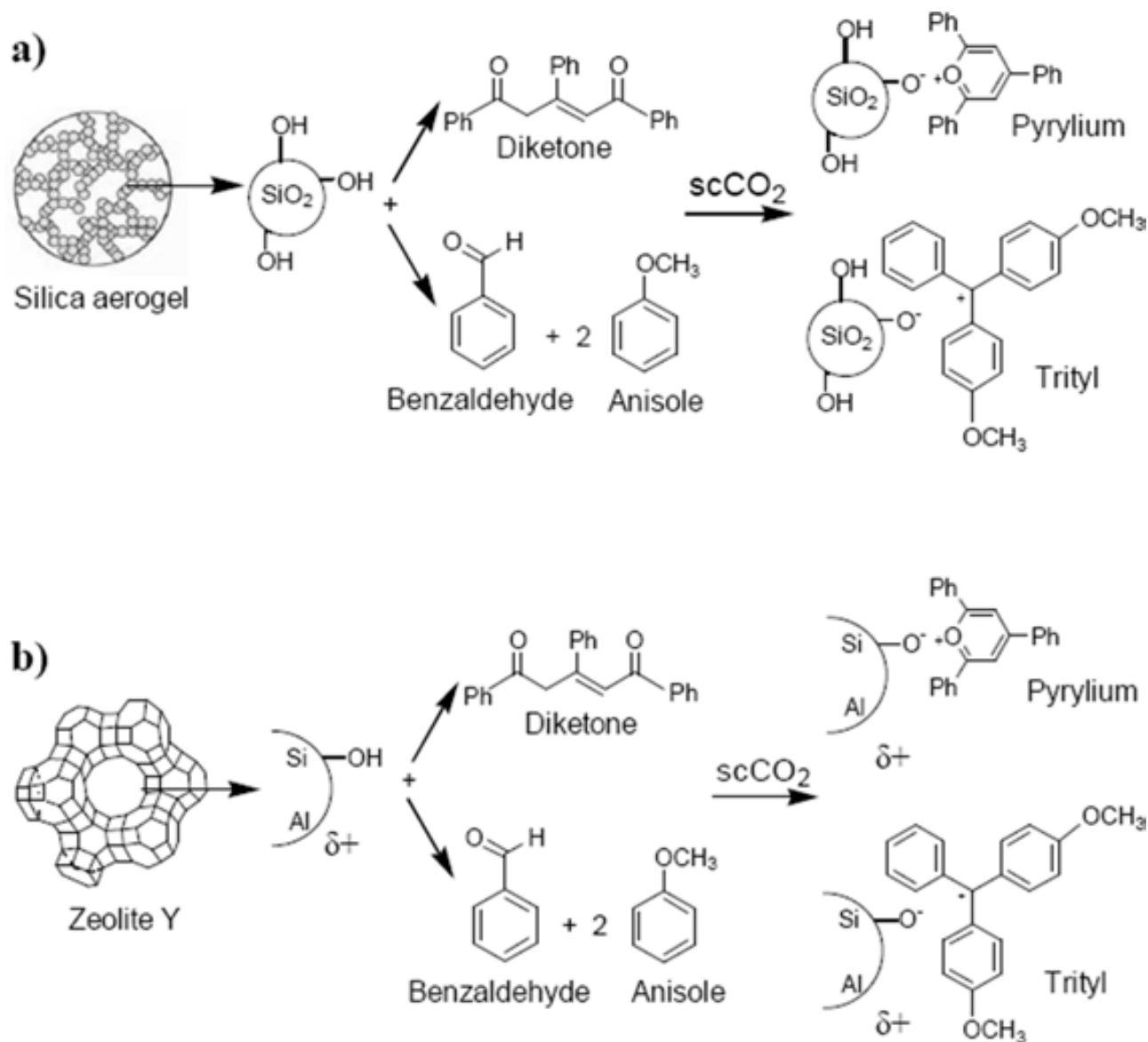
Fig. 1 A schematic representation of the encapsulation reactions studied for the different matrices: (a) monolith or particulate aerogel and (b) zeolite Y.

205 m^2 g^{-1}, respectively. The silica aerogel monoliths are amorphous mesoporous materials (20–100 nm pore size) with high tortuosity coefficients and applications as diverse as drug delivery or thermal insulators.[47–50] On the other hand, aerogel-like particles could be considered as an intermediate material between zeolites and aerogel monoliths.[51] They consist of a fine powder with a mean pore size of 1.5–2 nm, similar to that of zeolites. However, some other characteristics, such as the non-ordered pore structure, are close to monolithic silica aerogels. For the calcined zeolite (ZY), the measured surface area was 700 m^2 g^{-1}. The zeolite architecture was defined as almost spherical cavities of 1.3 nm in diameter that were accessible through tetrahedral windows of 0.74 nm arranged in a tridirectional ordered structure.[52]

After impregnation of the aerogel monolith and zeolite supports with pyrylium cations, their specific surface area was only slightly diminished to values of 410 and 500 m^2 g^{-1},

respectively. Contrarily, a drastic drop (about 80%) was obtained for the impregnated aerogel-like particles. For the three studied supports, the reduction in the measured value of the surface area is evidence of a successful solute adsorption by the matrices' cavities. The low values found for the aerogel particles point towards the blocking of the channels, probably due to reduced pore interconnectivity in this matrix with respect to the aerogel monolith and zeolite particles.

IR spectroscopy

In the IR spectra (Fig. 4a) of the pristine matrices, both aerogel and zeolite, where the characteristic bands of the principal organic functional groups of pyrylium and trityl cations appear.

Intense absorption bands appear for these matrices in the 900–1200 cm^{-1} region, which correspond to the stretching vibrations of the O–Si–O bond in the SiO$_4$ tetrahedrons of zeolite or in

Fig. 2 Optical photographs of: (a) pristine monolithic aerogel (AM), and impregnated samples (b) [Py$^+$@AM] and (c) [C$^+$@AM]; (d) pristine aerogel particles (AP), and impregnated samples (e) [Py$^+$@AP]$_{SC}$ and (f) [C$^+$@AP]; and (g) pristine zeolite Y, and impregnated samples (h) [Py$^+$@ZY]$_{SC}$ and (i) [C$^+$@ZY]$_{SC}$.

Fig. 3 TGA curves of (a) pristine matrices, (b) commercial salts, and samples obtained after impregnation with (c) pyrylium and (d) trityl cations. Curves labeled as d([cation@matrix]) are the derivatives of the respective TGA curves.

the skeleton of the aerogel. The low intensity band sometimes appearing at 1620–1650 cm^{-1} is due to the bending frequency of adsorbed molecular water into the matrices. The typical bands of Ph$_3$Py$^+$ appear between 1550 and 1650 cm^{-1} for the commercial compound[53] (sample c-Py$^+$ in Fig. 4a) and at the same energies for the encapsulated products (Fig. 4b). The lack of C=O vibration bands at 1680–1650 cm^{-1}, characteristic of the diketone precursor, indicates a high degree of purity for samples impregnated with pyrylium cations. The FTIR spectra of commercial Ph$_3$CBF$_4$ (sample c-C$^+$ in Fig. 4a) present peaks at 1489 and 1445 cm^{-1} corresponding to C–C stretches in the phenyl ring and a signal at 1384 cm^{-1} assigned to C–Ph stretching.[54] This latter signal did not appear in any of the building blocks used and therefore was specially useful to monitor the presence of the trityl cation. For the trityl-impregnated products, the most intense peaks of the C–C ring stretching mode in the (CH$_3$O)$_2$Ph$_3$C$^+$ cation are found between 1495–1500 and 1440–1450 cm^{-1}, while the most representative band corresponding to the C–Ph bond appears at 1384–1381 cm^{-1}. Consequently, it can be assumed that the preparation of the (CH$_3$O)$_2$Ph$_3$C$^+$ cation was successfully achieved.

Diffuse reflectance UV-vis and fluorescence spectroscopies

All the matrices used were quite transparent to UV-vis radiation above *ca.* 250–300 nm. Fig. 5a shows the diffuse reflectance spectra in the UV-vis range of the commercial Ph$_3$PyBF$_4$ salt and the matrices loaded with Py$^+$. The solid spectrum of commercial Ph$_3$PyBF$_4$ displayed a broad band between 320 and 530 nm. For all the prepared pyrylium samples, a similar absorption band between 330 and 500 nm was found, which suggests cation formation. Analogously, Fig. 5b shows the diffuse reflectance
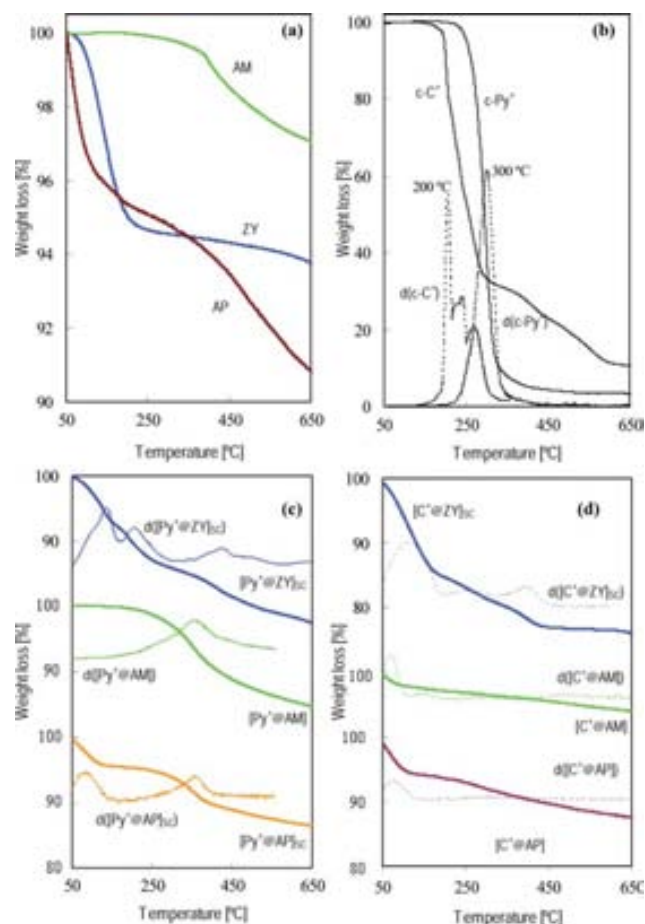
spectrum of the commercial Ph$_3$CBF$_4$ salt as well as the matrices loaded with C$^+$. The spectrum of the commercial product is characterized by a broad absorption band from 320 to 530 nm. For the trityl-impregnated aerogel samples, the absorption in the range 352–525 nm is weak, which was related to the relatively low amount of impregnation (Table 1). On the other hand, the diffuse reflectance UV-vis spectrum of sample [C$^+$-ZY]$_{SC}$ shows two separated maxima at 417 and 506 nm, characteristic of substituted trityl cations with optical asymmetry.

Room temperature emission fluorescence microscopy was used to investigate the fluorescence of the AM and ZY impregnated samples upon excitation at 420 nm. Control experiments with the pristine matrices did not show any significant fluorescence. The emission spectra of the matrices with entrapped pyrylium cations (samples [Py$^+$@AM] and [Py$^+$@ZY]$_{SC}$) are presented in Fig. 6a. In particular, pyrylium salts in solution have a fluorescence band with a maximum at 470–480 nm.[55,56] This value is similar to that found for the prepared solid pyrylium samples, which clearly showed a strong fluorescence band centered close to 500 nm. In contrast to pyrylium, trityl cations exhibited a much weaker fluorescence[57,58] and low intensity emission spectra were registered for the matrices with entrapped trityl cations (not shown). For samples

Fig. 6 Fluorescence data upon 420 nm excitation: (a) emission spectra of encapsulated pyrylium and (b) microscope images of encapsulated trityl.

Leaching behaviour in water

The present study was designed to elucidate the possible leaching of the impregnated compounds from the nanoporous matrices into water and, at the same time, the stability in water of the encapsulated cation. For this purpose, prepared samples were submerged in distilled water for a total of 12 d. Importantly, after this relatively long period of time, the materials still maintained their characteristic yellow/orange color of the impregnated products, indicating that both leaching and degradation of the cation were minor.

To study the leaching behaviour of the different materials, aliquots of the liquid phase were withdrawn at given times and analyzed by UV-vis spectrophotometry. The UV-vis spectra of the triphenylpyrylium and trityl salts in organic solution present a broad band between 370–480 nm, generated by two independent chromophores,[59,60] while their precursors have appreciable absorption at wavelengths between 200 and 350 nm. Preliminary tests showed that both cations were unstable in water at neutral pH, being transformed in colorless low molecular weight degradation products. Following the designed leaching protocol, after 5 d in water, the spectra of the as-prepared aerogel samples (encapsulating either pyrylium or trityl cations
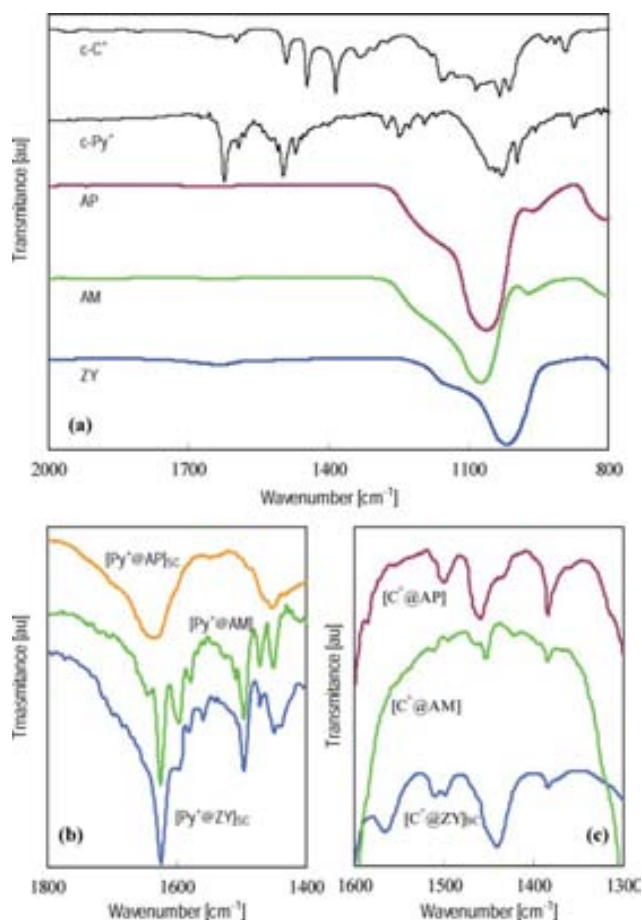

Fig. 4 FTIR spectra of: (a) pristine matrices and commercial cations, and impregnated matrices with (b) pyrylium and (c) trityl cations.

$[C^+@ZY]_{SC}$ and $[C^+@AM]$, fluorescence microscopy indicated that samples were also fluorescent in the blue region (Fig. 6b). It is of importance that fluorescent optical images showed a homogeneous distribution of dyes in the matrices, even in the large pieces of the aerogel monolith.
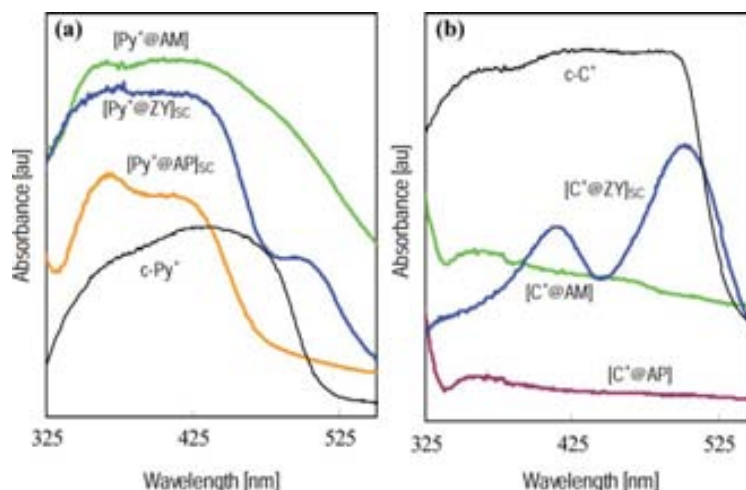

Fig. 5 Diffuse reflectance UV-vis spectra of: (a) commercial pyrylium product and the different studied matrices impregnated with Py^+ and (b) commercial trityl product and the different studied matrices impregnated with C^+.
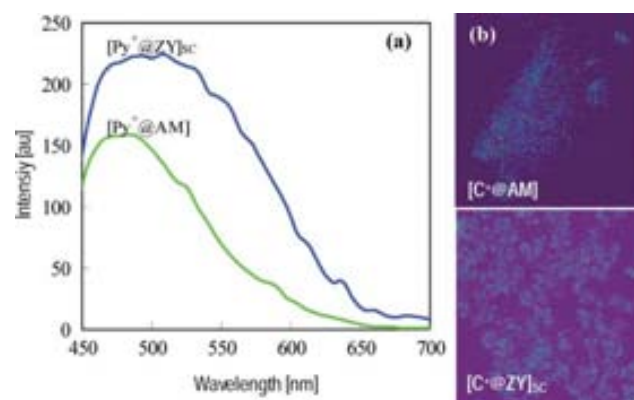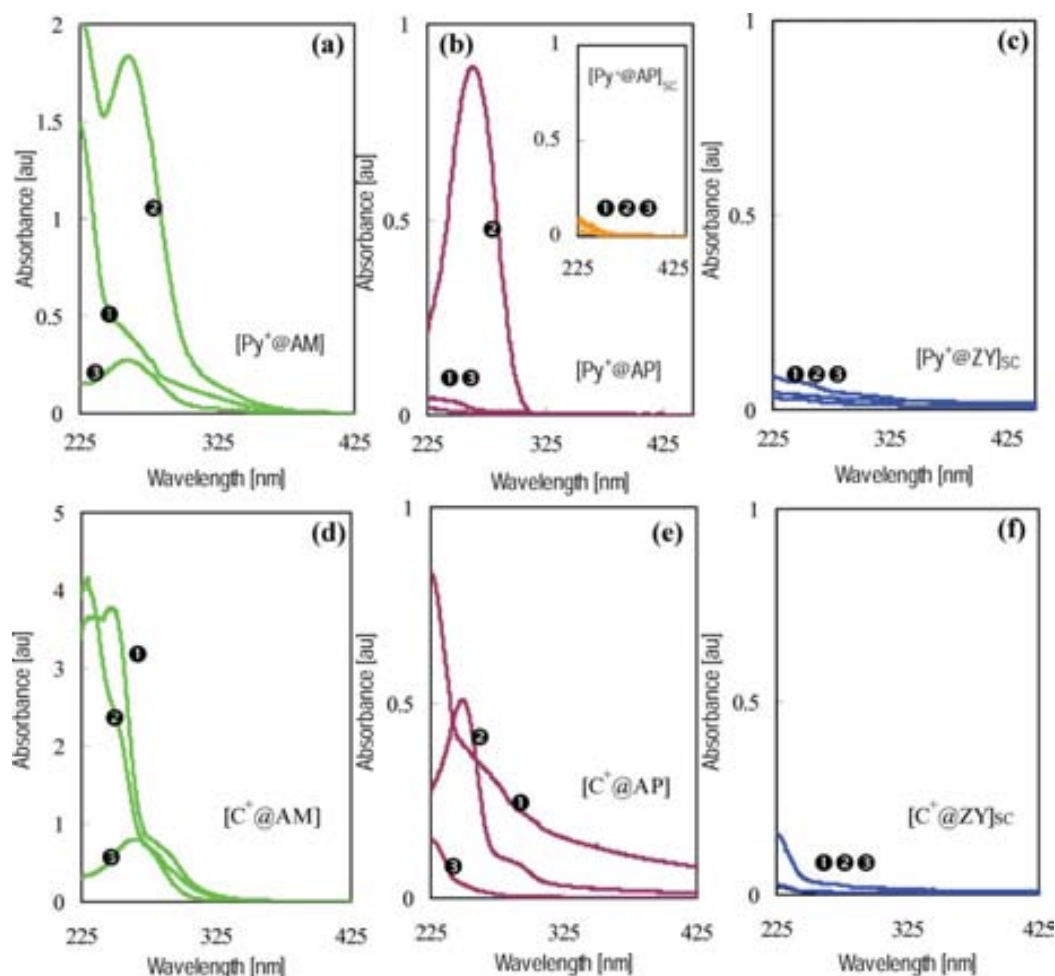
Fig. 7 The leaching behaviour in water of the different prepared samples measured using UV-vis spectroscopy: (a), (b) and (c) matrices impregnated with pyrylium cation; and (d), (e) and (f) matrices impregnated with trityl cation. The numeric notation indicates the timing of aliquot absorption measurements: ❶ after 1 d, ❷ after 5 d and ❸ after 12 d with refreshed mother liquid.

in Fig. 7a, b and 7d, e, respectively) showed an appreciable absorption between 225 and 325 nm. However, they did not show the presence of any significant amount of organic compounds in the refreshed water added afterwards and measured on day 12. On the other hand, the supercritically-washed samples $[Py^+@AP]_{SC}$, $[Py^+@ZY]_{SC}$ and $[C^+@ZY]_{SC}$ (Fig. 7b, c and f) did not suffer any significant leaching during the studied time period, indicating that the washing procedure was effective at eliminating the residual reagents and unbonded chromophore molecules and that the remaining impregnated material was stable and strongly interacting with the matrix.

In Fig. 8a, b the leaching behaviour in water of the three studied matrices charged with either pyrylium or trityl cation is compared. Some leaching was only observed for samples that were not previously washed with $scCO_2$. Even in these cases, the desorption of material only occurred in the first stage, suggesting that the leaching originated from impregnated organics located on the most external part of the matrices where the cation was less stabilized than in the most internal nanopores. It has been previously reported that simple deposition of these cations on the external surface of silica does not prevent hydrolysis.[61] In our case, cation leaching behaviour was probably diffusion

controlled through the nanopores, since the UV-vis absorption at day 1 was much lower than at day 5. For all the studied matrices, the impregnated cations showed a higher hydrolysis stability when encapsulated than in their crystalline form.

Conclusions

The combination of a nanoporous host and a photoactive guest renders solid photocatalysts in which the high surface area and adsorbent capacity provided by the nanopores are expected to increase the efficiency of light activated processes. Positive effects derived from the encapsulation of the guest molecules inside the nanoporous matrices are the photostability of the sensitizer and a favorable polar environment for photoinduced electron transfer. Cations supported in the mesoporous aerogel underwent some initial hydrolysis, while those encapsulated into the microporous zeolite were totally stable. However, the cations supported in the transparent mesopore aerogel exhibited a high intrinsic photocatalytic activity due to the absence of both solvent and light diffusion restrictions. On the other hand, the accessibility of organics to be oxidized to the encapsulated photocatalyst may be difficult in microporous zeolite matrices.
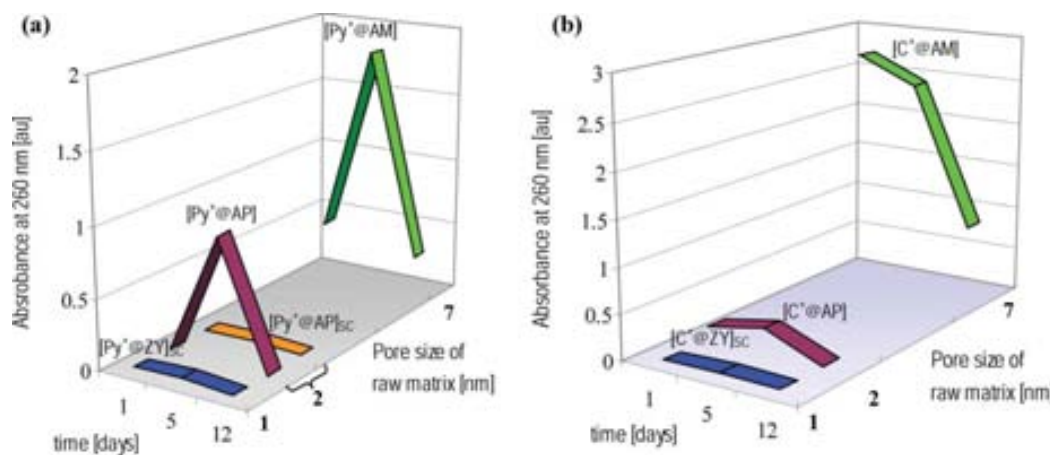
Fig. 8 Leaching behaviour of samples involving: (a) pyrylium and (b) trityl cations. Axis Y indicates the average pore diameter of the raw matrices estimated by BET (4 × pore volume/surface area), corresponding to ~1.2 for zeolites, ~1.8 for aerogel particles and ~7 for aerogel monoliths.

$scCO_2$ fluid technology can be used for upscaling the production of complex high purity nanoproducts at a reasonable cost and with positive green chemistry implications. In particular, the synthesis and impregnation of organic cations in nanoporous solids in $scCO_2$ as the reaction medium was designed as a time and load efficient route to a variety of nanoporous matrices, yielding nanocomposite hybrid materials with excellent stability.

Acknowledgements

References

1 R. Roque-Malherbe, in *Adsorption and diffusion in nanoporous materials*, Taylor & Francis Group, New York, 2007, ch. 7, pp. 195–198 and ch. 8, pp. 227–234.

2 J. Caro, M. Noack, in *Advances in Nanoporous Materials*, ed. S. Ernst, Elsevier, Amsterdam, 1st edn, 2009, vol. 1, ch. 1, pp. 49–62.

3 R. P. Townsend, R. Harjula, in *Molecular Sieves-Science and Technology*, ed. H. G. Karge and J. Weitkamp, Springer, Berlin, 2002, vol. 3, ch. 3, pp. 29–38.

4 L. W. Hrubesh, *J. Non-Cryst. Solids*, 1998, **225**, 335.

5 M. Stolarski, J. Walendziewski, M. Steininger and B. Pniak, *Appl. Catal., A*, 1999, **177**, 139.

6 L. Moscou, E. M. Flanigen, in *Introduction to Zeolite Science and Practice*, H. Van Bekkum, E. M. Flanigen and J. C. Jansen, Elsevier, Amsterdam, 1991, vol. 58, ch. 1, pp. 1–12 and ch. 2, 13–33.

7 A. Corma and H. García, *Eur. J. Inorg. Chem.*, 2004, 1143.

8 G. Shulz-Ekloff, D. Wöhrle, B. Van Duffel and R. A. Schoonheydt, *Microporous Mesoporous Mater.*, 2002, **51**, 91.

9 O. García, R. Sastre, D. Del Agua, A. Costela, I. García-Moreno and A. Roig, *Chem. Phys. Lett.*, 2006, **427**, 375.

10 D. L. Plata, Y. J. Briones, R. L. Wolfe, M. K. Carroll, S. D. Bakrania, S. G. Mandel and A. M. Anderson, *J. Non-Cryst. Solids*, 2004, **350**, 326.

11 A. Corma, H. Garcia, G. Sastre and P. M. Viruela, *J. Phys. Chem. B*, 1997, **101**, 4575.

12 P. K. Dutta and Y. Kim, *Curr. Opin. Solid State Mater. Sci.*, 2003, **7**, 483.

13 A. Corma and H. Garcia, *Chem. Commun.*, 2004, 1443.

14 A. Corma, V. Fornés, H. García, M. A. Miranda and M. Sabater, *J. Am. Chem. Soc.*, 1994, **116**, 9767.

15 A. M. López-Periago, J. Fraile, C. A. García-González and C. Domingo, *J. Supercrit. Fluids*, 2009, **50**, 305.

16 A. M. López-Periago, C. A. García-González, J. Saurina and C. Domingo, *Microporous Mesoporous Mater.*, 2010, **132**, 357.

17 A. Sanjuán, G. Aguirre, M. Alvaro and H. García, *Appl. Catal., B*, 1998, **15**, 247.

18 M. A. Miranda and H. Garcia, *Chem. Rev.*, 1994, **94**, 1063.

19 A. Williams, *J. Am. Chem. Soc.*, 1971, **93**, 2733.

20 V. D. Toncheva and R. S. Velichkova, *Makromol. Chem.*, 1983, **184**, 2231.

21 C. Elvira, A. Fanovich, M. Fernandez, J. Fraile, J. San Roman and C. Domingo, *J. Controlled Release*, 2004, **99**, 231.

22 A. I. Cooper, S. G. Kazarian and M. Poliakoff, *Chem. Phys. Lett.*, 1993, **206**, 175.

23 I. Kikic and F. Vecchione, *Curr. Opin. Solid State Mater. Sci.*, 2003, **7**, 399.

24 A. R. C. Duarte, A. L. Simplicio, A. Vega-Gonzalez, P. Subra-Paternault, P. Coimbra, M. H. Gil, H. C. De Sousa and C. M. M. Duarte, *Curr. Drug Delivery*, 2008, **5**, 102.

25 A. López-Periago, A. Argemí, J. M. Andanson, V. Fernández, C. A. García-González, S. G. Kazarian, J. Saurina and C. Domingo, *J. Supercrit. Fluids*, 2009, **48**, 56.

26 C. Domingo, J. García-Carmona, J. Llibre and R. Rodríguez-Clemente, *Adv. Mater.*, 1998, **10**, 672.

27 J. García-Carmona, M. A. Fanovich, J. Llibre, R. Rodriguez-Clemente and C. Domingo, *Microporous Mesoporous Mater.*, 2002, **54**, 127.

28 Y. Shin, T. S. Zemanian, G. F. Fryxell, L.-Q. Wang and J. Liu, *Microporous Mesoporous Mater.*, 2000, **37**, 49.

29 C. García-González, J. Saurina, J. A. Ayllón and C. Domingo, *J. Phys. Chem. C*, 2009, **113**, 13780.

30 C. García-González, J. Fraile, A. M. López-Periago and C. Domingo, *J. Colloid Interface Sci.*, 2009, **338**, 491.

31 C. Domingo, E. Loste and J. Fraile, *J. Supercrit. Fluids*, 2006, **37**, 72.

32 E. Loste, A. Fanovich, J. Fraile and C. Domingo, *Adv. Mater.*, 2004, **16**, 739.

33 J. A. Darr and M. Poliakoff, *Chem. Rev.*, 1999, **99**, 495.

34 T. S. Zemanian, G. E. Fryxell, J. Liu, S. V. Mattigod, Y. Shin, J. A. Franz, O. Ustyugov, Z. Nie, *Proceedings of the 1st IEEE Conference on Nanotechnology*, Maui, 2001.

35 C. A. Eckert, B. L. Knutson and P. G. Debendetti, *Nature*, 1996, **383**, 313.

36 R. Amandi, J. R. Hyde, T. Lotz, S. K. Ross and M. Poliakoff, *Green Chem.*, 2005, **7**, 288.

37 T. Moreno, J. García-Serna and M. J. Cocero, *Green Chem.*, 2010, **12**, 282.

38 N. Baccile, F. Babonneau, B. Thomas and T. Corading, *J. Mater. Chem.*, 2009, **19**, 8537.
39 A. M. Amat, A. Arques, S. H. Bossmann, A. M. Braun, S. Gob and M. A. Miranda, *Angew. Chem., Int. Ed.*, 2003, **42**, 1653.
40 A. Corma, V. Fornés, H. García, M. A. Miranda, J. Primo and M. J. Sabater, *J. Am. Chem. Soc.*, 1994, **116**, 2276.
41 M. L. Cano, A. Corma, V. Fornés, H. García, M. A. Miranda, C. Baerlocher and C. Lengauer, *J. Am. Chem. Soc.*, 1996, **118**, 11006.
42 M. Moner-Girona, A. Roig, E. Molins and J. Llibre, *J. Sol-Gel Sci. Technol.*, 2003, **26**, 645.
43 A. Roig, I. Mata, E. Molins, C. Miravitlles, J. Torras and J. Llibre, *J. Eur. Ceram. Soc.*, 1998, **18**, 1141.
44 V. G. Kharchenko and N. V. Pchelintseva, *Chem. Heterocycl. Compd.*, 1996, **32**, 1113.
45 R. M. Saunders, H. P. Schwarz and J. C. Stewart, *Anal. Chem.*, 1967, **39**, 550.
46 M. S. Shchepinov and V. A. Korshun, *Chem. Soc. Rev.*, 2003, **32**, 170.
47 M. Schmidt and F. Schwertfeger, *J. Non-Cryst. Solids*, 1998, **225**, 364.
48 I. Smirnova, J. Mamic and W. Arlt, *Langmuir*, 2003, **19**, 8521.
49 I. Smirnova, S. Suttiruengwong and W. Arlt, *J. Non-Cryst. Solids*, 2004, **350**, 54.
50 L. Martín, J. O. Ossó, S. Ricart, A. Roig, O. García and R. Sastre, *J. Mater. Chem.*, 2008, **18**, 207.
51 E. Taboada, R. Solanas, E. Rodríguez, R. Weissleder and A. Roig, *Adv. Funct. Mater.*, 2009, **19**, 2319.
52 J. A. Lercher, A. Jentys, in *Handbook of Porous Solids*, ed. F. Schüth, K. Sing and J. Weitkamp, Wiley-VCH, Weinheim, 2002, vol. 2, ch. 4, pp. 1097.
53 *Infrared Spectra of Adsorbed Molecules*, ed. L. H. Little, Willmer Brothers, Ltd. New York, 1996.
54 O. K. Eide, M. Ystenes, J. A. Stovneng and J. L. Eilertsen, *Vib. Spectrosc.*, 2007, **43**, 210.
55 Y. Chen and S.-K. Wu, *J. Photochem. Photobiol., A*, 1997, **102**, 203.
56 P. Atienzar, A. Corma, H. García and J. M. Serra, *Chem.–Eur. J.*, 2004, **10**, 6043.
57 M. Cano, F. L. Coznes, H. García, V. Martí and J. C. Scaiano, *J. Phys. Chem.*, 1996, **100**, 18152.
58 S. Adolph, S. Spange and Y. Zimmermann, *J. Phys. Chem. B*, 2000, **104**, 6429.
59 M. Fakis, G. Tsigaridas, I. Polyzos, V. Giannetas, P. Persephonis, I. Spiliopoulos and J. Mikroyannidis, *Chem. Phys. Lett.*, 2001, **342**, 155.
60 D. F. Duxbury, *Chem. Rev.*, 1993, **93**, 381.
61 M. A. Miranda, A. M. Amat and A. Arques, *Catal. Today*, 2002, **76**, 113.

This journal is © The Royal Society of Chemistry 2010

Nanostructured silica-based drug delivery vehicles for hydrophobic and moisture sensitive drugs

Nerea Murillo-Cremaes [a], Ana M. López-Periago [a], Javier Saurina [b], Anna Roig [a,*], Concepción Domingo [a,*]

[a] *Instituto de Ciencia de Materiales de Barcelona (ICMAB-CSIC), Campus UAB, 08193 Bellaterra, Spain*
[b] *Department of Analytical Chemistry. University of Barcelona, Martí i Franquès 1-11, Barcelona E-08028, Spain*

ARTICLE INFO

ABSTRACT

Facile and robust fabrication methodologies of complex materials with high added value for controlled drug delivery systems are highly sought-after in the pharmaceutical industry. Here, we have relied on the use of supercritical fluids for the matrix synthesis as well as for the drug impregnation process. As a model system of a hydrophobic and moisture sensitive active agent, triflusal was impregnated in different aerogel and polymeric matrices using supercritical CO_2. *In vitro* release profiles of drug carriers consisting of SiO_2 aerogels as mesoporous monoliths and as microporous nanospheres loaded with triflusal are reported and compared to a more conventional polymeric system (PMMA). Silica-based matrices are found to prevent the hydrolization of the active ingredient more efficiently than the polymeric matrix and displayed much faster release kinetics. Moreover, the triflusal is dispersed in a molecular form inside the silica-based materials. Such features are considered of great interest to enhance the bioavailability of low solubility drugs.

1. Introduction

In traditional pharmaceutical formulations, large doses are generally administered to the patients to reach therapeutic levels of the drug. In contrast, new formulation approaches based on drug delivery systems with an engineered biodistribution profile may be exploited to overcome problems related to side effects, insufficient drug concentration at targeted sites, rapid metabolization or drug degradation. The paradigm of using nanoparticulate carriers to enhance the *in vivo* efficiency of active agents has been well established over the past decade [1–3]. Their use aims to facilitate prolonged circulation after being administered, to increase bioavailability and, at the same time, to enhance the percentage of unaltered active agent reaching the pathological area. Some of those carriers have already made their way into the clinical arena (*i.e.*, polymeric particles), while others are still under preclinical development (*i.e.*, liposomes) or at initial clinical research stages (dendrimers and quantum dots).

Current technology for controlled drug delivery is mainly based on the use of micron or submicron matrices of polymers, in which the drug is either encapsulated or dispersed, either adsorbed or chemically bonded on the internal surface [4]. Nanoporous inorganic materials, such as silica (SiO_2) with

several levels of sophistication in their architecture and/or composition have also been proposed as drug delivery devices [5–8]. Moreover, mesoporous silica magnetic nanocomposites are being studied for simultaneous application in diagnosis (magnetic resonance imaging) and therapy (hyperthermia and externally guided drug-delivery vehicles) [9,10]. Unlike polymer-based systems, silica-based particles are highly stable under various thermal and chemical conditions. In addition, problems related to aggregation of lipophilic polymeric nanoparticles upon its intravenous administration causing embolism or local toxicity could be overcome by using hydrophilic inorganic systems [11]. Many of the marketed polymeric drug delivery carriers are adequate for the sustained release of water-soluble drugs. On the other hand, inorganic porous silica particles are mostly applied to obtain an immediate optimal drug dosage of poorly water-soluble compounds at the desired target site [5,6]. Another technological challenge for SiO_2 drug delivery systems is to warrant the full preservation of the drug activity during its storage and administration period.

Here, we use triflusal (Trf), a drug practically insoluble in water as defined by the European Pharmacopoeia 5.0 and with an estimated log P (log octanol/water partition coefficient) of 2.09 [12], as the model active agent to be encapsulated. Triflusal is an antiplatelet agent that irreversibly acetylates cyclooxygenase isoform 1 and, therefore, inhibits thromboxane biosynthesis [13]. The main metabolite of Trf, the 2-hydroxy-4-trifluoromethyl benzoic acid (HTB), also possesses some anti-aggregation activity. Trf has a structural analogy to aspirin, with a trifluoromethyl group in the

* Corresponding authors. Tel.: +34 935801853.
  E-mail addresses: roig@icmab.es (A. Roig), conchi@icmab.es (C. Domingo).

C_4 position of the aromatic ring. Although both drugs are widely used, Trf has less risk of producing hemorrhagic complications due to their acidic nature. At the same time, care must be taken to ensure that the drug does not extensively hydrolyze before it can be absorbed. Therefore, the pharmaceutical industry is promoting the development of alternative forms of Trf administration but the main problems associated to that are its low solubility and its high instability at alkaline pH. The use of micelles in the pharmaceutical formulae has been the most investigated approach to enhance Trf water dissolution and to protect the active agent from degradation by alkaline hydrolysis [14]. Moreover, the use of a polymeric delivery system based on a copolymer of an acrylic derivative of triflusal has been commercialized [15].

In a previous work, we reported on the preparation of a homopolymeric delivery system in which Trf was impregnated [16]. Although the system exhibited a good response, it released the drug very slowly due to its high hydrophobicity. In this work, three aerogel silica-based materials are introduced as potential drug delivery carriers for triflusal and their behavior is compared with the previously reported polymer system. The purpose of using inorganic matrices is to improve both the drug dissolution profile and to increase the preservation of the therapeutic agent. The use of silica aerogels as potential carrier materials in medicine has been reported previously [17–20]. In this work, several grades of porous silica aerogels with different properties, such as composition, particle size, pore diameter and structure and degree of hydrophilicity are studied [21–23]: (i) mesoporous silica aerogel monoliths, (ii) microporous silica nanospheres, and (iii) magnetite/silica ($Fe_3O_4@SiO_2$) nanospheres. These biocompatible materials were prepared in our laboratories following a previously reported synthetic route that combines sol–gel chemistry and supercritical fluids [21,22,24].

In the last years, the unique properties of $scCO_2$, which are intermediate between those of the liquid (high density) and those of the gas (low viscosity and null surface tension), have been advantageously exploited in innovative processes designing drug delivery systems of poorly water-soluble drug substances, since a high solubility of hydrophobic compounds in $scCO_2$ is usually found [25,26]. Specifically, the benefit of using $scCO_2$ as the impregnation medium to fabricate host–guest systems has been previously demonstrated on polymeric [27–29] and inorganic matrices [30–34]. For the matrices described in this work, two processing characteristics of the supercritical fluid technology are significantly more efficient than when applying other more conventional solvents. First, the null surface tension of a supercritical fluid allows the drying of silica gels while preserving their porosity to form silica aerogels and aerogel-like nanoparticles. Second, due to the low viscosity and high diffusivity, $scCO_2$ solutions have the ability to penetrate and efficiently impregnate porous matrices without damaging the porous structure. Notice that simple solvent impregnation procedure is not feasible for aerogel materials. The avoidance or little use of organic solvents, the intrinsic sterility of $scCO_2$ and the fact that the final product is in a dry form and is produced in confined autoclaves are also of particular interest for pharmaceutical products manufacturing [35,36].

The objective of this study is to use a generic $scCO_2$ method for the impregnation of both polymeric and inorganic matrices with Trf and to compare the release profiles. First, polymethylmethacrylate (PMMA) was studied. These polymeric substrates interact with $scCO_2$, since the adsorption of $scCO_2$ into the PMMA leads to polymer swelling and the creation of the necessary voids for drug impregnation. Second, inorganic SiO_2 aerogels and aerogel inspired particles were analyzed. These inorganic substrates do not interact with $scCO_2$, but already possess intrinsic porosity. The quantification of the amount of drug entrapped and the characterization of the release profiles were carried out by high performance liquid chromatography (HPLC). Solid state characterization was used to demonstrate that the release behavior of the drug is largely dependent on the composition and structure of the matrix. The amount of Trf and HTB inside the different matrices was correlated to the effectiveness of the matrices to act as a hydrolysis preventing barrier. Other factors, such as the physical state of the drug inside of the matrix, the homogeneity of the drug dispersion and the chemical interactions of the drug with the matrix are also discussed in the light of the release profile.

2. Materials and methods

2.1. Materials

2-Acetyloxy-4-(trifluoromethyl) benzoic acid (triflusal, Trf) was used as a model drug to be impregnated. The metabolite of Trf (4-(trifluoromethyl) salicylic acid, HTB) was also analyzed to follow the evolution of the drug degradation with time. Both, Trf and HTB, were kindly donated by Uriach S.A., Spain. CO_2 (99.995 wt%, Carburos Metálicos, Spain) was used as the impregnation solvent. The used PMMA polymer (350.000 g mol^{-1}, Bonar Polymers, UK) was in the form of beads. Silica-based porous matrices were synthesized in our laboratory by the hydrolysis and polycondensation of tetramethylorthosilicate (TMOS, 98%, Sigma–Aldrich) and high temperature supercritical drying, according to the following procedures:

Silica aerogel monoliths (samples AM) were obtained from a mixture of methanol (absolute grade, Panreac):TMOS:water (12.25:1:4 molar ratio) in the presence of a small amount of ammonium hydroxide (32%, Aldrich) used as a catalyst. The solution was poured in separate pyrex tubes and let to gellify for three minutes. The gels were subjected to supercritical drying using a 2 L automated high pressure reactor (Autoclave Engineers). To exceed the critical point of the mixtures CO_2/methanol, the temperature was increased stepwise to 220 °C, reaching a final pressure of 250 bar. After 2 h at these conditions, the reactor was depressurized and before getting to ambient pressure was washed up for 30 min with a flow of fresh CO_2 (having a flow rate of 3 kg/h). The autoclave was then depressurized completely and let it to cool down overnight. The material collected was in the shape of transparent cylinders of about 0.8 cm × 2.4 cm and a density of 0.1 g cm^{-3}.

Silica aerogel nanoparticles (samples AP) were precipitated from a mixture of acetone (Panreac):TMOS:H_2O (88.34:1:2 molar ratio) and without the use of a catalyst. A sol with the reactants was placed in a 1 L Pyrex beaker and introduced into the high pressure autoclave. The pressure inside the reactor was increased to *ca.* 50 bar by adding CO_2. Next, the temperature was increased stepwise to 250 °C, with the corresponding pressure rise to 280 bar. After 2 h at these conditions, fresh CO_2 was forced to circulate through the reactor for 2 h at different flow rates ensuring the displacement of the whole volume of CO_2 with the purpose to extract any alkoxide precursor residue. System was then depressurized and the solid material was washed up for 30 min with a flow of fresh CO_2 at 3 bar (with a flow rate of 3 kg/h). Finally, it was let to cool down overnight. The dry solid collected was powdered, light and white and it was homogenously dispersed at the reactor walls.

Fe_3O_4 composite silica aerogel nanoparticles (samples AP$_{Fe}$). Typically, reagents with a mass composition TMOS:H_2O:acetone:Fe_3O_4 (previously synthesized in our laboratory):hexane (0.92:0.22:95.6:0.04:3.19% weight ratio) were mixed in a 1 L Pyrex vessel at ambient conditions and the same procedure as described before for silica aerogel nanoparticles was followed. The resulting material consisted of a dry, light and brown powder

homogeneously distributed around the reactor walls with super-paramagnetic properties at room temperature.

2.2. scCO₂ impregnation procedure

Impregnation process in scCO₂ was performed in a high pressure equipment described elsewhere [16]. Experiments were carried out in batch mode. The autoclave (100 mL) was charged with drug and matrix in a weight ratio of *ca.* 1:2. Aerogel particulate and monolithic matrices were first dehydrated by heating in a tubular oven (Carbolite 3216) at 300 °C for 2 h under a flow of nitrogen. The aerogel monolith was also micronized in pieces between 2 and 5 mm. Each matrix separately was then wrapped in a cylinder made of 0.45 μm pore filter paper, and added to the reactor maintaining a physical separation from the drug of 2–3 cm. The reactor was then filled with pressurized CO₂ up to 200 bar and heated to 45 °C. In all the experiments performed, the amount of commercial Trf was added in excess ensuring saturation of the scCO₂ phase. In a typical run, the charged autoclave was magnetically stirred at 300 rpm during 6 h for the aerogel matrices and 24 h for PMMA. Experiments performed at longer running times did not lead to higher uptakes, indicating that likely maximum loading was reached under chosen working conditions. PMMA polymer needed longer reaction time to induce the swelling previous to impregnation. For aerogel samples, pressurization and depressurization were carried out slowly and stepwise to avoid the formation of liquid CO₂ in the autoclave, which could damage the fragile porous structure of the aerogels. This impregnation methodology is reproducible and it has been demonstrated by repeating the experiments at least three times and obtaining similar results. The resulting materials from the impregnation of the AP, AP$_{Fe}$, AM and PMMA matrices are labeled as Trf@AP, Trf@AP$_{Fe}$, Trf@AM and Trf@PMMA, respectively.

2.3. Characterization

Morphological characterization was based on transmission (JEOL JEM-1210, TEM) and scanning (Hitachi S570, SEM) electron microscopies for SiO₂ and PMMA matrices, respectively. Textural characteristics of bare and impregnated matrices were studied by low-temperature N₂ adsorption–desorption analysis (ASAP 2000 Micromeritics Inc. instrument). Prior to measurements, samples were dried under reduced pressure (<1 mPa) at 150 °C (AM) or 300 °C (AP and AP$_{Fe}$) for 24 h. Specific surface area (S_a) was determined by the BET method. Regarding the pore volume (P_v), the mesopore volume was determined from the adsorption isotherm using the BJH method, while the micropore volume was estimated by the t-method. The average pore diameter (D_p) was calculated from the S_a and P_v by considering cylindrical pores. Thermal transitions were studied by differential scanning calorimeter (822e/400 Mettler Toledo, DSC) under N₂ atmosphere with a 10 °C min⁻¹ heating rate. The possible drug–matrix interactions were evaluated by Fourier transform infrared (FTIR) spectroscopy using a Perkin-Elmer Spectrum One equipment Materials. Crystallinity was analyzed by X-ray powder diffraction (Rigaku Rotaflex RU-200 B, XRD).

HPLC was used to determine the overall amount of drug contained in the samples, as well as to follow the kinetics of the release. The percentages of drug impregnated in the polymeric and silica-based matrices were determined as follows. Accurately weighed sample amounts of 3–5 mg were treated with 50 mL of either acetone (for PMMA) or water (for aerogels) to completely extract and dissolve the drug contained in the matrices. The solvent was evaporated under a nitrogen flow and the dry residue was redissolved in 20 mL of mobile phase. 20 μL of the resulting solution were injected into the chromatograph to quantify total loading. Since both Trf and HTB resulted in separated peaks, the HPLC method

was also used to evaluate the progress of Trf degradation. The drug delivery profiles were evaluated *via* leaching in 10 mM HCl (pH 2) and 10 mM Na₂HPO₄/NaH₂PO₄·2H₂O (pH 7.4) aqueous solutions to simulate gastric and plasmatic conditions, respectively. In these experiments, a given amount of sample (∼5 mg) was placed in a vessel containing solvent volumes of 12.5 ml (AP sample), 25 ml (AP$_{Fe}$ sample) and 100 ml (AM and PMMA samples). Stirring rate and temperature were fixed at 60 rpm and 37 °C, respectively. The kinetic curves were monitored chromatographically to obtain the corresponding delivery profiles.

3. Results and discussion

Table 1 shows electron microscopy images and textural characteristics of the studied matrices. For non-porous PMMA, impregnation must be preceded by polymer swelling. On the other hand, inorganic SiO₂ matrices have an inherent pore volume ready to be loaded. The aerogel monolith has a surface area, S_a, of *ca.* 476 m² g⁻¹ and an internal porosity of *ca.* 0.75 cm³ g⁻¹ that it is constituted by a network of interconnected pores of a diameter typically in the range of 5–50 nm. Moreover, microporous nanospheres (AP and AP$_{Fe}$) were also analyzed. Those materials have a mean pore size of *ca.* 2 nm comparable to that of the size of the studied drug, with a total pore volume of 0.10–0.15 cm³ g⁻¹ and S_a values of 150–200 m² g⁻¹.

Trf has a chemical structure similar to that of acetyl salicylic acid, the active agent of aspirin (Scheme 1). As acetyl salicylic acid, Trf undergoes a progressive hydrolization in the water being HTB the resulting metabolite. Trf molecules most likely stabilize forming dimmers in both the crystalline and solution states, as determined by comparison with other structurally similar carboxylic acid compounds [37–41]. On the other hand, the metabolite HTB prefers to form intramolecular H-bonds (Scheme 1). Differently to acetyl salicylic acid, the presence of an additional hydrophobic trifluoromethyl group in the Trf molecule renders a pronounced effect in the interaction of Trf with scCO₂ and thus on its solubility. The Trf solubility in scCO₂ at the working temperature and pressure was found to be in the order of 3×10^{-2} mole fraction, which is a value relatively high for a scCO₂/solute system [16].

3.1. Estimation of drug loading and formulation stability

The percentage of drug loaded in each sample was determined by HPLC [41]. In all cases, three independent replicates were carried out and the following mean values were obtained: 16 ± 1, 17 ± 2, 3.3 ± 0.2 and 4.1 ± 0.2 wt% for samples Trf@PMMA, Trf@AM, Trf@AP and Trf@AP$_{Fe}$, respectively. To calculate the amount of impregnated drug both the Trf and the HTB contributions were considered. For the silica matrices, drug load could be correlated with the mesopore volume available (see Table 1). AM matrix had the highest value of mesopore volume, and, thus, the highest impregnation capacity. AP and AP$_{Fe}$ matrices had similar values of total pore volume, but the AP$_{Fe}$ matrix had a greater value of mesopore void (*ca.* 0.10 cm³ g⁻¹) than AP matrix (*ca.* 0.05 cm³ g⁻¹) and, thus, drug impregnation was slightly higher for AP$_{Fe}$ than for AP nanoparticles. Since in this study we were interested in drug stability, the amount of Trf and HTB was evaluated separately by chromatographically monitoring the decomposition of Trf in water, hydrochloric acid solution (pH = 2.0) and hydrogen phosphate basic solution (pH = 7.4) in initial blank assays. As shown in Fig. 1a, the Trf hydrolysis was faster in water and basic media than in acid medium. In water and at pH = 7.4, the degradation of Trf to HTB was completed in 10 days, while for acid solutions the process lasted for 1 month. The transformation into HTB of impregnated Trf for the different matrices was studied after 6 months of samples preparation. Samples were stored

Table 1
Characteristics of the matrices and drug load impregnation values.

Matrix		AM	AP	AP_{Fe}	PMMA
Microscopy image					
Schematic representation					
Particle size [nm]		---	300	65	500-1000
Polydispersity [%]		---	9	19	20
s_s [m^{2}g^{-1}]		475	200	160	0.07
P_v [cm^{3}g^{-1}]	Mesopore (BJH)	0.76	0.05	0.10	---
	Micropore (t-method)	---	0.07	0.04	---
d_p [nm]		7.4	1.7	1.5	---
Impregnation Loads	Loading [wt%]	17	3.3	4.1	16
	Filled volume [cm^{3}g^{-1}]	0.30	0.03	0.05	---
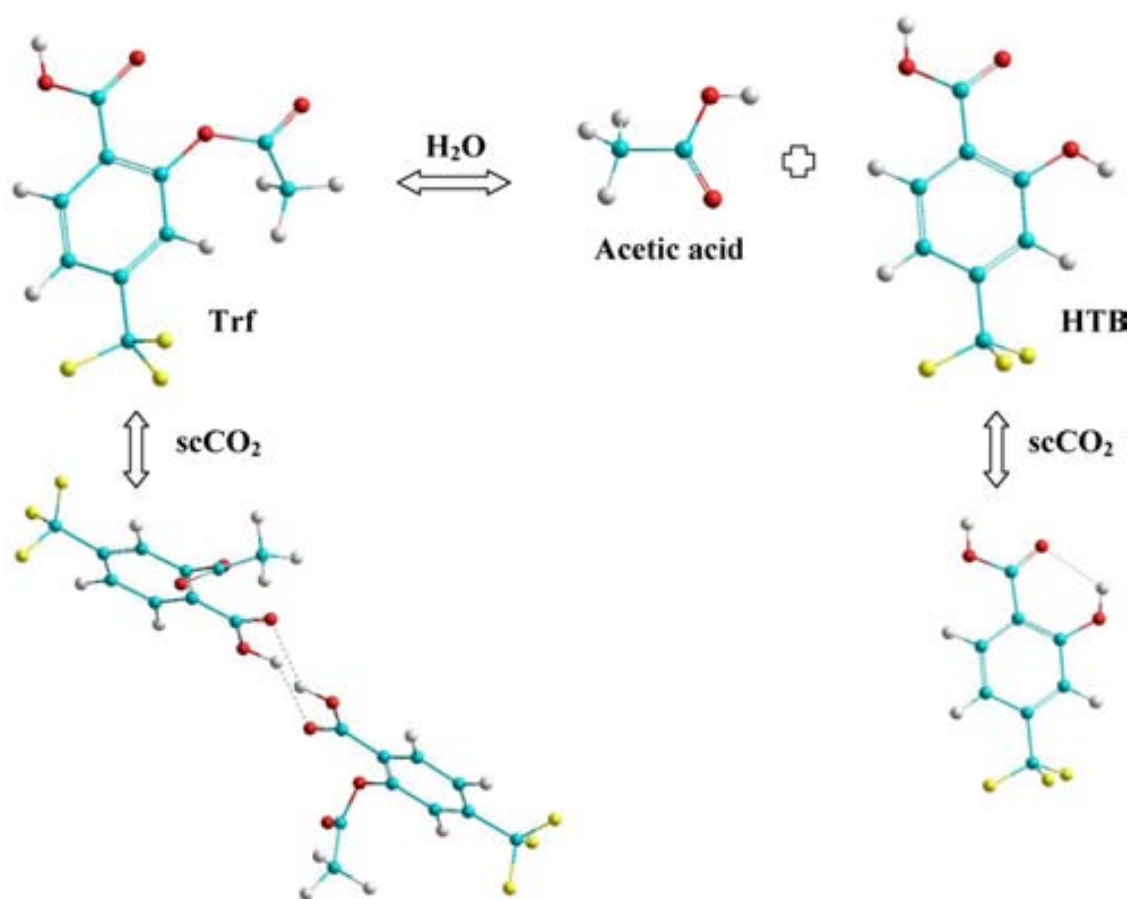
Scheme 1. 3D-conformations of the Trf and the HTB metabolite (HyperChem 8.03). The equilibrium conformations *via* H-bonds of the molecules dissolved in scCO$_2$ are also shown.
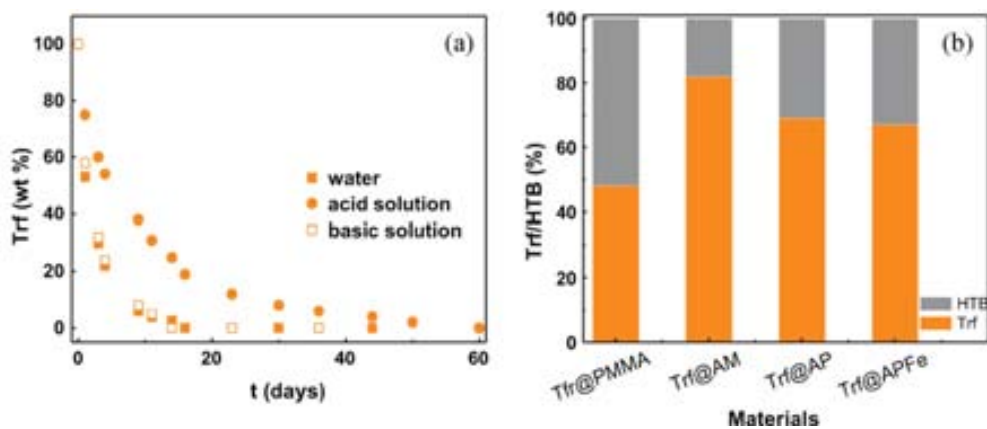
Fig. 1. Hydrolization of triflusal: (a) time evolution of Trf crystals dissolved in aqueous solutions (pH = 7), 10 mM HCL (pH = 2) and 10 mM Na$_2$HPO$_4$/NaH$_2$PO$_4$·2H$_2$O (pH 7.4), and (b) percentage of the two species inside the studied matrices after 6 months of storage (21 °C and 60–65% relative humidity).

under ambient conditions (*i.e.*, 21 °C and 60–65% relative humidity). The percentages of Trf and HTB were calculated from the corresponding chromatographic peaks at the initial stages of the release. Those values were considered to mirror the degree of hydrolysis of the encapsulated drug, and were related to the percentage of drug degradation during preparation and storage. As shown in Fig. 1b, the hydrolysis degree ranged from *ca.* 18 wt% in Trf@AM to more than 50 wt% in Trf@PMMA. Intermediate values of *ca.* 30 wt% were found for Trf@AP and Trf@AP$_{Fe}$. It is noteworthy that the highest value of HTB among the prepared drug delivery system was found for the most hydrophobic matrix, the PMMA, being the Trf better preserved inside the hydrophilic aerogel matrices. This behavior was attributed to the acidity provided to the adsorbed water by the SiO$_2$ matrix, which in turn stabilized the Trf molecules against hydrolysis. Hence, for those drugs susceptible of hydrolysis, the use of aerogel matrices as drug delivery carriers have the additional advantage of contributing more efficiently to drug preservation than when using hydrophobic polymeric microparticles. Comparing Trf stability in the three silica matrices, it was found that the mesoporous aerogel monolith was more effective than the microporous nanoparticles. We argue that this finding could be related to two different geometrical conformations adopted by the Trf molecule inside of the pores as explained below in the structural analysis.

3.2. Structural analysis

XRD was used to assess the occurrence or the absence of crystalline arrangement for the impregnated drug. Spectra were recorded in the 2θ range of 10–40° (Fig. 2). Trf could be readily identified in this range by its two most intense peaks at 2θ = 19.38 and 25.92°, while HTB displayed two intense peaks at 2θ = 16.64

and 24.48° (Fig. 2a). PMMA presented a broad amorphous band at 2θ = 10–30°, while for the aerogel matrices appeared the typical broad band of amorphous silica centered at 2θ = 22° (Fig. 2b). Concerning AP$_{Fe}$ matrix, the same silica band appeared together with the characteristics (2 2 0) and (3 1 1) peaks of magnetite at 2θ = 30 and 36°. Diffraction peaks of the Trf (or HTB) crystalline form did not appear in the XRD patterns of the prepared composite products, in which only the amorphous hill of the matrix was clearly observed (Fig. 2c), thus indicating that the drug did not crystallize during supercritical impregnation. Complementarily, DSC analysis was used to further confirm the desirable absence of drug crystals or amorphous forms (Fig. 3). Unsupported triflusal has a melting point of 118 °C. The glass transition of the PMMA appears at around 125 °C. Within the studied temperature interval (up to 450 °C), thermal transitions are inexistent for silica matrices. The melting peak of Trf was not observed in any of the four samples. As an example, Fig. 3a and b show the DSC curves of Trf@PMMA and Trf@AM samples loaded with the highest drug percentages (*ca.* 16–17 wt%). Thus, XRD and DSC results indicated that Trf was most likely dispersed inside the matrices at a molecular level. In fact, to generate crystalline particles inside of the pores a sudden change in solubility, created, for instance, by fast pressure release, would be necessary [42].

FTIR spectroscopy was used to monitor the presence of the drug and the chemical interactions with the host matrices (Fig. 4). Fig. 4a depicts the spectra of the raw materials. The spectrum of PMMA showed the C=O vibration at 1718 cm^{-1} as the most characteristic band. For all the studied silica matrices, intense absorption bands appeared in the 900–1200 cm^{-1} region, which corresponded to the stretching vibrations of the O—Si—O bond in the SiO$_4$ tetrahedrons of the aerogel skeleton. The band at 1620–1650 cm^{-1} was due to the bending frequency of molecular water adsorbed into
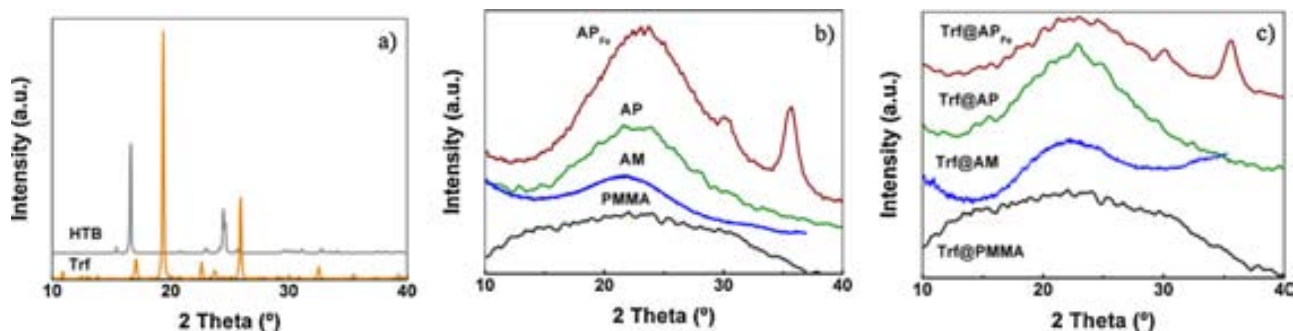

Fig. 2. X-ray diffractograms of (a) the therapeutic agent and its metabolite, (b) the pristine matrices and (c) the impregnated matrices.
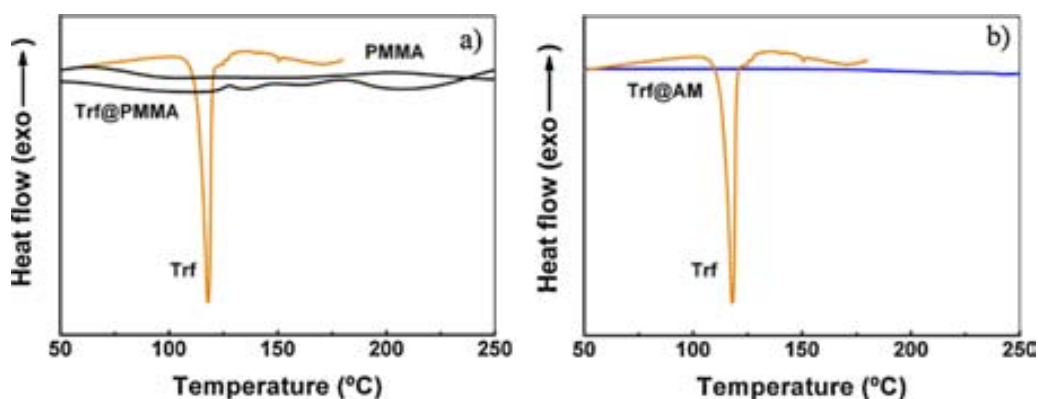
Fig. 3. Differential scanning calorimetry thermographs of Trf crystals and impregnated matrices: (a) PMMA and (b) AM.
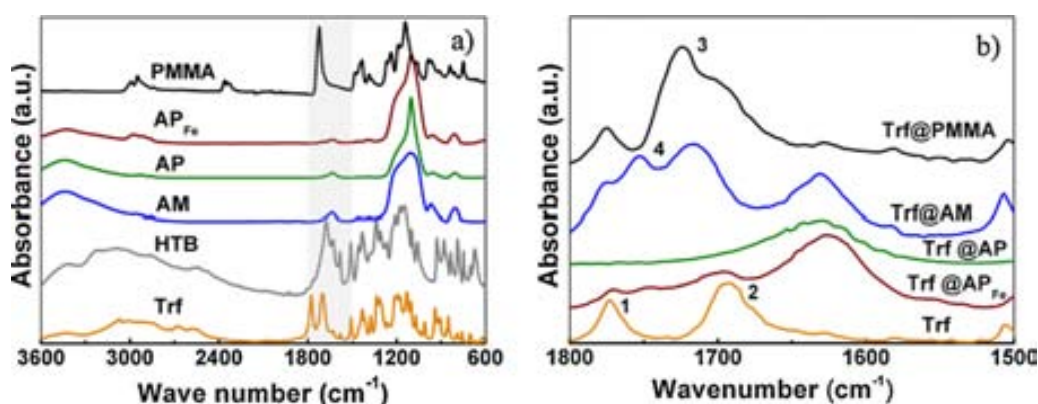

Fig. 4. Fourier transformed infrared spectroscopic analysis of: (a) the starting materials and (b) the impregnated matrices, in which the wave number range of 1800–1500 cm^{-1} has been selected for a more detailed analysis. In (b), the different C=O bands are identified as **1** (C=O of the ester in the Trf molecule), **2** (C=O of the carboxylic group in the Trf molecule), **3** (C=O of the ester group in the PMMA matrix) and **4** (C=O of the carboxylic group of the acetic acid).

the matrices. Moreover, the spectra of the aerogel matrices exhibited the characteristic bands of the asymmetric and symmetric modes of alkyl at 2955 and 2860 cm^{-1}, respectively, corresponding to residual reagents used to fabricate the aerogel. The useful FTIR region of solid Trf (1800–1500 cm^{-1}) contained a band at *ca.* 1510 cm^{-1} corresponding to the benzene ring, and two bands at 1770 (band **1**) and 1685 cm^{-1} (band **2**) corresponding to the carbonyls (C=O) (Scheme 1). In the triflusal crystals, the band at 1685 cm^{-1} is shifted to a lower wavenumber than regular carbonyl range, 1730–1740 cm^{-1}, due to both conjugation with C=C in the attached benzene ring and Trf–Trf dimmer formation with the consequent weakening of the C=O bond. The main characteristic peak of HTB is associated to the carbonyl group and appears at 1671 cm^{-1} (Fig. 4a). The presence of Trf in the impregnated matrices was monitored by the C=O band of the ester appearing at 1770 cm^{-1} (band **1** in Fig. 4b). This band was more evident in the Trf@PMMA and the Trf@AM samples than in the nanoparticulate systems, thus indicating the higher loads achieved in the first cases. In the impregnated Trf@AM sample, the 1770 cm^{-1} band appeared together with an additional carbonyl mode at 1752 cm^{-1} (band **4**) that was attributed to carboxylic acid species formed *via* cleavage of the ester and decomposition of Trf into HTB (Scheme 1). In the Trf@PMMA sample, the band **4** was imbibed by the C=O band of the ester in the polymer. In both samples, the C=O band **1** at 1770 cm^{-1} was not shifted between the crystalline and impregnated forms of Trf, indicating an equivalent structure. However, the C=O band **2** at 1685 cm^{-1} in the crystalline Trf was shifted to the high-wavenumber region of 1700–1720 cm^{-1} (band **3**) in PMMA and AM impregnated matrices. This behavior indicated breakage of the self-association in the Trf molecules and the formation of H-bonding

with the ester or OH groups existing in PMMA or SiO$_2$ matrices, respectively. Amorphous silica particles present a large number of silanol groups on their surfaces, which may be able to form hydrogen bonds with carboxylic groups of drug molecules. The extent of hydroxyl-coverage in aerogels is ~5 OHnm^2, a value consistent with other forms of silica. It has been suggested the formation of a six-membered hydrogen bonding intermediate formed by the reaction of OH in the SiO$_2$ with carboxylic acid containing compounds *via* adsorbed H$_2$O [37]. The intermediate can transform to a carboxylate (COO$^-$) ion by transference of the acidic H. However, carboxylate peaks at *ca.* 1580–1590 cm^{-1} did not appear in any of the impregnated materials, thus suggesting that the acid–base reaction between OH in SiO$_2$ and the carbonyl acid of the drug did not take place. However, neither the formation of H-bonds with the surface nor the carboxylate salt was observed by FTIR for the nanoparticulate aerogel-like systems. The FTIR bands in the Trf@AP matrix were not defined enough to be well analyzed due to low loading, but for sample Trf@AP$_{Fe}$, the shift on the C=O band **2** was not detectable, indicating that Trf molecules were likely placed in the pores in a similar conformation that in the solid crystal, *i.e.*, forming dimmers.

The differences in the molecular conformation of impregnated molecules for both types of aerogel matrices could be related to their different pore size (Table 1). For the AM matrix, the formation of hydrogen bonding between the matrix and the drug did not have any esteric impediment, since most of the pores were between 5 and 50 nm and the length of the Trf molecule in this configuration is of ~1.13 nm. On the other hand, esteric impediments and polar repulsions, caused by close contact between the hydrophobic CF$_3$ group in the Trf and the hydrophilic adsorbed water on the other
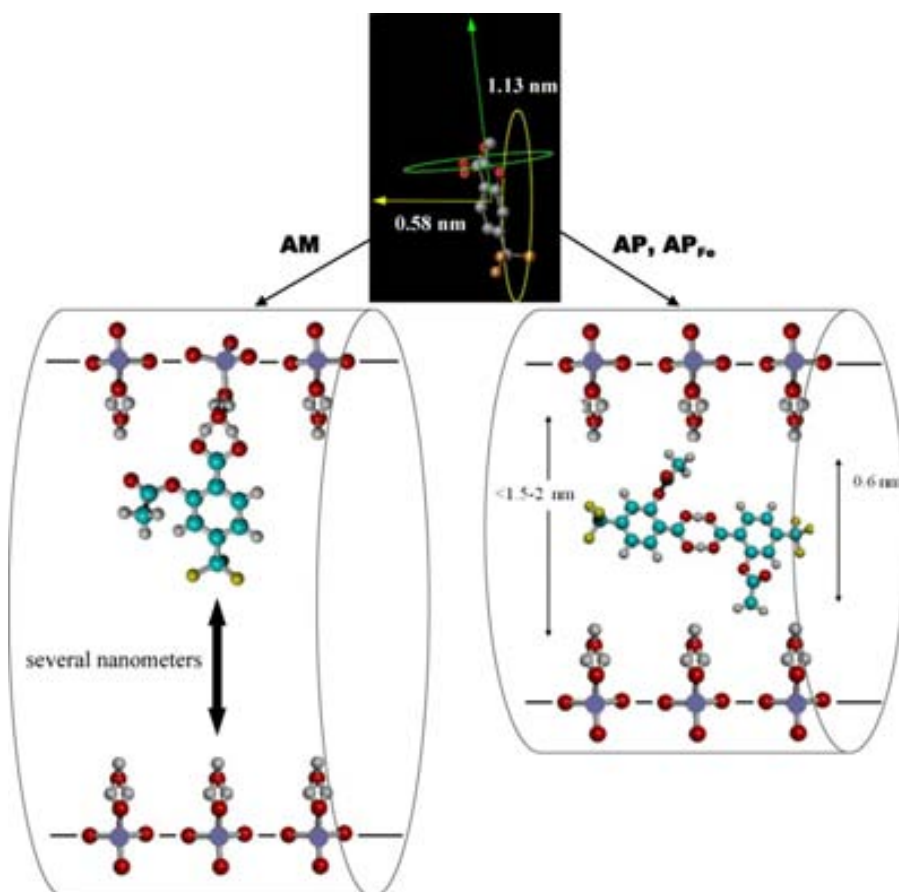
Scheme 2. Proposed conformations of the triflusal molecules inside the aerogel pores (AM) forming H-bonds with the water adsorbed at the pore surface and triflusal molecules forming dimmers inside the smaller pores of the particles (AP, AP$_{Fe}$). Calculations were performed with the HyperChem 8.03 software.

extreme of the SiO$_2$ pore wall, are expected in the small pores of the AP and AP$_{Fe}$ matrices. Consequently, impregnation in the form of dimmers was likely favored (Scheme 2). Moreover, it appears that hydrogen bonding of Trf molecules with the surface of the AM stabilizes the Trf against hydrolysis more efficiently than the dimmers occurring in the aerogel nanoparticles, since a higher degree of hydrolization (and faster release) was obtained in the impregnated AP and AP$_{Fe}$ (Fig. 1b).

The Van der Waals-surface-bounded molecular volume of the triflusal molecule was calculated using QSAR (quantitative structure–activity relationship) module together with Hyperchem 8.03 program [43]. The calculated volume of the Trf molecule was 619 Å^3 while the volume of the dimmer was 1138 Å^3. Thus, the occupied pore volume by Trf molecules was of 40–50% of the total available mesopore volume in the aerogel (Table 1). However, the molecular Van der Waals volume only counts the volume occupied by the molecules, and it is insensitive to molecular packing or conformational structures. For the monolith sample, the BJH pore volume reduction was from 0.75 to 0.42 cm^{3}g^{-1}, in agreement with the occupied volume estimated using the Van der Waals approximation. Similarly, using a value of 60 Å^2 for the area occupied by a Trf molecule when adsorbed, the covered surface was estimated to be around 300 m^2 g^{-1}. This value corresponded to more than 50% of the BET surface area in the pristine matrix, hence, indicating the formation of an adsorbed monolayer of Trf. During adsorption, the average separation in the adsorbate molecules approaches that of a liquid, and a monolayer with a liquid-like density is formed. As in liquids, molecules on the surface have mobility. As a result of this mobility and conformational changes, the real volume occupied by each Trf molecule is higher than the estimated Van der

Waals value. Hence, the empty mesopore volume after impregnation could be even smaller than the calculated value of 50–60%. Total coverage was not achieved since also the pore size distribution plays an important role in the adsorption process. It has been demonstrated that the adsorption in large mesopores is more effective than in the smaller ones due to better diffusion and less steric impediments [44]. It should be taken into account that smaller pores contribute more largely to surface area. Hence, and since crystallization was avoided, it is likely that the maximum possible loading was achieved. Indeed, by modifying processing conditions, such as pressure or reaction time, the maximum loading was not varied.

3.3. Release profiles and impregnated drug stability

Release kinetics were followed under gastric (pH = 2.0) and plasmatic (pH = 7.4) pH-conditions (Fig. 5a and b, respectively). Drug dissolution profiles (i.e., Trf and HTB) at pH = 2 for samples Trf@PMMA, Trf@AM, Trf@AP and Trf@AP$_{Fe}$ are shown in Fig. 5a. For silica aerogel nanospheres (Trf@AP), the drug release in acid pH occurred almost instantaneously and the 97% of the drug was dissolved completely in 1 min. The behavior of the sample Trf@AP$_{Fe}$ was very similar to that of the Trf@AP, being the 90% of Trf + HTB released in the first minute. The drug delivery profile of the monolithic aerogel Trf@AM was different, ca. 70% of the drug was dissolved during the first 5 min and a progressive release of the remaining 30% occurred during the next 2 h. Reasons of prolonged released could be related to both the different conformation of the drug inside the pores (Scheme 2) and to the longer diffusional channels that the molecules have to follow to reach the bulk
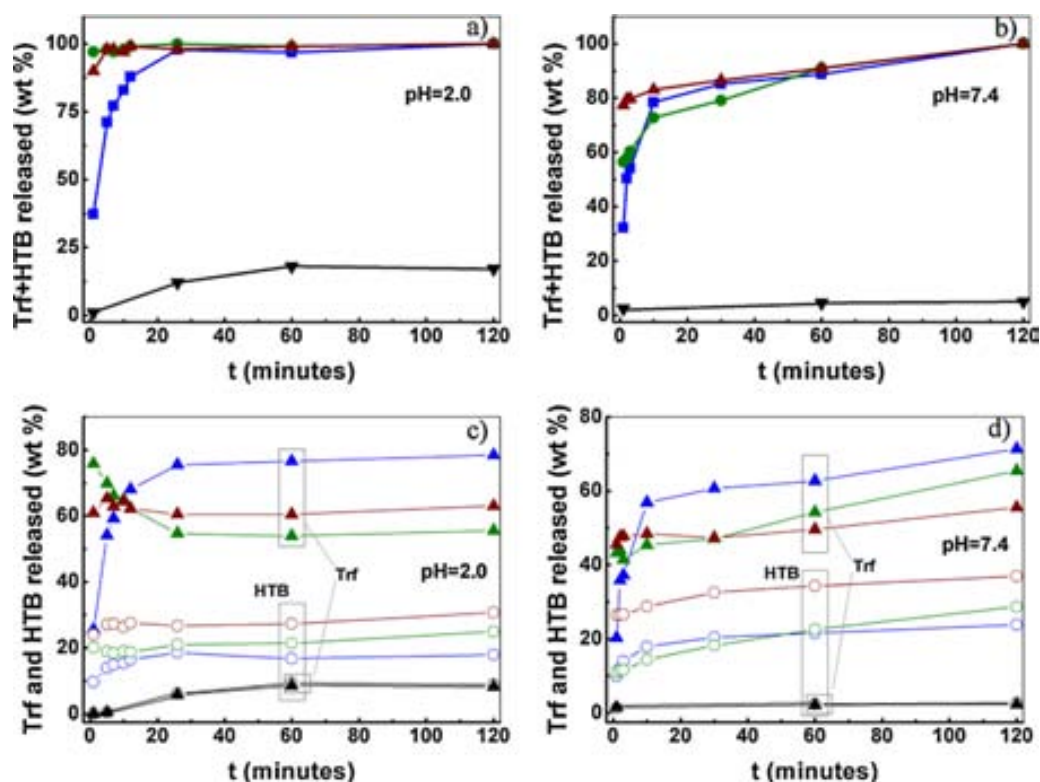
Fig. 5. Overall drug release profiles (Trf + HTB) obtained with the continuous-flow spectrophotometric and chromatographic procedures for the investigated materials at the two studied conditions: (a) acid pH, and (b) basic pH: ■, Trf@AM; ●,Trf@AP; ▲, Trf@AP$_{Fe}$; ▲, Trf@PMMA. Separated release profiles for Trf and for HTB for the same matrices at (c) acid pH, and (d) basic pH are depicted. Full triangles correspond to Trf and empty circles to HTB, while blue correspond to Trf@AM, green to Trf@AP, brown to Trf@AP$_{Fe}$ and black to Trf@PMMA. In all panels, solid lines are included as guide to the eye. (For interpretation of the references to color in this figure legend, the reader is referred to the web version of the article.)

solution in the monolithic aerogels. No consideration was given to the mechanism of drug delivery related to silica pore network collapse due to the fast release of the drug. The slowest release kinetics was obtained with the impregnated PMMA. In this case, the delivery of Trf from the sample to gastric medium lasted several days having only the 18% released in the first 60 min. Slightly slower dissolution rates were measured in experiments performed at pH 7.4 (Fig. 5b), but the same general tendency as in acid solutions is observed. Particulate materials have the 56% and 77% of the drug delivered in the first minute and the 79% and 86% in 30 min (for Trf@AP and Trf@AP$_{Fe}$, respectively). The monolith Trf@AM showed a similar release profile with the 32% of the drug delivered in 1 min. The fast drug release observed when the materials were submerged in the acid solution is explained by a favored hydrolysis of the ester group when a high concentration of H$^+$ is present in the medium. Once more, for the sample Trf@PMMA a sustained release lasting more than 1 month was observed (only the 4.5% of the drug is discharged after 60 min) and almost instantaneous release for the rest of the samples. Separated release profiles for Trf and HTB for all matrices in acidic and basic conditions are depicted in Fig. 5c and 5d respectively.

4. Conclusions

The possibilities of controlling the dissolution rate of hydrophobic poorly water-soluble drugs were demonstrated by the adsorption of triflusal on both PMMA polymer beads and SiO$_2$-based materials (aerogel monoliths and nanospheres). Triflusal, an antithrombotic agent, was here chosen as an excellent model compound for the study of the impregnation processes based on supercritical CO$_2$. The scCO$_2$ loading procedure allowed us the homogeneous impregnation of the drug inside of the matrices in percentages of the order of 16 wt% for PMMA and aerogel monolith and 3–4 wt% for aerogel nanoparticles. The drug was distributed at a molecular level and no crystals or amorphous forms of the drug were detected. Carboxylic H-bonding was determined to be the most feasible conformation for triflusal adsorbed in the PMMA and aerogel monolith matrices. In contrast, due to steric reasons dimmer was the most likely conformation of the Trf molecules inside the aerogel nanoparticles. An *in vitro* release study demonstrated a sustained release lasting for several days in the polymeric Trf@PMMA system, in which the induction of polymer swelling was required previous to drug dissolution. In these systems, drug release is usually controlled by the rate of polymer swelling by body fluids. On the contrary, the dissolution experiments of aerogel matrices showed that more than 80% of triflusal was dissolved in the media within the first minutes. Although these systems could not be used for prolonged release, they could be highly attractive for enhancing the bioavailability of poorly water-soluble drugs in intravenous or gastric conditions. The molecular dispersion of Trf in the SiO$_2$ aerogel matrices was relatively stable against hydrolysis for at least six months when stored under ambient conditions, while under the same storage conditions, Trf in the PMMA gradually changed to the HTB metabolite. From the point of view of the pharmaceutical processing technologies, the stabilization of drugs as molecular dispersions is highly desirable.

References

[1] V.P. Torchilin, Multifunctional nanocarriers, Advanced Drug Delivery Reviews 58 (2006) 1532–1535.

[2] S.K. Sahoo, V. Labhasetwar, Nanotech approaches to drug delivery and imaging, Drug Discovery Today 8 (2003) 1112–1120.

[3] D. Peer, J.M. Karp, S. Hong, O.C. Farokhzad, R. Margalit, R. Langer, Nanocarriers as an emerging platform for cancer therapy, Nature Nanotechnology 2 (2007) 751–760.

[4] D. Oupicky, Design and development strategies of polymer materials for drug and delivery applications, Advanced Drug Delivery Reviews 60 (2008) 957.

[5] K.K. Qian, R.H. Bogner, Application of mesoporous silicon dioxide and silicate in oral amorphous drug delivery systems, J. Pharmaceutical Sciences 101 (2012) 444–463.

[6] M. Manzano, M. Vallet-Regí, New developments in ordered mesoporous materials for drug delivery, J. Materials Chemistry 20 (2010) 5593–5604.

[7] Q. He, J. Shi, Mesoporous silica nanoparticles based nano drug delivery systems: synthesis, controlled drug release and delivery, pharmacokinetics and biocompatibility, J. Materials Chemistry 21 (2011) 5845–5855.

[8] J. Lu, M. Liong, J.I. Zink, F. Tamanoi, Mesoporous silica nanoparticles as a delivery for hydrophobic anticancer drugs, Small 3 (2007) 1341–1346.

[9] I. Chen, C. Hangrong, D. Seng, Y. Tian, F. Chen, J. Feng, J. Shi, Core/shell structured hollow mesoporous nanocapsules: a potential platform for simultaneous cell imaging and anticancer drug delivery, ACS Nano 4 (2010) 6001–6013.

[10] M. Liong, S. Angelos, E. Choi, K. Patel, J.F. Stoddart, J.I. Zink, Mesostructural multifunctional nanoparticles for imaging and drug delivery, J. Materials Chemistry 19 (2009) 6251–6257.

[11] J.E. Lee, N. Lee, T. Kim, J. Kim, T. Hyeon, Multifunctional mesoporous silica nanocomposite nanoparticles for theranostic applications, Accounts of Chemical Research 44 (2011) 893–902.

[12] US Environmental Agency's EPISuiteTM v4.10.

[13] D. Murdoch, G.L. Plosker, Triflusal: a review of its use in cerebral infarction and myocardial infarction, and as thromboprophylaxis in atrial fibrillation, Drugs 66 (2006) 671–692.

[14] M. Ferrit, C. Del Valle, F. Martínez, The study of the influence of surfactant charge on alkaline hydrolysis reactions of acetylsalicylic acid (ASA) and triflusal (TFR) using spectrophotometric methods, European Journal of Pharmaceutical Sciences 31 (2007) 211–220.

[15] G. Rodríguez, M. Fernández-Gutiérrez, J. Parra, A. López-Bravo, N.G. Honduvilla, J. Buján, M. Molina, L. Duocastella, J. San Román, Bioactive polymeric systems with platelet antiaggregating activity for the coating of vascular devices, Biomacromolecules 11 (2010) 2740–2747.

[16] A. López-Periago, A. Argemí, J.M. Andanson, V. Fernández, C.A. García-González, S.G. Kazarian, J. Saurina, C. Domingo, Impregnation of a biocompatible polymer aided by supercritical CO_2: evaluation of drug stability and drug–matrix interactions, J. Supercritical Fluids 48 (2009) 56–63.

[17] F. Schwertfeger, A. Zimmermann, H. Krempel, US Patent 6,280,744 (2001).

[18] I. Smirnova, W. Arlt, 2003, DE Patent 10214226A1.

[19] I. Smirnova, J. Mamic, W. Arlt, Adsorption of drugs on silica aerogels, Langmuir 19 (2003) 8521–8525.

[20] M. Alnaief, I. Smirnova, Effect of surface functionalization on silica aerogel on their adsorptive and release properties, J. Non-Crystalline Solids 356 (2010) 1644–1649.

[21] M. Moner-Girona, A. Roig, E. Molins, J. Llibre, Sol–gel route to direct formation of silica aerogel microparticles using supercritical solvents, J. Sol-Gel Science and Technology 26 (2003) 645–648.

[22] E. Taboada, R. Solanas, E. Rodríguez, R. Weisssleder, A. Roig, Supercritical fluid assisted one-pot synthesis of biocompatible core(γ-Fe_2O_3)@shell(SiO_2) nanoparticles as high relaxivity T_2-contrast agents for magnetic resonance imaging, Advanced Functional Materials 19 (2009) 2310–2324.

[23] N. Murillo-Cremaes, A.M. Lopez-Periago, J. Saurina, A. Roig, C. Domingo, A clean and effective supercritical carbon dioxide method for the host–guest synthesis and encapsulation of photoactive molecules in nanoporous matrices, Green Chemistry 12 (2010) 2196–2204.

[24] D.X. Chen, E. Taboada, A. Roig, Experimental study on T2 relaxation time of protons in water suspensions of iron-oxide nanoparticles: cases of composite nanospheres, J. Magnetism and Magnetic Materials 323 (2011) 2487–2492.

[25] A. Martín, M.J. Cocero, Micronization processes with supercritical fluids: fundamentals and mechanisms, Advanced Drug Delivery Reviews 60 (2008) 339–350.

[26] T. Yasuji, H. Takeuchi, Y. Kawashima, Particle design of poorly water-soluble drug substances using supercritical fluid technologies, Advanced Drug Delivery Reviews 60 (2008) 388–398.

[27] I. Kikic, F. Vecchione, Supercritical impregnation of polymers, Current Opinion in Solid State and Materials Science 7 (2003) 399–405.

[28] S. Uzer, U. Akman, O. Hortacsu, Polymers welling andi mpregnation using supercritical CO_2: a model-component study towards producing controlled-release drugs, J. Supercritical Fluids 38 (2006) 119–128.

[29] C. Elvira, A. Fanovich, M. Fernandez, J. Fraile, J. San Roman, C. Domingo, Evaluation of drug delivery characteristics of microspheres of PMMA–PCL–cholesterol obtained by supercritical-CO_2 impregnation and by dissolution–evaporation techniques, J. Controlled Release 99 (2004) 231–240.

[30] A.I. Cooper, Porous materials and supercritical fluids, Advanced Materials 15 (2003) 1049–1059.

[31] J. Garcia-Carmona, M.A. Fanovich, J. Llibre, R. Rodriguez-Clemente, C. Domingo, Processing of microporous VPI-5 molecular sieve by using supercritical CO_2: stability and adsorption properties, Microporous and Mesoporous Materials 54 (2002) 127–137.

[32] Y. Shin, T.S. Zemanian, G.F. Fryxell, L.Q. Wang, J. Liu, Supercritical processing of size selective microporous materials, Microporous and Mesoporous Materials 37 (2000) 49–56.

[33] R. Gläser, Novel process options for application of zeolites in supercritical fluids and ionic liquids, Chemical Engineering and Technology 30 (2007) 557–568.

[34] A.M. López-Periago, C.A. García-González, J. Saurina, C. Domingo, Preparation of trityl cations in faujasite micropores through supercritical, CO_2 impregnation, Microporous and Mesoporous Materials 132 (2010) 357–362.

[35] E. Schutz, Supercritical fluids and applications—a patent review, Chemical Engineering and Technology 30 (2007) 685–688.

[36] www.nektar.com (EC), www.ferro.com (USA) and www.lavipharm.gr (EC-USA).

[37] M.K. Gupta, A. Vanwert, R.H. Bogner, Formation of physically stable amorphous drugs by milling with Neusilin, J. Pharmaceutical Sciences 92 (2003) 536–551.

[38] J.M. Andanson, A. López-Periago, C.A. Garcıa-Gonzalez, C. Domingo, S.G. Kazarian, Spectroscopic analysis of triflusal impregnated into PMMA from supercritical CO_2 solution, Vibrational Spectroscopy 49 (2009) 183–189.

[39] C. Domingo, E. Berends, G.M. van Rosmalen, Precipitation of ultrafine organic crystals from the rapid expansion of supercritical solutions over a capillary and a frit nozzle, J. Supercritical Fluids 10 (1997) 39–55.

[40] S.G. Kazarian, G.G. Martirosyan, Spectroscopy of polymer/drug formulations, processed with supercritical fluids: in situ ATR-IR and Raman study of impregnation, of ibuprofen into PVP, International Journal of Pharmaceutics 232 (2002) 81–90.

[41] A. Argemi, A. Lopez-Periago, C. Domingo, J. Saurina, Spectroscopic and chromatographic characterization of triflusal delivery systems prepared by using supercritical impregnation technologies, J. Pharmaceutical and Biomedical Analysis 46 (2008) 456–462.

[42] B.S.K. Gorle, I. Smirnova, W. Arlt, Adsorptive crystallization of benzoic acid in aerogels from supercritical solutions, J. Supercritical Fluids 52 (2010) 249–257.

[43] HyperChem (Molecular Modeling System), Hypercube, Inc., Gainesville, FL, USA, 2007 http://www.hyperchem.com/

[44] I. Smirnova, S. Suttiruengwong, W. Artl, Feasibility study of hydrophilic and hydrophobic silica aerogels as drug delivery systems, J. Non-Crystalline Solids 350 (2004) 54–60.

PAPER

Preparation and study of naproxen in silica and lipid/polymer hybrid composites

Nerea Murillo-Cremaes,[a] Pascale Subra-Paternault,*[b] Concepción Domingo*[a] and Anna Roig*[a]

Three different powdered hybrid inorganic–organic composites for pharmaceutical use have been successfully obtained using CO_2 as an antisolvent in a batch mode process. Naproxen was chosen as the hydrophobic Class II model drug, for which its dissolution rate in water must be enhanced. As excipients, two kind of commercial lipids (G44/14 and G50/13) and a mixture of Eudragit RS100 and Eudragit RL100 polymers were used. Silica microparticles have also been incorporated into the formulation to restrict the naproxen crystals growth and to obtain a powdered material with appropriate micromeritic properties. The morpho-chemical characteristics of these microcomposites and their different release profiles are reported. Importantly, the components have not suffered structural or chemical modifications during the processing and no specific chemical bonds were detected between them. High drug loading has been achieved in the three cases. Water dissolution of the drug formulations is controlled mainly by the wetting properties and nature of the excipients and by the size of the crystals. Among the materials prepared, samples made with Gelucires (hydrophilic species) result in the fastest release of naproxen. We thus conclude that lipid-based ternary formulations display a synergetically accelerated release compared to binary mixtures.

1. Introduction

The oral route is the preferred one for drug administration especially in the case of chronic therapies. Over eighty percent of marketed drugs are sold as tablets. Drug absorption in the gastrointestinal tract is controlled by membrane permeability and drug dissolution rate.[1] Around 30% of the orally administered drugs belong to Class II (low solubility and high permeability) in the Biopharmaceutics Classification System (BCS).[2,3] More importantly, around 70% of the drugs in the R&D pipeline fit into that class presenting low solubility and thus low oral bioavailability.[4,5] Thus, studies on novel drug formulations able to modulate the solubility of common drugs are highly relevant.

Silica, especially mesoporous silica particles, is one of the most well studied materials to be used as solid carrier for drug delivery applications. Biocompatibility, non-toxicity and excellent textural and structural properties easy to be modulated, make of mesoporous silica particles an excellent candidate for hosting different types of pharmaceutical ingredients.[6–9]

Regarding the oral administration of drugs, the incorporation of silica into the pharmaceutical formulations enhances their flowability.[10] Among other excipients employed to better control drug release, hydrophilic lipid-based compounds accelerate the dissolution rate by increasing the wettability of the solid dispersions. In particular, the family of lipids named Gelucires® allows a relatively precise modulation of the drug solubility due to the different hydrophilic–lipophilic balances for each type of lipid.[11,12] The release rate of the therapeutic agent can be decreased by adding a water insoluble polymer to the solid formulation. Some of the polymers used in the pharmaceutical industry are the Eudragits®, that possess relevant properties for biomedical applications, such as water permeability, permitting the diffusion of the drug to the concomitant media.[13,14] Naproxen ((S)-2-(6-methoxynaphthalen-2-yl)propanoic acid, $C_{14}H_{14}O_3$) is a non-steroidal anti-inflammatory drug of the Class II family whose bioavailability is rate-limited by its dissolution. It is commonly used to treat mild to moderate pain, fever, inflammation and stiffness. However, in some patients it can induce gastrointestinal problems. Formulations and drug delivery carriers for naproxen as Class II model drug to modulate its solubility and, thus, its dissolution rate or to decrease its side effects have been described. For instance, the formulation of naproxen as a commercially available sodium salt is more rapidly absorbed than the neutral molecular form causing a faster peak plasma level. More recently, drug release profiles of naproxen using periodic SBA-15 and MCM-41 mesoporous silica

[a] Institut de Ciència de Materials de Barcelona (CSIC), Campus de la UAB, 08193 Bellaterra, Catalonia, Spain. Fax: +34 93 580 5729; Tel: +34 93 580 1853. E-mail: conchi@icmab.es; roig@icmab.es

[b] Université Bordeaux, CBMN UMR 5248, Bat B14 bis, Allée Geoffroy St Hilaire, 33600 Pessac, France. Fax: +33 (0)5 40 00 22 00; Tel: +33 (0)5 40 00 68 32. E-mail: subra@enscbp.fr

Paper

matrices have been published.[15,16] Still other studies reported on the comparative release profiles of naproxen loaded in layered double hydroxides (LDH), mesoporous silica (MCM-41) and porous alumina.[17] Authors showed a similar drug payload in the mesoporous matrices though this being smaller than the amount incorporated in the layered compound. They also reported on a much slower kinetics for the naproxen loaded in the three matrices when compared with free naproxen release. Nevertheless, the release profile from the LDH matrix was much faster than for the mesoporous matrices. Other works were dedicated to investigate the formulation of naproxen with a water insoluble copolymer such as Eudragit® RS100.[18,19] In this case naproxen was successfully encapsulated in Eudragit microparticles by a quasi-emulsion diffusion method. The resultant particles had appropriate micromeritic properties and were suitable to be incorporated into capsules, while *in vitro* release profiles confirmed its gastroresistance (moderate dissolution in the stomach), thus allowing pH-dependent release of naproxen in the gastrointestinal track. Finally, another study investigated the use of the lipid Gelucire® 44/14 as a self-emulsifying drug delivery system containing naproxen.[20] Gelucire® improved the solubility of naproxen, this improvement was more noticeably under conditions where the solubility was the limiting parameter (at pH = 1.2).

Recently feasibility studies have been reported on the preparation of complex formulations of hydrophobic drugs in the presence of a polymer and silica particles or other ternary formulations.[21–23] For instance, in ref. 12, they demonstrated that compressed CO_2 as the antisolvent medium can induce both the drug (tolbutamide) and polymer co-precipitation on the silica microparticles. They also showed that the presence of silica particles influences in several ways the processing route and the product characteristics. Silica particles acted as a passive spacer to deagglomerate both the drug and the polymer and as a wetting agent. In addition, we have also recently reported several studies describing the engraftment of molecules of interest in porous silica materials by its solubilization in supercritical CO_2.[24,25]

The present study focuses on the morpho-chemical properties and release kinetics of ternary hybrid composites (organic–inorganic) microparticles obtained in one-step batch mode by antisolvent precipitation in compressed CO_2. The solid dispersions contained naproxen as a model hydrophobic therapeutical agent whose dissolution in water needs to be enhanced, silica microparticles (5 μm) and two types of polymers capable of modifying the dissolution behavior of the drug. Two organic commercially available components were selected; the crystalline lipid Gelucire® and the amorphous polymer Eudragit®. Aspects as drug loading efficiency, thermal stability and textural parameters of the composites are discussed together with a comparative study of the release profiles for the various formulations at neutral pH.

2. Experimental

2.1. Materials

Naproxen (NPX, 98 wt% purity) was purchased from Sigma-Aldrich. Its chemical structure is shown in Fig. 1a. Gelucire®
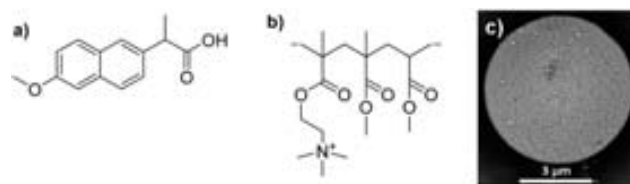

Fig. 1 Chemical structure of (a) naproxen, (b) the excipient Eudragit, and (c) SEM image of a SiO_2 microparticle.

lipids (44/14 and 50/13) were kindly supplied by Gattefossé (France). Gelucire® lipid-based compounds are commonly used as excipients[26] and they can be labeled as GX/Y, where X is the melting temperature and Y is the hydrophilic–lipophilic balance (HLB). G44/14 and G50/13 types are composed by a mixture of mono-, di- and triglycerides, mono- and di-fatty acid esters of PEG 1500, and free PEG. Their difference relies in the fatty acid distribution, with most acids being palmitic and stearic for Gelucire 50/13 contrary to the unique balance of short, medium and long chain fatty acids for Gelucire 44/14. Eudragit® polymers (RL100 and RS100) from Evonik Rohm Pharma Polymer (Degussa) were kindly supplied by IMCD (France). Eudragit® compounds are copolymers of acrylic and methacrylic acid esters branched with various functional groups that provide flexible solutions for drug release (http://eudragit.evonik.com/product/eudragit).[27] The Eudragit® RL- and RS types have a quaternary ammonium as the functional group and, contrary to Gelucire®, are water insoluble but swellable. In this study a mixture of the RL100 and RS100 types was used. The chemical structure of this polymer appears in Fig. 1b. Sodium dodecyl sulfate (SDS) was received from Merck. Acetone (99.8 wt% purity) and CO_2 (99.5 wt% industrial grade) were purchased from VWR and Air Liquide (France) respectively. Silica Ultiprep120 (SiO_2-UP120, Interchim., France) is composed of porous spheres of 5 μm in size and approximately 12 nm of pore diameter (Fig. 1c). Silica is a pharmaceutically acceptable inorganic excipient used in industry to reduce the cohesive behavior of drug nanoparticles and improve the free flowing of the formulation.[28]

All materials were used as-received.

Gas CO_2 antisolvent batch process. Experiments were performed in a Gas Antisolvent (GAS) home-made apparatus working in the discontinuous mode (Fig. 2). The set-up is described elsewhere in detail.[29] Briefly, the reaction vessel is a stainless steel autoclave of 0.5 L that includes a stirrer ended by a Rushton-type turbine plunging vertically into the solution. It is provided with an inner glass cylinder to facilitate the powder collection and four baffles to exclude the formation of a central vortex. The CO_2, delivered by a high-pressure pump, is introduced into the solution through the turbine. The temperature of the vessel is controlled by heating jackets. The bottom of the vessel has a stainless steel filter (5 μm mesh) surmounted by two membranes of 0.22 μm to collect the obtained solid material.

In the lipid experiments, silica particles, the selected Gelucire® and the drug were weighed (*ca.* 1 g of NPX) in a mass ratio of 1/1/1 and mixed with 40 mL of acetone. For experiments
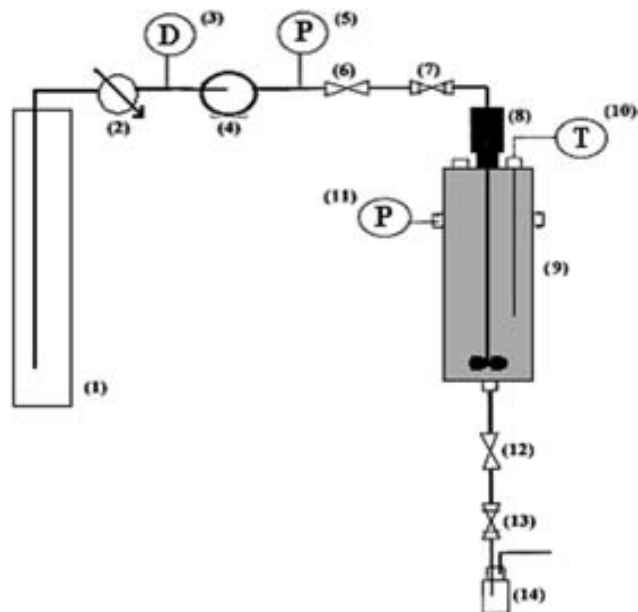
Fig. 2 Schematic representation of the experimental set-up. (1) CO_2 cylinder, (2) cooling exchanger, (3) flow meter, (4) CO_2 pump, (5) pressure sensor, (6) valve, (7) micrometering valve, (8) stirrer, (9) high pressure vessel, (10) temperature sensor, (11) pressure sensor, (12) valve, (13) micrometering valve and (14) solution recovery.

carried out with Eudragit®, RL100 and RS100 were added as a mixture in a mass ratio of 1/2, so that the global mass ratio of silica, polymers and NPX was 1/0.7/1 with *ca.* 1 g of NPX. After sonicating the suspension for 15 min, it was introduced into the vessel and the CO_2 was gradually added resulting in an increase of the pressure in the chamber. The temperature was fixed at 23 °C and the stirrer at 500 rpm. The gas flow could be adjusted by a needle valve and the pressure was risen up to 100 bar approximately. Progressively enriched in CO_2, the expanded liquid phase reaches a composition in which the NPX and the coater are not soluble, thus causing the beginning of precipitation. To clean the precipitated material, fresh CO_2 was flushed from top to the bottom of the autoclave in two steps: 60 min at 26 °C and 100 bar and 30 min at 30 °C and 100 bar. The pressure was kept constant by opening or closing the exit valve, while the particles were retained by the filtering devices. The as-obtained material was a white powder which was weighed and used for further characterization and were labeled as, G44F, G50F and EudF in reference to the type of organic material used. For comparison purposes, six more samples were also analyzed: commercial NPX, a physical mixture of NPX, silica and Gelucire 44/14 (PMG44F), CO_2 processed NPX (processed NPX), NPX and G50/13 (NPX : G50/13), NPX and silica particles (NPX : silica) and NPX, silica particles and Eudragit in a different ratio: 1/3 of the initial amount (EudF/3). The physical mixture was prepared by mixing and grinding the three components in the same mass ratio as the equivalent formulation synthesized trough the gas antisolvent process. The last three samples were produced following the same batch process than the one followed to prepare the inorganic–organic solid formulations described before.

2.2. Characterization techniques

Morphological characterization. Morphological characterization was based on scanning electron microscopy (SEM) (Quanta FEI 200F operating at 20 kV). Materials were sputtered with gold for 4 minutes with an intensity of 25 mA. The particle size distribution and the shape of the materials were evaluated by using a static image analysis equipment (Morphologi G3, Malvern) that allows size measurements between 0.5 and 3000 μm, as well as detailed shape analysis of the particles.

Fourier transform infrared spectroscopy (FTIR). FTIR spectra of the solid samples mixed with KBr were recorded on a Perkin Elmer Spectrum One instrument and were used to monitor the success of the processing technique by signaling the presence of the different components (naproxen, SiO_2 and the corresponding lipid or polymer).

Thermal analysis. Naproxen loading, percentages of Gelucire® and Eudragit® in the formulations and mass ratios between all the components were evaluated by thermogravimetric analysis (TGA) (system NETZSCH-STA 449 F1) under N_2 atmosphere with a 10 °C min^{-1} heating rate.

Powder X-ray diffraction (PXRD). Materials crystallinity was analyzed by X-ray powder diffraction (Rigaku Rotaflex RU-200 B, XRD) using a Cu anode with $\lambda_{K\alpha1} = 1.5406$ Å and $\lambda_{K\alpha2} = 1.5444$ Å in the 2θ range of 5–60°.

Drug loading and drug release profiles. The percentages of drug impregnated in the hybrid composites and the release kinetics at neutral pH were done using UV spectrometry. To determine the total amount of NPX in each sample, a calibration curve was first done by measuring the absorbance of NPX solutions in acetone at 332 nm in an UV spectrophotometer (UVIKON XS, Secomam). The range of concentrations used was between 0.0094 and 0.1 mg mL^{-1}. A certain amount of each sample (typically between 20 and 30 mg) was weighed and the required volume of acetone was added. After vigorous manual stirring, the polymer (or the lipid) and the NPX were dissolved, while the silica particles remained suspended. Once the silica was deposited at the bottom and the solution was clearly transparent, an aliquot was taken and measured in the spectrophotometer.

The NPX release profile was obtained by applying a dissolution test already used by various authors and called Blade. The dissolution medium consisted in 900 mL of 0.3% SDS stirred by a paddle at 50 rpm and thermostated at 37.0 °C. The medium was suitable to discriminate naproxen formulations compared to a phosphate buffer in which pure naproxen dissolved in less than 40 min.[21] The amount of powder to be analyzed was previously weighed to have the final drug content close to 30 mg. A peristaltic pump was connected to the dissolution tank allowing recirculation through the UV flow cell of the spectrophotometer Uvikon ($\lambda = 272$ nm) for the *in situ* monitoring of the concentration of NPX in the dissolution medium. Dissolution kinetics was monitored during 240 min or more if needed to reach a constant value of the absorbance. Three replicates for each formulation were made (slightly varying the soaking conditions of the three components prior to the antisolvent precipitation) which yielded in each case the same amount of NPX and very similar release kinetics.

Paper

3. Results and discussion

Three formulations of NPX–lipids/polymers–silica (labeled as, G44F, G50F and EudF in reference to the type of organic material used) were prepared by the gas antisolvent method. The mass ratio between the drug, the silica particles and the lipids was kept equal. In the case of the polymer, a slightly smaller amount of it was employed. This amount was chosen to reach a compromise between obtaining a non-sticky material (larger polymer concentration resulted in sticky material loosing the pluviometric properties seeked here) and a sustained release of the drug that is characteristic for this excipient. Acetone was the solvent of choice because it dissolves both the drug and the lipidic/polymeric excipients, it is easily eliminated from the autoclave and is much less toxic than other organic solvents. With the initial solution containing a suspension of silica particles, likely those acted as nucleation sites promoting precipitation in their vicinity. The experimental conditions were chosen according to previous work using NPX and these excipients in presence of CO_2–acetone.[11,30]

3.1. Composition and morphology of NPX–lipids/polymers–silica formulations

Previous experiments on NPX precipitation from an acetone solution in CO_2 lead on a product recovery of 50 wt%, showing that the NPX has certain solubility in the mixture of solvents, as expected from its thermodynamic data.[31,32] Thus, an initial amount of starting NPX product as high as 1 g was used. Silica UP120 5 µm sized particles present in addition inner porosity with a mean pore size of 12 nm permitting the therapeutic agent

to precipitate not only around the spheres, but also inside theses cavities eventually as amorphous entities. A mass yield between 56 and 67 wt% was achieved in all cases and around 2 g of material was collected in each batch. To demonstrate the possibility of increasing the amount of NPX in the formulation, a batch experiment was done with double amount of NPX with respect to silica and Gelucire. The as-obtained formulation yielded more NPX and a slower release rate that could come to an insufficient coating of all NPX particles (results not shown).

Fig. 3 contains SEM images of single components and of the binary and the ternary organic–inorganic composite materials. As it can be seen in Fig. 3a, the commercial naproxen consists of small platelet-like crystals of 5–10 µm in diameter and around one micron in thickness. When those are dissolved and recrystallized in compressed CO_2, the crystals show a needle-like morphology and they are much larger in size (Fig. 3b) (approximately $300 \times 8 \times 55$ µm). When the process is carried out in the presence of silica microparticles, the crystals are of smaller sizes and of different shapes (approximately 20–30 µm in diameter). The NPX crystals are partially covered by the silica particles even though a portion of these particles are detached (see Fig. 3c and d). For the ternary formulations, the resulting materials are homogeneous as can be observed by the SEM images (Fig. 3f–h). In the higher magnification images (Fig. 3j–l), it can be clearly seen that the formulations are composed by drug crystals coated by silica microparticles. G44F and G50F exhibit long and elongated NPX needles, while in EudF the drug precipitates in crystals of various shapes. Although the presence of lipids/polymers is not so obvious in these images, we believe they act as agglomerating agents between the silica microspheres and the NPX crystals. Some differences in the homogeneity of the silica

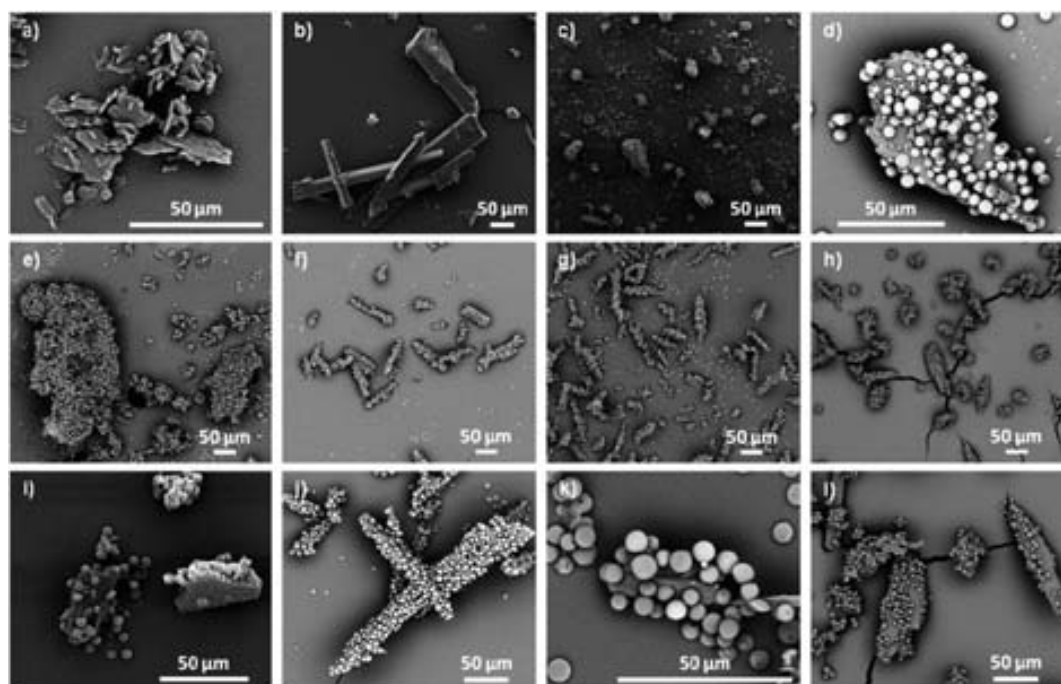Fig. 3   SEM images of (a) commercial NPX, (b) as-obtained CO_2 processed NPX and (c and d) NPX + SiO_2, (e and i) the physical mixture PMG44F, and solid formulations at low and high magnification of (f and j) G44F, (g and k) G50F and (h and l) EudF.

layer around the NPX can be observed depending on the lipid/polymer used. G44F and G50F present a compact and homogeneous silica particles coating around the drug crystal. The EudF formulation presents a less homogeneous silica coating, uncoated areas can be observed in every crystal. In all cases, a small number of non-attached silica particles could be detected. The additional material prepared with one third of Eudragit (named EudF/3) was also observed by SEM. The resulting material consisted in a larger number of individual silica particles non-attached to NPX crystals (results not shown). This could indicate that the amount of Eudragit in the formulation (7%) is not enough to coat NPX and silica particles. Moreover, the physical mixture, labeled as PMG44F, is composed by very broad crystal sizes distribution of NPX, partially coated by silica particles as well as silica aggregates, probably glued by the lipid (Fig. 3e and i). Considering the heterogeneity of the mixture, no further characterization was performed.

A more accurate and detailed statistics analysis of the materials morphological parameters was done with the optical microscope and software Morphologi G3. Obtained mean sizes are summarized in Table 1. The two most differentiated samples G44F (Fig. 4a) and EudF (Fig. 4b) were more deeply studied. In contrast with the electronic microscope, this optical equipment statistically analyses a large area and thus a representative portion of the sample can be investigated. Furthermore, many parameters related to the shape of the scanned materials can be calculated by the equipment software. In our samples, it is especially interesting to know the length and width of the coated NPX needles. The obtained mean values are 65 μm in length and 31 μm in width for G44F and 64 μm and 32 μm for EudF resulting in aspect ratios of 0.48 and 0.50 respectively. In Fig. 4, it can be observed that the silica coating is more homogenous and conformal in the G44F formulation compared to the EudF one.

FTIR spectroscopy was used to confirm the presence of all components and to investigate if chemical modifications had taken place during the batch process in compressed CO_2. Fig. 5a and b depict the IR spectra of the ternary lipidic formulations and includes the spectra of the constituent components (silica particles, commercial NPX and lipids) at different wave number ranges. Silica presents intense absorption bands in the region 900–1200 cm^{-1} due to the stretching vibrations of the O–Si–O bonds of the SiO_4 tetrahedrons. NPX exhibits a peak at 1726 cm^{-1}, which corresponds to the stretching vibration of its carboxylic group (C=O), and a peak at 1603 cm^{-1} corresponding to the breathing vibrations of C=C bonds in the aromatic ring. Ether's C–O–C asymmetric stretching mode appear at 1092 and 1072 cm^{-1}.[33] The C–H vibrations are located at 896 cm^{-1}. The two lipids Gelucire® 44/14 and Gelucire® 50/13 have similar chemical structures presenting the following bands: the stretching vibration from the O–H bond at 2921 and 2915 cm^{-1}, respectively,[34] two bands at 2857 and 2850 cm^{-1} corresponding to the stretching mode of the C–H,[35] the stretching vibration of the carbonyl group at 1732 and 1736 cm^{-1} and the characteristics ones from PEG around 1470, 1106 and 960 cm^{-1}.[36,37] The spectra of the composite organic–inorganic materials show the broad band of the O–Si–O stretching, evidencing the presence of silica particles in the composite samples. NPX existence can only be clearly detected from the peak at 1603 cm^{-1} of the aromatic ring, since the C=O vibrations are also present in the lipidic excipients and the C–H vibration band overlapped with the broad one of SiO_2. Even so, incipient peaks at 1090 cm^{-1} for the case of the solid formulation G44F and at 1071 cm^{-1} for both lipidic systems are observed. They come from the ether's groups vibrations of the NPX and they are in the range that the broad band of O–Si–O appears. Similar signals are found for the two lipids in the solid formulations spectra, where only the band due to the O–H vibration around 2915 cm^{-1} and the one from PEG at 1455 and

Table 1 Composition, NPX content obtained by spectroscopic and TG measurements, morphological properties and approximated volumes of the studied materials

Materials	Polymer/lipid + SiO$_2$ (5 μm)	Naproxen content by UV spectroscopy (wt%)	Naproxen, polymer/lipid and SiO$_2$ content by TG measurements (wt%)	Microparticle mean size length × width (μm) aspect ratio from Morphologi	Approx. crystal volumes (μm^3)
Commercial NPX		100			
Processed-NPX		100			
NPX–Silica		54[a]			
NPX–G50F		46[a]			
G44F	Gelucire 44/14 + SiO$_2$	38	23 Naproxen 20 G44/14 57 SiO$_2$	65 × 31 0.48	9800
G50F	Gelucire 50/13 + SiO$_2$	27	16 Naproxen 19 G50/13 65 SiO$_2$		
EudF	Eudragit RS/RL100 + SiO$_2$	40[a]	25 Naproxen 20 Eud. RS/RL100 55 SiO$_2$	64 × 32 0.50	8200
EudF/3	Eudragit RS/RL100 + SiO$_2$	37	31 Naproxen 7 Eud. RS/RL100 62 SiO$_2$	51 × 31 0.6	11000

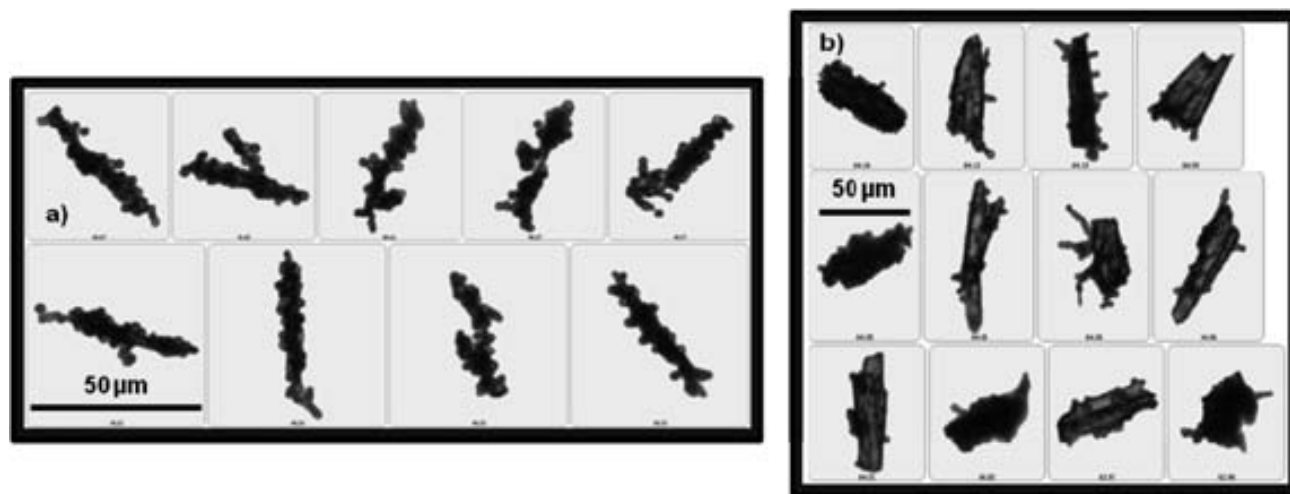[a] Data were taken from the plateaux of the release curves.

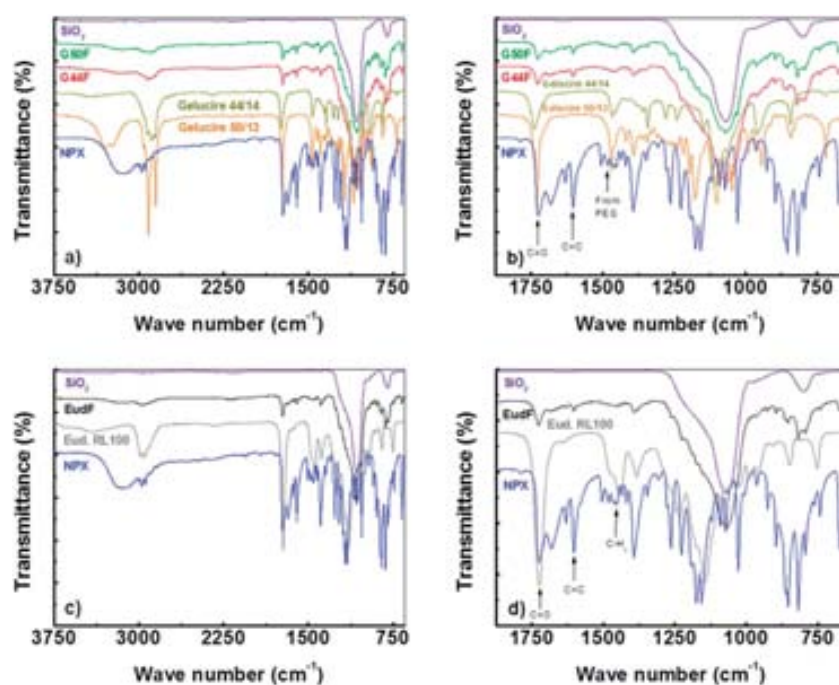Fig. 4 Optical microscope pictures of (a) G44F and (b) EudF.

Fig. 5 FTIR spectra of samples (a and b) G44F and G50F, and (c and d) EudF, both including the starting materials.

1457 cm^{-1} for the G44F and G50F, respectively, are clearly visible. The PEG peak at 1106 cm^{-1} is overlapped with the silica band, but the one at 960 cm^{-1} can be observed in both materials. In all the species a broad band between 3550 and 3100 cm^{-1} appears assigned to free O–H stretching vibrations. Thus, from the FTIR data, it can be concluded that the starting products have not suffered any change in their chemical structure; neither any new chemical bond seems to be formed during the preparation process in presence of CO_2. In Fig. 5c and d, the spectra of the polymeric composite and of the raw starting materials can be observed at broad and narrow range of wave number respectively. Only Eudragit® RL100 spectra is shown, since Eudragit® RS100 presents an identical IR spectrum. The two polymers only

differ in their quaternary ammonium groups composition; being higher for Eudragit® RL100 (this feature gives the polymer its permeability characteristics). The IR spectrum of Eudragit® RL100 presents peaks at 2990 and 2950 cm^{-1} that come from the absorbance of the alkyl groups (–CH_3 and –CH_2) stretching vibrations.[38] The corresponding absorbance of bending vibrations appears as a shoulder at 1480 cm^{-1} and as two peaks at 1447 and 1384 cm^{-1}. The sharp peak of the stretching vibration of the carbonyl group occurs at 1726 cm^{-1}. A band between 1300 and 935 cm^{-1} also appears, and it is attributed to the polymer C–O double bond stretching mode. Moreover, the broad band from the free O–H stretching vibrations is located in the range of 3600 and 3100 cm^{-1}. The spectrum of the composite material

EudF has the characteristic signals of silica, NPX and the mixture of polymers. To distinguish between the drug and the coaters the bands at 1603 and 1449 cm^{-1} were used. The peak at 1603 cm^{-1}, assigned to the C=C vibration of the aromatic ring, identify the NPX; while the peak at 1449 cm^{-1} indicates the presence of C–H$_x$ bending vibrations typical of the polymer.

The compositions of resulting materials are summarized in Table 1. Similar loading percentage in weight of NPX can be observed in all samples (ranging from 27 wt% to 40 wt%) when measured by UV spectrophotometry. Somehow, smaller contents were found when evaluating the drug load by thermogravimetry (ranging from 16 wt% to 25 wt%). The spectrophotometric method has been considered as the most precise; therefore, UV results should be taken into consideration to assess the NPX load. However, the amount of lipid/polymer could only be assessed thermogravimetrically. The silica content was estimated from the weight remaining in the TGA curves at *ca.* 450 °C. In Fig. 6a and b the temperature ranges in which the commercial materials decompose are shown, while Fig. 6c shows the thermal degradation of the solid formulations under study. Thus, the mass ratios of lipid or polymer–NPX was 0.9/1 in G44F, 1.2/1 in G50F, 0.8/1 in EudF and 0.2/1 in EudF/3, mirroring the nominal initial concentration between organic binders and NPX and confirming what was already observed by SEM, that 'naked' NPX crystals or polymeric particles were not present. The obtained ratios also confirm the fact that the lipids/polymer served as a binder between the NPX needles and the silica particles, since the samples with low polymer percentage, as Eudragit composite materials, have a higher number of silica spheres unattached to the drug particles. Moreover, the presence of silica in the formulations enables the recovery of a fine and free-flowing powder with reproducible NPX content and dissolution kinetics pointing to a good

homogeneity of the material. In Fig. 6d the TGA of commercial raw materials and the Gelucire 50F sample is depicted together with the derivative curves. The curves showed that the temperature at the maximum in the derivative curve obtained for raw and composite materials was very similar, indicating that the addition of silica or polymer do not have any effect on the thermal stability of the drug.

In Fig. 7a, XRD patterns of commercial Gelucire 44/14 and Gelucire 50/13 are depicted. They show peaks at 19 and 23.2° that are typical from PEG.[39] On the contrary, Eudragit® RL100 exhibits a broad band in the range of 10 and 20° due to its amorphous nature (Fig. 7b). The diffractogram of the commercial NPX presents the typical peaks of its crystalline form at 6.5, 12.4, 16.6, 19, 20, 22.2, 23.8 and 28.2°. The presence of the drug in a crystalline form after the antisolvent process is evidenced by the appearance of the characteristic NPX diffraction peaks in the diffraction patterns of the G50F, G44F and EudF samples.[9]

3.2 Drug release

Fig. 8 shows the drug release profiles of the various formulations and of pure naproxen (commercial or processed). The binary CO$_2$-processed formulations of NPX : silica and NPX : G50/13 are also included to evaluate the effect of processing three components.

Let first consider the dissolution of CO$_2$-processed NPX compared to commercial NPX. The main difference resides in the initial stages of the release, since in the first four minutes, almost 35 wt% of the drug is dissolved for the commercial sample while only the 15 wt% was dissolved in the CO$_2$-processed one. But, after 45 minutes, the 75 wt% of NPX has been dissolved from the two materials. This is related with the size of
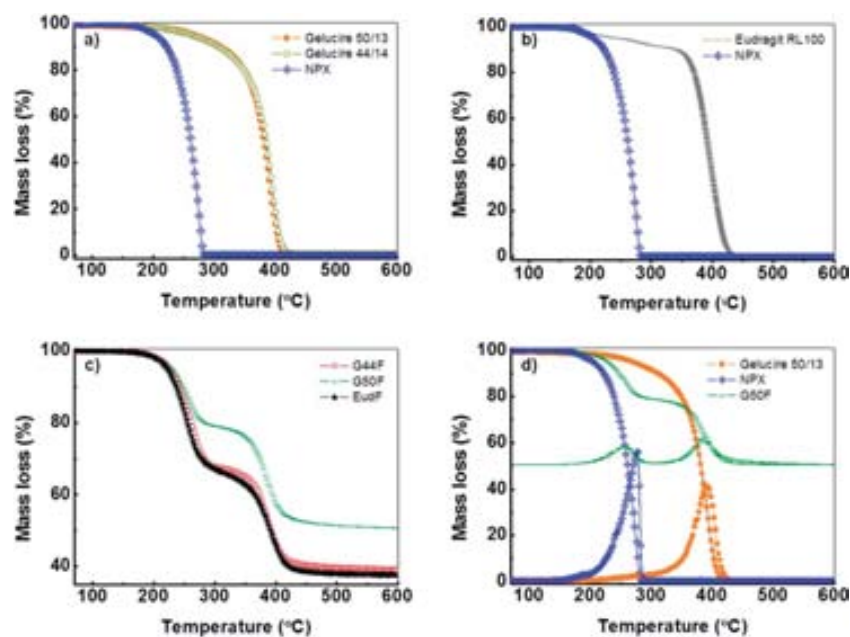

Fig. 6 Thermogravimetric analysis of (a) the raw lipids and commercial NPX, (b) the raw polymers and commercial NPX, (c) the synthesized materials G44F, G50F and EudF, and (d) G50F compared with raw Gelucire® 50/13 and with commercial NPX as well and the derivatives of the curves.
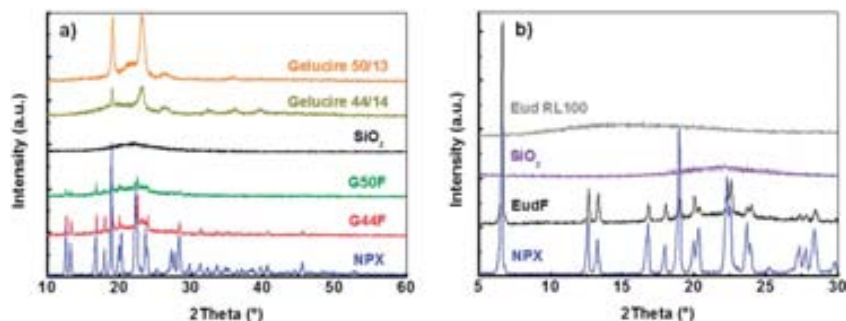
Fig. 7 X-ray spectra of raw materials and (a) Gelucires 44/14 and 50/13, and (b) Eud RL100.

the NPX particles; the smaller the particles the faster the dissolution. When the drug is precipitated in CO_2 in the presence of silica particles, the NPX crystals were significantly smaller than without them (Fig. 3). This implies a faster release profile of the drug, further enhanced by a de-agglomeration effect provided by silica particles (Fig. 8). A very similar release profile was observed for the NPX : G50/13 binary mixture as compared to the NPX : silica one. The possibilities for improving drug dissolution under constant hydrodynamic conditions pass by increasing the surface area available for dissolution, modifying the crystal habit, or optimizing the wetting characteristics of the compound surface. This can be done by micronization, preparing nanosuspensions, precipitating different polymorphs or the amorphous form of the drug, complexation, drug dispersion in carriers and formation of salts or co-crystals.[40] Within produced formulations, naproxen particles themselves were not small and they were produced as crystals and not in amorphous form, two characteristics that do not help the dissolution. Silica was used with the primary goal to act as a spacer during the precipitation process to reduce the agglomeration of drug particles. This beneficial effect was evidenced macroscopically by recovering a powder that flew more freely than the commercial or CO_2 processed NPX. In addition,

the de-agglomerated NPX crystals exhibit an increased surface area that improves its dissolution rate. Gelucire carriers enhance dissolution by a different mechanism. As surface-active agents also possessing self-emulsifying properties, they can adsorb drugs thereby altering the surface or the interfacial free energy to reduce the surface or the interfacial tension, through which the dissolution can be increased by preventing the formation of any water-insoluble surface layer.[41] Thus, effects of silica and Gelucire were combined in the lipid-based ternary formulations since those systems exhibited the fastest dissolution rates compared to materials containing only lipid (NPX : G50/13) or only SiO_2 particles (NPX : silica): within the first 10 min, almost 90% of the drug was released. The release order of the G44F or G50F > NPX : silica > NPX fits with literature that attributed the prime effect of Gelucire to a better wetting, micellar solubilization, reduced hydrophobic interaction, or both mechanism (Chauhan 2005). When Eudragit® was used instead of lipids, the release of NPX was slower; lipidic formulations dissolve between 59 and 75 wt% of the total amount of the encapsulated drug in the first two minutes and EudF only 20 wt%. The swellability and permeability of those carriers induce drugs embedded in their matrices to be released by diffusion. It is interesting to note that within the first 10 min, the dissolution rate of the EudF sample was comparable to that of pure naproxen as if uncoated and agglomerated crystals were present. As expected, the PEG based lipids lead in the fastest release. To evaluate the possible contribution of particle size to their different release profiles, the volumes of the solid formulations were approximately calculated (see Table 1) and similar values were obtained for EudF and G44F. This was done by assuming the crystals to be orthohedrons, considering the width and length values from Morphologi data and the height from a mean value of several SEM images. This finding seems to indicate that the kinetics of naproxen release is mainly influenced by the nature of the carrier rather by the size of the crystals.

4.   Conclusions

Supercritical carbon dioxide is an ideal processing medium because of its relatively mild critical conditions and holds a GRAS (generally recognized as safe) status. New processes, such as the one presented here, that partially rely on the replacement
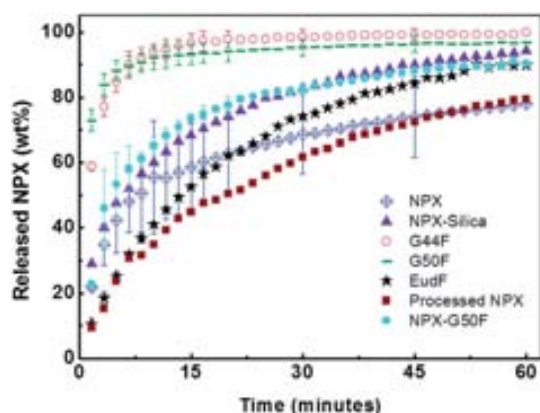

Fig. 8 Drug dissolution profiles at neutral pH (in water + SDS 0.3% w/v) of commercial NPX, and processed NPX, binary formulations: NPX–silica particles and NPX–G50F and ternary formulations: G44F, G50F and EudF. Depicted points are the mean values calculated from two replicates and the error bars are calculated from those replicas.

of organic solvents with $scCO_2$ are of great interest and may result in environmentally friendly options for drug loading and coating processes. Interestingly, we have presented a feasibility study on the use of $scCO_2$ to fabricate three-component (organic–inorganic) homogeneous pharmaceutical formulations which present superior characteristics when compared with a physical mixture of the components. The design of a one-pot process in which the silica free-flow agent is directly introduced in the solution and co-processed promotes the recovery of particulate material, which is difficult to obtain with amorphous or semi-crystalline carriers processed by CO_2. In addition, the ternary formulations with lipid carriers are powders of good flowability and not sticky, which is advantageous for the product manufacturing. Naproxen was chosen as a model drug, the dissolution rate of which was aimed to be enhanced. As excipients, two kind of commercial lipids and a polymer were used. Moreover, silica microparticles were also incorporated into the formulation to restrict the NPX crystal growth and to obtain appropriate micromeritic properties. The morphochemical characteristics of these microcomposites and, particularly, their different release profiles are reported. High drug recovery has been achieved in the three cases. The resulting materials are composed of NPX crystals coated with silica microspheres glued by the lipids or the polymer. None of the components suffered structural or chemical modifications during the processing and naproxen was produced as a crystalline material. Water dissolution of a drug formulation is mainly controlled by the wetting properties of the excipients, by the size of the crystals and by the nature of the excipients. Since NPX crystals become larger when precipitated by CO_2, its dissolution profile is slower than for commercial NPX. Confronting ternary formulation, note that the release is synergetically accelerated, as a consequence of the wettability and dissolution enhancement, in the case of the lipids Gelucire, while for the polymer Eudragit, the formulation follows the same trend as for the naproxen silica binary mixture.

Acknowledgements

References

1 N. Jagadeesh Badu and A. Nangia, Solubility advantage of amorphous drugs and pharmaceutical cocrystals, *Cryst. Growth Des.*, 2011, **11**, 2662–2679.

2 G. L. Amidon, H. Lennernäs, V. P. Shah and J. R. Crison, A theoretical basis for a biopharmaceutic drug classification: the correlation of *in vitro* drug product dissolution and *in vivo* bioavailability, *Pharm. Res.*, 1995, **12**, 413–420.

3 A. Dahan, J. M. Miller and G. L. Amidon, Prediction of solubility and permeability class membership: provisional BCS classification of the world's top oral drugs, *AAPS J.*, 2009, **11**, 740–746.

4 Y. Kawabata, K. Wada, M. Nakatani, S. Yamada and S. Onoue, Formulation design for poorly water-soluble drugs based on biopharmaceutics classification system: basic approaches and practical applications, *Int. J. Pharm.*, 2011, **420**, 1–10.

5 T. Taupitz, J. B. Dressman, C. M. Buchanan and S. Klein, Cyclodextrin-water soluble polymer ternary complexes enhance the solubility and dissolution behavior of poorly soluble drugs. Case example: Itraconazole, *Eur. J. Pharm. Biopharm.*, 2013, **83**, 378–387.

6 S. Nastase, L. Bajenaru, C. Matei, R. A. Mitran and D. Berger, Ordered mesoporous silica and aluminosilicate-type matrix for amikacin delivery systems, *Microporous Mesoporous Mater.*, 2013, **182**, 32–39.

7 Q.-Z. Zhai, Y.-Y. Wu and X.-H. Wang, Synthesis, characterization and sustaining controlled release effect of mesoporous SBA-15/ramipril composite drug, *J. Inclusion Phenom. Macrocyclic Chem.*, 2013, **77**, 113–120.

8 Z. Li, J. C. Barnes, A. Bosoy, J. F. Stoddart and J. I. Zink, Mesoporous silica nanoparticles in biomedical applications, *Chem. Soc. Rev.*, 2012, **41**, 2590–2605.

9 C. Domingo and J. Saurina, An overview of the analytical characterization of nanostructured drug delivery systems: towards green and sustainable pharmaceuticals: a review, *Anal. Chim. Acta*, 2012, **744**, 8–22.

10 A. Tan, S. Rao and C. A. Prestidge, Transforming lipid-based oral drug delivery systems into solid dosage forms: an overview of solid carriers, physicochemical properties, and biopharmaceutical performance, *Pharm. Res.*, 2013, **30**, 2993–3017.

11 B. Chauhan, S. Shimpi and A. Paradkar, Preparation and characterization of etoricoxib solid dispersions using lipid carriers by spray drying techniques, *AAPS PharmSciTech*, 2005, **6**, E405–E412.

12 Y. B. Pawar, H. Purohit, G. R. Valicherla, B. Munjal, S. V. Lale, S. B. Patel and A. K. Bansal, Novel lipid based oral formulation of curcumin: development and optimization by design of experiments approach, *Int. J. Pharm.*, 2012, **436**, 617–623.

13 S. K. Basu and R. Adhiyaman, Preparation and characterization of nitrendipine-loaded Eudragit RL 100 microspheres prepared by an emulsion-solvent evaporation method, *Trop. J. Pharm. Res.*, 2008, **7**, 1033–1041.

14 R. Pignatello, C. Bucolo, G. Spedalieri, A. Maltese and G. Puglisi, Flurbiprofen-loaded acrylate polymer nanosuspensions for ophthalmic application, *Biomaterials*, 2002, **23**, 3247–3255.

15 D. Halamová, M. Badaničová, V. Zeleňák, T. Gondová and U. Vainio, Naproxen drug delivery using periodic mesoporous silica SBA-15, *Appl. Surf. Sci.*, 2010, **256**, 6489–6494.

16 D. Halamová and V. Zeleňák, NSAID naproxen in mesoporous matrix: drug uptake and release properties, *J. Inclusion Phenom. Macrocyclic Chem.*, 2012, **72**, 15–23.

17 D. Carriazo, M. Del Arco, C. Martín, C. Ramos and V. Rives, Influence of the inorganic matrix nature on the sustained release of naproxen, *Microporous Mesoporous Mater.*, 2010, **130**, 229–238.

18 K. Adibkia, Y. Javadzadeh, S. Dastmalchi, G. Mohammadi, F. K. Niri and M. Alaei-Beirami, Naproxen–Eudragit® RS100 nanoparticles: preparation and physicochemical characterization, *Colloids Surf., B*, 2011, **83**, 155–159.

19 M. Maghsoodi, Physicochemical properties of naproxen-loaded microparticles prepared from Eudragit L100, *AAPS PharmSciTech*, 2009, **10**, 120–128.

20 O. Chambin, T. Karbowiak, L. Djebili, V. Jannin, D. Champion, Y. Pourcelot and P. Cayot, Influence of drug polarity upon the solid-state structure and release properties of self-emulsifying, *Colloids Surf., B*, 2009, **71**, 73–78.

21 P. Subra-Paternault, D. Vrel and C. Roy, Coprecipitation on slurry to prepare drug–silica polymer formulations by compressed antisolvent, *J. Supercrit. Fluids*, 2012, **63**, 69–80.

22 B. Chauhan, S. Shimpi and A. Paradkar, Preparation and evaluation of glibenclamide–polyglycolized glycerides solid dispersions with silicon dioxide by spray drying technique, *Eur. J. Pharm. Sci.*, 2005, **26**, 219–230.

23 M.-S. Kim, J.-S. Kim and S.-J. Hwang, Enhancement of wettability and dissolution properties of cilostazol using the supercritical antisolvent process: effect of various additives, *Chem. Pharm. Bull.*, 2010, **58**, 230–233.

24 N. Murillo-Cremaes, A. M. López-Periago, J. Saurina, A. Roig and C. Domingo, A clean and effective supercritical carbon dioxide method for the host–guest synthesis and encapsulation of photoactive molecules in nanoporous matrices, *Green Chem.*, 2010, **12**, 2196–2204.

25 N. Murillo-Cremaes, A. M. López-Periago, J. Saurina, A. Roig and C. Domingo, Nanostructured silica-based drug delivery vehicles for hydrophobic and moisture sensitive drugs, *J. Supercrit. Fluids*, 2013, **73**, 34–42.

26 M. K. Gupta, Y.-C. Tseng, D. Goldman and R. H. Bogner, Hydrogen bonding with adsorbent during storage governs drug dissolution from solid-dispersion granules, *Pharm. Res.*, 2002, **19**, 1663–1672.

27 R. Pignatello, M. Ferro, G. De Guidi, G. Salemi, M. A. Vandelli, S. Guccione, M. Greppi, C. Forte and G. Puglisi, Preparation, characterisation and photosensitivity studies of solid dispersions of diflusanil and Eudragit RS100 and RL100, *Int. J. Pharm.*, 2001, **218**, 27–42.

28 M. Vallet-Regí, L. Ruiz-González, I. Izquierdo-Barba and J. M. González-Calbet, Revisiting silica based ordered mesoporous materials: medical applications, *J. Mater. Chem.*, 2006, **16**, 26–31.

29 A. R. C. Duarte, C. Roy, A. Vega-González, C. M. M. Duarte and P. Subra-Paternault, Preparation of acetazolamide composite microparticles by supercritical anti-solvent techniques, *Int. J. Pharm.*, 2007, **332**, 132–139.

30 P. Subra-Paternault, P. Gueroult, D. Larrouture, S. Massip and M. Marchivie, *Preparation de formulations solides par voie supercritique*, 7° Colloque Sciences et Technolpogie des Poudres (STP2012), Toulouse, 2012.

31 M. Muntó, N. Ventosa, S. Sala and J. Veciana, Solubility behaviors of ibuprofen and naproxen drugs in liquid "CO_2–organic solvent" mixtures, *J. Supercrit. Fluids*, 2008, **47**, 147–153.

32 A. Montes, A. Bendel, R. Kürti, M. D. Gordillo, C. Pereyra and E. J. Martínez de la Ossa, Processing naproxen with supercritical CO_2, *J. Supercrit. Fluids*, 2013, **75**, 21–29.

33 C. Thammawong, P. Sreearunothai, A. Petchsuk, P. Tangboriboonrat, N. Pimpha and P. Opaprakasit, Preparation and characterizations of naproxen-loaded magnetic nanoparticles coated with PLA-*g*-chitosan copolymer, *J. Nanopart. Res.*, 2012, **14**, 1046.

34 R. H. K. Potluri, S. Bandari, R. Jukanti and P. R. Veerareddy, Solubility enhancement and physicochemical characterization of carvedilol solid dispersion with Gelucire 50/13, *Arch. Pharm. Res.*, 2011, **34**, 51–57.

35 D. Wehrung, W. J. Geldenhuys and O. Oyewumi, Effects of Gelucire content on stability, macrophage interaction and blood circulation of nanoparticles engineered from nanoemulsions, *Colloids Surf., B*, 2012, **94**, 259–265.

36 R. M. Martins, S. Siqueira, L. A. Tacon and L. A. P. Freitas, Microstructured ternary solid dispersions to improve carbamazepine solubility, *Powder Tech.*, 2012, **215**, 156–165.

37 B. Albertini, N. Passerini, M. Di Sabatino, D. Monti, S. Burgalassi, P. Chetoni and L. Rodriguez, Poloxamer 407 microspheres for orotransmucosal drug delivery. Part I: formulation, manufacturing and characterization, *Int. J. Pharm.*, 2010, **399**, 71–79.

38 Y. Wang, R. N. Dave and R. Pfeffer, Polymer coating/encapsulation of nanoparticles using a supercritical anti-solvent process, *J. Supercrit. Fluids*, 2004, **28**, 85–99.

39 T. Ozeki, Y. Takashima, T. Nakano, H. Yuasa, M. Kataoka, S. Yamashita, T. Tatsumi and H. Okada, Preparation of spray-dried microparticles using Gelucire 44/14 and porous calcium silicate or spherical microcrystalline cellulose to enhance transport of water-insoluble pranlukast hemihydrate across Caco-2 monolayers, *Adv. Powder Technol.*, 2011, **22**, 623–628.

40 C. Leuner and J. Dressman, Improving drug solubility for oral delivery using solid dispersions, *Eur. J. Pharm. Biopharm.*, 2000, **50**, 47–60.

41 P. H.-L. Tran, T. T.-D. Tran, J. B. Park and B.-J. Lee, Controlled Release Systems Containing Solid Dispersions: Strategies and Mechanisms, *Pharm. Res.*, 2011, **28**, 2353–2378.

ORIGINAL CONTRIBUTION

Compressed antisolvent process for polymer coating of drug-loaded aerogel nanoparticles and study of the release behavior

Nerea Murillo-Cremaes · Pascale Subra-Paternault ·
Javier Saurina · Anna Roig · Concepción Domingo

Abstract The overall objective of the present work was to modulate the release behavior of drug-impregnated silica particles from almost instantaneous release to a more sustained delivery, prolonged during several hours. Triflusal was chosen as a model drug of the low biodisponibility type. The process is based in the coating with Eudragit® RL 100 polymer of aerogel-like silica particles. Materials were processed in compressed CO_2 by using the batch and semicontinuous antisolvent coating methods. Triflusal release from Eudragit-coated aerogel particles was compared with the dissolution profiles recorded for pristine triflusal and for triflusal impregnated into polymer or non-coated aerogel particles. The release profiles were determined by high-performance liquid chromatography. Eudragit-coated materials presented an intermediate drug-release rate between this obtained for the infused polymer and that of the impregnated aerogel particles. Diffusion-governed mechanisms were found for the studied aerogel-like systems after fitting the release data to both Korsmeyer-Peppas and Baker-Lonsdale equations. The major advantage of the compressed CO_2 antisolvent approach was the ability to physically coat very fine particles (<100 nm).

N. Murillo-Cremaes · A. Roig (✉) · C. Domingo (✉)
Institut de Ciència de Materials de Barcelona (CSIC),
Campus de la UAB, 08193 Bellaterra, Spain
e-mail: roig@icmab.es
e-mail: conchi@icmab.es

N. Murillo-Cremaes
e-mail: nmurillo@icmab.es

P. Subra-Paternault (✉)
Université Bordeaux, CBMN UMR 5248, Bat B14 bis,
Allée Geoffroy St Hilaire, 33600 Pessac, France
e-mail: subra@enscbp.fr

J. Saurina
Department of Analytical Chemistry, University of Barcelona,
Martí i Franquès 1-11, 08028 Barcelona, Spain

Moreover, the stability of the studied drug in water increased after coating.

Keywords Supercritical processing · Nanoparticles · Polymers · Controlled release

Introduction

Polymer coating of micro- and nanoparticles is presently a widely used technique for powder processing in various important industries, including pharmaceuticals, food, fertilizers, cosmetics, electronics, etc. [1–3]. Most of the coating materials are natural or synthetic polymers [4–6], but fats, lipids, and waxes can also be used for encapsulation [7–9]. Polymer coating usually modify several physical characteristics of the original material, such as hydrophility, appearance, or mechanical strength. Encapsulation can also result in more uniform particle size distribution, smoother surfaces, and enhanced flowability. Regarding the chemical characteristics, coating aids to protect unstable ingredients from external degradation factors, such as moisture, air, or light, and can enhance compatibility and wettability. In the particular case of controlled drug delivery, encapsulation is used to modulate the release rate of an active pharmaceutical ingredient to the organism. Other advantages attained by coating are better dispersion and deagglomeration, as well as enhanced functionality when coated with specific polymers such as polyethylene glycol that gives amphiphilic character and prevent recognition by the immune system [10, 11]. Many of the marketed polymeric drug delivery carriers are adequate for the sustained release of water-soluble drugs. For low water-solubility drugs, polymeric systems could also exhibit a good response but often release the drug very slowly due to its high hydrophobicity. As an alternative, the relevance in controlled drug delivery of inorganic materials such as silica, titania, or magnetic iron oxide

particles, either alone or combined with polymers in hybrid matrices, is increasing [12–14]. Inorganic porous particles are mostly applied to obtain an immediate drug dosage of poorly water-soluble compounds at the desired target site.

The technologies currently used in the industry for coating solid particles, based on either mechanical movement (agitation) or solid fluidization (Wurster process), mainly involve organic solution chemistry and the use of high temperatures to evaporate the solvent [15–17]. In these processes, the replacement of organic solvents with supercritical and compressed carbon dioxide (CO_2) results in an environmentally friendly option with a near-zero waste production. CO_2 is an ideal processing medium at high pressure, because of its relatively mild critical conditions (31.1 °C and 73.8 bar) and generally recognized as safe (GRAS) status. The applicability of the already known supercritical micronization techniques to coating depends primarily on the solubility of the coating material in compressed CO_2 [18, 19]. In general, compressed CO_2 has a limited solvent strength for many polymers of interest. Hence, most of the work performed in coating using compressed CO_2 has been carried out by antisolvent methods [20, 21] and only a few by polymer precipitation from the solvent, as in the rapid expansion of supercritical solutions (RESS) process [22–25]. In a further evolution, the RESS and the fluidized bed technologies have been combined, using supercritical CO_2 as the fluidizing gas and as a solvent [26–31]. The precipitation from gas saturated solutions (PGSS) process and the co-injection route, in which the supercritical CO_2 is dissolved in a polymer to reduce its melting temperature, are used to coat thermally sensitive compounds [32, 33]. However, individual coating is difficult to achieve using these processes, especially for small-sized particles. In a different approach, particles have been coated by in situ dispersion polymerization in supercritical CO_2 [34, 35]. This coating method has shown excellent results for the encapsulation of fine particles; however, it would be severely limited for drug-coating applications due to residual monomers. Spouted bed technology has recently been applied to coat large micrometric silica aerogel particles [36] and surface-initiated polymerization for the coating of aerogel disks with a hydrogel [37].

In previous works, we reported on the supercritical preparation of impregnated drug delivery systems involving triflusal (Trf) drug, based in either homopolymers [38] or aerogel-like silica matrices [39]. Trf is a drug practically insoluble in water and highly unstable at a neutral and alkaline pH. The in vitro release study demonstrated a sustained release prolonged for several days in the polymeric system [38], while more than 80 % of triflusal was dissolved in the media within the first minutes for the aerogel matrices [39]. In this study, we have extended our background in supercritical and compressed CO_2 impregnation and antisolvent precipitation to the deposition of polymeric thin films of Eudragit® RL 100 on the surface of silica aerogel-like fine particles, either as synthetized or previously impregnated with Trf. Two different types of particulate silica were studied: sub-micron size silica particles (SiO_2 300 nm) [40] and magnetite-silica ($Fe_3O_4@SiO_2$ 65 nm) nanospheres [41].

CO_2 antisolvent approaches have often been successfully applied to the coating of micrometric organic and inorganic particles [10, 42–44], although only in some particular cases they are used for the coating of nanometric particles. For example, the compressed antisolvent coating technique was used for the surface modification of superparamagnetic iron oxide nanoparticles of 10–15 nm diameter [45, 46]. The magnetic particles have been long commercialized as contrast agents for magnetic resonance imaging and are coated to reduce magnetic agglomeration [47]. In our study, the used superparamagnetic Fe_3O_4 nanoparticles embedded as a core into a SiO_2 matrix ($Fe_3O_4@SiO_2$) present low magnetic agglomeration [41]. In this work, both the batch gas antisolvent (GAS) and the semicontinuous precipitation compressed antisolvent (PCA) techniques were used for particle encapsulation. Results showed that particle encapsulation was achieved in both cases. In vitro characterization by high-performance liquid chromatography (HPLC) proved that the deposited coating acted as a drug-release barrier, thus obtaining delivery rates that are in between those attained with polymeric systems and uncoated aerogel particles. Moreover, drug stability in water increased in the hybrid matrix constituted by aerogel particles and polymer with respect to the rest of studied encapsulation systems.

Experimental

Materials

2-Acetyloxy-4-(trifluoromethyl) benzoic acid or triflusal (Trf) was kindly donated by Uriach S.A., Spain. Eudragit® RL 100 amorphous polymer (Evonik Rohm Pharma Polymer, Degussa) was selected as the coating element and was kindly supplied by IMCD, France. It is a copolymer of acrylate and methyl methacrylate with a low content of methacrylic acid ester and quaternary ammonium groups. This polymer is water insoluble, but swellable, with a relatively high permeability that comes from the presence of the ammonium salt. Sub-micron silica aerogel-like particles (AP) and magnetite-silica composite nanoparticles (AP_{Fe}), with diameters of 300 and 65 nm, respectively, were synthesized in our laboratory by hydrolysis and polycondensation of tetramethylorthosilicate (TMOS, 98 %, Sigma-Aldrich) and high temperature supercritical drying, according to the procedures described elsewhere [40, 41]. These particles had a surface area of near 200 m^2 g^{-1} and a pore volume of ca. 0.07 cm^3 g^{-1}. Some AP_{Fe} nanoparticles were impregnated with Trf by a supercritical method, as previously reported [39], thus obtaining Trf@AP_{Fe} nanoparticles. The Trf loading was in the order of ca. 4 wt% of

Trf. Acetone (99.8 wt% purity, VWR) was used to suspend the inorganic nanoparticles and CO_2 (industrial grade, Air Liquid) as the antisolvent.

CO_2 antisolvent processes

First experiments were performed in a GAS home-made batch apparatus, consisting of a 0.5-L autoclave that at the bottom has a membrane filter of 0.22 μm placed on the top of a stainless steel frit (5 μm mesh). The setup is described elsewhere in detail [48, 49]. In the batch approach, compressed CO_2 was introduced into the vessel that contained the acetone suspension of sub-micron silica particles and the dissolved polymer. The vessel was equipped with a stirrer plunged in the solution, thus maintaining the particles in suspension. In a typical GAS experiment, AP and drug were weighed in a mass ratio of 1.1:1.7 (ca. 0.25 g of Trf) and mixed with 40 mL of acetone. The obtained mixture was soaked overnight under mild conditions of stirring, previous to Eudragit addition in a polymer:silica mass ratio of 1:1.1. The temperature of the vessel was controlled by heating jackets and maintained at 26 °C during the polymer precipitation step. Compressed CO_2 was added resulting in a gradual increase of the pressure in the chamber up to 100 bar. After 1 h, the exit valve was opened, and the product was washed at 30 °C with a fresh flow of CO_2.

A second set of experiments, aiming at coating the smallest silica particles (65 nm), was performed using the PCA semicontinuous approach. The equipment is fully described elsewhere [48]. In the PCA technique, the liquid phase involving dispersed silica nanoparticles and a dissolved polymer was sprayed into a continuous feed of CO_2. In the PCA1 experiment, the acetone suspension had concentrations of pre-impregnated Trf@AP$_{Fe}$ and polymer of 4 and 8 mg mL^{-1}, respectively. The mixture was sonicated during 15 min before pumping. In the PCA2 experiment, a weighted amount of Trf calculated to reach a concentration of 6.5 mg mL^{-1} was added to acetone containing dispersed AP$_{Fe}$ particles (5 mg mL^{-1}) and dissolved polymer (20 mg mL^{-1}). The high pressure autoclave was first heated at 30 °C and filled with CO_2 at a pressure of 90 bar, and then, the acetone suspension was sprayed into the vessel at a flow rate of 1.5–2.0 mL min^{-1}. A capillary nozzle (180 μm diameter) was used to deliver the suspension. Liquid CO_2 was continuously pumped to the vessel at a rate of 15–25 g min^{-1} during acetone injection and, afterwards, for 1 h to wash the obtained product. The coated material was recovered on a 5-μm filter overtopped by two membranes of 0.22 μm placed at the bottom of the autoclave.

Characterization

Fourier transform infrared spectroscopy (FTIR, Perkin Elmer Spectrum One instrument) was used to monitor the success of the processing technique by signaling the presence of the different components (Trf, SiO_2, and the polymer). Thermogravimetric analysis (TGA, system NETZSCH-STA 449F1) was used to estimate the percentage of organic components in the recovered products. Morphological characterization was based on scanning (SEM, Hitachi S570) and transmission (TEM, JEOL JEM-1210) electron microscopies. Mean particle size and polydispersity of each system were obtained by using the ImageJ software package, adjusting the particle size histogram obtained from 200 counts in the TEM images to a Gaussian distribution. Drug-release kinetic profiles were monitored using a Trf-established HPLC method described elsewhere [50]. The delivery of the active component was studied at pH 2 in a 0.01 M HCl medium, fixing the stirring rate and temperature at 60 rpm and 37 °C, respectively. Acid pH was chosen to simulate physiological conditions at the stomach. The metabolite of Trf (4-(trifluoromethyl) salicylic acid, HTB) was also quantified. To calculate the amount of impregnated drug, both the Trf and the HTB contributions were considered. The kinetic curves were monitored chromatographically, measuring the UV absorption at 280 nm, to obtain the corresponding delivery profiles. Total loading was obtained from HPLC data at 100 % release.

Results and discussion

The antisolvent process is based on solute precipitation occurring when compressed CO_2 and an organic liquid phase that contains the solute come into contact [51, 52]. The interdiffusion of the organic solvent and CO_2 creates conditions of solute supersaturation in the organic phase, since the newly formed CO_2 solvent mixture exhibits lower solubilization ability than that of the pure solvent. Besides the precipitation of a single specie, the formation of complex mixtures can be also carried out through the CO_2 antisolvent coprecipitation of two or more solutes dissolved in the liquid phase [44, 53]. In the process used in this work, fine aerogel-like particles were suspended in a liquid solution containing the dissolved polymer. The CO_2 addition provoked the precipitation of the polymer embedding the inorganic particles and giving place to hybrid products. The used experimental conditions are shown in Table 1 together with some end-product characteristics. Under working conditions, the process yield was typically below 50 wt%, likely due to the high solubility of Trf and Eudragit in acetone. The yield was also reduced due to the nanometric character of the inorganic nanoparticles that could easily bypass the used filter at the bottom of the reactor. Moreover, Trf has a relatively high solubility in compressed and supercritical CO_2. For instance, a mole fraction of 3×10^{-2} was measured at 200 bar and 35 °C [38]. Experiments were performed at temperature lower than the critical temperature

Table 1 Composition of the processed slurry and recovered powder, in regard to polymer, silica matrix, and triflusal drug, for the performed antisolvent experiments

| Sample	Matrix composition before coating		Slurry composition	Composition of as-recovered samples		
	Silica aerogel	Trf (wt%)	Eudragit:silica:Trf ratio [mg mL^{-1}]	Silica (wt%)	Trf (wt%)	Eudragit (wt%)
GAS1	AP	0	1:1.1:1.7	60	1	39
PCA1	Trf@AP$_{Fe}$	4.1	1:0.5:0.05	43	1	56
PCA2	AP$_{Fe}$	0	1:0.25:0.3	47	2	51

of CO_2 to reduce drug solubility in the solvent mixture and to prevent polymer swelling in the liquid phase. Organic compounds solubility in CO_2+solvent mixtures increase generally with temperature [51, 54], thus processing at low temperature reduced the risk of losing the Trf drug by dissolution. Regarding the mixing behavior of the solvent and CO_2, 3D simulation showed that the mixing plume did not differ notably in the interval from 25 to 45 °C, since convection and not diffusion is the mechanism that dominates mass transfer [51].

When performing the PCA experiments, a part of the coated material was found stacked to the filter as a cake due to the continuous flow. The rest of the product was recovered from the body of the reactor as a free-flowing powder. In Fig. 1a, a SEM picture of the filter cake product is shown, in which aggregates of nanoparticles entrapped in a polymeric

mass can be observed. SEM (Fig. 1b) and TEM (Fig. 1c) characterization of the as-recovered flowing powder for the PCA1 experiment showed that it consisted of small-agglomerated entities immersed in a continuous polymer film. The flowing powder can be further dispersed by rinsing it with a minimum amount of a proper solvent (acetone, ethanol, or methanol) to eliminate the excess of polymer (Fig. 1d). A liquid solvent washing of the excess polymer was not strictly necessary for controlled drug delivery applications; however, it was considered desirable to reduce particle aggregation while still having a polymer coating, as was later confirmed by FTIR and TGA measurements.

Batch GAS approach was applied to modify the surface of the 300-nm AP particles. The feasibility of this precipitation-

Fig. 1 Images of the collected product from experiment PCA1: SEM pictures of **a** the cake and **b** the as-recovered powder, and TEM images of the flowing powder **c** as-recovered and **d** after rinsing it with methanol
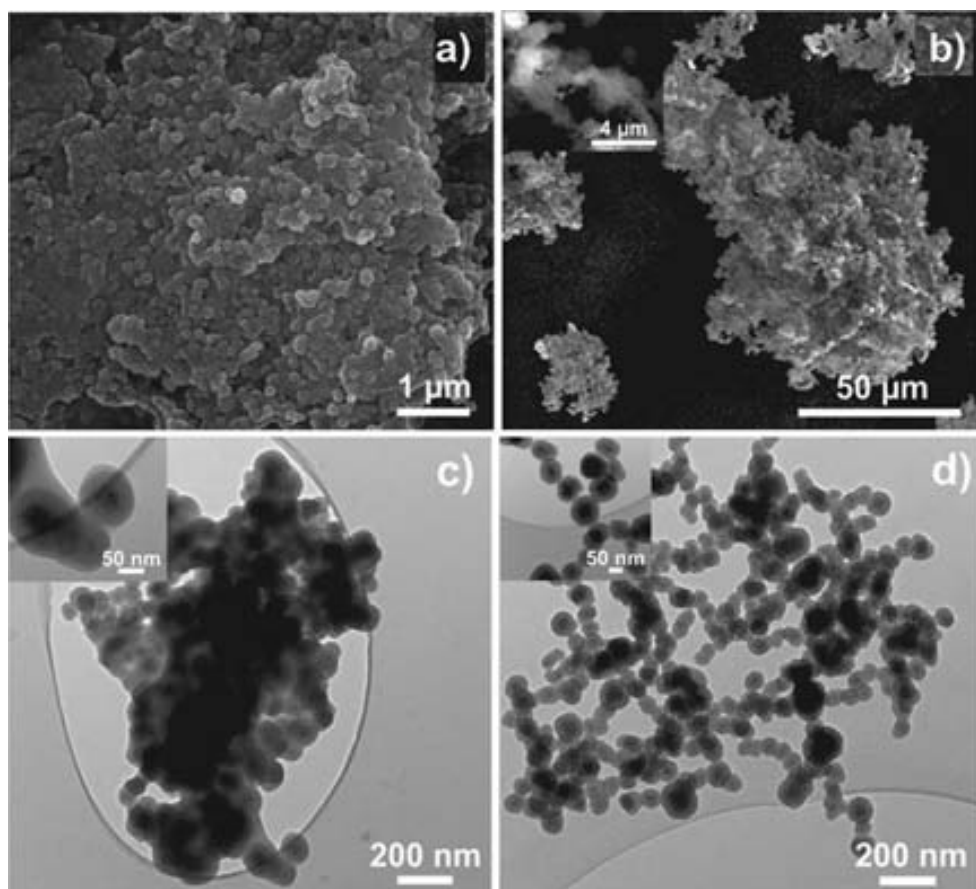
on-slurry technique has been demonstrated previously for micrometric particles [49]. This approach was selected preferably to the semicontinuous PCA mode to coat the largest silica particles that are difficult to pump avoiding sedimentation. The PCA approach could be applied only for the coating of the nanometric 65-nm AP_{Fe} particles, avoiding flow instabilities and nozzle plugging occurring when pumping large particles. For Trf pre-impregnated samples, it was observed that the drug loading was reduced after antisolvent processing, likely due to partial dissolution of the drug in both the compressed CO_2 and in the liquid phase. To avoid this problem, GAS experiments were performed starting from a non-impregnated AP sample that was soaked overnight with a solution of Trf in acetone (GAS1 experiment). The performed soaking step was envisioned as a way to infiltrate the drug into the silica pores [55]. Using the PCA approach, samples were prepared either directly from a triflusal pre-impregnated material, Trf@AP_{Fe}, (PCA1 experiment) or by first soaking pristine AP_{Fe} nanoparticles in acetone with Trf overnight (PCA2 experiment).

Sample composition

FTIR spectroscopy was used to monitor the presence of the different components in the precipitated products involving Trf drug, silica matrix, and Eudragit polymer as a coating agent. The spectra of the different products obtained following the different antisolvent routes are shown in Fig. 2. The as-recovered samples were rinsed with methanol before analysis. The most distinctive band in the spectrum of Eudragit was the C=O vibration appearing at ca. 1,725 cm^{-1}. Moreover, the spectra of the polymer exhibited the characteristic bands of the asymmetric and symmetric alkyl stretching modes at 2,990 and 2,950 cm^{-1}, respectively. The corresponding absorbance of bending vibrations was shown as a shoulder at ca. 1,480 cm^{-1} and as two peaks at ca. 1,445 and 1,385 cm^{-1}. For all the studied silica matrices, intense absorption bands
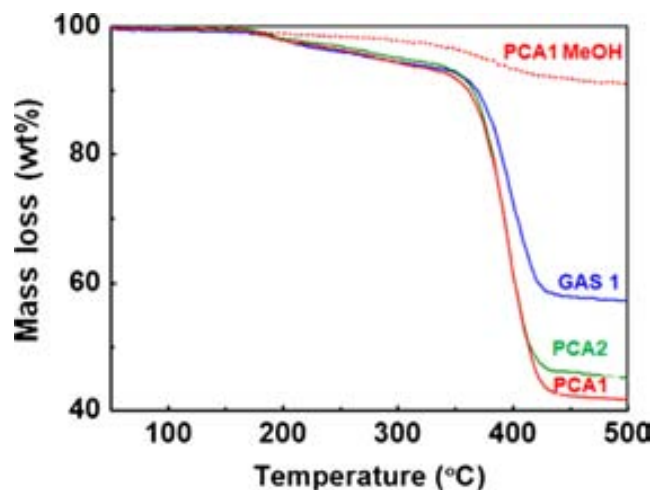
Fig. 3 Thermal analysis of the as-recovered-coated powder in the GAS1, PCA1, and PCA2 experiments, and sample PCA1 also after rinsing it with methanol (PCA1 MeOH)

appeared in the 900–1,200 cm^{-1} region, which corresponded to the stretching vibrations of the O–Si–O bond in the SiO_4 tetrahedrons of the aerogel skeleton. The band at 1,620–1,630 cm^{-1} was due to the bending frequency of molecular water adsorbed in the silica. The broad band from the free O–H stretching vibration was observed in the range of 3,600–3,100 cm^{-1}. The useful FTIR region of solid Trf/HTB contained bands at 1,770 and 1,685 cm^{-1} corresponding to the carbonyls (C=O). The presence of Trf in the coated matrices was difficult to assess, due to the low percentage of drug in the samples. However, for some samples, the Trf could be tentatively monitored by the C=O band of the ester appearing at a frequency near 1,770 cm^{-1}, as a shoulder of the more intense carbonyl band associated to the polymer occurring at a slightly higher frequency (1,725 cm^{-1}).

The quantification of the organic and inorganic phases was performed by sample pyrolysis using TGA analysis (Fig. 3). The thermogravimetric curves obtained indicated that Eudragit polymer decomposed in the temperature interval 350–430 °C. The lost of Trf occurred in the range 150–350 °C. However, the amount of Trf in the samples was too small to be quantified following this procedure. The residue lasting after heating up to 450 °C was assigned to the
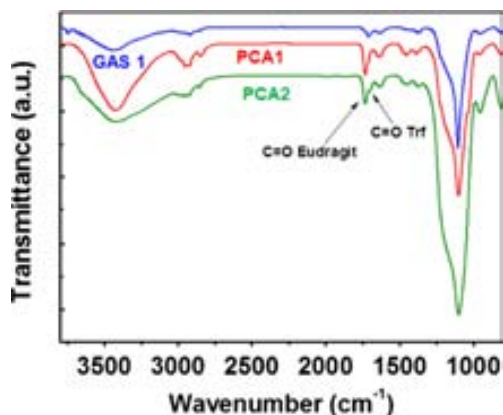

Fig. 2 FTIR spectroscopic analysis of the Eudragit-coated products, indicating the C=O carbonyl functionality for the polymer and, tentatively, also for the drug
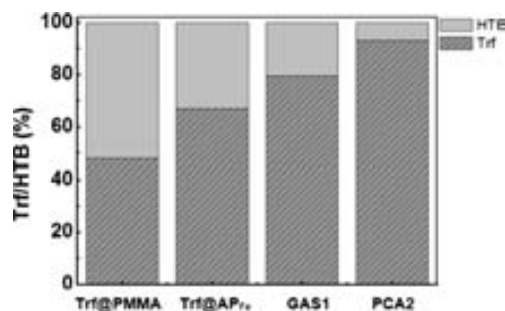

Fig. 4 Percentage of Trf and HTB in the studied matrices after 6 months of storage

inorganic phase. In the GAS1 sample, the percentage value of the residue at 450 °C corresponded to ca. 60 wt% of the total composite mass, while in the PCA precipitated products, this percentage was reduced to values of less than 50 wt%. After rinsing PCA1 sample with methanol, the percentage of polymer was reduced to values of 10–20 wt%.

The preservation of the Trf form, in terms of hydrolysis to HTB, inside the silica matrices during preparation and storage was studied and compared with the behavior observed for the pure drug, the Trf@AP$_{Fe}$ sample before coating and with a polymeric system involving Trf impregnated in polymethylmethacrylate particles (sample Trf@PMMA). The transformation was evaluated after 6 months of storing the samples under ambient conditions, i.e., 21 °C and 60–65 % relative humidity [39]. The amount of either Trf or HTB was determined from the corresponding chromatographic peaks at the initial stages of the release. Figure 4 shows that the Trf transformation for the different samples was of more

Fig. 5 TEM images of the following: **a** pristine AP particles, **b** as-recovered GAS1 sample, **c** GAS1 sample rinsed with methanol, **d** pristine AP$_{Fe}$ nanoparticles, **e** as-recovered PCA2 sample, and **f** PCA2 sample rinsed with methanol
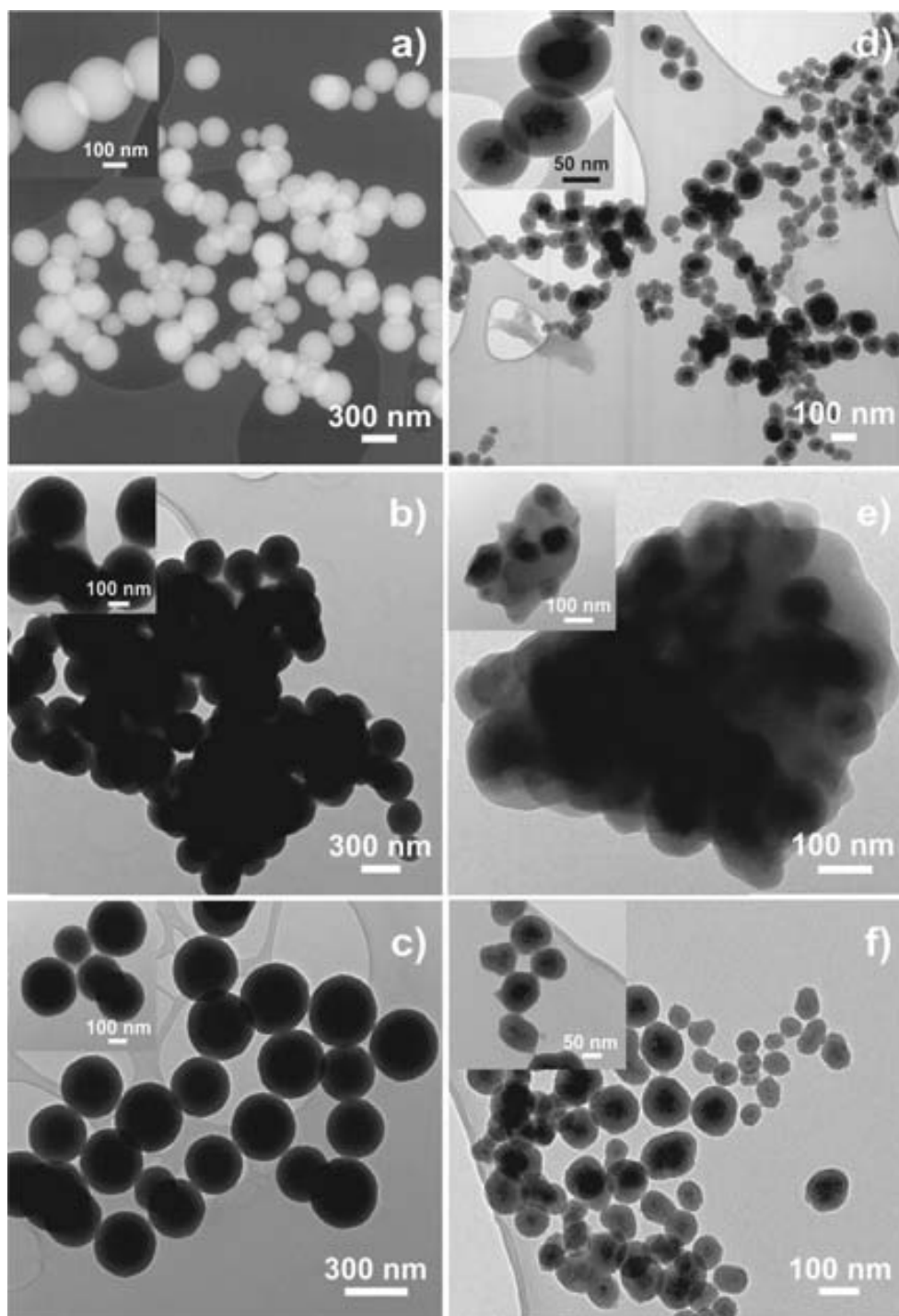
than 50 % for the PMMA-based matrix to less than 5 % for the Eudragit-coated AP_{Fe} particles. An intermediate situation was observed for the uncoated $Trf@AP_{Fe}$ and Eudragit-coated AP samples, which had hydrolysis degrees of 20–30 %. In principle, the preservation of the ester form present in non-hydrolyzed Trf could be presumed for hydrophobic polymeric matrices. However, hydrophilic environments, such as the one existent inside of the pores of the silica aerogel-like particles, preserved the water-sensitive drug more efficiently than the PMMA beads. This finding was attributed to the acidity that silica materials provided to the adsorbed water. Trf is a drug with a relatively high stability in acid media [50]. After impregnation, the PMMA matrix would have an internal porosity induced by CO_2 swelling [38]. This feature allowed the incorporation of neutral water to the matrix, which led to a high hydrolysis degree of the Trf drug. For the inorganic particles, the coating with Eudragit likely avoided the diffusion of water into the material, minimizing the subsequent drug hydrolysis.

Sample morphology

The bare AP matrix consisted of spherical fine particles of 300-nm mean diameter with a 9 % polydispersity (Fig. 5a). The inset in Fig. 5a evidences that the spheres were not aggregated, and necking between them were not observed. After GAS precipitation, the as-recovered particles were clearly embedded in a continuous mass of polymer (Fig. 5b). The thickness of the polymer film could be reduced by rinsing the sample with methanol (Fig. 5c), thus producing an easily flowable-coated powder. The presence of the polymer after rinsing was not easily seen in the images, and only a thin layer of the organic material connecting the particles was visible (see the inset in Fig. 5c).

The AP_{Fe} particulate matrix was characterized by a mean diameter of 65 nm and 20 % size dispersion (Fig. 5d). The nanocomposite was constituted by a core of magnetite nanoparticles (ca. 6 nm diameter) surrounded by a shell of porous silica. This core/shell structure is easily distinguishable in the image inset of Fig. 5d. After loading with Trf, the particles did not show morphological differences (image not shown). Similar behavior to that explained for GAS1 sample was observed for PCA1 and 2 samples. The PCA coating process produced particles embedded in a polymer mass (Fig. 5e), which was partially eliminated with methanol giving place to almost individually coated particles (Fig. 5f). The polymer can be still observed as a thin layer that covers and attaches the nanoparticles together (inset of Fig. 5f).
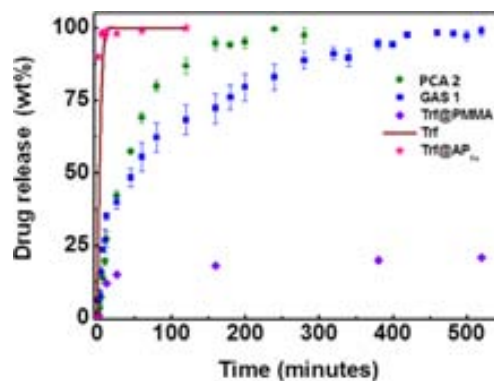

Fig. 6 Drug delivery profiles for pure Trf (*solid line*), Trf pre-impregnated PMMA (Trf@PMMA), and AP_{Fe} (Trf@AP_{Fe}) samples, and powder recovered from GAS1 and PCA2 experiments

Drug-release profiles

The percentage of drug loaded in each as-recovered powder was determined by HPLC (Table 1). Obtained values were in the order of 1 wt% for GAS1 and PCA1 samples and of 2 wt% for PCA2 sample. For samples GAS1 and PCA2, release kinetics were followed under gastric pH conditions (Fig. 6). The carboxylic acid of the Trf molecule is protonated at the acid stomach pH, and the drug is completely absorbed before reaching the intestine. Drug dissolution profile of pure Trf is also shown in the figure for comparison, together with the Trf release curves of samples Trf@AP_{Fe} and Trf@PMMA. For uncoated silica aerogel nanospheres (Trf@AP_{Fe}), the drug release in acidic pH occurred almost instantaneously, and 95 % of the drug was dissolved within the first minute. At pH=2, pure triflusal was fully dissolved in a period of 15 min. In contrast, the slowest release kinetics was obtained for the sample Trf@PMMA. In this case, the delivery of Trf from the sample to gastric medium lasted several days, having only the 18 % released in the first 60 min. The measured drug delivery profiles of the coated samples GAS1 and PCA2 were intermediate between those of Trf@AP_{Fe} (fastest kinetics) and Trf@PMMA (slowest kinetics). For coated samples, ca. 25 % of the drug was dissolved during the first 10 min, and a progressive release of the remaining 75 % occurred during the next 5–8 h. For instance, at 60 min, the released percentages were of 55 and 70 % for GAS1 and PCA2 samples, respectively. Reasons of prolonged released in the coated systems were related to the necessity of swelling the polymer before diffusion

Table 2 Release parameters estimated from the fits of the experimental data to the Korsmeyer-Peppas model for samples GAS1 and PCA2

Sample	R^2	n	a (h^{-n})
GAS1	0.9838	0.49	0.55
PCA2	0.9965	0.42	0.92

and the long diffusion channels that the drug molecules have to follow to reach the bulk solution.

To better understand the mechanism of the drug delivery from the Eudragit-coated aerogel-like silica nanoparticles, the release data was fitted in the light of two different mathematical models. The first one, the Korsmeyer-Peppas model [56, 57], is a simple semi-empirical model which follows Eq. (1) and includes the possibility of a burst effect:

$$\frac{M_t}{M_\infty} = at^n + b \tag{1}$$

where M_t represents the amount of the drug released at time t; M_∞, the total amount of drug released over a long period of time (it is considered equivalent to the drug loading); a, the kinetics constant that is related to structural and geometrical characteristics of the carrier; t, the elapsed time; n, the release exponent, indicative of the drug-release mechanism; and b, the parameter that introduces the burst effect. This model is commonly used to describe the drug release from polymeric systems and when the kinetics of the process is unknown. The second model is the Baker-Lonsdale [57] that interprets the diffusion of the drug from a spherical matrix, being adjusted to the expression shown in Eq. (2):

$$f_i = \frac{3}{2}\left[1-\left(1-\frac{M_t}{M_\infty}\right)^{2/3}\right] - \frac{M_t}{M_\infty} = kt \tag{2}$$

where M_t is the drug-released amount at time t and M_∞ is the amount of drug released at an infinite time. For a heterogeneous system with structural features that influence the drug discharge mechanism, k can be written as depicted in Eq. (3):

$$k = \frac{3D_f K C_{fs}}{r_0^2 \tau} \tag{3}$$

being D_f the diffusion coefficient, K the drug specific volume, C_{fs} the drug solubility in the liquid surrounding the matrix, r_0

the radius of the spherical matrix, and τ the tortuosity factor of the system. The use of this approach requires the total drug loading to be greater than its solubility in the matrix.

The dissolution data of drug for samples GAS1 and PCA2 were both fitted to Eq. (1) and for sample GAS1 also to Eq. (2). For Eq. (1), only the first 60 % of the cumulative release points was considered, as the Korsmeyer-Peppas model demands. Correlation coefficients (R^2) were employed to evaluate the quality of the fit. In Table 2, the "n" values, the kinetic constants and the correlation coefficients resulting from fitting the curves with the Korsmeyer-Peppas equation are presented" for clarity sake of the text. On the basis of this model, reasonable values of R^2 were obtained, especially for the case of PCA2 sample (0.9965). In addition, the n exponents were determined to be equal to 0.42 and 0.49 and the kinetic constants to 0.92 and 0.55 for PCA2 and GAS1 samples, respectively (see Fig. 7a, b). According to these results, the drug was released by a Fickian diffusion mechanism in PCA2 sample. The sample GAS1 did not seem to be governed by a Fick's law [58] but could be described by anomalous transport, as Peppas et al. determined for spherical polymeric matrices [59]. The release data of GAS1 sample was also fitted to the Baker-Lonsdale equation, obtaining a correlation coefficient value of 0.9888 (Fig. 7c).

Conclusions

Compressed CO_2 antisolvent route was here presented as a versatile approach for coating fine particles and preparing hybrid composites made of aerogel-like particles, a polymeric coating, and an active pharmaceutical ingredient. For relatively large particles (300 nm), the coating was based on mixing an acetone slurry of aerogel nanoparticles and dissolved polymer with pressurized CO_2 in a batch antisolvent mode (GAS method). A semicontinuous antisolvent mode (PCA method) could be applied to encapsulate nanometric aerogel particles

Fig. 7 Drug-release data fitted with the Korsmeyer-Peppas equation for the following: a PCA2 and b GAS1 samples, and with the Baker-Lonsdale equation for c GAS1 formulation. Symbols correspond to experimental data and solid lines to fitted profiles
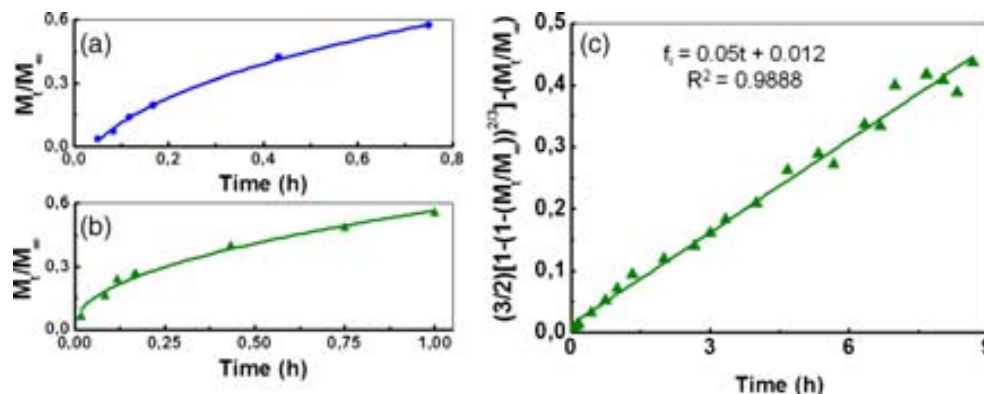
(65 nm). The coating was performed without any prefunctionalization of the surface of the silica nanoparticles, although, in some cases, they were supercritically pre-impregnated with the therapeutic agent. Our results showed that sub-micron and nanometric porous silica particles were successfully coated by the polymer Eudragit forming loose agglomerates while simultaneously incorporating the drug. At low pH, triflusal-loaded aerogel nanoparticles released almost 100 % of the drug in the first 5 min, whereas coating with Eudragit enabled a significant reduction to less than 25 % in the first 10 min and prolonging further the release to several hours. In addition, the kinetics of the release was shown to obey the Baker-Lonsdale model indicating a diffusion-controlled delivery of the drug for the sample obtained using the GAS method and the Korsmeyer-Peppas model for the sample prepared by PCA, exhibiting a Fickian diffusional mechanism. Compressed CO_2 antisolvent processes are environmentally friendly techniques for fine particles encapsulation/coating with diverse solutes, which have applications as high-added-value pharmaceutical products in relation with their surface chemistry and delivery characteristics.

References

1. Feng W, Patel SH, Young M-Y, Zunino JL III, Xanthos M (2007) Smart polymeric coatings-recent advances. Adv Polym Technol 26: 1–13
2. Aguirre M, Paulis M, Leiza JR (2013) UV screening clear coats based on encapsulated CeO_2 hybrid latexes. J Mater Chem A 1: 3155–3162
3. Nam J, Won N, Bang J, Jin H, Park J, Jung S, Jung S, Park Y, Kim S (2013) Surface engineering of inorganic nanoparticles for imaging and therapy. Adv Drug Deliv Rev 65:622–648
4. Yan FY, Gross KA, Simon GP, Berndt CC (2003) Peel-strength behavior of bilayer thermal-sprayed polymer coatings. J Appl Polym Sci 88:214–226
5. Skirtach AG, Volodkin DV, Möhwald H (2010) Bio-interfaces-interaction of PLL/HA thick films with nanoparticles and microcapsules. Chem Phys Chem 11:822–829
6. Leyton P, Domingo C, Sanchez-Cortes S, Campos-Vallette M, Garcia-Ramos JV (2005) Surface enhanced vibrational (IR and Raman) spectroscopy in the design of chemosensors based on ester functionalized p-tert-butylcalix[4]arene hosts. Langmuir 21:11814–11820
7. Gomes JFPS, Rocha S, Do Carmo Pereira M, Peres I, Moreno S, Toca-Herrera J, Coelho MAN (2010) Lipid/particle assemblies based on maltodextrin-gum arabic core as bio-carriers. Colloids Surf B: Biointerfaces 76:449–455
8. SarkarR PP, Mahato M, Kamilya T, Chaudhuri A, Talapatra GB (2010) On the origin of iron-oxide nanoparticle formation using phospholipid membrane template. Colloids Surf B: Biointerfaces 79:384–389
9. Vezzù K, Campolmi C, Bertucco A (2009) Production of lipid microparticles magnetically active by a supercritical fluid-based process. Int J Chem Eng 781247:1–9
10. Marre S, Cansell F, Aymonier C (2008) Tailor-made surface properties of particles with a hydrophilic or hydrophobic polymer shell mediated by supercritical CO_2. Langmuir 24:252–258
11. Orts-Gil G, Natte K, Thiermann R, Girod M, Rades S, Kalbe H, Thünemann AF, Maskos M, Österle W (2013) On the role of surface composition and curvature on biointerface formation and colloidal stability of nanoparticles in a protein-rich model system. Colloids Surf B: Biointerfaces 108:110–119
12. Roca AG, Costo R, Rebolledo AF, Veintemillas-Verdaguer S, Tartaj P, González-Carreño T, Morales MP, Serna CJ (2009) Progress in the preparation of magnetic nanoparticles for applications in biomedicine. J Phys D Appl Phys 42:224002
13. Sanchez C, Belleville P, Popall M, Nicole L (2011) Applications of advanced hybrid organic–inorganic nanomaterials: from laboratory to market. Chem Soc Rev 40:696–753
14. Murakami T, Tsuchida K (2008) Recent advances in inorganic nanoparticle-based drug delivery systems. Mini-Rev Med Chem 8: 175–183
15. Domingo C, Saurina J (2012) An overview of the analytical characterization of nanostructured drug delivery systems: towards green and sustainable pharmaceuticals. Anal Chim Acta 744:8–22
16. Fan J, Chen S, Gao Y (2013) Coating of gold nanoparticles with peptide molecules via a peptide elongation approach. Colloids Surf B: Biointerfaces 28:199–207
17. Ebrahiminezhad A, Ghasemi Y, Rasoul-Amini S, Barar J, Davaran S (2013) Preparation of novel magnetic fluorescent nanoparticles using amino acids. Colloids Surf B: Biointerfaces 102:534–539
18. Domingo C, Vega A, Fanovich MA, Elvira C, Subra P (2003) Behavior of poly(methyl methacrylate)-based systems in supercritical CO_2 and CO_2 plus cosolvent: solubility measurements and process assessment. J Appl Polym Sci 90:3652–3659
19. Roy C, Vega-González A, García-González CA, Tassaing T, Domingo C, Subra-Paternault P (2010) Assessment of $scCO_2$ techniques for surface modification of micro- and nanoparticles: process design methodology based on solubility. J Supercrit Fluids 54:362–368
20. Cansell F, Aymonier C (2009) Design of functional nanostructured materials using supercritical fluids. J Supercrit Fluids 47:508–516
21. Seremeta KP, Chiappetta DA, Sosnik A (2013) Poly(ε-caprolactone). Eudragit® RS 100 and poly(ε-caprolactone)/Eudragit® RS 100 blend submicron particles for the sustained release of the antiretroviral efavirenz. Colloids Surf B: Biointerfaces 102:441–449
22. Kim J-H, Paxton TE, Tomasko DL (1996) Microencapsulation of naproxen using rapid expansion of supercritical solutions. Biotechnol Prog 12:650–661
23. Mishima K, Matsuyama K, Tanabe D, Yamauchi S, Young TJ, Johnston KP (2000) Microencapsulation of proteins by rapid expansion of supercritical solution with a nonsolvent. AIChE J 46:857–865
24. Glebov EM, Yuan L, Krishtopa LG, Usov OM, Krasnoperov LN (2001) Coating of metal powders with polymers in supercritical carbon dioxide. Ind Eng Chem Res 40:4058–4068
25. Ovaskainen L, Rodriguez-Meizoso I, Birkin NA, Howdle SM, Gedde U, Wa gberg L, Turner C (2013) Towards superhydrophobic coatings made by non-fluorinated polymers sprayed from a supercritical solution. J Supercrit Fluids 77:134–141
26. Vogt C, Schreiber R, Werther J, Brunner G (2004) Coating of particles in a fluidized bed operated at supercritical fluid conditions. Chem Eng Technol 27:943–945
27. Tsutsumi A, Nakamoto S, Mineo T, Yoshida K (1995) A novel fluidized-bed coating of fine particles by rapid expansion of supercritical fluid solutions. Powder Technol 85:275–278

28. Wang TJ, Tsutsumi A, Hasegawa H, Mineo T (2001) Mechanism of particle coating granulation with RESS process in a fluidized bed. Powd Technol 118:229–235

29. Kröber H, Teipel U (2005) Microencapsulation of particles using supercritical carbon dioxide. Chem Eng Process 44:215–219

30. Rodríguez-Rojo S, Marienfeld J, Cocero MJ (2008) RESS process in coating applications in a high pressure fluidized bed environment: bottom and top spray experiments. Chem Eng J 144:531–539

31. López-Periago AM, Vega A, Subra P, Arguemí A, Saurina J, García-González CA, Domingo C (2008) Supercritical CO_2 processing of polymers for the production of materials with applications in tissue engineering and drug delivery. J Mater Sci 43:1939–1947

32. Calderone M, Rodier E, Lochard H, Marciacq F, Fages J (2008) A new supercritical co-injection process to coat microparticles. Chem Eng Process 47:2228–2237

33. García-González CA, Sampaio da Sousa AR, Argemí A, López Periago AM, Saurina J, Duarte CMM, Domingo C (2009) Production of hybrid lipid-based particles loaded with inorganic nanoparticles and active compounds for prolonged topical release. Int J Pharm 382:296–304

34. Yue B, Yang J, Wang Y, Huang C-Y, Dave R, Pfeffer R (2004) Particle encapsulation with polymers via in situ polymerization in supercritical CO_2. Powd Technol 146:32–45

35. Lock EH, Merchan-Merchan W, D'Arcy J, Saveliev AV, Kennedy LA (2007) Coating of inner and outer carbon nanotube surfaces with polymers in supercritical CO_2. J Phys Chem C 111:13655–13658

36. Alnaief M, Antonyuk S, Hentzschel CM, Leopold CS, Heinrich S, Smirnova I (2012) A novel process for coating of silica aerogel microspheres for controlled drug release applications. Microporous Mesoporous Mater 160:167–173

37. Giray S, Bal T, Kartal AM, Kizilel S, Erkey C (2012) Controlled drug delivery through a novel PEG hydrogel encapsulated silica aerogel system. J Biomed Mater Res 100A:1307–1315

38. López-Periago AM, Argemí A, Andanson JM, Fernández V, García-González CA, Kazarian SG, Saurina J, Domingo C (2009) Impregnation of a biocompatible polymer aided by supercritical CO_2: evaluation of drug stability and drug-matrix interactions. J Supercrit Fluids 48:56–63

39. Murillo-Cremaes N, López-Periago AM, Saurina J, Roig A, Domingo C (2013) Nanostructured silica-based drug delivery vehicles for hydrophobic and moisture sensitive drugs. J Supercrit Fluids 73:34–42

40. Moner-Girona M, Roig A, Molins E (2003) Sol–gel route to direct formation of silica aerogel microparticles using supercritical solvents. J Sol–gel Sci Technol 26:645–649

41. Taboada E, Solanas R, Rodríguez E, Weissleder R, Roig A (2009) Supercritical-fluid-assisted one-pot synthesis of biocompatible core(γ-Fe$_2$O$_3$)/Shell(SiO$_2$) nanoparticles as high reflexivity T2-constrast agents for magnetic resonance imaging. Adv Funct Mater 19:2319–2324

42. García-González CA, Vega-González A, López-Periago AM, Subra-Paternault P, Domingo C (2009) Composite fibrous biomaterials for tissue engineering obtained using a supercritical CO_2 antisolvent process. Acta Biomater 5:1094–1103

43. Wang Y, Dave RN, Pfeffer R (2004) Polymer coating/encapsulation of nanoparticles using a supercritical anti-solvent process. J Supercrit Fluids 28:85–99

44. Wang Y, Pfeffer R, Dave RN (2005) Polymer encapsulation of fine particles by a supercritical antisolvent process. AIChE J 51:440–455

45. Chen A-Z, Kang Y-Q, Pu X-M, Yin G-F, Li Y, Hu J-Y (2009) Development of Fe$_3$O$_4$-poly(L-lactide) magnetic microparticles in supercritical CO_2. J Colloid Interface Sci 330:317–322

46. Adami R, Reverchon E (2012) Composite polymer-Fe$_3$O$_4$ microparticles for biomedical applications, produced by supercritical assisted atomization. Powd Technol 218:102–108

47. Barbé C, Bartlett J, Kong L, Finnie K, Lin HQ, Larkin M, Calleja S, Bush A, Calleja G (2004) Silica particles: a novel drug delivery system. Adv Mater 16:1959–1966

48. Duarte ARC, Roy C, Vega-González A, Duarte AMM, Subra-Paternault P (2007) Preparation of acetazolamide composite microparticles by supercritical anti-solvent techniques. Int J Pharm 332:132–139

49. Subra-Paternault P, Vrel D, Roy C (2012) Coprecipitation on slurry to prepare drug-silica-polymer formulations by compressed antisolvent. J Supercrit Fluids 63:69–80

50. Argemí A, López-Periago AM, Domingo C, Saurina J (2008) Spectroscopic and chromatographic characterization of triflusal delivery systems prepared by using supercritical impregnation technologies. J Pharm Biomed Anal 46:456–462

51. Erriguible A, Laugier S, Laté M, Subra-Paternault P (2013) Effect of pressure and non-isothermal injection on re-crystallization by CO_2 antisolvent: solubility measurements, simulation of mixing and experiments. J Supercrit Fluids 76:115–125

52. Kikic I, De Zordi N, Moneghini M, Solinas D (2010) Solubility estimation of drugs in ternary systems of interest for the antisolvent precipitation processes. J Supercrit Fluids 55:616–622

53. Yeo S-D, Kiran E (2005) Formation of polymer particles with supercritical fluids: a review. J Supercrit Fluids 34:287–308

54. Revelli AL, Laugier S, Erriguible A, Subra-Paternault P (2014) High-pressure solubility of naproxen, nicotinamide and their mixture in acetone with supercritical CO_2 as anti-solvent. Fluid Phase Eq 373:29–33

55. Xu Y, Qu F, Wang Y, Lin H, Wu X, Jin Y (2011) Construction of a novel pH-sensitive drug release system from mesoporous silica tablets coated with Eudragit. Solid State Sci 13:641–646

56. Kim H, Fassihi R (1997) Application of binary polymer system in drug release rate modulation. 2. Influence of formulation variables and hydrodynamic conditions on release kinetics. J Pharm Sci 86:323–328

57. Costa P, Sousa Lobo JM (2001) Modeling and comparison of dissolution profiles. Eur J Pharm Sci 13:123–133

58. Guo R, Li L-L, Yang H, Zhang M-J, Fang C-J, Zhang T-L, Zhang Y-B, Cui G-H, Peng S-Q, Feng W, Yan C-H (2012) Tuning kinetics of controlled-release in disulfide-linked MSN-folate conjugates with different fabrications procedures. Mater Lett 66:79–82

59. Siepmann J, Peppas NA (2001) Modelling of drug release from delivery systems based on hydroxypropyl methylcellulose (HPMC). Adv Drug Deliv Rev 48:139–157

A Novel Solventless Coating Method to Graft Low-Molecular Weight Polyethyleneimine on Silica Fine Powders

Nerea Murillo-Cremaes,[1] Pedro López-Aranguren,[1,2] Lourdes F. Vega,[2,3] Javier Saurina,[4] Anna Roig,[1] Concepción Domingo[1]

[1]Institut de Ciència de Materials de Barcelona (CSIC), Campus de la UAB, 08193 Bellaterra, Spain
[2]MATGAS Research Center, Campus de la UAB, 08193 Bellaterra, Spain
[3]Carburos Metálicos, Air Products Group, c/Aragón 300, 08009 Barcelona, Spain
[4]Department of Analytical Chemistry, University of Barcelona, Martí i Franquès 1–11, 08028 Barcelona, Spain
Correspondence to: C. Domingo (E-mail: conchi@icmab.es) or A. Roig (E-mail: roig@icmab.es)

ABSTRACT: The overall objective of the present study was to modulate the surface characteristics of aerogel-like submicron and nanometric particles by coating them with polyethyleneimine (PEI) to suit specific biological applications. A new process for the covalent grafting of low-molecular weight PEI chains has been described, based on the use of compressed CO_2 as the initiator of the ring opening polymerization of the ethyleneimine monomer, which was performed in the presence of silica particles. Coating was done at low pressure and temperature and in the absence of any organic solvent. Obtained materials were compared with a product prepared following the standard soaking procedure for PEI coating. Materials were characterized regarding composition, structure, surface charge, particle size, morphology, and drug release. The developed process led to the covalent grafting of low-molecular weight PEI on the silica surface, which conferred an increased thermal stability for the coating and low cytotoxicity to the particles. © 2014 Wiley Periodicals, Inc. J. Polym. Sci., Part A: Polym. Chem. 2014, 52, 2760–2768

KEYWORDS: aziridine; compressed CO_2; polyethyleneimine; ring opening; silica particles

INTRODUCTION Polymer coating of micro and nanoparticles is a widely used approach for powder processing in the pharmaceutical industry.[1,2] Coating can modify several physicochemical characteristics of the original material, such as, its hydrophilic character or its degradation rate. There are many different biocompatible polymers that can potentially be used in the preparation of pharmaceutical systems. They include both naturally derived and synthetic materials. Coatings with natural polymers encompass hydrophilic carbohydrates (dextran, starch), hydrophilic proteins (albumin, RGD), and hydrophobic lipids and phospholipids. Regarding synthetic polymers, the most widely used are poly(ethyleneglycol) (PEG), polyvinyl alcohol (PVA), polyethyleneimine (PEI), and poly-L-lactic acid (PLA). Particle modification with these polymers provides organic linkers on the surface and, thus, a wide range of surface properties to suit various processes. The most common organic linkers are amine ($-NH_2$, $-NHR$, $-NR_2$), carboxylic acid ($-COOH$), aldehyde ($-CHO$), and thiol ($-SH$) groups.

PEI has been used for a long time in different industrial processes, such as paper production, water purification, and shampoo manufacturing.[3] In the pharmaceutical industry, a popular method to prevent burst release has relied on drug surface modification by coating with PEI.[4] PEI has also been used for the coating of stents to reduce inflammation and thrombogenicity.[5] Moreover, the PEI with amine linkers creates ionic interactions with protein molecules forming protein–polymer conjugates. PEI modified systems are utilized for prolonging the *in vivo* circulation half-live of therapeutic proteins, for reducing proteolysis, for avoiding chemical modification and denaturation during storage and administration, or for delivering targeted payloads of therapeutical proteins into specific tissues. Even though, the most generalized application of PEI involves *in vivo* gene delivery.[6,7] The transfer of DNA or siRNA into eukaryotic cells is considered a highly promising approach for the treatment of a wide spectrum of hereditary disorders. Many clinical trials have been performed with viral vectors for gene delivery, but the potential risks of undesired immune and toxic side reactions have raised some concerns.[8] As an alternative, non-viral vectors, such as cationic polymers, can be used as effective transfection reagents. Particularly for PEI, the large number of secondary amine groups in its cationic structure facilitates interaction with the negatively charged phosphate backbone of DNA. Indeed, PEI-coated magnetic nanoparticles was the first reported example of *in vitro* nanoparticle-mediated non-viral gene delivery.[9,10] Silica fine

powder have also been widely used for this purpose.[11,12] PEI coating enhances the cellular uptake of mesoporous silica particles and allows safe delivery of siRNA and DNA constructs.[13] For instance, in situ polimerization of aziridine in the presence of silica particles suspended in a liquid has been shown to form densely packed hyperbranched PEI grafted on the silica surface.[14]

Many other different techniques can be used to coat the surface of small particles, among others, dip coating, spray coating, sputtering, and layer-by-layer assembly.[15] Dip coating involves soaking the powder in a polymer or a polymer–drug solution. Spray coating involves spraying micro-droplets of a polymer or a polymer–drug solution directly onto the particles surface. A very thin coating can be obtained by using the more recently developed layer-by-layer assembly technology, in which oppositely charged polymers and drugs can be sequentially deposited.[16] However, when using processes based on solution chemistry, individual particle coating is difficult to achieve mainly due to particles aggregation and agglomeration. The vapor-phase transport route has been recently introduced to prepare polyamine-oxide hybrid materials.[17] Alternatively, replacement of organic solvents with compressed CO_2 results in an environmental friendly option.[18,19] Most of the works involving polymer coating of fine powder by compressed CO_2 based-technology have been carried out using the antisolvent method since compressed CO_2 has a limited solvent strength for many polymers of interest.[20–23]

The main objective of this work is to develop an alternative PEI coating method for small silica particles. In previous publications, we have reported on the supercritical preparation of impregnated drug delivery systems involving triflusal (Trf) and aerogel-like silica particles.[24] In this study, we have extended our background on compressed CO_2 impregnation and particle coating to the deposition of polymeric PEI thin coatings on the surface of aerogel-like particles, either pristine or previously impregnated with Trf. The possibilities of small particles coating by the in situ polymerization of ethyleneimine in the absence of liquid solvents are here demonstrated. By using compressed CO_2, the process is carried out at lower temperatures and shorter reaction times than the conventional liquid–solvent process.[19,25] Aspects of samples composition and polymer molecular weight, coverage, thermal stability, and morphological parameters of the synthesized hybrid products are discussed, together with a comparative study of the zeta potential. Besides, in vitro characterization by high-performance liquid chromatography (HPLC) proved that the hydrophilic PEI coating did not significantly modify the drug release kinetics.

EXPERIMENTAL

Materials

Ethyleneimine monomer (aziridine) was kindly donated by Menadiona S.A. The used solvent for PEI synthesis from aziridine units was compressed CO_2 (99.999% Carburos

Metálicos S.A.). For comparison purposes, hyperbranched PEI was purchased from Aldrich, with a molecular weight of 25 kDa determined by light scattering. Two different types of aerogel particles with different properties, such as composition and particle size, were studied: sub-micron silica particles (SiO_2 of 300 nm diameter) and magnetite/silica nanospheres ($Fe_3O_4@SiO_2$ of 70–100 nm diameter) referred to as AP and AP_{Fe}, respectively. Both AP and AP_{Fe} samples were synthesized in our laboratory by hydrolysis and polycondensation of tetramethylorthosilicate (TMOS, 98%, Sigma-Aldrich) and high temperature supercritical drying, according to the procedures described elsewhere.[26,27] Before PEI deposition, some aerogel particles were impregnated with Trf (kindly donated by Uriach S.A.), a platelet aggregation inhibitor, by a supercritical method.[24] Obtained materials were labeled as pre-impregnated Trf@AP and Trf@AP$_{Fe}$.

Equipment and Procedure
In Situ Synthesis of PEI-Coated Particles

The in situ coating of particles with PEI was carried out in a high-pressure reactor (Autoclave Engineers) of 100 mL running in the batch mode.[19] The vessel was charged with about 0.2 g of powder enclosed in a cylindrical cartridge made of 0.45-µm pore filter paper. The cartridge was placed in the upper part of the autoclave using a stainless steel platform. Liquid ethyleneimine (ca., 0.7 mL) was added at the bottom of the reactor, avoiding solid–liquid contact. To promote the polymerization of the monomer, the vessel was pressurized to 5 MPa with CO_2 at room temperature and left to react for 30 min. Low-molecular weight chains of PEI$_{CO2}$ which were not strongly bonded to the surface were eliminated by cleaning with a flow of compressed CO_2. A dry sample was recovered after depressurization. AP, Trf@AP, and Trf@AP$_{Fe}$ particles were coated following this procedure, and the obtained materials were labeled as AP_PEI$_{CO2}$, Trf@AP_-PEI$_{CO2}$, and Trf@AP$_{Fe}$_PEI$_{CO2}$, respectively. A similar blank experiment was performed without the addition of the solid powder. The polymer recovered from this experiment was labeled as PEI$_{CO2}$.

Standard PEI Noncovalent Coating of Particles

AP and AP$_{Fe}$ particles were coated with commercial PEI, following a standard soaking dip-coating procedure,[25] and the obtained samples were labeled as AP_PEI and AP$_{Fe}$_PEI, respectively. This procedure consisted of first dispersing 50 mg of SiO_2 particles in 5 mL of ethanol containing commercial PEI at a concentration of 2.5 mg mL^{-1}. The suspension was then sonicated for 15 min and magnetically stirred for 30 more minutes. The particles were centrifuged to eliminate the liquid phase and washed three times with 10 mL of ethanol, following the protocol of first sonication for 5 min and then centrifugation at 5000 rpm for 20 min.

Characterization

The presence of the aminopolymer coating on the particles surface was confirmed by Fourier transformed infrared (FTIR) spectroscopy using a Perkin–Elmer Spectrum One
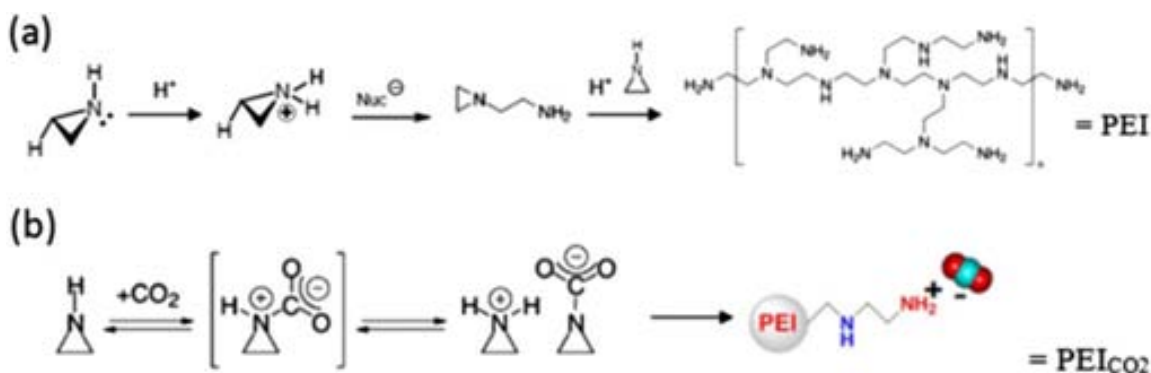
FIGURE 1 Schematic representation of different mechanisms established for the formation of hyperbranched PEI from aziridine under: (a) acid and (b) CO_2 catalysis. [Color figure can be viewed in the online issue, which is available at wileyonlinelibrary.com.]

instrument. Thermogravimetric analysis (TGA) of synthesized samples was performed with a TGA Instrument Q5000 IR under N_2 flow at a heating rate of 10 °C min^{-1}. Thermal transitions occurring in the raw synthesized polymer were analyzed by digital scanning calorimetry (DSC) using a Perkin Elmer DSC8500. Coated particles were morphologically characterized by transmission electron microscopy (TEM, JEOL JEM-1210 microscope). The hydrodynamic diameter (Φ_{hyd}) and the surface charge of the particles dispersed in water were measured at 25 °C using a Nano Zetasizer equipped with a He/Ne 633 nm laser (Malvern Instruments) by using the dynamic light scattering (DLS) method. The same equipment was used to estimate the molecular weight of the synthesized PEI_{CO2} by using the static light scattering (SLS) method. Four concentrations (0.25, 0.5, 0.75, and 1.00 g L^{-1}) of the polymer dissolved in deionized water were prepared. To determine the absolute molecular weight, a Debye plot was generated from the light scattering measurements performed for the solvent and polymer solutions. An Applied Biosystems Voyager 6214 time-of-flight mass spectrometer equipped with a matrix-assisted laser desorption/ionization source (MALDI-ToF) was also used to estimate the polymer molecular weight.

Drug release kinetic profiles were monitored by liquid chromatography, following a developed procedure described elsewhere.[28] The release of the active component was studied at pH = 2 in 0.01 M HCl medium, in which the stirring rate and temperature were fixed at 60 rpm and 37 °C, respectively. This pH was chosen to simulate physiological conditions at the stomach. Similar assays were performed at a pH of 7.4, in a mixture of phosphate salts at 0.01 M, used to simulate the blood plasma. Chromatograms were recorded by UV spectroscopy at 280 nm.

RESULTS AND DISCUSSION

PEI Polymerization Mechanism

PEI is a water soluble cationic polymer that can take both linear and branched forms.[29] The random branched structure is commonly produced by acid-catalyzed polymerization of aziridine monomers in aqueous or alcoholic solution.[30,31] The polymerization is activated by aziridine protonation, followed

of nucleophilic attack by a second aziridine molecule [Fig. 1(a)]. The ring opening polymerization can be also initiated by a Lewis acid, such as CO_2 [Fig. 1(b)].[32] For unsubstituted aziridine, CO_2 is not chemically incorporated to the polymer chain and the homopolymer is formed.[33] Unsubstituted aziridine reversibly generates the corresponding carbamic acid derivative in equilibrium with the corresponding ammonium carbamate.[34] The CO_2 sorbed into the synthesized PEI polymer is easily eliminated at temperatures of 80–100 °C.[35]

Currently, used methods to graft hyperbranched polyamines on inorganic surfaces need the use of organic solvents, catalysts, high temperatures, and/or long reaction times.[30,31] The present work tackles the possibility of simultaneous produce ethyleneimine polymerization and PEI grafting on the surface of small silica particles using compressed CO_2. The process takes place at low pressure and temperature and in the absence of any organic solvent.

Composition of Samples

FTIR spectroscopy was used to monitor the presence of the different components in the formed composites involving silica matrices, pre-impregnated Trf drug, and PEI as a coating agent.
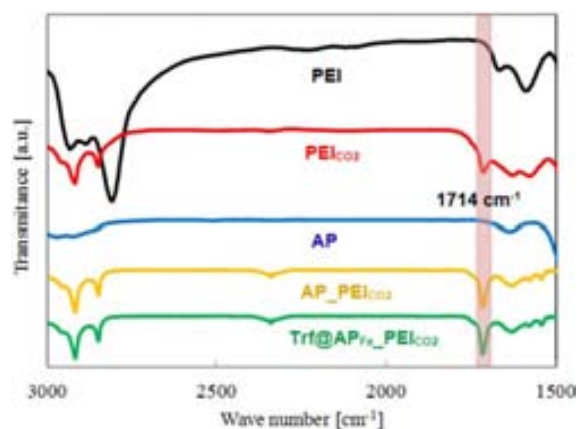

FIGURE 2 FTIR spectra in the range 3000–1500 cm^{-1} of the synthesized and commercial PEI polymers, and pristine, pre-impregnated and coated matrices. [Color figure can be viewed in the online issue, which is available at wileyonlinelibrary.com.]

Some representative spectra are shown in Figure 2 for samples PEI, PEI_{CO2}, AP, AP_PEI_{CO2}, and $Trf@AP_{Fe}\_PEI_{CO2}$ in the range of 3000–1500 cm^{-1}. Below 1500 cm^{-1}, intense absorption bands appear in the 900–1200 cm^{-1} region, corresponding to Si—O—Si vibrations in the aerogel skeleton, which complicated the observation of organic functional peaks. The band at 1620–1630 cm^{-1} was due to the bending frequency of molecular water adsorbed into the matrices. The useful FTIR region of solid Trf contained bands at about 1770 and 1685 cm^{-1} corresponding to the carbonyl groups of Trf and the hydrolyzed form, respectively. However, the presence of the preimpregnated drug in the coated matrices was difficult to assess using FTIR analysis, due to the low percentage of this organic compound in the composite samples.

The spectra of the PEI and PEI_{CO2} polymer exhibited the characteristic bands of the asymmetric and symmetric alkyl stretching modes at about 2990 and 2950 cm^{-1}, respectively. The most distinctive band in the spectrum of PEI_{CO2} was the C=O vibration appearing at about 1714 cm^{-1} and assigned to carbamate formed by interaction with CO_2 during *in situ* polymerization (Fig. 2). This band was also characteristic of PEI_{CO2} sample and did not appear in the spectrum of commercial PEI. The 1714 cm^{-1} carbonyl band was observed for PEI_{CO2} coated AP (AP_PEI_{CO2} sample) as well.

Polymer Molecular Weight and Structure

For PEI polymers, the average molecular weight achieved following the conventional liquid synthesis mode is typically within the range of 20–50 kDa.[36] The commercial PEI used in this work has a molecular weight of 25 kDa, as determined by light scattering. The molecular weight of a PEI_{CO2} sample was first determined using a SLS method, similarly to the approach used to determine the molecular weight of the commercial product. The estimated value was in the order of 8 ± 2 kDa, which corresponds to a low PEI molecular weight. To contrast the results, the PEI_{CO2} sample was also characterized by using the MALDI-ToF equipment. Significant amounts of 0.2–1 kDa chains were detected in the PEI_{CO2} by this technique [Fig. 3(a)], indicating a low molecular weight for the synthesized polymer, in agreement with the results obtained by SLS. Slight discrepancies on the absolute mass estimated using different characterization techniques are typical for such a low-molecular weight polymers, shifting the molecular weight distribution to lower masses for MALDI-ToF analysis.[37] The maximum peak intensity was centered at 132–304 Da, corresponding to 3 (129 Da)−7 (301 Da) repeating units (CH_2CH_2NH) in the protonated PEI molecule.

The process of PEI polymerization in aqueous or alcoholic solutions occurs in a homogeneous mixture, because of the high solubility of the monomer, the polymer, and the acid initiator in the continuous liquid phase. Solubilization of the polymer during polymerization results in the formation of high-molecular weight PEI. In contrast, due to the limited solubility of most polymers in compressed CO_2, low-molecular
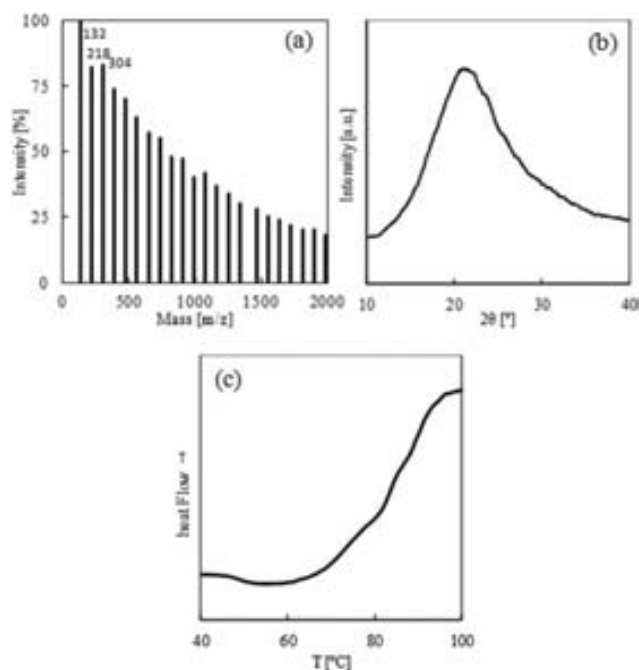

FIGURE 3 Characterization of synthesized PEI_{CO2} polymer: (**a**) MALDI-ToF mass spectrum, (**b**) X-ray diffractogram, and (**c**) DSC curve.

weight polymers are frequently obtained in supercritical and compressed CO_2 in the absence of surfactants.[38] The ring opening polymerization process carried out in the compressed fluid occurs at high reaction rates, since aziridine undergoes exothermic polymerization in contact with CO_2.[39] The quick heat release vaporized the monomer resulting in a visually observed vapor cloud, occurring at about 5 MPa under working conditions. Hence, the process featured an initially homogeneous vapor phase reaction, where monomer and initiator (in this case, the Lewis acid CO_2) are homogeneously mixed. During polymerization, the system became rapidly heterogeneous once the growing oligomeric chains reach a critical molar mass that exceeds the solubility limit in the compressed CO_2 vapor phase. Polymer precipitation would reduce significantly the molecular weight of the recovered PEI_{CO2}. In addition, polymer chains grafted on silica surface are expected to have a still lower molecular weight than the value found by SLS for PEI_{CO2} (ca., 8 kDa), due to factors related to strong steric hindrance occurring between the pendant polymer chains.[40] The high density of chains grafted onto the silica particles would interfere with the propagation of the hyperbranched tree-like structure, resulting in the decrease of the apparent molecular weight.[41,42]

High- and low-molecular weights polymers have different properties when considering their biomedical applications.[43–45] While high-molecular weight PEI (25–50 kDa) is quite effective for complexing and delivering nucleic acids, these systems repeatedly produce cytotoxicity due to the damage of cells, lysosomes, and mitochondrial membranes.[46,47] Decreasing PEI molecular weight to medium values (5–10 kDa) reduces cellular toxicity, while the
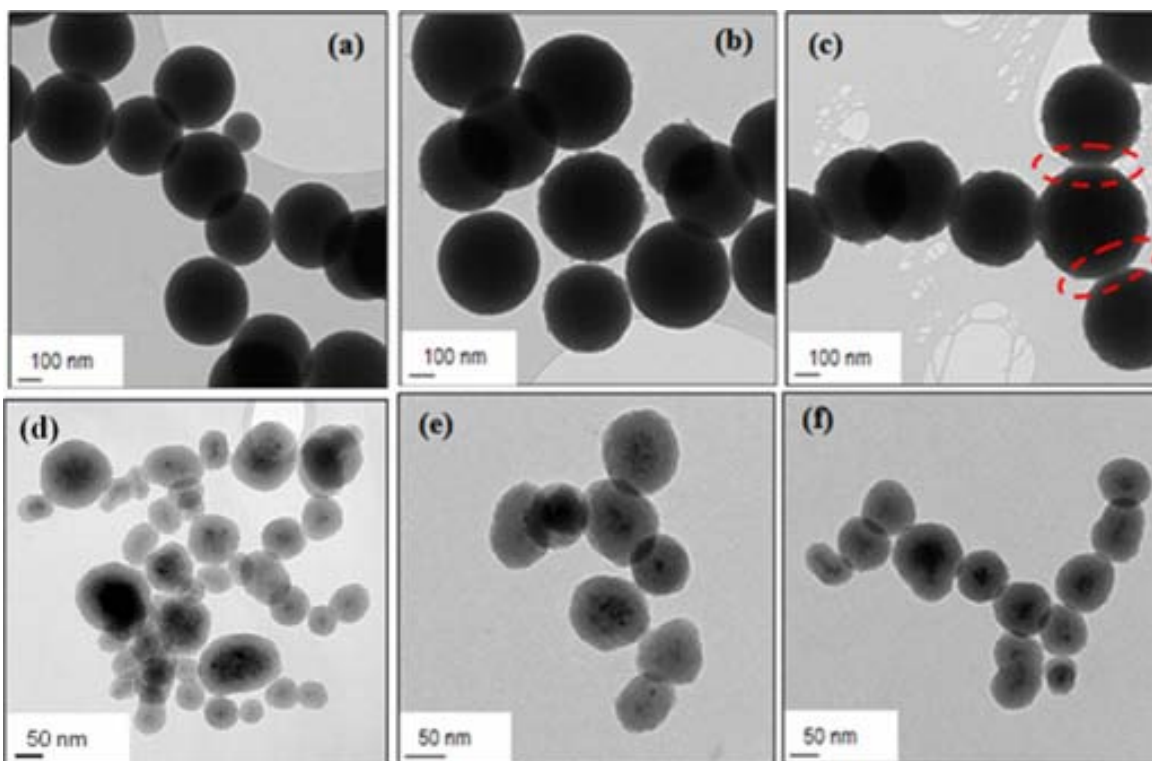
FIGURE 4 TEM micrographs of pristine, pre-impregnated, and coated particles: (**a**) AP, (**b**) AP_PEI, (**c**) AP_PEI$_{CO2}$, (**d**) AP$_{Fe}$, (**e**) AP$_{Fe}$_PEI, and (**f**) Trf@AP$_{Fe}$_PEI$_{CO2}$. [Color figure can be viewed in the online issue, which is available at wileyonlinelibrary.com.]

effectiveness of nucleic acid delivery is maintained. Finally, despite being ineffective at transfecting nucleotides, coating with low-molecular weight PEI (0.6–1.8 kDa) is efficient to several drug delivery applications. The molecular weight values estimated in this work for the *in situ* synthesized PEI$_{CO2}$ polymers are in the medium–low values, thus, resulting in compounds with a reduced cytotoxicity and biological potential applicability.

XRD analysis of synthesized PEI$_{CO2}$ indicated that the polymer had an amorphous structure [Fig. 3(b)], which suggested a highly branched configuration. Amorphous PEI$_{CO2}$ synthesized in CO_2 exhibited a glass transition step between 50 °C and 90 °C [Fig. 3(c)], similar to the one described for the 25 kDa commercial PEI centered at about 65 °C.[48]

Hybrid Composites Morphology
The bare AP matrix consists of spherical particles of 300 nm mean diameter with a 9% polydispersity [Fig. 4(a)]. After treatment with PEI, the as-recovered sub-micron particles had a similar morphology, but they were individually coated by the polymer, as it can be clearly observed in Figure 4(b,c) for coating with commercial PEI and PEI$_{CO2}$, respectively. In some photographs, a thin polymer layer joining two particles can be observed [Fig. 4(c)].

The AP$_{Fe}$ particulate matrix is characterized by a mean diameter of 70–100 nm and a 20% size dispersion [Fig. 4(d)]. The AP$_{Fe}$ nanocomposite was previously described of con-

sisting of a core of magnetite nanoparticles (ca., 6 nm diameter) surrounded by a shell of porous silica.[27] Similar coating to that observed for AP samples was observed for AP$_{Fe}$ samples after PEI coating [Fig. 4(e,f)].
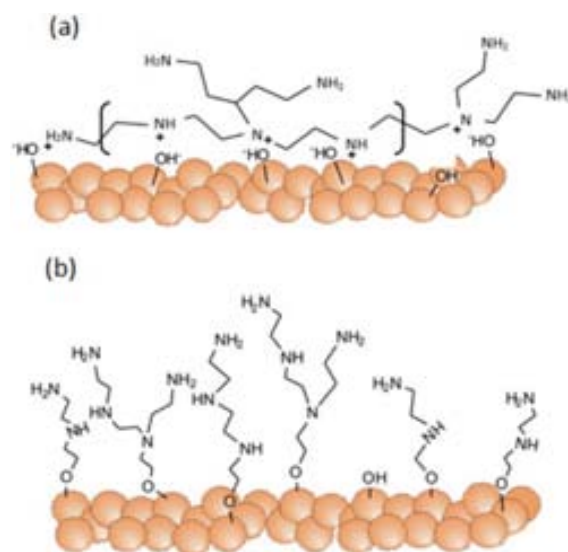

FIGURE 5 Schematic representation of different possible configurations of PEI on the surface of silica particles: (**a**) PEI deposited by electrostatic interactions and (**b**) PEI$_{CO2}$ grafted on the silanol groups. [Color figure can be viewed in the online issue, which is available at wileyonlinelibrary.com.]
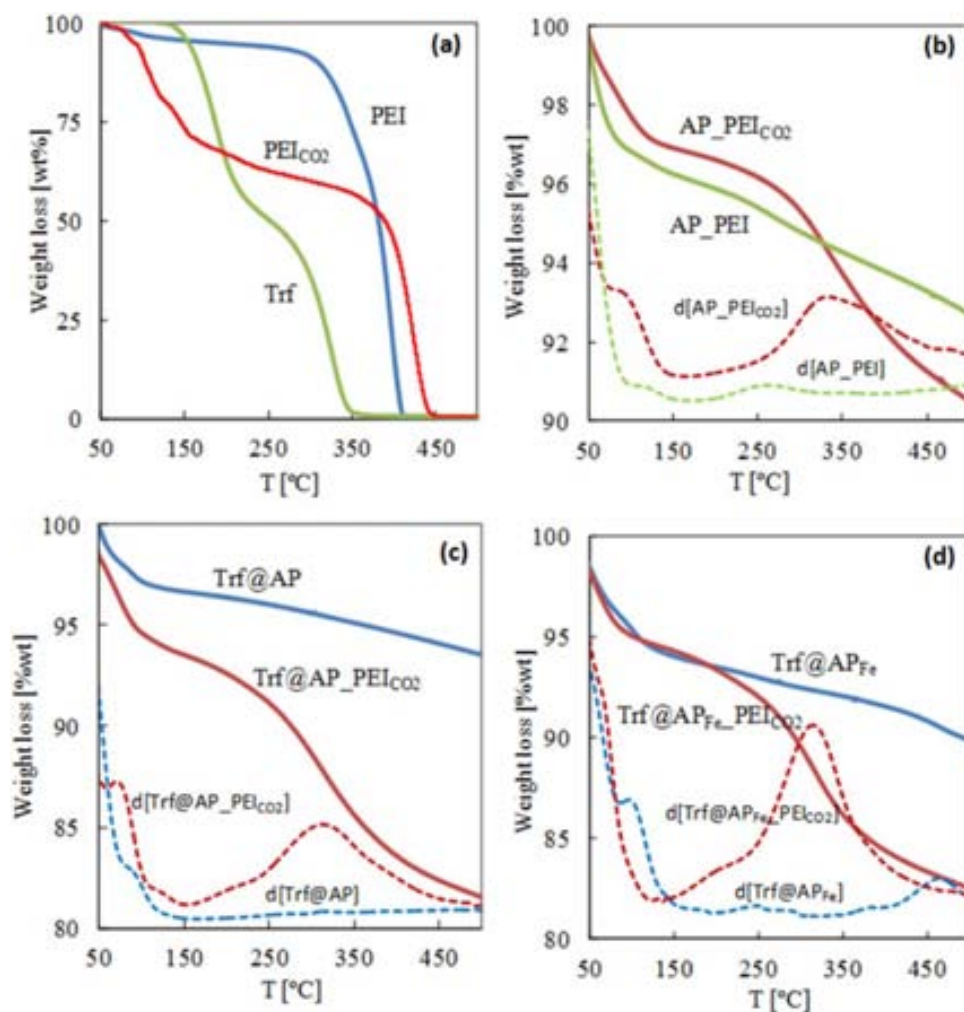
FIGURE 6 TGA profiles: (**a**) raw organics, (**b**) PEI and PEI$_{CO2}$ coated AP particles, and pre-impregnated and coated (**c**) AP particles and (**d**) AP$_{Fe}$ particles. d[xx] profiles correspond to the first derivative curves. [Color figure can be viewed in the online issue, which is available at wileyonlinelibrary.com.]

The aerogel-like pristine particles had a surface area of near 200 m^2 g^{-1} and a pore volume of about 0.07 cm^3 g^{-1}. They had a pore diameter in the order of 1.5–1.7 nm, which is a relatively small size, although still can easily accommodate organic molecules like Trf. However, hyperbranched PEI chains are expected to be predominantly accommodated on the external surface of the particles due to molecular size impediments, rather than embedded into the pores.[49] Some important differences regarding PEI and PEI$_{CO2}$ configuration on the particles surface are related with the preparation mode (Fig. 5).

For the high molecular mass PEI, which was here added to a particles suspension as a hyperbranched polymer, the most probable configuration is the one resulting from its electrostatic adsorption on the silica surface [Fig. 5(a)]. However, strong covalent links between the branched PEI$_{CO2}$ and the supports have been described for in-situ polymerization of aziridine in the presence of silica [Fig. 5(b)].[19,50,51]

Polymer Loading and Thermal Stability

PEI featured three-step weight decays in the temperature interval of 50°–500 °C, as recorded in the TGA measure-

ments [Fig. 6(a)]. Up to 150 °C, the weight loss was assigned to water evaporation for commercial PEI (5 wt %), and to water and CO$_2$ elimination for *in situ* prepared PEI$_{CO2}$ (25 wt %). PEI began to decompose above 150 °C and up to 375 °C the weight loss is gradual, with values of 50 and 30 wt % for PEI and PEI$_{CO2}$, respectively. When the temperature was increased above 375 °C, the degradation rate increased for both polymers, indicating that a different decomposition process took place.

At 500 °C, both studied PEI polymers were completely decomposed and removed as volatile species. TGA analysis indicated that samples consisting of PEI or PEI$_{CO2}$ deposited on the surface of the aerogel-like particles decomposed in a similar temperature range [ca., 150 °C–500 °C in Fig. 6(b)] than pristine polymers. Trf molecules were eliminated between 150 °C and 350 °C [Fig. 6(a)]. For samples containing aerogel particles, a plateau in the weight loss is not reached, even at temperatures of 500 °C. Indeed, aerogel matrices have a continuous weight loss at temperatures higher than 450 °C–500 °C and up to 800 °C–900 °C, due to

TABLE 1 Prepared samples and PEI weight percentage estimated from TGA data

Sample	PEI (wt %)	Z-Potential (mV)	Φ_{hyd} (nm)
AP	–	−55	575
AP_PEI	3.7	45	603
AP_PEI$_{CO2}$	6.5	58	771
Trf@AP	–		
Trf@AP_PEI$_{CO2}$	10	60	739
AP$_{Fe}$	–	−40	416
AP$_{Fe}$_PEI	5.5	33	239
Trf@AP$_{Fe}$	–		
Trf@AP$_{Fe}$_PEI$_{CO2}$	8.5	55	418

Measured values of zeta potential and cluster size, expressed as Φ_{hyd} in volume/intensity in water, are also given.

material densification occurring by the condensation of internal silanol groups and the concomitant loss of water.[52–54] The first derivative graphs are depicted in the figures involving silica matrices to indicate the temperature intervals used for weight lost calculations. Table 1 shows the mass of deposited polymer for the coated samples calculated using the TGA data. The accuracy of this method has previously been confirmed in similar silica–PEI composite samples by contrasting results with values obtained by elemental analyis.[17,19,55] PEI coated particles in compressed CO_2 showed a larger PEI % wt.

For Trf pre-impregnated samples, the drug incorporated was estimated from TGA weight loss measured in the 150 °C–350 °C range [Fig. 6(c,d)]. The estimated drug percentages were 2.1 and 3.3 wt % for Trf@AP and Trf@AP$_{Fe}$, respectively. The amount calculated for the PEI phase was found to be 5–10 wt %.

Zeta Potential

Important features of PEI are its high cationic charge density and the presence of reactive amine linkers. This characteristic overcomes one of the main drawbacks of the most extensively used PEG coating, which is the difficulty to further functionalize it with active biomolecules. Hence, PEI-based systems are widely used for gene delivery thanks to their ability to complex with DNA, to facilitate endosomal release via the "proton sponge effect", and to guide intracellular trafficking of their cargo into the nucleus. In the literature, it is shown that a positive net charge and, thus, a positive zeta potential, is necessary to allow complexes entering into the cells.[56] The silica surface of the studied aerogel-like systems had a negative zeta potential of −55 and −40 mV for AP and AP$_{Fe}$ samples, respectively. The coating with cationic PEI led to a sharp increase in the zeta potential, resulting in positive values of +30 to +60 mV for both Trf free and pre-impregnated samples (Table 1).

Data on the mean cluster hydrodynamic size, measured by dynamic light scattering, is also shown in Table 1. Encoun-

tered particle size values were higher than the values measured by TEM for the individual particles, due to clustering effects in the liquid suspension. Cluster size was not affected by coating with commercial PEI following the standard procedure. However, the hydrodynamic size of the clusters increased after PEI coating by using the CO_2-based procedure, reflecting the relatively high amount of deposited PEI$_{CO2}$ with respect to PEI [Fig. 6(b), Table 1]. As it was observed in the TEM micrographs for the PEI$_{CO2}$ coated particles, the polymer can joint several particles together to form clusters, thus, increasing the measured particle size [Fig. 4(c)].

Drug Release Profiles

Uncoated Trf@AP$_{Fe}$ and coated Trf@AP$_{Fe}$_PEI$_{CO2}$ samples were analyzed by HPLC to assess the influence of the coating in the drug release profile (Fig. 7). The percentage of Trf incorporated in each pre-impregnated sample was first determined by HPLC. Values obtained were in the order of 2.1 and 1.9 wt % for Trf@AP$_{Fe}$ and Trf@AP$_{Fe}$_PEI$_{CO2}$ samples, respectively. Impregnated Trf values measured using
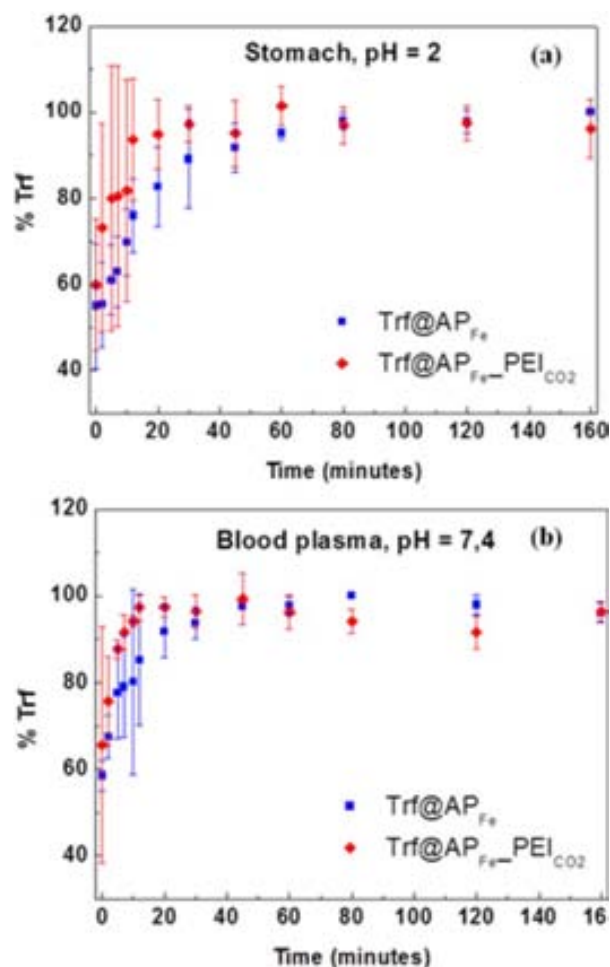

FIGURE 7 Trf delivery profiles obtained for uncoated and coated Trf@AP$_{Fe}$ particles in: (**a**) acid and (**b**) phosphate buffer media. [Color figure can be viewed in the online issue, which is available at wileyonlinelibrary.com.]

the HPLC approach were slightly lower than the values estimated by TGA, but nevertheless comparable. Release profiles were not significantly modified by polymer encapsulation when measured in either stomach [pH = 2 in Fig. 7(a)] or blood plasma [pH = 7.4 in Fig. 7(b)] simulated fluid.[57] For coated and uncoated silica aerogel nanospheres, the drug release occurred very fast and 95% of the drug was dissolved within the first 30 min.

CONCLUSIONS

PEI-coated aerogel silica fine powder is presented here as a versatile delivery system, which can facilitate cellular uptake to increase drug delivery payload, and also be utilized to improve nucleic acids delivery for therapeutic use. PEI was grafted to particles surface through covalent bonding by using a designed solventless compressed CO_2 procedure, starting with the ring-opening polymerization of aziridine. The achieved covalent grafting confers a high thermal and chemical stability. Moreover, the low molecular weight of PEI prepared following the *in situ* polymer synthesis (ca., 8 kDa by SLS) should result in a toxicity decrease of the PEI coated particles. Owing to the relatively low pressure used in the PEI synthesis procedure, drug pre-impregnated systems could be coated with PEI, avoiding drug degradation, a significant loss of the loaded drug and the modification of pre-designed release profiles.

REFERENCES AND NOTES

1 W. R. Gombotz, D. K. Pettit, *Bioconjugate Chem.* **1995**, *6*, 332–351.

2 G. A. Hughes, *Nanomed. Nanotechnol. Biol. Med.* **2005**, *1*, 22–30.

3 R. L. Davidson, M. Sittig, Water-soluble resins, **1968**; Reinhold Book Corp., ISBN 0278916139.

4 X. Huang, C. S. Brazel, *J. Control. Release* **2001**, *73*, 121–136.

5 G. Acharya, K. Park, *Adv. Drug Deliv. Rev.* **2006**, *58*, 387–401.

6 R. Kircheis, L. Wightman, E. Wagner, *Adv. Drug Deliv. Rev.* **2001**, *53*, 341–358.

7 D. W. Pack, A. S. Hoffman, S. Pun, P. S. Stayton, *Nat. Rev. Drug Discov.* **2005**, *4*, 581–593.

8 K. Kunath, A. von Harpe, D. Fischer, H. Petersen, U. Bickel, K. Voigtc, T. Kiss, *J. Control. Release* **2003**, *89*, 113–125.

9 F. Scherer, M. Anton, U. Schillinger, *Gene Ther.* **2002**, *9*, 102–109.

10 O. Veiseh, J. W. Gunn, M. Zhang, *Adv. Drug Deliv. Rev.* **2010**, *62*, 284–304.

11 B. Steitz, H. Hofmann, S. W. Kamau, P. O. Hass, M. O. Hottiger, B. von Rechenberg, M. Hofmann-Amtenbrink, A. Petri-Fink, *J. Magn. Magn. Mater.* **2007**, *311*, 300–305.

12 S. C. McBain, H. H. P. Yiu, J. Dobson, *Int. J. Nanomed.* **2008**, *3*, 169–180.

13 T. Xia, M. Kovochich, M. Liong, H. Meng, S. Kabehie, S. George, J. I. Zink, A. E. Nel, *ACS Nano* **2009**, *3*, 3273–3286.

14 C. O. Kim, S. J. Cho, J. W. Park, *J. Colloid Interf. Sci.* **2003**, *260*, 374–378.

15 F. Caruso, *Adv. Mater.* **2001**, *13*, 11–22.

16 K. Ariga, J. P. Hill, Q., Ji, *Phys. Chem. Chem. Phys.* **2007**, *9*, 2319–2340.

17 W. Chaikittisilp, S. A. Didas, H.-J. Kim, C. W. Jones, *Chem. Mater.* **2013**, *25*, 613–622.

18 A. I. Cooper, *J. Mater. Chem.* **2000**, *10*, 207–234.

19 P. López-Aranguren, L. F. Vega, C. Domingo, *Chem. Commun.* **2013**, *49*, 11776–11778.

20 F. Cansell, C. Aymonier, *J. Supercrit. Fluids* **2009**, *47*, 508–516.

21 K. P. Seremeta, D. A. Chiappetta, A. Sosnik, *Colloid Surf. B: Biointerf.* **2013**, *102*, 441–449.

22 A. Vega-González, P. Subra-Paternault, A. M. López-Periago, C. A. García-González, C. Domingo, *Eur. Polym. J.* **2008**, *44*, 1081–1094.

23 S. G. Kazarian, *Polym. Sci. Ser. C* **2000**, *42*, 78–101.

24 N. Murillo-Cremaes, A. M. López-Periago, J. Saurina, A. Roig, C. Domingo, *J. Supercrit. Fluids* **2013**, *73*, 34–42.

25 H. Meng, M. Xue, T. Xia, Z. Ji, D. Y. Tarn, J. I. Zink, A. E. Nel, *ACS Nano* **2011**, *5*, 4131–4144.

26 M. Moner-Girona, A. Roig, E. Molins, *J. Sol-Gel Sci. Technol.* **2003**, *26*, 645–649.

27 E. Taboada, R. Solanas, E. Rodríguez, R. Weissleder, A. Roig, *Adv. Funct. Mater.* **2009**, *19*, 2319–2324.

28 A. Argemí, A. López-Periago, C. Domingo, J. Saurina, *J. Pharm. Biomed. Anal.* **2008**, *46*, 456–462.

29 R. Kircheis, L. Wightman, E. Wagner, *Adv. Drug Deliv. Rev.* **2001**, *53*, 341–358.

30 S. Minakata, Y. Okada, Y. Oderaotoshi, M. Komatsu, *Org. Lett.* **2005**, *7*, 3509–3512.

31 P. Kubisa, S. Penczek, *Prog. Polym. Sci.* **1999**, *24*, 1409–1437.

32 T. Sakakura, J.-C. Choi, H. Yasuda, *Chem. Rev.* **2007**, *107*, 2365–2387.

33 K. Soga, S. Hosoda, S. Ikeda, *Macromol. Chem. Phys.* **1974**, *175*, 3309–3314.

34 D. B. Dell'Amico, F. Calderazzo, L. Labella, F. Marchetti, G. Pampaloni, *Chem. Rev.* **2003**, *103*, 3857–3897.

35 M. Schladt, T. P. Filburn, J. J. Helble, *Ind. Eng. Chem. Res.* **2007**, *46*, 1590–1597.

36 A. von Harpe, H. Petersen, Y. Li, T. Kissel, *J. Control. Release* **2000**, *69*, 309–322.

37 E. Rivera-Tirado, C. Wesdemiotisa, *J. Mass. Spectrom.* **2011**, *46*, 876–883.

38 F. Rindfleisch, T. P. DiNoia, M. A. McHugh, *J. Phys. Chem.* **1996**, *100*, 15581–15587.

39 A. Dermer, Ethylenimine and Other Aziridines: Chemistry and Applications; Academic Press, Inc.: UK, **1969**.

40 M. Khan, W. T. S. Huck, *Macromolecules* **2003**, *36*, 5088–5093.

41 Y. Kaneko, Y. Imai, K. Shirai, T. Yamauchi, N. Tsubokawa, *Colloids Surf. A: Physicochem. Eng. Aspects* **2006**, *289*, 212–218.

42 Y. Yu, M. Z. Rong, M. Q. Zhang, *Polymer* **2010**, *51*, 492–499.

43 D. Fischer, T. Bieber, Y. Li, H.-P. Elsasser, T. Kissel, *Pharm. Res.* **1999**, *16*, 1273–1279.

44 M. Neu, D. Fischer, T. Kissel, *J. Gene. Med.* **2005**, *7*, 992–1009.

45 X. Huang, M. S. Heo, J.-W. Yoo, J.-S. Choi, I. Kim, *J. Polym. Sci., Part A: Polym. Chem.* **2014**, *52*, 1643–1651.

46 W. Shao, A. Paul, S. Abbasi, P. S. Chahal, J. A. Mena, J. Montes, A. Kamen, S. Prakash, *Int. J. Nanomed.* **2012**, *7*, 1575–1586.

47 D. L. Clemens, B.-Y. Lee, M. Xue, C. R. Thomas, H. Meng, D. Ferris, A. E. Nel, J. I. Zink, M. A. Horwitz, *Antimicr. Agents Chemother.* **2012**, 2535–2545.

48 M. M. Mady, W. A. Mohammed, N. M. El-Guendy, A. A. Elsayed, *Int. J. Phys. Sci.* **2011**, *6*, 7328–7334.

49 J. P. Reynhardt, Y. Yang, A. Sayari, H. Alper, *Adv. Funct. Mater.* **2005**, *15*, 1541–1646.

50 Y. K. Buchman, E. Lellouche, S. Zigdon, M. Bechor, S. Michaeli, *J.-P. Lellouche. Bioconjugate Chem.* **2013**, *24*, 2076–2087.

51 J. H. Drese, S. Choi, R. P. Lively, W. J. Koros, D. J. Fauth, M. L. Gray, C. W. Jones, *Adv. Funct. Mater.* **2009**, *19*, 3821–3832.

52 C. P. Jaroniec, R. K. Gilpin, M. Jaroniec, *J. Phys. Chem. B* **1997**, *101*, 6861–6866.

53 R. P. W. Scott, S. Traiman, *J. Chromatogr.* **1980**, *196*, 193–205.

54 M. L. Pena, V. Della Rocca, F. Rey, A. Corma, S. Coluccia, L. Marchase, *Micropor. Mesopor.* **2001**, *44*, 345–356.

55 J. C. Hicks, PhD dissertation: Organic/inorganic hybrid amine and sulfonic acid tethered silica materials: synthesis, characterization and application, Georgia Institute of Technology, **2007**.

56 T. Nomura, S. Nakjima, K. Kawabata, F. Yamashita, Y. Takakura, M. Hashida, *Cancer Res.* **1997**, *57*, 2681–2686.

57 C. Ghoroi, L. Gurumurthy, D. J. McDaniel, L. J. Jallo, R. N. Davé, *Powder Technol.* **2013**, *236*, 63–74.